Osteochondral Tissue Engineering for the TMJ Condyle Using a Novel Gradient Scaffold

By

Milind Singh

Submitted to the Department of Chemical and Petroleum Engineering and the
Faculty of the Graduate School of the University of Kansas
In partial fulfillment of the requirements for the degree of
Doctor of Philosophy

Committee members

Dr. Michael Detamore, Committee Chair

Dr. Cory Berkland

Dr. Elizabeth Topp

Dr. Kenneth Fischer

Dr. Stevin Gehrke

Date defended

The Dissertation Committee for Milind Singh certifies
that this is the approved version of the following dissertation:

Osteochondral Tissue Engineering for the TMJ Condyle
Using a Novel Gradient Scaffold

Committee members

Dr. Michael Detamore, Committee Chair

Dr. Cory Berkland

Dr. Elizabeth Topp

Dr. Kenneth Fischer

Dr. Stevin Gehrke

Date defended

ABSTRACT

The articulation of the temporomandibular joint (TMJ), or the jaw joint, is one of the most complex and least studied joints of the musculoskeletal system. Painful disorders of the TMJ, known as temporomandibular disorders (TMDs), have considerable prevalence with over 10 million patients in the United States alone, which may severely interfere with everyday activities like chewing, yawning, talking, and laughing. Within the TMJ, the inferior joint space, which includes the mandibular condyle, typically sustains the greatest damage in TMDs. The objective of this dissertation was to characterize the condylar cartilage biomechanics, and to explore novel routes to fabricate integrated gradient-based osteochondral constructs. Pioneering efforts were made toward understanding structure-function correlations for the condylar cartilage. A greater stiffness of the condylar cartilage in the anteroposterior direction than in the mediolateral direction under tension was observed, corresponding to the never before seen anteroposterior organization of collagen fibers. A positive correlation between the thickness and stiffness of the cartilage under compression suggested that their regional variations may be related phenomena caused in response to cartilage loading patterns. Beyond these vital biomechanical characterization efforts, novel microsphere-based gradient scaffolds were developed to address functional osteochondral tissue regeneration. Novel microsphere sintering routes, using ethanol as an anti-solvent or sub-critical CO_2 for melting point depression, were established to construct microsphere-based scaffolds. A technique to create opposing macroscopic gradients of encapsulated growth factors

using poly(D,L-lactide-co-glycolic acid) microspheres was developed, and *in vitro* studies with human umbilical cord stem cells provided promising results for osteochondral tissue regeneration. By encapsulating nanoparticles in the microspheres, a proof-of-concept was provided for creating functional scaffolds with a gradient in stiffness. This dissertation lays down the foundation for a combined growth factor-stiffness gradient approach that could lead to a translational-level regenerative solution to osteochondral tissue regeneration with extended applications in other areas, including tissue engineering of heterogeneous/interfacial tissues.

ACKNOWLEDGMENTS

I gratefully acknowledge funding from the National Institute of Dental and Craniofacial Research NIH-NIDCR grant 1R21 DE017673-01A1 and the Juvenile Diabetes Research Foundation. I would like to acknowledge Drs. Michael Detamore, Cory Berkland, Stevin Gehrke, Kenneth Fischer, and Elizabeth Topp for serving on my dissertation committee and for their valuable guidance in the preparation of this Ph.D. dissertation. I would also like to acknowledge those who have provided guidance and assistance toward this dissertation project over the years, which include Mr. Alan Walker and Mr. Scott Ramskill for their assistance in building the bath-grip-platen assembly, Dr. David Moore for his instrumental guidance with operating the SEM and confocal microscopes, Dr. Eric Munson for providing access to a DSC facility, Mr. Rasesh Kapadia of Scanco Medical for helping with the microCT scanning and analysis, Dr. Terence McIff for his collaborative contribution with a preliminary *in vivo* study, Dr. Lynda Bonewald and Ms. Jennifer Rosser for their guidance in the preparation of *in vivo* tissue samples, Dr. Mark Weiss and Dr. Kiran Babu Seshareddy for their generous contribution of the HUCMSCs for the sub-critical CO_2 study, Dr. Aaron Scurto for providing access to the facilities in his lab and his guidance in the sub-critical CO_2 study, Dr. Eiji Tanaka for providing valuable data relevant to a manuscript, and Dr. James Bresnahan for his assistance in the preparations of the IACUC protocols.

I would like to offer thanks to the undergraduate students who completed projects under my supervision, including Grant Snider, Ryan Ellis, Jordan Christian,

Brindar Sandhu and Jeannie Salash, for their intelligent, intuitive, and productive work that they performed in an efficient manner. I would also like to thank my other lab members, who constantly helped me. In particular, thanks to undergraduates Chris Roach and Mihael Lazebnik for their contribution with the lab maintenance, and for having countless long philosophical discussions on relevant and non-relevant topics. Thanks to Dr. Liang Zhao for his guidance with flow cytometry. Thanks to Mr. Nathan Dormer for providing valuable help with the AFM characterization and stiffness gradient study. A special thanks to Dr. Limin Wang for the continuous exchange of ideas and providing help on countless occasions with many protocols.

I am indebted to my advisor, Dr. Michael Detamore, for being a truly exceptional mentor, for providing continuous support and guidance regarding professional as well as personal matters each and every day, and for leading me to the path that I have chosen. A special recognition goes to my co-advisor, Dr. Cory Berkland, who was insightful, motivating and very supportive towards my academic pursuits throughout.

Finally, I want to thank my parents, Mahendra and Shashi, my sibling, Prateek, my girlfriend, Shilpi, and my extended family for their unconditional love and support, providing me the motivation and a reason to look forward to the future.

TABLE OF CONTENTS

LIST OF FIGURES

CHAPTER 9

CHAPTER 10

No Figures

LIST OF TABLES

CHAPTER 1: Introduction

The overall objective of this dissertation was to characterize the condylar cartilage biomechanics, and to explore novel routes to fabricate integrated functional osteochondral constructs. In the characterization phase, the objective was to determine and model the tensile and compressive properties of the mandibular condylar cartilage. The next phase was then to develop integrated osteochondral scaffolds and evaluate them for osteochondral tissue regeneration. The characterization stage provided important mechanical property data that were largely missing from the literature, providing a 'gold standard' reference, which may serve as the design criteria for future condylar cartilage and mandibular condyle tissue engineering studies. In the scaffold development stage, a combination of microparticle technology and unconventional microsphere-sintering techniques (i.e., ethanol sintering, sub-critical CO_2 processing) were applied toward the fabrication of seamless gradient scaffolds containing opposing gradients of encapsulated factors. The scaffolds were evaluated for their tissue engineering performance *in vitro*, and important steps were taken toward the functional regeneration of interfacial tissues by introducing macroscopic stiffness gradient scaffolds. To achieve the overall objective, three Specific Aims were designed:

1) To characterize the mechanical properties of the condylar cartilage. This aim was accomplished via biomechanical testing under tension and compression, and viscoelastic modeling. It was hypothesized that *the condylar cartilage would*

exhibit a greater stiffness in the anteroposterior direction than in the mediolateral direction under tension due to collagen fiber orientation, and would exhibit a regional heterogeneity correlated with the regional cartilage thickness under compression. Uniaxial tensile testing was performed in two different directions with three regions per direction, and unconfined compression was performed for five different regions.

2) To develop integrated osteochondral constructs using novel microsphere-sintering techniques. This aim consisted of two phases, which were performed in parallel. One phase consisted of the development of a novel gradient scaffold fabrication technology, which was utilized to fabricate microsphere-based scaffolds using an ethanol sintering technique. In phase two, an alternate method of microsphere sintering – CO_2 processing at sub-critical conditions – was developed and refined for the fabrication of microsphere-based scaffolds. Using microspheres encapsulated with model factors or nanoparticles, it was hypothesized that *the sintering techniques could be applied to fabricate microsphere-based scaffolds that possess opposing gradients of encapsulated growth factors or a gradient in scaffold stiffness, and a CO_2 processing method would provide a cytocompatible route to fabricate such scaffolds.*

3) To evaluate the integrated osteochondral constructs for tissue regeneration *in vitro.* To accomplish this aim, a 6 wk *in vitro* study was performed using bone marrow stromal stem cells with the signal gradient scaffolds designed in Specific Aim 2, and validated with a biomechanical design criterion developed in Specific

Aim 1. Constructs containing opposing gradients of bone and cartilage promoting growth factors were compared against a control group having no growth factors. The hypothesis was that *the gradient scaffolds would outperform blank scaffolds for* in vitro *tissue regeneration*

The organization of the remaining chapters is as follows:

Chapters 2 and 3 serve to provide background information, where the literature pertinent to the subsequent chapters is comprehensively reviewed. In Chapter 2, a review of the biomechanical properties of the condylar cartilage is provided, highlighting its structure-function correlations in relation to the TMJ disc, citing the deficiencies in the mechanical characterization data, and delineating its importance for the TMJ finite element modeling community. Chapter 3 provides a rationale to the tissue engineering community for the incorporation of signal and biomaterial-based gradients in scaffold design, where several gradient generation methodologies from different areas of scientific research are brought together and presented to address biomimetic, functional, and/or interfacial tissue regeneration. After the background information is established in Chapters 2 and 3, Chapters 4 – 9 address the experiments performed to satisfy the aforementioned Specific Aims.

Chapters 4 and 5 serve to address Specific Aim 1. Chapter 4 corresponds to the tensile testing of the native condylar cartilage, where stress relaxation and viscoelastic modeling were performed. Chapter 5 constitutes the regional compressive characterization of the native condylar cartilage under high strain compression, followed by viscoelastic modeling.

Specific Aim 2 is addressed in Chapters 6–8. In Chapter 6, a scaffold fabrication set-up was designed and built that allowed controlled positioning of the microspheres along the axis of the cylindrical molds. In Chapter 7, an attempt was made to mimic the mechanical properties of the interfacial region. Using microspheres encapsulating nano-phase filler materials (i.e., nano-phase $CaCO_3$ or TiO_2), initial steps were taken toward the development of stiffness gradient scaffolds that may allow functional regeneration of interfacial tissues, in general. In Chapter 8, a novel cytocompatible technique was developed to produce cell-loaded shape-specific scaffolds and patches using a single-step sub-critical CO_2 sintering of microspheres in the presence of cells at near-ambient temperatures.

Chapter 9 focuses on Specific Aim 3, which involved *in vitro* osteochondral tissue engineering, where bone marrow stromal stem cells (BMSCs) were induced with simultaneous osteogenesis and chondrogenesis with opposing gradients of bone morphogenic protein (BMP)-2 and transforming growth factor (TGF)-β_1, respectively.

Chapter 10 is the conclusion, where findings are summarized in a global context and exciting directions that may be pursued in the imminent future are discussed.

CHAPTER 2: Biomechanical Properties of the Mandibular Condylar Cartilage and Their Relevance to the TMJ Disc*

ABSTRACT

Mandibular condylar cartilage plays a crucial role in temporomandibular joint (TMJ) function, which includes facilitating articulation with the TMJ disc, reducing loads on the underlying bone, and contributing to bone remodeling. To improve our understanding of TMJ function in normal and pathological situations, accurate and validated three-dimensional (3-D) finite element models (FEMs) of the human TMJ may serve as valuable diagnostic tools as well as predictors of thresholds for tissue damage resulting from parafunctional activities and trauma. In this context, development of reliable biomechanical standards for condylar cartilage is crucial. Moreover, biomechanical characteristics of native tissue are important design parameters for creating functional tissue-engineered replacements. Towards these goals, biomechanical characteristics of the condylar cartilage have been reviewed here, highlighting the structure-function correlations. Structurally, condylar cartilage, like the TMJ disc, exhibits zonal and topographical heterogeneity. Early structural investigations of the condylar cartilage have suggested that the tissue possesses a somewhat transversely isotropic orientation of collagen fibers in the fibrous zone. However, recent tensile and shear evaluations have reported a higher stiffness of the tissue in the anteroposterior direction than in the mediolateral direction,

*Chapter submitted to J Biomech as Singh and Detamore, "Biomechanical Properties of the Mandibular Condylar Cartilage and Their Relevance to the TMJ Disc", September 2008.

corresponding to an anisotropic fiber orientation comparable to the TMJ disc. In a few investigations, condylar cartilage under compression was found to be stiffer anteriorly than posteriorly. As with the TMJ disc, further compressive characterization is warranted. To draw inferences for human tissue using animal models, establishing stiffness-thickness correlations and regional evaluation of proteoglycan/glycosaminoglycan content may be essential. Efforts directed from the biomechanics community for the characterization of TMJ tissues will facilitate the development of reliable and accurate 3-D FEMs of the human TMJ.

INTRODUCTION

The mandibular condyle, the temporomandibular joint (TMJ) disc and the fossa-eminence complex together form the two-compartment articulation of the TMJ.[1] Disorders of the TMJ, known as temporomandibular disorders (TMDs), have considerable prevalence with 16–59% of the population having symptoms and 33–86% having clinical signs.[2] According to the diagnostic classification system of the American Academy of Orofacial Pain (AAOP), TMDs are subcategorized in two primary classes: articular and muscle-related disorders, based on their anatomic origin.[3] Biomechanics as a field is important for the TMJ for two primary reasons. First, biomechanical dysfunctions (such as clicking, locking, or lateral deviation in mouth opening) are symptoms that generally accompany many TMDs of articular origin. The other reason, of special interest to the clinical community, is that biomechanics is a likely contributor in the development of such TMDs, e.g.,

biomechanical alterations resulting from parafunctional behavior or trauma that may lead to the development of or exacerbate an existing pathological condition. In other words, we are interested in TMJ biomechanics from both the cause and effect perspectives in relation to TMDs.

What kinds of forces are necessary to irreparably damage the tissues in the TMJ, and what are the associated magnitudes and durations of these forces? Fortunately, a growing number of researchers are building three dimensional (3-D) finite-element models (FEMs) of the human TMJ to answer this question. A major limitation with such models pertains to the inclusion of material properties that do not represent the constituent tissues, which may render them inaccurate. In this context, development of reliable biomechanical standards for TMJ cartilaginous tissues, including the mandibular condylar cartilage, will be a useful input to further the development of 3-D FEMs of the human TMJ. Among biomechanical studies of the cartilaginous tissues of TMJ, the TMJ disc has by far received the most attention (see reviews by Detamore and Athanasiou[4, 5]). This review primarily focuses on the mandibular condylar cartilage, an articular cartilage that is distinct from the articular hyaline cartilages of appendicular skeleton,[6] specifically inspecting independent evaluations of biomechanical properties of the tissue as a reflection of the known extracellular matrix (ECM) organization, and providing recommendations to validate critical structure-function correlations. A brief perspective on 3-D FEMs of the human TMJ is also provided, highlighting potential applications of such computational models. Highly accurate and validated models would be valuable tools

for clinical diagnosis of TMJ disorders, and could be useful for evaluating the implications of parafunctional activity (*e.g.*, bruxism) and trauma as a means to substantiate preventive measures for TMJ disorders.

BIOMECHANICAL PROPERTIES OF THE CONDYLAR CARTILAGE AS A REFLECTION OF ECM ORGANIZATION

Condylar cartilage is a viscoelastic tissue that exhibits characteristic responses of creep, stress relaxation and hysteresis.[7-9] The tissue functions in a complex force-field, experiencing simultaneous compression and shear.[10] The cartilage ECM is heterogeneous both topographically and zonally, reflecting its versatility in responding to varying functional demands. Conflicting views remain for the schemes of zonal delineation and terminologies used to describe the zone-based histological architecture of the condylar cartilage.[11, 12] For a comparative analysis, the commonly used zonal classification of four zones has been used in this review: *fibrous zone*, *proliferative zone*, *mature zone*, and *hypertrophic zone*, categorized in a distal-proximal manner relative to the subchondral bone of the condyle (Fig. 2.1). Furthermore, to compare the regional variations in properties, we have divided the condylar cartilage anteroposteriorly into three regions (anterior, superior and posterior), and mediolaterally into three sections (medial, central and lateral). Major ECM components discussed in the manuscript are collagen (types I and II) and proteoglycans. Proteoglycans are glycoproteins, having a long core protein with at least one associated anionic glycosaminoglycan (GAG) side-chain.[13, 14] Among

primary GAG molecules in this context are chondroitin sulfate (CS), keratin sulfate (KS), and dermatan sulfate (DS). Large chondroitin sulfate proteoglycans (CSPGs), such as aggrecan (with CS and KS side-chains) and versican (with CS side-chains exclusively), contain several GAG moieties. In contrast, dermatan sulfate proteoglycans (DSPGs) are small proteoglycans with one (decorin) or two (biglycan) GAG side-chains. Biomechanical characterization studies of the condylar cartilage are discussed under the following two subsections – a) tension/shear, and b) compression, where ECM organization with respect to aforementioned major ECM components is discussed, followed by a synopsis of important future considerations.

Tension and Shear

Condylar cartilage experiences tensile loads primarily due to shear and friction produced by mandibular motion especially in the regions closer to the joint synovium.[9] Unlike under compression, viscoelasticity of the articular cartilage under tension is primarily governed by the solid constituents in a relatively flow-independent manner.[15] Collagen, which forms more than 60% of the dry weight of condylar cartilage (in rabbits),[16] is the primary ECM component responsible for the tensile resistance of the soft tissues.[15] In the following sub-sections, tensile and shear properties of the condylar cartilage and collagen organization in the tissue are reviewed. In addition, distribution of dermatan sulfate proteoglycans (DSPGs), which also play a role in the enhancement of tensile properties,[4] are briefly discussed.

Tensile and shear evaluations

There are four studies that have reported the tensile or shear evaluations of porcine condylar cartilage.[9, 17-19] Specimen preparation-wise, cartilage specimens were tested in only one study,[9] while cartilage-bone specimens were utilized in the others. Tensile evaluations confirmed the viscoelastic nature of the tissue.[9, 17] Interestingly, the directional differences (anteroposterior vs. mediolateral) in the elastic moduli were found to be statistically significant in both tensile and shear testing,[9, 17, 18] where a higher stiffness in the anteroposterior direction than in the mediolateral direction was reported. Intuitively, it may indicate a relationship between shear and tension somewhat analogous to a cause and effect relationship, respectively. So far, data for the failure properties,[17] stress relaxation behavior[9] and shear dynamics of porcine condylar cartilage[18, 19] are available, which are summarized in Table 2.1.

While these pioneering efforts certainly provide valuable property data, the characterization of tensile and shear properties is not complete. To provide specific examples: 1) strain-rate dependent behavior of the condylar cartilage under tension remains unexplored, as the tensile properties of the tissue were measured at fixed strain-rate values; 2) failure properties of the tissue were not determined at physiological temperature ;[17] 3) viscoelastic creep for the tissue under tension has not been tested yet; 4) human tissues have yet to be tested; and 5) shear has so far been evaluated in only one of the several possible jaw configuration (i.e., at a constant compression level of 10% strain; corresponding to maximum clenching, as the

authors noted).[18, 19] In addition, considering parafunctional activities, where loading conditions are different than those under normal function, a broader range of test parameters (i.e., load levels, strain rates, frequencies) that may include levels of physiological extremities may be desired. Further testing is required to fully characterize the tensile and shear properties of the tissue, including the probing of regional and zonal differences in the tissue.

Organization and distribution of collagen

With regard to the collagen fiber organization and orientation, light and transmission electron microscopic observations of condylar cartilage from primate and rodent models have indicated that the cartilage possesses a zonal heterogeneity. At the level of individual collagen fibrils, the average diameter of the fibrils was observed to vary from one zone to another (average diameters ~100 nm).[20] Table 2.2 summarizes available data for the fiber/fibrils diameters. Regarding orientation, previous microscopic structural investigations of the condylar cartilage indicated that the collagen fibers in the fibrous zone appear to run predominately parallel to the surface but not to each other, forming sheet-like structures,[20-24] indicating a transversely isotropic fiber orientation. However, in a recent macroscopic investigation of the condylar cartilage, an anisotropic fiber orientation in the fibrous zone of porcine condylar cartilage was observed via polarized light, where the predominant orientation of collagen fibers was in the anteroposterior direction,[9] which coincides well with the mechanical anisotropy of the tissue.[9, 17] The crimped

state of fibers at the articular surface, as observed earlier,[25] is consistent with the non-linear stress-strain response of the tissue under continuous tensile deformation.[9, 17] In contrast, the mature and hypertrophic zones exhibited an arrangement of randomly oriented fiber bundles,[20, 21] suggesting an isotropic distribution of fibers. The proliferative zone contained mostly scattered individual fibrils and a few collagen fiber bundles.[20, 22] Elastic fibers were also found to be present in the rat condylar cartilages.[26] These observations suggest that the tissue has a bi-layered arrangement in terms of fiber orientation, where an anisotropic layer (proximal to the joint synovium) transitions into an isotropic layer (proximal to the subchondral bone). The cartilage overall is expected to exhibit anisotropic mechanical characteristics, the extent of which may primarily depend on the thickness ratio of the fibrous zone to the entire cartilage.

It is known that tensile forces correspond more to fibroblastic activity, leading to the production of collagen type I, while compressive forces tend to be correlated with chondrocytes and the increased production of collagen type II and large chondroitin sulfate proteoglycans.[27] Therefore, the distribution of the primary collagen types (I and II) in the condylar cartilage may reflect biomechanical/functional requirements of the tissue.[28] Major collagen types specific to condylar cartilage are summarized in Table 2.2. Immunohistochemical evidence suggests that collagen type I, although distributed throughout the condylar cartilage, is present in considerably higher concentrations in the fibrous and proliferative zones.[28-30] In addition, localization of collagen type I was noted in the mature and

hypertrophic zones of the posterior margins, which may be due to the attachment of this region to the tensile load bearing retrodiscal tissue, as suggested by the authors.[28] Collagen type I has also been localized in the lacunae of hypertrophic chondrocytes, most likely an indicative of a phenotypic change (from chondrogenic to osteogenic).[20] In contrast, collagen type II has been detected almost exclusively in the mature and hypertrophic zones,[10, 28, 30] and to a lesser degree in the proliferative zone.[31] The distribution of collagen types I and II may suggest tension to be the primary mode of loading in the fibrous zone, and compression to be the primary mode in the mature and hypertrophic zones, except for the posterior margins that may experience considerable tensile loads.

In addition to zonal heterogeneity, regional differences in the tensile and shear properties, which were found to be significant for the TMJ disc,[13, 32-36]can be expected as the condylar cartilage functions in a multi-directional force field. Although regional differences in tensile properties of the condylar cartilage in a given direction were found not to be significantly different,[9] regional data for collagen content and degree of anisotropy may provide valuable validation.

Distribution of dermatan sulfate proteoglycans (DSPGs)

Decorin is an ECM component considered to enhance the tensile properties by increasing the collagen fiber diameter and modulating fibril synthesis (reviewed by Detamore and Athanasiou[5]). A higher expression of decorin in the fibrous zone of the cartilage compared to other zones, as observed in rat models,[37] may reflect the

fulfillment of the functional demand, i.e., enhancement of the tensile resistance due to the presence of considerably higher tensile loads. Condylar cartilage showed no presence of biglycan in rat condylar cartilages.[38]

Summary: structure-property-function correlation under tension

In summary, these studies suggest that shear forces have a pronounced effect on the condylar cartilage in the fibrous zone, especially near the articular surface, as evidenced by the anisotropic distribution of collagen fibers, almost exclusive presence of collagen type I, and considerable localization of decorin. In addition, it is likely that the surface of the condyle is exposed to predominately anteroposterior shear, which is caused by the primarily anteroposterior movement of the mandibular condyle and results in a preferred anteroposterior collagen fiber alignment in the fibrous zone,[9] leading to a higher tensile and shear stiffness of the cartilage in anteroposterior direction. The predominance of collagen fiber orientation in the anteroposterior direction has also been seen in the anatomically and functionally related TMJ disc.[13, 32, 34, 35] Due to the animal and species differences, further validation may be required (e.g., investigation of collagen types in porcine condylar cartilage or fiber architecture in primate condylar cartilage) to make coherent and conclusive arguments. Furthermore, the collagen content of the condylar cartilage, which has only been characterized in rodent models (Table 2.3), should be investigated in higher animal models such as a porcine model.

Compression

Compression appears to be the primary mode of loading on the osseous portion of the condyle, as discovered using *in vivo* strain measurement at the condylar neck during mastication in pigs,[39, 40] and deduced from the structure of the bone, suggesting the predominance of a somewhat superoinferior direction of forces at the condyle.[41, 42] In the following sub-sections, compressive properties of the condylar cartilage have been reviewed, and comparisons to regional proteoglycan/GAG distribution in the tissue have been made.

Compressive evaluations

Four compressive characterization studies of the condylar cartilage are currently available in the literature. Detailed descriptions of testing parameters and results from these compressive indentation tests are summarized in Table 2.1. Specimen preparation-wise, *in situ* testing of porcine cartilage over the intact condyle was performed in one study,[8] while porcine/rabbit cartilage-bone sections were utilized in the other studies.[43-45] So far, data for the creep[8] and dynamic properties[43-45] are available. The cartilage deforms more with sustained compression than with intermittent compression, and a higher stiffness was observed at greater loads.[8] This phenomenon of strain stiffening under compression has also been observed with the TMJ disc.[46] While exploring regional differences using dynamic nano-indentation experiments, a decrease in the stiffness (elastic moduli), average Poisson's ratio and surface roughness from the anterior to the posterior side and a relatively smaller

decrease from the medial to the lateral side were reported, demonstrating the heterogeneity of the condylar cartilage.[43, 44] The differences in the regional properties were statistically significant for 6 week old rabbits, but not for 7 day old rabbits, suggesting that the regional heterogeneity of the articular surface evolves with time. In another study, regional dynamic indentation tests of porcine condylar cartilages were performed by applying sinusoidal strains with a wide range of loading frequencies, and complex, storage (proportional to energy storage in a deformation cycle) and loss (proportional to energy dissipated in a deformation cycle) moduli were reported.[45] The complex, storage and loss moduli all increased with an increase in frequency. In agreement with the aforementioned nano-indentation experiments, the anterior region of the condyle had larger complex, storage and loss moduli than the posterior region (in general) at a given frequency, with the stiffness being highest in the anteromedial region of the four regions explored (see Table 2.1). Interestingly, in our observations (unpublished data), a relationship between the stiffness and thickness of the regions was observed, where the average elastic modulus was found to increase with the thickness. A thickness-stiffness correlation can also be gleaned from the study by Tanaka *et al.*,[45] where specimens from the stiffer regions were generally thicker. Validation of the thickness-stiffness correlation for the condylar cartilage is certainly required. Moreover, exploration of zonal property differences may provide valuable information regarding zonal structure-material property relationship.

Spatial variation of proteoglycans/GAGs

Among different zones, aggrecan, the primary proteoglycan in condylar cartilage, was found to be localized mainly in the mature and hypertrophic zones using immunohistochemical methods in porcine[47] and rat[10] models. Using immunohistochemistry, the presence of CS-rich versican-like proteoglycans were detected in the fibrous and proliferative zones in porcine and rat models,[38, 47] possibly owing to the fibroblastic[38] or progenitor cell activity.[47] Interestingly, immunohistochemical analysis of primate condylar cartilages located keratan sulfate and chondroitin sulfate only in the mature and hypertrophic zones, while their presence in the fibrous zone was not observed.[30] This observation is not in accord with other observations[38, 47] unless it is due to the differences in animal models. Among regions, the maximum synthesis of CS-rich proteoglycans was reported to be in the posterosuperior region of the rabbit condylar cartilage.[48] Histochemical observation of the condylar cartilages of rabbits showed the amount of CS-rich proteoglycans in the anterior and posterosuperior regions to be higher than in the superior region, with the highest content in the anterior region.[49] Some of the studies where sulfated GAG content of condylar cartilage (observed in rodent models) was quantified are summarized in Table 2.3 as a reference.

Although some information about occurrence of proteoglycans is available, the literature lacks a comprehensive regional quantification data of proteoglycans in the condylar cartilage. One limitation of the previous efforts to quantify proteoglycan content was the lack of thickness characterization, i.e., specimen preparation

protocols did not clearly indicate the methods employed to affirm the nature of the specimen (a cartilage section, entire cartilage or cartilage-bone). Another important issue pertains to the animal models used in many of these studies. Due to the small size and anatomical differences of the rodent TMJ relative to the human TMJ,[50] further quantification of these components (regional and overall) in more suitable animal models (e.g., porcine or primate) may be desired. It is worth noting that results of biochemical assays between rats and higher animal models have also exhibited general inconsistencies with TMJ disc studies as well.[5]

Summary: structure-property-function correlation under compression

Condylar cartilage has a heterogeneous nature in terms of both structure and mechanics. There are indications that the tissue may have a positive correlation between regional thickness and corresponding stiffness, which may imply that regional variations in the stiffness and thickness are related phenomena, developed in response to regional loading patterns. It may also indicate that the role of the cartilage is to sustain a heterogeneous *in vivo* biomechanical environment, where cartilage possibly experiences higher loads in the thicker regions. Valuable data regarding the thickness of human condylar cartilage are available in the literature,[51-53] and summarized in Table 2.4. Validation of the thickness-stiffness correlation in humans may improve our understanding of the nature and extent of condylar loads. If indeed such a correlation exists, it may have a direct influence on the FEMs of the human TMJ in the future, where *in vivo* imaging techniques will facilitate the

determining of material properties of condylar cartilage in a subject-specific manner. Regarding the structure, localization of aggrecan mainly in the mature and hypertrophic zones and absence from the fibrous zone supports the notion that the zones proximal to the subchondral bone are more hyaline-like in nature and primarily serve to resist the compression. However, comprehensive regional and zonal quantification of proteoglycans and GAGs may be warranted to clearly establish the structure-property-function correlation. A possible variation of compressive properties as a function of depth, also observed in knee cartilage,[54] can be anticipated, where hyaline-like mature and hypertrophic zones would be stiffer under compression than the fibrous zone. In addition, the extent of collagen fiber reinforcement, known to affect viscoelasticity via impeding the fluid flow that results in fluid pressurization,[55] against compression in the condylar cartilage is required to be understood. This leads to two important questions: i) is there any significant difference in the collagen content of the condylar cartilage compared to the other articular cartilages? and ii) how does the difference in the collagen architecture affect the fiber reinforcement and interstitial fluid flow in the condylar cartilage?

A PERSPECTIVE ON 3-D COMPUTATIONAL RECONSTRUCTION OF THE HUMAN TMJ

Due to the difficulties associated with *in vivo* estimation of the stress distribution using invasive experimental techniques, *e.g.*, strain measurement using strain gauge devices, which may develop/exacerbate a pathological situation, 3-D

TMJ computational reconstruction approaches are attractive alternatives[56] (see reviews [57, 58]). Efforts are being made by the TMJ modeling community worldwide, including groups from Japan,[59-63] the Netherlands,[56, 64-68] Spain[69-73] and Switzerland.[74-76] These models rely on an accurate replication of *in vivo* conditions and reliable biomaterial properties of TMJ structures. In this respect, the lack of universally agreed upon material properties of the condylar cartilage has been a limitation. The literature shows that FEM models of the TMJ have generally either not included the condylar cartilage[69, 70] or have incorporated only approximate material properties for the condylar cartilage as an isotropic elastic material[62, 77] or hyperelastic material,[68, 78] with rare exceptions, e.g., a study that incorporated heterogeneous material properties of the condylar cartilage obtained from a previous nanoindentation test.[79]

Potential applications of accurate and validated FEMs of the human TMJ are vast. Such models can allow characterization of the thresholds of normal function and parafunction, which may help to explain the etiology of TMJ disorders. The direct applications of these computational techniques are to track the 3-D motions of the joint and to note the distribution of the stress-fields inside the TMJ in prescribed situations. These models may be used to evaluate force-fields that accompany different activities, e.g., talking, chewing gum, bruxism or whiplash, and to predict which activities might lead to tissue damage. This would also be valuable to clinicians by assessing loads in the TMJ during various procedures (e.g., third molar extraction) as a means to evade iatrogenicity. For surgeons, one implication could be

to serve as a guide to the biomechanical environment and functionality of the joint before and after surgery [80], for example to evaluate implant performance. Another application of FEMs of the human TMJ could be in understanding the cause of functional adaptation and growth. Cellular and molecular regulation effects associated with functional remodeling of the condylar cartilage are being explored;[11, 81] however, mechanical changes that lead to remodeling have not been well-characterized. 3-D FEM models of the TMJ can be used to assess the changes in the mandibular environment and the forces experienced by the tissue, which could be related to the heterogeneous histological alterations that follow. Because these models require only computational effort, they may be used to perform hundreds of thousands of cycles of patient-specific implant testing, at no material cost and with full-patient compliance. Moreover, models could possibly be used to test the mechanical integrity required of a tissue-engineered construct. Currently, diagnosis of TMJ disorders is based on clinical, radiographic and morphological evaluations. Patient-specific models of motion and forces are expected to add another dimension to diagnose TMJ patients of the future.

DISCUSSION

The current literature for the mechanical characterization of the condylar cartilage is limited. To develop reliable biomechanical standards for the tissue that can be utilized in the FEMs of the human TMJ, several important issues should be considered. The ideal method is to determine mechanical properties by *in vivo*

biomechanical characterization in humans that can be readily applied in the FEMs. However, due to the relative unavailability of human tissue and possibility of degenerative changes in preserved cadaver tissues, a fundamental issue is which animal model should be regarded as ideal in lieu of the human TMJ tissues.[82] Researchers have shown growing interest in the porcine model due to the anatomical and functional resemblance of the porcine TMJ to the human TMJ,[50, 83, 84] although differences do exist, e.g., in the frequency of chewing.[18, 19] The model, age, gender and weight are all among well-known important animal selection parameters that can indirectly affect the biomechanical properties. In addition to these, the loading history of the subject tissues is another factor that may alter the biomechanical properties of the tissues, as the condylar cartilage is known to undergo adaptation and remodeling (reflected by changes in extracellular matrix composition) following the changes in the stress-fields over the condyle.[10, 49, 85-88] Apart from animal selection, another important issue is the mode of testing - *in vitro* or *in situ*? Likely due to the lack of accurate *in vivo* stress-strain measurement techniques, most of the macromechanical characterization studies for the condylar cartilage have been performed *in vitro* on tissue samples isolated from the joints. However, *in situ* testing of intact condylar cartilage may represent the *in vivo* conditions more closely than confined or unconfined compression, which may better suit finite element models of the TMJ. From a computational modeling perspective, an important issue is to consider the activity being modeled (e.g., clenching, chewing or trauma). Mechanical properties of the condylar cartilage under functional loading and parafunctional

loading may differ, as the tissue most likely experiences, for example, a greater level of strain in clenching or a considerably high strain rate in trauma compared to the physiological levels. Considering such parafunctional activities, where loading conditions are different than those under normal function, in is important to note that mechanical properties corresponding to a broader range of test parameters (i.e., load levels, strain rates, frequencies) must be explored, which will allow the selection of more accurate material properties. To determine intrinsic material properties, explain the mechanics and predict the tissue behavior under various conditions of loading, mathematical modeling using constitutive material models (such as, viscoelastic, biphasic or triphasic models) is usually performed. In this respect, there is scarce information available in the literature with respect to the condylar cartilage, due to which little is currently known about the mechanical properties of the condylar cartilage with regard to its permeability, moduli and Poisson's ratio. Comprehensive biomechanical characterization efforts, incorporating the existing or evaluated knowledge about the geometry, anisotropy and heterogeneity of condylar cartilage is essential to develop a standard for biomaterial properties.

In addition to the condylar cartilage, similar characterization of other TMJ tissues is also desired for the development of reliable 3-D FEMs of the human TMJ. For example, although the TMJ disc received much attention from the FEM community, the tensile force-bearing retrodiscal tissue is another TMJ structure that we believe is important to TMJ function, and which may have a possible initiating role in anterior disc displacement. The retrodiscal tissue also behaves as a

viscoelastic material, which has been evaluated for its tensile and compressive properties (Table 2.5).[89-91] Characterization with regard to the plastic deformation or failure data of the retrodiscal tissue, which have been made available to an extent by only one study, would be highly relevant to modeling and better understanding of internal derangement and its etiology.

SUMMARY

Condylar cartilage possesses a unique architecture with zonal and regional heterogeneity, reflected in its compressive biomechanical properties. The condylar cartilage also exhibits anisotropy under tension, which is consistent with the primarily anteroposterior motion of the condyle, and suggests that the fibrous zone of the cartilage may be comparable in some regards to the fibrocartilaginous TMJ disc. For example, both the fibrous zone of the condylar cartilage and the TMJ disc exhibit circumferentially and anteroposteriorly aligned collagen fibers, resulting in a tissue that is anisotropic under tension and shear. In the future, further explorations of tensile and compressive properties of the condyle are needed, and deficiencies with regard to the viscoelastic and biphasic models should be addressed to determine the material properties of the condylar cartilage. Although the TMJ disc[5, 46, 71, 92-98] is more well-characterized than the mandibular condyle in terms of biomechanical properties, more extensive data under a wide variety of conditions (impact, high strain, degeneration, etc.) are required for both. Establishment of biomechanical standards for condylar cartilage, the TMJ disc, and other tissues of the TMJ such as

the retrodiscal tissue, will provide necessary data for FEMs, provide validation standards for tissue-engineered constructs, and ultimately lead to a better understanding of TMJ biomechanics, which will ultimately have clinical application in the prevention (evaluating the implications of various activities), diagnosis (tracking motion and forces), and treatment (providing engineering design requirements) of TMJ disorders.

CHAPTER 3: Strategies and Applications for Incorporating Physical and Chemical Signal Gradients in Tissue Engineering*

ABSTRACT

From embryonic development to wound repair, concentration gradients of bioactive signaling molecules guide tissue formation and regeneration. Moreover, gradients in cellular and extracellular architecture as well as in mechanical properties are readily apparent in native tissues. Perhaps tissue engineers can take a cue from nature in attempting to regenerate tissues by incorporating gradients into engineering design strategies. Indeed, gradient-based approaches are an emerging trend in tissue engineering, standing in contrast to traditional approaches of homogeneous delivery of cells and/or growth factors using isotropic scaffolds. Gradients in tissue engineering lie at the intersection of three major paradigms in the field – biomimetic, interfacial and functional tissue engineering – by combining physical (via biomaterial design) and chemical (with growth/differentiation factors and cell adhesion molecules) signal delivery to achieve a continuous transition in both structure and function. This review consolidates several key methodologies to generate gradients, some of which have never been employed in a tissue engineering application, and discusses strategies for incorporating these methods into tissue engineering and implant design. A key finding of this review was that 2-D physicochemical gradient substrates, which serve as excellent high-throughput screening tools for optimizing

*Chapter published as Singh, Berkland, and Detamore, "Strategies and Applications for Incorporating Physical and Chemical Signal Gradients in Tissue Engineering", Tissue Eng Part B Rev, Epub ahead of print, 2008.

desired biomaterial properties, can be enhanced in the future by transitioning from 2-D to 3-D, which would enable studies of cell-protein-biomaterial interactions in a more native tissue-like environment. In addition, biomimetic tissue regeneration via combined delivery of graded physical and chemical signals appears to be a promising strategy for the regeneration of heterogeneous tissues and tissue interfaces. In the future, *in vivo* applications will shed more light on the performance of gradient-based mechanical integrity and signal delivery strategies compared to traditional tissue engineering approaches.

INTRODUCTION

From rocks[99] to squid beaks[100], nature is rich with gradients. Chemical signal gradients drive embryonic development, whereas gradients in cellular-extracellular architecture exist throughout the human body, within tissues and at tissue interfaces, to satisfy spatially diverse functional needs. To engineer complex tissues, gradient-based strategies can be incorporated into tissue engineering.

In this review, we discuss gradient-generation methodologies, some of which have been applied in tissue engineering investigations, while many others hold potential to be incorporated into biomaterial design or for spatially-controlled delivery of bioactive factors. From the perspective of traditional tissue engineering, gradient-based substrates have provided a quick single-experiment route to optimize biomaterial characteristics without introducing the experimental artifacts generated due to discrete substrate preparations, thus serving as a tool for high throughput

screening of biomaterials. More importantly, chemical and/or physical gradients can be directly incorporated into the design of biomaterials to engineer heterogeneous tissues and tissue interfaces. Combined with spatially- and temporally-controlled delivery of exogenous bioactive factors, gradient-based tissue engineering approaches may provide an effective scheme to engineer tissues and organs. The known sensitivity of cells to various physical and chemical stimuli, which cause cell migration (or "-taxis") (Table 3.1),[101, 102] has yet to be fully utilized in tissue engineering. Integration of spatially controlled signal gradients with tissue engineering may lead to dynamic cellular machineries that could enhance such cell-based therapies.

Gradient-based devices and strategies are employed in practice in a plethora of fields commercially, such as in electrophoresis,[103] dielectrophoresis,[104] chromatography (e.g., gradient elution generators in liquid chromatography), the aerospace industry,[105] and the discovery of drugs, materials and catalysts.[106] Here, we concisely present gradient generation techniques relevant to the tissue engineering community, *many of which have never before been employed in tissue engineering applications*, and emphasize specific possible future roles of mechanical and signal gradients in next-generation tissue engineering strategies.

BIOMATERIAL-BASED "PHYSICAL" SIGNAL GRADIENTS

Tissues consist of cells and extracellular matrix, and differ in type, content, and organization of the constituent cells and extracellular matrix components. In

tissue engineering, these differences must be considered before selecting biomaterials and designing scaffolds for a specific application. In addition, findings of several studies probing cell-biomaterial interactions suggest that biomaterials at the micro-/nano-scale may also act as a "physical" signal that may affect cell behavior, such as adhesion, spreading, motility, survival and differentiation. The following is a discussion of the importance of gradient-based strategies that – 1) can be utilized in the identification of optimal scaffold design parameters for traditional homogeneous scaffolds, and 2) can directly be incorporated as physical and chemical signals in the heterogeneous scaffold design for specific tissue engineering applications. We also briefly discuss the use of gradient-based approaches in the design of implants used for orthopedic and orthodontic repair procedures.

Polymeric materials

In this section, we discuss the strategies that have been applied for creating polymer-based gradients, and also emphasize the possible applications of these gradients from a tissue engineering perspective. Among several scaffold design parameters, we have considered a select few: pore-size, porosity, material stiffness, and surface physicochemical characteristics, which are of high interest.

Pore-size/porosity gradients

Among several scaffold design parameters, pore size and porosity bear prime importance. Pore size is known to affect cellular affinity and viability by influencing

cellular movement, binding and spreading, intracellular signaling, and transport of nutrients and metabolites.[107] Porosity governs the maximum possible accommodation of cell mass in the scaffold;[108] however, high porosity values often compromise mechanical properties of the scaffold.[109] From an application standpoint, pore size and porosity also affect neovascularization *in vivo*.[108] In addition, the scaffold architecture also requires consideration. An interconnected pore network is desired to minimize dead volume, and tortuosity of the network requires attention from a mass transport perspective.[110] Pore shapes may also critically affect the cellular organization in the scaffolds,[111, 112] as substantiated by several studies based on the contact guidance theory. The importance of scaffold architecture in tissue engineering is increasingly being realized, which has resulted in a change in trend in the designs of scaffolds, from isotropic scaffolds to heterogeneous and anisotropic "biomimetic" scaffolds, with the goal being to mimic the organization of the cells (such as, alignment or clustering) and/or the extracellular matrix of the tissue under consideration.

For designing isotropic scaffolds, the required range of optimal pore sizes depends on the intended tissue engineering application (i.e., the type(s) of cells/tissues that will interact with the scaffold).[107, 108, 113] In this regard, scaffolds containing a pore size gradient provide a rapid screening tool to probe *in vitro* cell-scaffold or *in vivo* tissue-scaffold interactions, as demonstrated earlier,[107] which may help in the identification/validation of the optimal pore sizes. Such graded porous scaffolds can be instrumental in the engineering of specific tissues that possess highly

zonal architecture or interfacial tissues, consisting of organized multiple cell layers and extracellular environments. So far, only a few such reports exist, e.g., where native zonal organization of the cartilage was accounted for in the scaffold design by utilizing an anisotropic gradient-based pore architecture,[114] or where heterogeneous organization of an osteochondral tissue was considered by including gradients in material composition (and thus, mechanical properties) and pore size in the scaffold design.[115] In one study, a prototype of graded bone implant with spatially varying pore size and porosity (in the radial direction) was created.[116] Gradients in material composition at the transition region may also reduce or eliminate the problem of delamination that is commonly observed in similar biphasic scaffold designs.[115] Scaffolds exhibiting pore size and porosity gradients can also provide control over cell migration, where the migration can be restricted in the direction of decreasing pore sizes by appropriately selecting the pore sizes,[117] or can be facilitated in the direction of increasing porosity to guide tissue in-growth.[118]

Application of pore size gradients is common in pore gradient gel electrophoresis.[119] Due to its purpose, the size of the pores in such gels allows permeability at the protein-size level, not at the cellular level. To create continuous gradients in pore size as well as porosity in macro-porous scaffolds (permitting movement at the cellular level), techniques that have been developed include a centrifugation–heat sintering method,[107] a combination of melt pressing and porogen leaching,[116] a centrifugation–freeze drying method,[117] and a phase separation–freeze drying method.[120, 121] Using a 3-D printing technique in combination with porogen

leaching, scaffolds having gradients in porosity with near-uniform pore sizes were created.[115, 118] Solid free-form fabrication (SFF) methods would in general be quite amenable to creating pore-size and other structure-based gradients. A novel 3-D fiber deposition technique was utilized in creating scaffolds that contained a gradient in pore size with a uniform porosity.[114] Table 3.2 summarizes the specifics of the aforementioned studies, which provide routes to creating 3-D scaffolds with a pore-size and/or porosity gradient(s).

Substrate stiffness gradients

Substrate stiffness affects cellular adhesion, spreading, motility, survival, and differentiation (for details, see reviews[122-124]). Research with fibroblasts, epithelial cells, and smooth muscle cells has demonstrated that cell-contact with the substrate diminishes on increasingly softer substrates,[125, 126] and cells migrate from softer regions to stiffer regions when exposed to a gradient in substrate stiffness,[101, 127-130] a phenomenon termed "durotaxis" or "mechanotaxis" (Table 3.1). A recent review by Georges and Janmey[131] summarizes findings with various cell types (e.g., endothelial cells, neurons, hepatocytes) that provide corroborating evidence for the importance of substrate stiffness as a physical signal for cells. An "effective" stiffness range, however, varies between cell types and leads to cell-specific responses.[131] For example, fibroblasts placed on various soft polyacrylamide substrates (shear modulus: <1.6 kPa;[132] Young's modulus (AFM): 14 kPa,[101] ~2.7 kPa;[133] Young's modulus (bulk): 1.8 kPa,[127] ~4.4 kPa[133]) display a change in their cytoskeletons (destabilized

focal adhesions, and loss in actin filament or "stress fiber" expression, resulting in a rounded cellular morphology) compared to corresponding stiffer substrates (shear modulus >3.6 kPa;[132] Young's modulus (AFM): 30 kPa,[101] ~7.7 kPa;[133] Young's modulus (bulk): 34 kPa,[127] 12.4 kPa[133]), where these cells adapt a flat morphology. Neurons preferentially branch on soft substrates (50 Pa) compared to stiff surfaces (550 Pa), while the range of stiffness that is relevant to neurons may not affect fibroblasts.[133, 134] Smooth muscle cells prefer *moderately* stiff surfaces (E ~ 8 –10 kPa) to display tissue-like actomyosin patterns and cellular spreading areas compared to softer or stiffer substrates.[135, 136] Also, the response of the cells to the physical cues is generally not isolated from the presence of cell-to-cell interaction and haptotactic (surface-bound) cues.[132, 137] These pioneering studies have proven the importance of substrate stiffness for cells; however, many of these studies utilized homogeneous or step gradient substrate preparations possessing randomly selected stiffnesses, which provided little information regarding the "threshold values" of stiffness that critically alter the behavior (e.g., morphology, clustering, apoptosis) of a particular type of cell. In this regard, use of substrates containing continuous gradients with a large range in stiffness may provide a means to systematically study the cell response to substrate stiffness and accurately identify the threshold substrate properties critical to cellular behavior.[130] Continuous gradient surfaces may also facilitate the understanding of molecular mechanisms of cellular dependence on substrate stiffness.

Strategies to design tissue-engineered replacements require judicious selection of the biomaterials with one of the goals being to satisfy the biomechanical

requirements of musculoskeletal tissues. Material selection and scaffold design become particularly important when developing heterogeneous tissues or tissue interfaces that are biomechanically anisotropic and endowed with gradients in stiffness by nature, such as an osteochondral tissue, the intervertebral disc, skin layers, blood vessel walls, etc. Importantly, some investigations suggest that a tissue-like *in vitro* growth of cells (such as tissue-like striated actomyosin patterns and cellular spreading areas, as in the case of smooth muscle cells, or elevated branching, as in the case of neurons) requires substrate mechanical properties to be close to that of the extracellular matrix (ECM) of the native tissue.[134-136] While these findings certainly require validation of the relationship between physiologically relevant cellular morphology and cell functions,[130] the implication of these findings could be relevant to tissue engineers because it may provide justification to the current criteria of biomaterial selection and design. It may further implicate the need to design heterogeneous constructs for interfacial tissue regeneration, containing built-in continuous 3-D gradients in stiffness imparted by the specific biomaterials, which may not only lead to a mechanically robust tissue-engineered replacements, but may also prove useful in cell-mediated tissue repair. In addition, *in vivo* cellular infiltration in the biomaterial from the surrounding tissue can be optimized by suitably selecting material properties that may promote durotaxis towards the tissue-engineered replacement. Also, due to the diversity in the ranges of effective stiffness to which a cell responds (as mentioned earlier), gradient substrates hold potential to be utilized in durotaxis-driven cell separation and sorting applications commercially.

2-D Substrates containing both a step-transition and a continuous gradient in stiffness have been made in the past. Using soft lithography, poly(dimethylsiloxane) (PDMS) substrates containing near-absolute step gradients in stiffness were fabricated, and utilized to study durotaxis and micro-patterning of cells.[127] In some studies (including the breakthrough work by Wang and colleagues), a diffusion-based photopolymerization approach was utilized to create substrates that contained a sharp transition in material stiffness with a thin (extending to several microns) stiffness-gradient region.[101, 127, 128] To fabricate substrates containing controlled continuous stiffness gradients at macro- and micro-scales, controlled photopolymerization processes have been utilized in the past, where gradients were generated by controlled photo-exposure (using a gradient photomask[129, 138] or by varying photo-exposure time[139]) or by precisely altering the cross-linker concentration using a microfluidic device.[130, 135] In many of these early investigations, polyacrylamide gels served as tools to create step and continuous compliance substrates. Various other materials that have similarly been used to create substrates with continuous stiffness gradients include a two-component dimethacrylate blend,[139] styrenated gelatin,[128] and PEG-diacrylate.[140]

In summary, the utility of stiffness gradient surfaces has so far been realized in studying durotaxis phenomena, micropatterning of cells, and high throughput screening of materials. Probing other possible cell-biomaterial combinations using continuous stiffness gradient surfaces (as a screening tool) may provide useful information to the tissue engineering community. Stiffness gradient constructs may

also be useful in interfacial tissue regeneration; however, it will require a transition from 2-D surfaces to 3-D environments. The challenge lies in gathering further knowledge and combining it towards designing "active" optimal bioengineered constructs.

Surface gradients in physicochemical characteristics

Surface physicochemical characteristics of a biomaterial (e.g., wettability (hydrophilicity), roughness, crystallinity, charge, functionality) may critically influence the host response to an engineered replacement by affecting protein-biomaterial and cell-biomaterial interactions *in vivo*, directly or indirectly (as reviewed by Ruardy *et al*.[141]). Tailoring the surface features in a user-specified manner can provide spatial control over relevant phenomena, such as protein adsorption and cellular adhesion, proliferation and morphology, selectively or non-selectively. For example, cell repellant surface functional groups can be utilized and/or surface wettability can be controlled to diminish scar tissue formation or reduce platelet adhesion and activation.[142] For a different application, the same functional groups can be exploited to immobilize nanospheres that may alter cellular spreading and morphology, or to immobilize bioactive factors of interest over the surface (for example, by utilizing surface carboxyl or amine functionalities) to impart other desired features.[143, 144] For tissue engineering advancements, surface physicochemical gradients continue to serve as a fast-screening tool to identify the threshold regimes in physicochemical characteristics to optimize biomaterial

properties (e.g., improved biomaterial coatings, application-specific protein and cell interaction with the biomaterial, etc.).[145] In addition, patterned and gradient substrates can be utilized to alter site-specific biomaterial properties.[142] In the following paragraphs, we highlight some of the well-developed surface chemistry gradient generation methodologies (summarized in Table 3.3). These continuous surface chemistry gradient generation methodologies can be divided into two major groups, as described by Genzer and Bhat:[146] 1) top-down (involving modification of a substrate via physical and/or chemical treatments) or 2) bottom-up (involving deposition onto the substrate). For a more detailed overview, we recommend recent review articles by Kim *et al*.[145] and Genzer and Bhat,[146] where surface chemistry gradients and characterization techniques have been comprehensively discussed.

Wettability gradient surfaces have been produced using surface etching techniques, such as, UV-ozonolysis (UVO),[147-149] radio-frequency gas plasma discharge,[150-153] power-graded corona discharge treatment,[154-161] or a combination (UVO-plasma).[162] Peroxide initiators generated during the etching process lead to oxidation of the substrate surface and induce oxygen-based hydrophilic functionalities (such as, -OH, -COOH, -COOR). By varying a process-specific parameter continually (such as exposure intensity, exposure time, power, etc.), a surface with a continuously increasing surface energy and wettability results. Deposition of monomer(s) during the induction or graft-co-polymerization following the induction of these functionalities results in polymer-templated substrates, where gradients can be produced by monomer composition and/or by varying a process-

specific parameter in a controlled manner. Examples include UV grafting,[139, 162-165] grafting following power graded corona discharge,[166-171] and plasma deposition[172-175] (Table 3.3). With a proper choice of monomers, the chargeable functional group gradients were created to investigate the effect of charge density over cell behavior.[170, 171] In addition to the functional group density and wettability gradients, a gradient in nano-scale thickness of the substrate usually develops following the graft-co-polymerization, where the grafted polymer shows a transition from a loosely packed "mushroom" regime to a densely packed "brush" regime.[176] Other creative methods utilized to fabricate wettability gradient surfaces include diffusive deposition from a vapor or liquid phase absorbent (organosilanes) to hydrophilic substrates,[177-181] a density gradient method,[182] spatially varying electrochemical desorption/adsorption of alkane thiols on gold electrodes,[143] hyperthermal polyatomic ion deposition,[183] atom transfer radical polymerization (ATRP) (grafting from initiator gradients generated via diffusion,[184, 185] continuous depletion of monomer solution[184, 186]), thermochemical manipulation of aliphatic tert-butyl ester functionalized self-assembled monolayers (SAM),[187] and continuous immersion techniques (polyvinyl carbonate films in NaOH solution,[142] gold substrate in alkanethiol solutions,[188] gradient chemisorption in ATRP initiator solution,[176] and a metal oxide substrate into a solution of polycationic polymer (electrostatic interaction).[189] These methods result in a gradient in surface functional group density that can generally be translated into gradients in polymer grafting density (or molecular weight), surface nanoparticle

density (by covalent or charge[190, 191] interactions), and/or immobilized bioactive factor density.

Development of two-dimensional gradient substrates with continuously modified polymer compositions has been one of the central themes in combinatorial polymer research.[192, 193] Gradients in thickness and nanostructure were achieved by block co-polymer thin film casting using accelerated knife-edge coating followed by annealing.[194, 195] A gradient in morphology and nanoscale roughness was achieved by using a constant thickness thin film casting followed by temperature gradient annealing.[196] Utilizing a 3-syringe pump system, polymer composition gradients were generated by thin film casting followed by annealing, where an appropriate choice of polymers along with acceleration of the knife-edge coater and annealing temperature can lead to gradients in other properties (such as thickness, chemistry, crystallinity, stiffness, microstructure, roughness, wettability, degradation rate or a combination).[197-201] In particular, coating velocity and acceleration affect the thickness of the film, and temperature affects the morphological appearance and roughness (as rate of crystallite nucleation is a function of temperature).[196] By combining UV ozonolysis pre-treatment, surface energy gradients were also introduced to the substrates.[202] Utilizing one or a combination of these continuous gradient generation methodologies, two-dimensional "orthogonal" gradient libraries were also created, where gradual variation in one or more properties occurred orthogonal to each other independently; for example, orthogonal gradients of molecular weights or molecular weight–graft density generated through ATRP, or an

orthogonal gradient in the thickness (h), temperature-induced roughness (T) or composition (φ) of polymeric thin films (i.e., h-T, h-φ and T-φ libraries).[111, 186, 198, 199, 201-204]

To summarize, a number of 2-D surface physicochemical gradient generation methodologies have been developed in the past and have served as a great high-throughput fast-screening tool. An important future step from a tissue engineering perspective will be the advancement of such methodologies from 2-D flat substrates to 3-D polymeric scaffolds, and recording/validating the phenomena observed on 2-D substrates in a 3-D environment, as cellular responses in 2-D environments are known to be different from those in 3-D environments.[205, 206]

Metal or bioceramic materials

A major area of contemporary research is the development of biomaterial-based implants for orthopaedic and orthodontic applications (including, maxillofacial, hip or knee replacements). Unlike tissue engineered constructs, such implants are usually non-degradable and devoid of cells by design, usually lacking in self-repairing ability. Nevertheless, such "spare-parts" appear promising due to their "off-the-shelf" nature. Two major categories of such implants are metallic implants and bioceramic implants. Gradient-based strategies can be integrated in the design of such implants to address some of the major concerns associated with them. In this section, we highlight some of the interesting and relevant current trends in implant design (Table 3.4).

Due to the relatively inferior biocompatibility and poor corrosion resistance of metallic implants, bioceramic or polymeric coatings are usually applied. The bioconductive nature of bioceramic coatings, or degradable nature of the polymeric coatings, imparts on them the ability to induce/promote bone in-growth and to help in the integration of the implant with the surrounding tissue. However, the durability of the coating-substrate interface is a common concern.[207] This issue has been addressed by using coatings made of so-called functionally-graded materials, which are non-uniform composites containing a continuous or multi-layered structure, varying in composition (and other desired properties) from one end of the composite to the other.[207-210] Using a bioconductive ceramic (such as hydroxyapatite, β-tricalcium phosphate or bioglass) as the outer surface, a metallic/tough bioceramic (TiO_2, Al_2O_3, ZrO_2, etc.) as the inner surface (contacting the substrate) and a gradient of the materials in between, the desired balance between the mechanical properties and bioconductivity can be achieved.[207, 211, 212] In a similar manner, graded-polymeric coatings or graded-composite (polymer-bioceramic) coatings were employed to achieve gradient transitions in mechanical properties and degradation, where degradation of the coating can be programmed to match the bone in-growth, ideally.[213] Polymeric coatings can also be utilized as a controlled delivery vehicle of osteogenic factors that may enhance bone in-growth. Likewise, gradient surface treatments of metal implants were utilized to reduce the metal ion release, enhance corrosion resistance, and improve the biocompatibility of the surface layer, while preserving the superior mechanical properties of the implant with a durable interface

between the coating and the implant.[214-216] For example, electrochemical oxidation processes were used to form graded TiO_2 coatings on Ti-based implants with a porous outer coating to enhance integration with the bone, and a dense inner coating to reduce metal ion release.[216] Similarly, addressing wear-induced osteolysis as a result of ultra-high molecular weight polyethylene (UHMWPE) debris formation following total joint arthroplasty, a gradient surface treatment using a low energy electron beam resulted in depth-dependent gradient cross-linking that yielded a UHMWPE surface with high wear resistance and superior mechanical properties in the interior (due to low cross-linking).[217, 218] In a different approach, a gradient interpenetrating polymer network (IPN), formed due to the diffusion of poly-L-lysine (PLL) into UHMWPE, was proposed to address UHMWPE wear, where recruitment of hyaluronic acid by PLL (via charge interaction) was hypothesized to decrease joint friction and wear.[219]

Another area of application for gradient-based strategies is in the design of the implant itself. To address detrimental bone resorption resulting from stress-shielding, a metal implant with a gradient in porosity was utilized to match the stiffness of the implant to that of the bone.[220] Graded structures were created to mimic the bone architecture (low porosity outside, as in cortical bone, and high porosity inside, as in cancellous bone)[209, 221] or to influence the bone in-growth while maintaining the mechanical integrity of the implant (high porosity inside and low porosity outside).[222, 223] These two approaches to create bimodal bone structures primarily depend on the desired mechanical characteristics of the engineered structure and influence the pore sizes. Functionally-graded implants have also been considered for other applications,

e.g., for the treatment of cranial defects[224] and spinal disc prosthesis.[225] Moreover, gradient-based structures may be instrumental in optimizing the biocompatibility of the implants. Such structures can be utilized as cost-effective fast-screening tools in determining the biocompatibility of the materials, as demonstrated earlier,[226] or can be utilized in the design of implants, both traditional and functionally-graded implants, to improve biocompatibility at desired locations.[227, 228]

Various techniques have been applied to create functionally-graded implants and coatings, resulting in desired spatial variation in properties of interest, while reducing or eliminating the interfacial stresses due to the material-property disparity that may cause delamination[99, 207] (summarized in Table 3.4). Many studies, at least preparation-wise, included the formation of graded structures in a multi-step, as opposed to continuous, manner. Although these techniques may have resulted in the formation of micro/sub-micron -range diffusion-based gradients at the interface, it may not be sufficient to avoid delamination or interfacial failure. Controlled continuous gradation can be employed to ensure a smooth transition, as opposed to step-wise transition, that may (or may not) be a concern for delamination. Another distinct benefit with the use of continuously graded structures is that many techniques for creating such continuously graded structures offer a one step fabrication method, which is more efficient than multiple processing steps commonly employed for step-wise gradation.[229] For example, a dual- torch plasma spraying was used to create decreasing titanium and increasing hydroxyapatite gradients towards the surface by independently adjusting the feed rate and plasma power of mixture gases to yield a

continuously varying gradient region.[207] Generally, a higher percent value of the thickness of the gradient region compared to the overall thickness of the implant/coating can be selected to eliminate the cause for concern (i.e., delamination); however, one must also take the envisioned application into consideration.

In summary, functionally-graded materials have tremendous application in the design of implants/implant coatings, which can either be fabricated or may result as an effect of transport-based surface-treatment methods (see reviews[230, 231]). Compared to multi-stepwise graded structures, continuous gradient-based approaches appear promising as they may provide more time-efficient and mechanically robust alternatives; however, they are still in their infancy. In this regard, development of novel fabrication techniques and comparison with the corresponding step-wise gradation will provide more insight regarding the usefulness of continuously graded structures.

"CHEMICAL SIGNAL" GRADIENTS

Concentration gradients of bioactive signaling molecules (hereafter, collectively referred to as chemical signals) play a crucial role in developmental and biological repair processes, including morphogenesis, wound healing, the immune response, vessel pathfinding, and axonal guidance, where cellular migration and/or differentiation is sensitively governed by spatially patterned endogenous chemical signals (see reviews[232-235]). A biomimetic approach towards tissue regeneration necessitates a proper consideration of the spatial and temporal aspects of exogenous

delivery of such signals in tissue engineering.[236, 237] The following sections contain a brief discussion of the importance of chemical signal gradients, and the techniques applied to generate chemical signal gradients in 2-D and 3-D environments.

Gradients of growth/differentiation factors and cell adhesion molecules (CAMs)

Spatial patterning of chemical signals is a field of growing interest for the tissue engineering community. Several of these bioactive factors are well characterized for different tissue engineering applications, are known to induce concentration-dependent cell-type specific responses, and usually work in a synchronized manner with other similar factors during the development or repair of a natural tissue.[238] While these factors are traditionally delivered homogeneously for *in vitro* or *in vivo* tissue engineering, both temporal and spatial control over the delivery of such factors is an understood requirement for biomimetic repair and regeneration.

Cell-extracellular matrix (ECM) interfacing is governed through a type of ligand-receptor binding primarily mediated by transmembrane adhesion proteins of the integrin family, where extracellular domains of the integrin receptors form anchoring junctions (such as focal adhesions, fibrillar adhesions and hemidesmosomes) by binding to certain ECM proteins, e.g., collagens, fibronectin, fibrinogen, vitronectin, etc.[239] Cell-matrix interaction, in turn, produces specific cell responses that influence cell adhesion, motility, shape, orientation, differentiation and survival. Specific parts of the ECM protein sequences act as cell adhesion ligands, and domains, RGD, YIGSR and IKVAV represent some well investigated peptide

sequences that are recognized by cells as adhesion sites (see reviews[240, 241]). The RGD sequence, for example, is a cell adhesion site found in active fibronectin, fibrinogen and laminin.

Continuous gradients of chemical signals are a form of spatially patterned signals that have been successfully developed and employed in various investigations, most notably, probing directed axonal regeneration,[162, 242-249] nerve regeneration,[250] controlled cellular migration, localization and/or alignment involving fibroblasts, endothelial cells, Chinese hamster ovary cells, vascular smooth muscle cells, leukocytes, and neutrophils.[140, 163, 167, 176, 251-260] In their soluble or immobilized forms, the chemical signal gradients induce specific cellular responses, which may include controlled cellular migration (a.k.a. chemotaxis or haptotaxis, respectively) (Table 3.1), usually in the direction of increasing concentration/surface density of the chemical signal. A positive effect on directed axonal growth has been demonstrated under the influence of various chemical signal gradients, including gradients of IKVAV-containing peptide,[261] laminin,[244-246] nerve growth factor (NGF),[242, 249] combined laminin and NGF,[250] and combined NGF and neurotrophin-3 (NT3),[243, 248] where neurite extensions were found to be superior in the presence of signal gradients compared to corresponding homogeneously delivered signals. Wound healing is another area of investigation. Controlled movement of fibroblasts is known to take place under the influence of chemotactic factors secreted by macrophages and platelets[262] and represents a key area to explore the effect of various chemical signal gradients on the migratory behavior of fibroblasts, leukocytes, and neutrophils. In

addition, the ability of chemical signal gradients (such as an RGD-containing peptide density gradient) to influence the alignment of the fibroblasts, as suggested by the authors, can also be exploited in the tissue engineering of ligaments and tendons.[251] Moreover, gradient substrates can also be used as a screening tool in optimizing the dosage of growth factors that lead to, for example, a higher cell proliferation rate or improved juxtracrine signaling.[255] In addition to chemical signals, a number of other model factor gradients (such as other proteins or fluorophores) have also been created during the development of gradient-generation techniques, some of which are summarized in Table 3.5.

Strategies to create gradients of growth/differentiation factors and CAMs

Chemical signal gradients can be broadly divided into two categories: 1) soluble and 2) immobilized. Other important categories include gradients in 2-D vs. 3-D, and the principle involved in gradient generation. Specifically, the methods to create signal gradients are based on either diffusion or convection-based approaches. In convection-based approaches, a gradient of the concentration/surface density of the bioactive factor is achieved by a gradual increase/decrease in the concentration of the factor itself, or continuous spatial variation in the chemistry/pre-processing of the substrate that leads to a gradient in the concentration/surface density of the factor. General methods used to create chemical signal gradients (for peptide and proteins) are summarized in Table 3.6.

Soluble

To study chemotactic responses of cells under the influence of gradients, the principle of molecular diffusion was first utilized to create soluble factor gradients in solutions (such as culture medium) using a Boyden chamber or its variants (such as Zigmond and Dunn chambers).[256, 258, 260] These chambers, although simple and inexpensive, have drawbacks in sustaining the concentration gradients of signals for a long period and do not provide a 3-D cell culture environment.[263] Similar creation of gradients in macroporous gels (such as agarose, fibrin or collagen) provided 3-D culture platforms. Approaches to generate signal gradients in such gels involves either a single source/chamber of bioactive factors (such as a chamber of bioactive factor-rich solution),[254, 264] or multi-source/chamber of factors (such as the gel in between two chambers of factor, or delivery of factors at multiple positions in gel);[242, 243, 257, 259] the latter enabling the generation of relatively more stable linear gradient profiles. A controlled microdispensing technique was recently developed to create patterns of chemical factors with user-defined profiles on the surface of thin 3-D gels, where gradients of these factors are established via diffusion in the gel, which were found to be stable for a day or more.[249, 263] Laminar flow-based microfluidic devices have also been developed that are capable of generating concentration gradients of chemical signals with highly stable spatial and temporal profiles, although these have mostly been applied to 2-D systems.[265-268] Devices based on controlled release principles, e.g., phosphatidyl choline-based lipid microtubules (LMTs) loaded in gels or microsphere-based scaffolds, have recently been applied to create gradients of

chemical signals/model factors.[250, 269, 270] Such devices may serve as long-term (several days to months) release vehicles for the generation of gradients of chemotactic factors.

Immobilized

The general techniques to create surface immobilized chemical gradients include adsorption of the molecule on the desired surface, covalent linking of the peptides/proteins via peptide bond formation through carboxylic acid (-COOH) or primary amine ($-NH_2$) moieties present on the original or modified surface (for example, using carbodiimide chemistry), or by derivatizing with photoreactive moieties (such as azidophenyl, benzophenone, acryloyl or aryl azide groups), all more or less governed by the chemistry of the substrate/scaffold, as reviewed earlier. General methods that have been utilized to create immobilized chemical signal gradients in 2-D and 3-D include single or dual source/chamber approaches,[245, 246, 250, 271] pump or gravity-driven flow of factor solution,[140, 244, 247, 248, 251-253, 271] capillary driven flow of factor solution,[272] automated printing,[273] and adsorption or covalent linking of proteins utilizing polymer-grafted/micropatterned substrates.[162, 163, 165, 176, 255, 274] Microfluidics, photopolymerization, atom transfer radical polymerization, and/or protein conjugation chemistry are among valuable flexible tools that were usually involved during the fabrication of immobilized protein gradients (Table 3.6).

Techniques to create bioactive factor gradients vary in terms of scale, accuracy, flexibility and stability of gradient profiles.[263] In summary, hydrogel-based

approaches have provided many routes to generate soluble or immobilized bioactive factor gradients in both 2-D and 3-D, which were widely used in studying the chemotaxis and haptotaxis. Surface modification and photopolymerization techniques have been successfully used to create gradients of surface-bound factors on polymeric surfaces. In contrast, fewer attempts have been made regarding the generation of such gradients in degradable 3-D macroporous scaffolds, a prototype that constitutes a significant percentage of commonly used tissue engineering scaffolds. In this regard, primary issues to be addressed appear to pertain to the translation of many 2-D physicochemical gradient generation techniques from 2-D to 3-D.

DISCUSSION

Integration of three schools of thought – *functional*, *interfacial* and *biomimetic* tissue engineering – can be addressed through gradient-based strategies by combining physical and chemical signal delivery. Various tissues display strong non-homogeneous characteristics in their morphology, cellular and extracellular matrix organization. For example, cartilage (superficial, middle, deep zones), bone (cortical, cancellous), blood vessels (media, intima, adventitia), skin (dermis, epidermis), or any interfacial tissue (such as bone-cartilage or muscle-tendon), all consist of graded zonal structures to satisfy diverse functional needs. Gradients in mechanical properties often exist within and between the tissues, which help in avoiding stress concentrations,[100] e.g., cartilage,[275] human crystalline lens,[276] and the dentin-enamel

junction.[277] A tissue-engineered replacement must satisfy at least the "minimum" functional requirements that may be addressed through the choice of biomaterials and the scaffold design. Incorporating gradient-based physical signal delivery strategies in the design of biomaterials, such as pore-size and porosity gradients or stiffness gradients, may thus improve the functional characteristics of and cellular remodeling in the scaffolds. Simultaneously, chemical signal gradients that are involved during the regeneration and repair of tissues can be incorporated in the design of scaffolds. Gradients of chemical signals may also offer single cell source tissue regeneration alternatives for the regeneration of interfacial tissues, where a stem cell population can be selectively differentiated into disparate lineages in a graded manner in the same construct. Thus, a biomimetic approach can be combined with a functional tissue regeneration approach by utilizing a combined physical and chemical signal delivery through gradient-based strategies. As an example, stiffness gradients could be combined with growth factor gradients that may yield a synergistic response of enhanced axonal branching[134] and guided axonal regeneration.

While a combination of physical and chemical signal gradients may not be necessary for all tissues, such an approach could be an interesting subject of investigation for interfacial tissue regeneration. From the perspective of interfacial tissue regeneration, a transition from homogeneous cell/growth factor/scaffold designs to signal gradient-based tissue engineering may be advocated for a number of reasons. First, the replacement of a tissue that is engineered in isolation requires a fixation or bridging with the adjacent tissue (such as suturing, press-fitting, or

gluing), which may not result in the best mechanical characteristics at the interface. Second, isolated tissue engineering may not be able to provide mutually inductive endogenous signals from the adjacent tissues that are involved during the tissue formation *in vivo*. In an extreme example, it is widely known that gastrulation and the subsequent fate of germ layers during embryogenesis depend on a series of spatially and temporally controlled inductive cell interactions.[278, 279] In a specific example, relevant to osteochondral tissue engineering, an *in vitro* culture study reported that only co-culture with chondrocytes (as opposed to fibroblasts or osteoblasts) was successful at promoting osteogenic differentiation of mesenchymal stem cells in a selective manner.[280] Even tumor cells display a strong neighbor-dependent behavior arising from cell-cell interactions.[281] Finally, stratified tissue regeneration techniques (e.g., utilizing bi- or multi-phasic scaffolds), the closest alternative to gradient-based signal delivery, may not effectively mimic the native tissue function, or may undergo delamination due to stress concentrations.

Along with spatial regionalization of chemical signals, another key aspect of biomimetic tissue engineering is the delivery of such signals in a temporally controlled manner, i.e., simultaneous or sequential release of multiple growth factors.[282, 283] In this regard, controlled drug delivery technologies can be combined with gradient fabrication strategies, e.g., phosphatidyl choline-based lipid microtubules (LMTs) or microsphere-based scaffolds.[250, 269, 270]

In summary, continuous gradients of physical and chemical signals can be considered as an important subset of spatially patterned signals, capable of driving

dynamic cellular phenomena and a cost-effective tool for high-throughput screening. A variety of gradient-generation techniques have been reviewed here, which are promising for biological and tissue engineering investigations. Controlled patterning of chemical signaling molecules combined with physical gradients of signals hold immense potential for complex tissue regeneration, which may be a missing ingredient in the quest to fulfill the true potential of the field of regenerative medicine. In the future, *in vivo* comparisons will be required to provide substantial evidence for the superior performance of gradient-based signal delivery strategies compared to traditional forms of tissue engineering.

ACKNOWLEDGMENT

The present work was supported by NIH/NIDCR grant 1 R21 DE017673-01A1, the Juvenile Diabetes Research Foundation and the University of Kansas General Research Fund.

CHAPTER 4: Tensile Properties of the Mandibular Condylar Cartilage*

ABSTRACT

Mandibular condylar cartilage plays a crucial role in temporomandibular joint function, which includes facilitating articulation with the temporomandibular joint disc and reducing loads on the underlying bone. The cartilage experiences considerable tensile forces due to direct compression and shear. However, only scarce information is available about its tensile properties. The present study aims to quantify the biomechanical characteristics of the mandibular condylar cartilage to aid future three-dimensional finite element modeling and tissue engineering studies. Porcine condylar cartilage was tested under uniaxial tension in two directions, anteroposterior and mediolateral, with three regions per direction. Stress relaxation behavior was modeled using the Kelvin model and a second order generalized Kelvin model, and collagen fiber orientation was determined by polarized light microscopy. The stress relaxation behavior of the tissue was bi-exponential in nature. The tissue exhibited greater stiffness in the anteroposterior direction than in the mediolateral direction as reflected by higher Young's (2.4 times), instantaneous (1.9 times) and relaxed (1.9 times) moduli. No significant differences were observed among the regional properties in either direction. The predominantly anteroposterior macroscopic fiber orientation in the fibrous zone of condylar cartilage correlated well

*Chapter published as Singh and Detamore, "Tensile Properties of the Mandibular Condylar Cartilage", J Biomech Eng, 130(1):011009, 2008.

with the biomechanical findings. The condylar cartilage appears to be less stiff and less anisotropic under tension than the anatomically and functionally related TMJ disc. The anisotropy of the condylar cartilage, as evidenced by tensile behavior and collagen fiber orientation, suggests that the shear environment of the TMJ exposes the condylar cartilage to predominantly but not exclusively anteroposterior loading.

INTRODUCTION

The mandibular condyle, along with the fossa-eminence complex and the TMJ disc, together form the articulation of temporomandibular joint (TMJ).[1] The articular condylar cartilage plays a crucial role in the adaptation of the TMJ to external muscular forces.[284] The cartilage facilitates articulation with the TMJ disc and distributes the compressive loads over the condyle during the normal function of a healthy joint.

Temporomandibular joint disorders (TMDs) have considerable prevalence with 16–59% of the population having symptoms and 33–86% having clinical signs.[2] While TMDs involving the TMJ disc (specifically, internal derangement) have been reported to be the most common,[285] the resulting biomechanical dysfunctions (such as clicking or locking) may lead to damage of the condylar cartilage.[62] Abnormal loading conditions, e.g., clenching or bruxism, are probable factors that contribute to the development of many TMDs. Osteoarthritis is one such example, where the biomechanical factors likely play a role in the progressive deterioration of the articular cartilages.[286, 287] However, the role of mechanics is still unclear. To

understand the TMJ function in normal and pathological conditions, three-dimensional finite element models of the human TMJ have emerged as valuable tools. The predictions by these mathematical models may be improved by incorporating more reliable biomechanical properties of the condylar cartilage. Therefore, the development of biomechanical standards for this tissue is important. Moreover, biomechanical properties of the native tissue are also necessary as design and validation criteria for an artificial or tissue-engineered replacement.

Although the loading condition of the condyle has been reported to be primarily compressive,[39, 40, 78] direct compression and shear forces generated due to mandibular motion may produce significant tensile loads on the collagen fibers in the condylar cartilage, especially in the regions closer to the joint synovium. The effects of the surrounding force environment are reflected in the heterogeneous zonal architecture of the condylar cartilage, which contains a fibrocartilaginous fibrous zone (adjoining the inferior joint compartment) and hyaline-like cartilage in lower zones. The fibrous zone contains primarily collagen type I with fibers aligned parallel to the surface,[20-22, 28, 30] and is mainly responsible for the tensile stiffness of the tissue in the plane parallel to the surface.

While there are a few studies that have investigated the compressive biomechanical behavior of condylar cartilage,[8, 43-45] there is only one previous tensile study, where the failure properties of the porcine condylar cartilage in the mediolateral and anteroposterior directions were characterized.[17] However, the tensile stress relaxation behavior of this viscoelastic tissue has never been

investigated, thus the tensile equilibrium moduli of the tissue are heretofore unknown. In addition, a higher stiffness in the anteroposterior direction compared to the mediolateral direction was reported in the lone tensile evaluation,[17] which implied preferred anteroposterior collagen fiber alignment. However, to the best of our knowledge, there has been no conclusive evidence to reflect a commensurate anisotropy of collagen fiber orientation in the condylar cartilage. Moreover, regional variations in the tensile properties, which were found to be significant for the TMJ disc,[13, 36, 288, 289] have yet to be explored in the condylar cartilage.

The goals of this study were to quantify the tensile biomechanical properties of the porcine condylar cartilage, to verify its anisotropy, and to explore the regional heterogeneity of the condylar cartilage. We hypothesized that fiber orientation in the condylar cartilage was predominantly anteroposterior due to primarily anteroposterior mandibular motion. A porcine animal model was selected due to the similarities in anatomy[50, 83] and function[84] between the pig TMJ and the human TMJ. Uniaxial tensile tests were performed in two directions (anteroposterior and mediolateral) with three regions in each direction (anterior, superior and posterior regions in the anteroposterior direction, and medial, central, and lateral regions in the mediolateral direction). We then compared the regional and directional properties of the condylar cartilage with that of the TMJ disc. In addition, we correlated the biomechanical properties of the condylar cartilage with its structure, as observed by polarized light microscopy.

MATERIALS AND METHODS

Specimen Preparation

Hog heads from 6-month-old females (Yorkshire cross, skeletally immature) weighing 70-85 kg (150-190 lb) were obtained from a local abattoir. TMJs were harvested from the heads with joint capsules intact within 24 h of death. Mandibular condyles from both sides were separated by opening the lower joint compartments carefully (Fig. 4.1). Subsequently, articular condylar cartilage and other joint components were assessed morphologically. Condyles from the TMJs with no signs of degeneration were wrapped in gauze, soaked in PBS (phosphate buffered saline – 0.138 M sodium chloride, 0.0027 M potassium chloride) and stored at -20 ºC. Left and right condyles were used to make specimens in the anteroposterior or mediolateral directions, respectively. A total of seven condyles were used for each direction tested, giving a sample size of n = 7.

Three cartilage specimens were created from each condyle, either in the anteroposterior or mediolateral direction (Fig. 4.2). Prior to specimen preparation, frozen condyles were thawed at room temperature and condylar cartilages with the subchondral bone attached were carefully isolated from the bulk of the condylar bone using a scalpel. Subsequently, the cartilage-bone samples were divided into three equal parts either in the anteroposterior or mediolateral direction. Each part was individually sectioned in a cryotome (Microm HM550, Richard-Allan Scientific, Kalamazoo, MI) to a uniform thickness of 250 μm with the articular surface intact.

To accomplish this task, a stage of frozen tissue embedding medium was prepared, which was cryotomed to create a surface that was flat and parallel to the cryostat blade. Using the *remaining travel* feature of the cryotome, the position (remaining travel = x μm) of the flat embedding medium surface along the line of travel of the stage was recorded. Subsequently, the articular surface of the cartilage was flattened against a flat freezing metal surface in the cryotome by very gently applying pressure on the sample. The sample was then firmly fixed to the embedding medium stage with its flattened surface facing the stage and covered in embedding medium. Starting from the uppermost subchondral bone, the sample was serially cryotomed until a distance of 250 μm was left from the recorded initial position of the flat embedding medium stage (*Remaining Travel* = 250+x μm), producing the 250 μm thick cartilage section with the articular surface intact. The integrity of the articular surfaces of the cartilage sections was confirmed by visual observation of the stage, where no tissue remnants were found. Rectangular tensile specimens were cut out from the 250 μm thick cartilage sections using an assembly of two parallel razor blades separated by a 1.8 mm thick aluminum spacer. Rectangular specimens have previously been used successfully to observe tensile stress relaxation behavior of articular cartilages.[290-293] To ensure that specimen thickness did not exceed cartilage thickness, a preliminary thickness measurement study, employing a needle penetration technique,[294] was performed. The study indicated cartilage thickness in all regions to be more than 300 μm and formed the basis of thickness selection. During the specimen preparation, complete removal of the subchondral bone region

was visually verified. Specimens were immediately wrapped in gauze, soaked in 0.01 M PBS, then frozen at -20 ºC until tested.

Tensile Tests

Tensile tests were performed using a uniaxial testing apparatus (Instron Model 5848, Canton, MA) having a displacement accuracy of 1 μm and a 50 N load cell with force resolution of 0.001 N and measurement accuracy of ± 0.5% of the measured force or better. A custom-made stainless steel bath and grip assembly, illustrated in Fig. 4.3, was mounted in the apparatus. To prevent slippage, squares of 220-grit waterproof sandpaper were glued to grip faces using cyanoacrylate adhesive that provided adequate roughness without damaging the specimens.[13] Specimens were kept hydrated in the bath with 0.01 M PBS during the testing.[13, 291, 292, 295-298] The temperature of the bath was regulated to 37±1 ºC.[13, 296, 298] Buoyant forces acting on the top grip were accounted for as described by Detamore and Athanasiou.[13] Briefly, the load of the top grip (F_b) was measured empirically as a function of grip-to-grip separation (d). Measured force (F_m) was calibrated to the actual force (F) by subtracting the effect of buoyancy, *i.e.*, $F(d) = F_m(d) - [F_b(d) - F_b(L_0)]$, where L_0 is the initial specimen length and is the reference point. For a consistent buoyant profile and to maintain ionic concentration,[299, 300] the bath height was held constant throughout all experiments. In addition, the bath surface was covered with parafilm to reduce evaporation due to heating. The change in bath volume was observed to be negligible at the end of each test.

Before testing, each specimen was thawed and equilibrated in 0.01 M PBS at 37 ºC for 1 h to achieve thermal, hydration and ionic equilibrium.[290, 295, 297, 299] Thus, all the specimens underwent three freeze-thaw cycles, which has been shown not to alter the mechanical properties of cartilaginous specimens.[301] Specimen dimensions, which changed due to swelling during the equilibration phase, were quickly measured at three sites using a micrometer (±0.001 mm) at 25X magnification.[13, 296] The specimen widths and thicknesses slightly increased, resulting in average widths of 2.0±0.1 mm and 1.9±0.1 mm and average thicknesses of 0.47±0.07 mm and 0.49±0.07 mm in the anteroposterior and mediolateral directions, respectively. Subsequently, the specimen was loaded into the grips. A tare load of 0.03N (~0.035MPa) was applied to remove the laxity of the specimen.[290, 292, 293, 295-297] The bath was filled with 0.1 M PBS at 37 ºC and the specimen was allowed to re-equilibrate under this tare load for 10 min.[290, 293, 295-298] Specimen grip-to-grip length after the tare load was taken as the initial specimen length. Although the porcine condylar cartilage is longer mediolaterally than anteroposteriorly, initial specimen lengths were taken in the same range (~9 mm) by placing a slightly higher percentage of mediolateral specimens into the grips, which was done to compare the results in the two directions without introducing differences in percent strain rate. Resulting average initial specimen lengths were 9.6±1.4 mm and 9.1±1.2 mm in the anteroposterior and mediolateral directions, respectively.

Following the re-equilibration phase, specimens were subjected to preconditioning by applying cyclic loads from 0 to 6% strain, a range corresponding to the initial exponential region,[7] at a rate of 10 mm/min.[13, 290, 295] Preliminary studies demonstrated that a total of 10 cycles were sufficient to produce repeatable stress-strain curves in successive cycles. Finally, preconditioned specimens were subjected to stress relaxation. A 20% ramp strain at 6 mm/min was applied to the specimen followed by a 1.5 h relaxation period. Given that the duration of the ramp strain was very short compared to the overall relaxation period, the ramp strain will be subsequently referred to as a step strain. Preliminary testing showed 20% strain to be safely below the onset of failure, which typically occurred from 24 to 44 %. Specimens that still failed (4%) during the testing led to the exclusion of all specimens from the condylar cartilage from which the specimens were made. Such exclusion was essential to avoid the interference of inter-condylar differences with the regional property comparisons. Thus, a total of 12% of all specimens were discarded from the data analysis. Preliminary tests also revealed a long relaxation phase for the tissue, where 100% equilibrium could not be achieved even after 8 h. However, a reasonable duration of 1.5 h was selected, which corresponded to approximately 90% relaxation of the tissue.

Stress-strain curves were generated from the continuous pull during the step strain to 20%. Young's moduli were obtained from the linear regions of the stress-strain curves. The stress was defined as the ratio of the load to the initial cross-

sectional area, and the strain was defined as the ratio of the change in the tare length to the original tare length.

Viscoelastic modeling

Two viscoelastic models were used to model the stress relaxation following the step strain: a) the Kelvin model, and b) a second-order generalized Kelvin model. As described by Fung,[7] stress relaxation that occurs on applying a step strain (ε_0) to the Kelvin model is represented by the relaxation function,

$$\sigma(t) = E_R\left[1+\left(\frac{\tau_\sigma}{\tau_\varepsilon}-1\right)\exp\left(-\frac{t}{\tau_\varepsilon}\right)\right]\varepsilon_0 \qquad (1)$$

where τ_σ, τ_ε and E_R are the creep time constant, stress relaxation time constant and equilibrium modulus, respectively. The instantaneous modulus E_0 is related to these parameters by the following equation,

$$E_0 = \frac{\tau_\sigma}{\tau_\varepsilon}E_R. \qquad (2)$$

The second order generalized Kelvin model is an extension of the Kelvin model, where an additional Maxwell element is attached parallel to the Kelvin element.[7] The relaxation function for the second order generalized Kelvin model, obtained by extending the first order analysis by Fung,[7] is given by

$$\sigma(t) = E_R\left[1+\left(\frac{\tau_{\sigma_1}}{\tau_{\varepsilon_1}}-1\right)\exp\left(-t/\tau_{\varepsilon_1}\right)+\left(\frac{\tau_{\sigma_2}}{\tau_{\varepsilon_2}}-1\right)\exp\left(-t/\tau_{\varepsilon_2}\right)\right]\varepsilon_0. \qquad (3)$$

The instantaneous modulus can be expressed as

$$E_0 = \frac{\sigma(0)}{\varepsilon_0} = E_R\left(\frac{\tau_{\sigma_1}}{\tau_{\varepsilon_1}} + \frac{\tau_{\sigma_2}}{\tau_{\varepsilon_2}} - 1\right). \quad (4)$$

To model the relaxation data of each specimen tested, the Kelvin model was first used. Modified relaxation curves were generated by excluding initial relaxation data collected up to 10 min (rationale explained later). The modified relaxation cureves were used for three-parameter curve-fitting in MATLAB (MATLAB 7.3, The MathWorks, Natick, MA) using Eq. (1) to obtain E_R, τ_σ and τ_ε. Overall relaxation curves were then fitted to the second order generalized Kelvin model, using the equilibrium modulus obtained from the Kelvin model. A four-parameter curve-fitting of all of the relaxation data was performed according to Eq. (3), yielding the time constants τ_{ε_1}, τ_{ε_2}, τ_{σ_1} and τ_{σ_2}. Subsequently, instantaneous moduli E_0 were calculated using Eq. (4).

Polarized Light Microscopy

Collagen fiber orientation was observed under polarized light. A fresh condylar cartilage sample was divided into three parts: medial, central and lateral regions. From each part, 30 μm thick transverse frozen sections were cryotomed from the fibrous zone and were mounted on slides for microscopy. Specimens were viewed using a Nikon microscope (Eclipse TS100-F) under polarized light at 100X magnification,[13] and images were captured using a high resolution camera.

Statistical Analyses

Properties, *i.e.,* moduli (Young's, instantaneous and equilibrium) and time constants (τ_{ε_1}, τ_{ε_2}, τ_{σ_1} and τ_{σ_2}), were compared among all regions using a single factor analysis of variance (ANOVA) and a Fisher's Protected Least Significant Difference *post hoc* test.

RESULTS

The porcine condylar cartilage demonstrated viscoelastic behavior under tension. When the tissue was stretched, resulting stress-strain curves had the characteristic non-linear "toe" region,[7] followed by the linear region (Fig. 4.4). The toe region was found to be consistent, extending to about 6% strain. Following a step change in the strain, a typical stress relaxation behavior was observed in all of the specimens, where the stress relaxed in a bi-exponential manner. The relaxation proceeded rapidly during the first 10 min (short relaxation time), followed by gradual relaxation at a very slow rate (long relaxation time) (Fig. 4.5). These phases with markedly different relaxation time constants will be referred to as the "*rapid*" and "*slow*" relaxation phases, respectively. Complete equilibration could not be achieved in the relaxation duration of 1.5 h, and may take more than 8 hours. To model the bi-exponential stress relaxation behavior, the Kelvin model was first used, which was found to be inadequate to fit the entire data set (Fig. 4.5). Therefore, a Kelvin fit for only the slow relaxation phase and the second order generalized Kelvin fit for the entire relaxation data were applied (Fig. 4.5). For all of the specimens, R^2 values of

greater than 0.99 for the Kelvin fit (slow phase) and greater than 0.97 for the second order generalized Kelvin fit (entire range) were achieved.

Directional and regional tensile stiffness of the condylar cartilage are summarized in Table 4.1, and respective time constants are summarized in Table 4.2. The anteroposterior direction was stiffer than the mediolateral direction, reflected by higher Young's, instantaneous and relaxed moduli (2.4, 1.9 and 1.9 times greater, respectively) in the anteroposterior direction ($p < 0.005$). In the anteroposterior direction, the central region was stiffer than the lateral region (1.3 times greater Young's modulus and 1.4 times greater instantaneous and relaxed moduli), which was in turn slightly stiffer than the medial region (1.1 times greater instantaneous modulus and 1.2 times greater relaxed modulus). In the mediolateral direction, the anterior and posterior regions had similar moduli, and were slightly stiffer than the superior region (1.1 times greater instantaneous and relaxed moduli). However, the regional differences in stiffness were not statistically significant in either direction.

Predictions from the second order generalized Kelvin model indicated that the rapid relaxation generally proceeded orders of magnitude faster than the slow relaxation. The stress relaxation time constants for the slow phase compared to the rapid phase ($\tau_{\varepsilon_1}/\tau_{\varepsilon_2}$) were 46 times and 52 times higher in the anteroposterior and mediolateral directions, respectively ($p < 10^{-15}$). In the anteroposterior direction, relaxation rates were highest for the central region as indicated by lower τ_{ε_1} and τ_{ε_2} values, followed by the medial and lateral regions, respectively. In the mediolateral direction, relaxation rates were highest for the anterior region,

followed by the superior and posterior regions, respectively. However, the differences in time constants between directions and between regions were not statistically significant.

Polarized light micrographs (Fig. 4.6) revealed that the fiber orientation was ring-like around the periphery and predominantly anteroposterior inside the periphery. Based on the polarized light micrographs and verified by visual inspection of the articular surface of the cartilage, a schematic of overall macroscopic fiber arrangement of the fibrous zone has been developed (Fig. 4.7).

DISCUSSION

The present study examined the regional variation of tensile properties of the condylar cartilage in both the mediolateral and anteroposterior directions to characterize the tensile stress relaxation behavior of the condylar cartilage. The only available previous tensile study of the condylar cartilage by Kang et al.,[17] testing the porcine condylar cartilage to failure at 0.05 mm/min, reported stiffness values (Young's moduli) of 9.04±1.73 MPa and 6.55±1.24 MPa in the anteroposterior and mediolateral directions, respectively. Our study supports their observation by confirming the anisotropic nature of the condylar cartilage under tension. However, Young's moduli in our study were found to be 24±12 MPa and 10.1±5.5 MPa in the anteroposterior and mediolateral directions, respectively, indicating the cartilage to be stiffer in both directions than Kang et al. reported. Moreover, a higher ratio of the mean Young's moduli in the anteroposterior direction to the mediolateral direction

was observed in the current study, showing the anteroposterior direction to be 2.4 times stiffer than the mediolateral direction, as opposed to a lower value of 1.4 times higher stiffness reported by Kang et al. The likely reasons for the discrepancy in the results include the animal differences (breed, age), differences in specimen preparation technique, temperature and especially the applied strain rate. The regions of the condyle from which the specimens were prepared were not indicated in the study by Kang et al.

With these data, we were able to make regional and directional comparisons to the tensile behavior of the anatomically and functionally related TMJ disc. Comparison of the regional tensile properties of the condylar cartilage with that of the TMJ disc reported by Detamore and Athanasiou[13] indicated the instantaneous modulus of the TMJ disc to be similar in the central region, 1.1 times higher in the medial region and 1.2 times lower in the lateral region in the anteroposterior direction. The relaxed moduli of the TMJ disc were higher than that of the condylar cartilage in all regions in the anteroposterior direction (the relaxed moduli being 2.3, 2.1 and 1.5 times greater in the medial, central and lateral regions, respectively). When compared to the stiffness of the condylar cartilage in the mediolateral direction, the TMJ disc had instantaneous and relaxed moduli that were higher (1.3 and 2.4 times, respectively) in the anterior region and considerably higher (3.1 and 6 times, respectively) in the posterior region. However, the superior region of the condylar cartilage was stiffer (8.9 times higher instantaneous modulus and 6.2 times higher relaxed modulus) than the corresponding intermediate zone of the TMJ disc. In the

tensile characterization study of the TMJ disc, the peak and relaxed moduli were reported following an incremental stress relaxation protocol at 6 mm/min. The peak moduli of the TMJ disc were compared to the Young's moduli of the condylar cartilage obtained in the present study. The two studies used the same animal species and had very similar specimen preparation technique. However, the studies had differences in the hog breed, the calculation of properties, and the tensile test modality (incremental stress relaxation vs. single step strain followed by relaxation).

A highly anisotropic macroscopic orientation of collagen fibers was demonstrated in the condylar cartilage using polarized light microscopy. Previous investigations of the fiber arrangement in the condylar cartilage, using light and transmission electron microscopy, revealed a sheet-like arrangement of collagen fibers in the fibrous zone with fibers running predominately parallel to the surface.[20-24] One of these studies reported that these fibers were aligned in two predominant directions, anteroposterior and mediolateral, with some fibers running oblique to these directions.[23] However, the dominance of anteroposterior fiber orientation was not conclusive. In our study, macroscopic fiber arrangement in the fibrous zone of the condylar cartilage was investigated, and the results indicated the presence of a predominantly anteroposterior fiber orientation. Fiber arrangement in the cartilage was observed to be somewhat analogous to an elliptical two-dimensional globe with majority of fibers aligned in bundles along the longitudes (Fig. 4.7). However, randomly oriented fibers were also seen, which presumably contributed to tensile integrity of the superior region in the mediolateral direction. The peripheral and

predominately anteroposterior orientation of fibers was strikingly similar to that of the TMJ disc.[13, 36, 302] However, the differences in the regional tensile properties of the condylar cartilage were found not to be statistically insignificant. Specimen preparation along the anteroposterior and mediolateral directions, which had regional differences in collagen fiber orientation, may have been one of the major determinants of regional heterogeneity along the two directions (Figs. 4.2 and 4.7). It is possible that statistical significance would be achieved, if anterior and posterior regions were taken at the periphery (Fig. 4.2), or if a much larger sample size were used. Based on the polarized light micrographs, it may be expected that preparation of specimens from the peripheral areas of the anterior and posterior regions may result in higher stiffness of these regions compared to the superior region in the mediolateral direction (Figs. 4.6 and 4.7). Nonetheless, the results indicated that the condylar cartilage may not exhibit tensile heterogeneity to the same degree as the TMJ disc. For validation of the results, tensile and shear testing of mature porcine and human cartilages will be of particular interest in the future.

The stress relaxation curves were observed to be bi-exponential in nature. The rapid and slow relaxation phases were indicative of the viscous nature of relaxation, which occurred at two distinct rates (Fig. 4.5). The Kelvin model was not suitable to fit the relaxation data (Fig. 4.5). Therefore, the second order generalized Kelvin model was selected, which has previously been used to model similar bi-exponential decay curves.[303-306] However, the second order generalized Kelvin model could not accurately predict the relaxed moduli (E_R). This was discovered in

preliminary testing, where tests that were performed for relaxation times up to 6 h showed that the final empirical stress values at the end of the relaxation period were less than corresponding stress values predicted by the second order generalized Kelvin model. Instead, the first order Kelvin model of the slow relaxation phase was used to provide the E_R, since both models share a common E_R (Eqs. (1) and (3) for $t \rightarrow \infty$). Experimental curves indicated that the initially higher relaxation rates subsided to low values at around 10 min, being the reason to select t = 10 min as the point of the relaxation phase transition (Fig. 4.5). Using the E_R values obtained by the Kelvin model, the bi-exponential relaxation behavior was then curve-fitted to the second order generalized Kelvin model (Fig. 4.5). It should be noted that the second order generalized Kelvin model could not accurately predict the small transition region at the end of the rapid relaxation phase. This is because the small transition phase had a relaxation rate intermediate to those of the two phases, while the model had the capability to account for only two relaxation rates (one Maxwell element accounting for each relaxation rate). Generalized Kelvin models of higher orders or a quasi-linear model could be expected to provide a better fit to this narrow transition. However, since the transition phase lasted only for a brief duration, the second order generalized Kelvin model served as the simplest viscoelastic model that fit the experimental stress relaxation data closely.

Both Young's moduli and instantaneous moduli obtained from the second order generalized Kelvin model were reported (Table 4.1). Higher values of Young's moduli (slope of linear region of the stress strain curve) than the instantaneous moduli

(ratio of stress at the onset of relaxation to step strain) were obtained, which is expected due to the presence of the toe region ($E_Y > E_0$), and thus the disparity between the two moduli is indicative of the extent of the toe region.

The specimen preparation technique used in this study to produce rectangular cartilage specimens provided a way to make uniform thickness pure-cartilage specimens, keeping the articular surfaces preserved. In addition, lengths and widths were also kept similar, which ensured similar aspect ratios for all the specimens. Full thickness pure-cartilage specimens could not be prepared due to the location-dependent variations in the thickness of the condylar cartilage.[51-53] It should also be noted that the true E_R values may be slightly lower than the reported E_R values because approximately 90% relaxation in peak stress could be achieved in the selected relaxation duration of 1.5 h.

In conclusion, the stress relaxation behavior of porcine condylar cartilage specimens was modeled using a combination of two viscoelastic models. The tensile properties were found to be anisotropic, having a higher stiffness in the anteroposterior direction than in the mediolateral direction. However, the regional differences in the tensile properties were found to be insignificant in this study. The anisotropy of the condylar cartilage suggests that the mechanical environment in the inferior joint space exposes the condylar cartilage to predominantly but not exclusively anteroposterior loading, which was also reflected in the results obtained by polarized light microscopy. The condylar cartilage was less stiff than the TMJ

disc in all regions, except the superior region, which was significantly stiffer in the mediolateral direction than in the corresponding intermediate zone of the TMJ disc.

CHAPTER 5: Stress Relaxation Behavior of Mandibular Condylar Cartilage Under High-Strain Compression*

ABSTRACT

During temporomandibular joint (TMJ) function, the mandibular condylar cartilage plays a prime role in the distribution and absorption of stresses generated over the condyle. Biomechanical characterization of the tissue under compression, however, is still incomplete. The present study investigates the regional variations in the viscoelastic properties and stress relaxation behavior of the condylar cartilage under high-strains using unconfined compression, with aims to facilitate future three-dimensional viscoelastic finite element modeling and tissue engineering studies. Porcine condylar cartilages from five regions (anterior, central, lateral, medial and posterior) were tested under unconfined compression. Stress relaxation behavior was modeled using the Kelvin model and a second order generalized Kelvin model. The posterior region was the stiffest, followed by the middle (medial, central and lateral) regions and the anterior region, respectively. Specifically, in terms of the equilibrium modulus, the posterior region was 1.4 times stiffer than the middle regions, which were in turn 1.7 times stiffer than the anterior region, and the difference was significant between anterior and posterior regions. No significant differences in stiffness were observed among the medial, central, lateral and posterior regions. A positive correlation between thickness and stiffness of the cartilage was observed,

*Chapter submitted to J Biomech Eng as Singh and Detamore, "Stress Relaxation Behavior of Mandibular Condylar Cartilage Under High-Strain Compression", Aug 2008.

reflecting that their regional variations may be related phenomena caused in response to cartilage loading patterns. Condylar cartilage was less stiff under compression than in tension. In addition, condylar cartilage under compression appears to behave in a manner similar to the TMJ disc in terms of the magnitude of moduli and drastic initial drop in stress after a ramp strain.

INTRODUCTION

The temporomandibular joint (TMJ) is a load-bearing joint, formed by the mandibular condyle along with the fossa-eminence and the TMJ disc.[1] Soft tissues of the joint, including the mandibular condylar cartilage, help in the adaptation of the TMJ to the joint forces during function.[284] Painful disorders of the joint (TMJ disorders or TMDs) affect a large population and have considerable prevalence with 16–59% of the population having symptoms and 33–86% having clinical signs.[2] While internal derangement of the TMJ disc is arguably the most common of all TMDs,[285] some studies suggest that the inferior joint space, including the condyle, sustains the greatest damage in such conditions.[307, 308]

In a healthy joint, the mandibular condylar cartilage plays crucial roles of stress absorption and stress distribution over the condyle. Abnormal loading conditions, due to parafunctional activities (e.g., clenching or grinding) or biomechanical dysfunctions caused by an existing TMD (e.g., locking of the jaw due to disc displacement), may lead to joint forces that exceed the functional limit of the condylar cartilage. Such conditions may favor mechanical induction of a TMD such

as osteoarthritis, or may exacerbate an existing condition.[286, 287] However, thresholds of normal and abnormal loading are unknown. In this regard, developments in the field of modeling (using three-dimensional finite element models of the human TMJ) are promising, which may provide insight into the role of mechanics in TMDs. For improved accuracy in the predictions by such finite element models, incorporation of reliable mechanical properties of the TMJ tissues is a must. Moreover, biomechanical properties of the native tissue are also necessary as design and validation criteria for tissue engineering. Complete biomechanical characterization of the condylar cartilage is, therefore, essential.

The condylar cartilage is heterogeneous, both topographically and zonally.[11, 12] While a combination of compressive and tensile forces acts on the condylar cartilage, reflected in its heterogeneous zonal architecture, the loading of the condyle is primarily compressive in nature.[40] Aggrecan, which is mainly responsible for the compressive integrity of the cartilage, is located in the hyaline-like mature and hypertrophic zones of the condylar cartilage (closer to the subchondral bone).[10, 38, 47] Moreover, the thickness and histological architecture of the condylar cartilage varies regionally, indicating the possibility of regional variations in its macroscopic compressive properties.

Poroelastic and biphasic models have been extensively used in the past for modeling the hyaline cartilage behavior under compression, and provide useful material properties, such as permeability and Poisson's ratio.[14, 309-311] More importantly, these models serve as an excellent tool to provide a physical explanation

of cartilage biomechanics. However, the diffusional drag between the solid and fluid phases, which is the basis of these models, may be limited in the cases of fibrocartilaginous tissues with lower GAG content compared to hyaline cartilages.[46, 93] In these cases, viscoelastic models provide a reliable representation of the cartilage response. With regard to the choice of the constitutive models, the present study utilized isotropic viscoelastic models to model the stress relaxation data as these models are capable of modeling time-dependent mechanical behavior under large deformations (similar to the strains applied in this study). One reason for selecting these models was to allow direct comparison with the tensile properties of the condylar cartilage obtained in our previous study.[9] Moreover, we are interested in obtaining the equilibrium modulus and understanding the time scales associated with tissue stress relaxation behavior for each region, and in comparing these regions, and the viscoelastic model allows us to collect these data of interest. The data obtained using viscoelastic models are highly relevant to tissue engineers, and favor the channeling of viscoelastic parameters into existing viscoelastic finite element models of the TMJ.[59, 93]

Compressive viscoelastic characterization of the condylar cartilage is incomplete. Previous compressive characterization studies of condylar cartilage, summarized in Table 5.1, investigated surface properties using atomic force microscopy,[43, 44] the creep response of the anterior half using indentation of cartilage-bone samples,[8] and strain-rate dependent behavior using dynamic indentation of cartilage-bone samples.[45] However, regional data for continuous and step

deformations of full-thickness condylar cartilage under compression are currently not available in the literature. Specifically, given the soft nature of the condylar cartilage and the significant loads that the tissue experiences during functional and parafunctional activities (e.g., chewing on ice, clenching, etc.), one might expect that high strains would not be uncommon. With this in mind, the aim of the present study was to investigate regional stress relaxation behavior of the condylar cartilage using unconfined compression under large deformation. Compressive stress relaxation experiments were performed for five regions (anterior, medial, central, lateral and posterior). A porcine animal model was selected due to the similarities in anatomy between the pig and human TMJ.[50, 83, 312, 313]

MATERIALS AND METHODS

Specimen Preparation

Hog heads from 7-month-old females (Duroc-White, skeletally immature) weighing 100-110 kg (220-250 lb) were obtained from a local slaughterhouse. TMJs were harvested from the heads with joint capsules intact within 24 h of death. Mandibular condyles from both sides were separated by opening the lower joint compartments carefully and were assessed morphologically. Condyles from the TMJs with no gross morphological signs of degeneration were wrapped in gauze, soaked in PBS (0.01 M phosphate buffered saline – 0.138 M sodium chloride, 0.0027 M potassium chloride) and stored at -20 ºC. Cartilage specimens were made from five different regions of the condyle: anterior, medial, central, lateral and posterior

(Fig. 5.1). A total of nine right condyles were used during specimen preparation. However, stress relaxation data from a medial and a lateral specimen could not be obtained because of a premature ending of a test (load cell limit of 9 N exceeded) and a computer system failure, respectively. Therefore, the sample size used in the study was n = 9, except for the medial and lateral regions (n = 8).

Prior to specimen preparation, frozen condyles were thawed at room temperature. Condylar cartilages with the subchondral bone attached were carefully isolated from the bulk of the condylar bone using a scalpel and were divided into five regions, resulting in five cartilage-bone samples per condyle (Fig. 5.1). Subsequently, the subchondral bone was removed from each cartilage-bone sample using a cryotome (Microm HM550, Richard-Allan Scientific, Kalamazoo, MI) to produce full-thickness cartilage sections of uniform thickness. A cylindrical cartilage specimen was cut out from the center of each cartilage section using a 5 mm diameter dermal biopsy punch. Specimens were immediately wrapped in gauze, soaked in PBS, then frozen at -20 ºC until tested.

Compression Tests

Unconfined compression tests were performed using a uniaxial testing apparatus (Instron Model 5848, Canton, MA) with a displacement accuracy of 1 μm and a 10 N load cell with a force resolution of 0.0002 N. A custom-made stainless steel bath and compression platen assembly, illustrated in Fig. 5.2, was mounted in the apparatus. Specimens were kept hydrated in the bath with PBS during the testing.

The bath height was kept to a low value (approximately 1.5 mm from the lower platen) and was kept constant throughout all experiments to help maintain ionic conditions.[300] Buoyant forces acting on the top platen, described by Detamore and Athanasiou,[13] were found to be negligible. The temperature of the bath was regulated to 37±1 ºC,[13, 296, 298] and the bath surface was covered with parafilm to reduce evaporation due to heating.

Prior to testing, each specimen was thawed at room temperature and equilibrated before testing in PBS at 37 ºC for 1 h to achieve thermal, hydration and ionic equilibrium. In total, the specimens underwent four freeze-thaw cycles, which has been shown not to alter the mechanical properties of cartilaginous specimens.[301] Following equilibration, the specimen diameter was quickly measured at two sites using a micrometer (±0.001 mm) at 25X magnification. The average specimen diameter was 4.73 ± 0.18 mm. Subsequently, the specimen was placed on the lower platen and a tare load of 0.1 N (~0.006 MPa) was applied to the specimen. The bath was then filled with PBS at 37 ºC and the specimen was allowed to re-equilibrate under this tare load for 10 min, which was found to be sufficient for re-equilibration during preliminary testing. The grip-to-grip distance after the tare load was taken as the initial specimen thickness. The specimen thicknesses were 0.39 ± 0.11 mm (anterior), 0.54 ± 0.07 mm (medial), 0.60 ± 0.11 mm (central), 0.63 ± 0.14 mm (lateral) and 0.78 ± 0.14 mm (posterior).

Following the re-equilibration phase, specimens were preconditioned by applying cyclic loads from 0 to 25% strain, a range corresponding to the initial

exponential toe region,[7] at a rate of 2 mm/min.[13, 290, 295] Preliminary studies indicated that a total of 10 cycles were sufficient to produce repeatable stress-strain curves in successive cycles. The preconditioned specimens were then subjected to stress relaxation. A 50% ramp strain at 0.5 mm/min was applied followed by a 1 h relaxation period. The rationale for using a moderate strain rate, close to ~1%/s,[314-317] was to obtain an elastic modulus from the stress-strain curve. Given the duration of the ramp loading time (~ 30 s) in comparison to the overall relaxation duration (60 min), the ramp strain serves as an approximation of a step strain for modeling purposes. The ramp strain level was chosen based on preliminary testing, which demonstrated a linear stress-strain behavior beyond the toe region up to 80% strain. Furthermore, preliminary tests conducted on specimens made from the adjacent locations showed no significant difference in the equilibrium moduli at increasing ramp strains (at 40%, 50% and 60% ramp strain). We therefore selected a value that was well beyond the toe region to ensure sufficient data were available from the linear region without reaching the load cell limit or tissue failure. In addition, we conducted preliminary recovery tests to verify that the selected ramp strain value did not cause irreversible or permanent deformation of the tissue. Preliminary tests also revealed that a relaxation duration of 1 h was sufficient for complete relaxation of the tissue.

Obtaining the elastic modulus

Stress-strain curves were generated from the continuous deformation during the ramp strain to 50%. Elastic moduli were obtained from the linear regions of the stress-strain curves. The stress was defined as the ratio of the load to the initial cross-sectional area, and the strain was defined as the ratio of the length change from the original tare length.

Viscoelastic modeling

Two viscoelastic models were used to model the stress relaxation following the ramp strain: a) the Kelvin model, and b) a second-order generalized Kelvin model. Briefly, the stress-time relationship governing the time-dependent stress relaxation behavior for the Kelvin model, as described by Fung,[7] is

$$\sigma(t) = E_R\left[1 + \left(\frac{\tau_\sigma}{\tau_\varepsilon} - 1\right)\exp\left(-\frac{t}{\tau_\varepsilon}\right)\right]\varepsilon_0 \qquad (1)$$

where τ_ε, τ_σ and E_R are the stress relaxation time constant, creep time constant and equilibrium modulus, respectively. The instantaneous modulus E_0 is related to these parameters by the following equation,

$$E_0 = \frac{\tau_\sigma}{\tau_\varepsilon} E_R \text{ (Kelvin model)} \qquad (2)$$

The second order generalized Kelvin model is an extension of the Kelvin model, where an additional Maxwell element is attached parallel to the Kelvin element.[7] The relaxation function for the second order generalized Kelvin model, analogous to equation (1), is expressed as

$$\sigma(t) = E_R\left[1 + \left(\frac{\tau_{\sigma_1}}{\tau_{\varepsilon_1}} - 1\right)\exp\left(-\,t/\tau_{\varepsilon_1}\right) + \left(\frac{\tau_{\sigma_2}}{\tau_{\varepsilon_2}} - 1\right)\exp\left(-\,t/\tau_{\varepsilon_2}\right)\right]\varepsilon_0 . \quad (3)$$

The second order and first order models both share the same equilibrium modulus. However, the instantaneous modulus for the second order model is expressed as

$$E_0 = \frac{\sigma(0)}{\varepsilon_0} = E_R\left(\frac{\tau_{\sigma_1}}{\tau_{\varepsilon_1}} + \frac{\tau_{\sigma_2}}{\tau_{\varepsilon_2}} - 1\right). \quad (4)$$

The relaxation curve was first fit with the Kelvin model in MATLAB (MATLAB 7.3, The MathWorks, Natick, MA), obtained after excluding the first 5 min of relaxation data (rationale explained later), using Eq. (1) to obtain E_R, τ_σ and τ_ε. Relaxation curves were then fit to the second order generalized Kelvin model, using the equilibrium modulus obtained from the Kelvin model. A four-parameter curve-fitting of all of the relaxation data was performed according to Eq. (3), yielding the time constants τ_{ε_1}, τ_{ε_2}, τ_{σ_1} and τ_{σ_2}. Subsequently, instantaneous moduli E_0 were calculated using Eq. (4). To validate the constitutive models, additional compression tests were conducted and comparisons were made between the tissue behavior and the model prediction.

Statistical Analyses

Moduli and time constants were compared among the regions using a five-level single factor analysis of variance (ANOVA), followed by a Tukey's Honestly Significant Difference *post hoc* test when significance was detected. The correlation

between stiffness and cartilage thickness was assessed with the Pearson correlation coefficient, r.

RESULTS

The porcine condylar cartilage demonstrated viscoelastic behavior under compression. Stress-strain curves had the characteristic non-linear "toe" region,[7] which extended up to 25–30% strain, followed by the linear region (Fig. 5.3). Following a ramp change in the strain, a typical stress relaxation behavior was observed in all the specimens, where the stress relaxed in a bi-exponential manner. The relaxation proceeded rapidly during the first 5 min (short relaxation time), followed by gradual relaxation at a very slow rate (long relaxation time) (Fig. 5.4). These phases with markedly different relaxation time constants will be referred to as the "*rapid*" and "*slow*" relaxation phases, respectively. The Kelvin model was first used, which was found to be inadequate to model the entire stress relaxation data set. Therefore, the Kelvin model was applied only to the slow relaxation phase (Fig. 5.4). For all of the specimens, R^2 values of greater than 0.99 for the Kelvin fit (slow phase) and greater than 0.98 for the second order generalized Kelvin fit (entire range) were achieved. Validation tests conducted on the samples made from different regions of the condylar cartilage demonstrated a similar bi-exponential behavior (Fig. 5.5), and the values were found to primarily lie within the upper and lower bounds (± 1 standard deviation) set by the predicted model.

Regional compressive moduli and time constants of the condylar cartilage are summarized in Table 5.2, and a summary of statistical comparisons is provided in Table 5.3. A comparison of moduli among regions reflected that the posterior region was stiffer than the anterior region after stress relaxation ($p < 0.05$), and that all regions were stiffer than the anterior region during initial loading (i.e., elastic and instantaneous moduli) ($p < 0.05$). Specifically, the equilibrium moduli for the posterior and the anterior regions were 1.4 times and 0.6 times that of the pooled middle regions, respectively. The regional differences in the stiffnesses among the medial, central, lateral and posterior regions were not statistically significant.

Predictions from the second order generalized Kelvin model indicated that the rapid relaxation proceeded orders of magnitude faster than the slow relaxation, in general. The stress relaxation time constants for the slow phase compared to the rapid phase ($\tau_{\varepsilon_1}/\tau_{\varepsilon_2}$) were 17–22 times higher. The stress relaxation rates for the rapid phase were similar among all regions as indicated by similar τ_{ε_2} values. The stress relaxation rates for the slow phase, however, were higher in the central region compared to the posterior region, as indicated by lower value of τ_{ε_1} for the central region ($p < 0.05$).

DISCUSSION

The elastic modulus values for the condylar cartilage used in some of the previous finite element modeling studies of the TMJ were 0.49[61] and 0.79[60, 64] MPa,

which are only slightly lower than the elastic moduli obtained in the present study. The average elastic modulus of the condylar cartilage under compression was found to vary from 0.8 MPa to 1.5 MPa, approximately matching the range of dynamic moduli reported in previous regional indentation studies (Table 5.1).[43, 45] In this study, the compressive stiffness of the condylar cartilage was found to increase from the anterior to the posterior side, whereas variations in the stiffness of the middle regions were statistically insignificant. In comparison, previous regional characterization studies reported a decrease in the stiffness of the cartilage from the anterior to the posterior side and a relatively smaller decreasing gradient from the medial to the lateral side.[43, 45] It is likely that the differences in qualitative trends and quantitative observations can be attributed to animal differences (i.e., species or breed/gender/weight) and differences in experimental methods (testing method, strain rate, final strain value, experimental protocol). Interestingly, we noticed that there was a relationship between the stiffness and thickness of the regions ($r = 0.61$), where the average elastic modulus was found to increase with the thickness. Such a correlation may imply that regional variations in the stiffness and thickness are related phenomena, developed in response to regional loading patterns. It may also indicate that the role of the cartilage is to sustain a heterogeneous *in vivo* biomechanical environment, where cartilage possibly experiences higher loads in the posterosuperior region compared to the anterior region. The correlation between stiffness and thickness can also be gleaned in the study by Tanaka *et al.*,[45] where specimens from the stiffer regions were generally thicker. Since cartilage samples

from skeletally immature porcine were utilized in the present study, regional compression and thickness characterization of mature porcine cartilage will be of particular interest in the future for validation of the results. Moreover, the compressive properties of human mandibular condylar cartilage have heretofore not been tested. However, studies of its thickness have revealed that anteroposteriorly, the middle region is the thickest, followed by the anterior and posterior regions, respectively;[51-53] and mediolaterally, the medial and central regions are thicker than the lateral region. Elucidation of the regional compressive behavior of human mandibular condylar cartilage in the future will reveal whether a similar correlation between thickness and stiffness also exists in humans.

Compared to the tensile properties of the condylar cartilage,[9] the compressive elastic and instantaneous moduli were an order of magnitude lower than the corresponding tensile moduli, and the compressive equilibrium moduli were two orders of magnitude lower. In addition, the ratio of elastic to instantaneous moduli was larger under compression (~2.5–3.5) than in tension (~1.4–2.1), which was due to the presence of a larger non-linear toe region in compression (~6% strain for tension vs. 25–30% for compression). Collectively, these comparisons show that the condylar cartilage is less stiff and exhibits a greater viscous character under compression than in tension. Compared to the instantaneous modulus of the TMJ disc under compression,[46] regional instantaneous moduli of the condylar cartilage were found to be higher with the exception of the anterior region. In contrast, regional equilibrium moduli of the condylar cartilage were found to be smaller than

that of the disc (22–38 kPa). This may indicate that the condylar cartilage has a relatively greater viscous character than the TMJ disc under compression. It should be noted that the two studies (TMJ disc and current) had possible animal differences and differences in experimental methods (incremental stress relaxation vs. single ramp strain, final ramp strain value, strain rate).

In the present study, a ramp strain value of 50% was selected, which is higher than the typical strain values used in previous reports of articular cartilage indentation. *In vivo* strain measurements in the TMJ, however, indicate that significant bone strains exist, ranging from 89 to 109 με during masseter contraction in miniature pigs.[318] In terms of condyle loading, axial compressive loads on the condyle of up to approximately 32 N in baboons were calculated in bite-force experiments,[319] and forces up to 210 N were reported on human condyles under simulated muscle activity. Moreover, the maximum regional compressive stresses achieved in the condylar cartilage samples following 50% strain ranged from 0.29 MPa (anterior) to 0.49 MPa (lateral). These values are, in general, similar to or lower than maximum principle stress levels in the compressed condylar regions during unloaded jaw-closing movement,[68] and are lower than parafunctional compressive stress levels (during clenching) in the compressed condylar regions,[60] as predicted by a finite element models of the TMJ. Based on such previous reports and the observed full-recovery of the cartilage following stress relaxation *in vitro*, it is conceivable and likely that strains up to or exceeding 50% may be present during normal/parafunctional jaw activities *in vivo*. It should be noted that a direct

correlation between the present test results and *in vivo* findings cannot be made, as *in vivo* environment is significantly different than the applied testing conditions (confined-dynamic vs. unconfined-fixed strain rate).

The constitutive models utilized in this study assume a linear viscoelastic response, while the tissue demonstrated a non-linear viscoelastic response (as shown in Fig. 5.3). The inability of the employed viscoelastic models to incorporate material non-linearity was a limitation of this model. In this regard, improvements can be made in the future by utilizing the quasi-linear viscoelastic (QLV) model[7, 320, 321] or non-linear viscoelastic models.[322-324] In addition, use of Lagrangian stresses (calculated from stresses in the present configuration to the cross-sectional area in the reference configuration) in such isotropic constitutive models, which are usually formulated for the Cauchy stresses, is also a potential limitation. Moreover, a ramp strain was applied in this study to approximate a step strain, so the actual values of instantaneous and relaxed modulus would be a little bit higher than the values predicted. To understand the cartilage biomechanics physically, use of more sophisticated constitutive models will provide relevant information in the future.[325]

Due to the bi-exponential decay in stress, the Kelvin model was not suitable to curve fit the relaxation data (Fig. 5.4). Therefore, the second order generalized Kelvin model was selected. There are previous reports where this model was used successfully to model similar bi-exponential decay curves.[303-306] However, the second order generalized Kelvin model could not accurately predict the equilibrium moduli here.[9] Instead, the first order Kelvin model of the slow relaxation phase was

used to provide the E_R, since both models share a common E_R (Eqs. (1) and (3) for t→∞). Experimental curves indicated that the initially higher relaxation rates subsided to low values at around 5 min, providing the rationale for selecting t = 5 min as the point of the relaxation phase transition (Fig. 5.4).

In this study, uniform pure-cartilage specimens were tested under unconfined compression. Variations in the thicknesses among regions resulted in regional differences in the applied percentage strain rate (%/s). However, the results reflect the relaxation behavior of full-thickness specimens at a given rate of deformation (mm/s), which we believe are more relevant to 3-D finite element modeling and tissue engineering communities.

In conclusion, the stress relaxation behavior of porcine condylar cartilage under compression was successfully modeled using a combination of two viscoelastic models. The posterior region was the stiffest, followed by the middle regions and then the anterior region, respectively. No statistically significant differences were observed among the middle regions. A possible relationship between thickness and stiffness of the cartilage was observed, suggesting that their regional variations may be related phenomena caused by variations in cartilage loading patterns. The stiffness of the condylar cartilage appears to be lower under compression than under tension. In addition, condylar cartilage under compression appears to behave in a manner similar to the TMJ disc in terms of the magnitude of moduli and drastic initial drop in stress after a compressive ramp strain. This study is an important early step in understanding the compressive behavior of the condylar cartilage. In the future, use

of lower strain values and constitutive models, having an ability to provide physical explanation of the non-linear condylar cartilage response, would be a significant step forward.

CHAPTER 6: Microsphere-Based Seamless Scaffolds Containing Macroscopic Gradients of Encapsulated Factors for Tissue Engineering*

ABSTRACT

Spatial and temporal control of bioactive signals in three-dimensional (3-D) tissue engineering scaffolds is greatly desired. Coupled together, these attributes may mimic and maintain complex signal patterns, such as those observed during axonal regeneration or neovascularization. Seamless polymer constructs may provide a route to achieve spatial control of signal distribution. In this study, a novel microparticle-based scaffold fabrication technique is introduced as a method to create 3-D scaffolds with spatial control over model dyes using uniform Poly(D,L-lactide-co-glycolide) (PLG) microspheres. Uniform microspheres were produced using the Precision Particle Fabrication technique. Scaffolds were assembled by flowing microsphere suspensions into a cylindrical glass mold, then microspheres were physically attached to form a continuous scaffold using ethanol treatment. An ethanol soak of 1 h was found to be optimum for improved mechanical characteristics. Morphological and physical characterization of the scaffolds revealed that microsphere matrices were porous (41.1 ± 2.1%) and well connected, and their compressive stiffness ranged from 142 to 306 kPa. Culturing chondrocytes on the scaffolds revealed the

*Chapter published as Singh, Morris, Ellis, Detamore, and Berkland, "Microsphere-Based Seamless Scaffolds Containing Macroscopic Gradients of Encapsulated Factors for Tissue Engineering", Tissue Eng Part C Methods, Epub ahead of print, 2008.

compatibility of these substrates with cell attachment and viability. In addition, bi-layered, multi-layered and gradient scaffolds were fabricated, exhibiting excellent spatial control and resolution. Such novel scaffolds can serve as sustained delivery devices of heterogeneous signals in a continuous and seamless manner, and may be particularly useful in future interfacial tissue engineering investigations.

INTRODUCTION

Engineering tissues and organs requires combinations of biomaterials, cells, and bioactive signaling molecules.[326] Bioactive signals may be exogenously supplied *via* either the nutrient media (possible in *in vitro* culture conditions), polymeric scaffolds (incorporated in a soluble or immobilized form), by utilizing growth factor-secreting natural or genetically modified cells, and/or by gene delivery,[238] and are most commonly delivered in a homogeneous manner. However, spatial patterning of biological cues is vital to some of the most fundamental aspects of life, from embryogenesis to wound healing to nerve cell signaling, all involving concentration gradients of signaling molecules. Spatial patterning of bioactive signals may thus be a critical design element in the engineering of tissues or organs.

Various strategies have been developed to create gradients of bioactive signals. As early as the 1960's, diffusion-driven two-dimensional non-linear gradients of soluble proteins were developed to identify chemotactic response.[256] A few recent studies reported innovative diffusion- or convection-dominated approaches of creating linear or non-linear protein gradients within three-dimensional

scaffolds.[243, 245, 271] Using photolithographic and soft lithographic techniques, many innovative methods of protein/cell patterning have been reported that provide micron-level positional accuracy; however, such techniques are largely limited to two-dimensional constructs (reviewed by Park and Shuler[327]). To fabricate three-dimensional scaffolds with embedded linear gradients, a commercially available gradient maker (Gradient maker, CBS Scientific, Del Mar, CA) has also been utilized in various studies.[247, 248, 252] A number of other innovative strategies that have been applied to create gradient-based substrates for highly diversified applications have been reviewed recently.[145, 146]

In the areas related to tissue engineering, gradient-based signal delivery systems have by far gained the most attention in the fields of neural tissue engineering[243, 245, 247] and in the study chemotaxis.[254] Interfacial tissue regeneration is another key area that may benefit from gradients of bioactive signals, as some studies have suggested that signals from a tissue may influence the development and growth of its neighbor. For example, it can be seen during embryonic development and morphogenesis that the fate of one germ layer depends on signals from its neighbor.[278] An *in vitro* culture study reported that only co-culture with chondrocytes (as opposed to fibroblasts or osteoblasts) was successful at promoting osteogenic differentiation of mesenchymal stem cells in a selective manner,[280] indicating the importance of simultaneous triggering of osteo- and chondro-induction for osteochondral tissue regeneration. An integrated scaffold with embedded gradients of

growth factors at the interface, therefore, may trigger simultaneous tissue formation, and may have an adjuvant effect on interfacial tissue regeneration.

Microparticles have been long studied as polymeric delivery devices for a variety of drugs due to the ease of fabrication, control over morphology, the ability to discretely control their physicochemical properties and versatility of controlling the release kinetics of loaded therapeutics.[328] Recently, microparticle-based approaches of scaffold design have received much attention in the field of tissue engineering, targeting regeneration/repair of a variety of tissues (*e.g.*, cartilage[329, 330], bone[331, 332], neural[333, 334]), where microparticles may act as supporting matrices for cell attachment and/or as carriers of bioactive agents for controlled delivery of exogenous signals. Poly(D,L-lactide-co-glycolide) (PLG), an aliphatic polyester, has been widely used in many of these investigations because the polymer is biocompatible and biodegradable. Moreover, the degradation kinetics of the polymer is flexible, which can be modulated by altering one or more of the factors, such as co-polymer ratio, molecular weight, end-group chemistry, crystallinity, glass transition temperature, etc.[335, 336] Some recent studies reported fabrication of matrices exclusively made of PLG microspheres utilizing heat-sintering[331, 337] dichloromethane vapor treatment[282, 338] or a solvent/non-solvent sintering method.[339, 340]

It is well known that microsphere size is one of the major determinants of polymer degradation rate, and is a primary factor governing the release kinetics of loaded molecules.[328] Unfortunately, microsphere fabrication using traditional methods (*e.g.*, emulsion or spraying technique) generates reproducible, but often

poorly controllable, sphere sizes and size distribution.[341] To achieve control over local growth factor concentrations in a microsphere-based scaffold, control over microsphere size is critical. Moreover, by controlling the microsphere sizes, precise spatial control over pore-sizes and macro-porosity may also be achieved.

In the present study, utilizing our ability to create relatively monodisperse microspheres,[341] we introduce a novel microparticle-based scaffold fabrication technique to create scaffolds with spatial control over active ingredients using uniform PLG microspheres and an ethanol treatment. As discussed later, such macroscopic gradients can particularly be useful for future interfacial tissue regeneration investigations.

MATERIALS & METHODS

Materials

Poly(D,L-lactide-co-glycolide) copolymer (50:50 lactic acid:glycolic acid; intrinsic viscosity 0.41 dL/g, Mw ~50,000 Da, density 1.34 g/mL) was purchased from Birmingham Polymers (Pelham, AL). Poly(vinyl alcohol) (PVA; 88% hydrolyzed, 25,000 Da) was obtained from Polysciences, Inc. (Warrington, PA). Rhodamine B base and fluorescein were obtained from Sigma (St. Louis, MO). Dichloromethane (DCM; HPLC grade) was obtained from Fisher Scientific (Pittsburgh, PA). Ethanol (Absolute - 200 Proof) was obtained in house.

Preparation of microspheres

Uniform PLG microspheres were prepared using technology from our previous reports.[341] Briefly, PLG dissolved in DCM (30% w/v) was sprayed through a small-gauge needle. The polymer stream was acoustically excited using an ultrasonic transducer (Branson Ultrasonics, Danbury, CT) controlled by a waveform generator (model 33220A, Agilent Technologies, Santa Clara, CA), resulting in regular jet instabilities that produced uniform polymer droplets. An annular carrier stream (~0.5 % PVA (a surfactant) w/v in distilled water) surrounding the droplets was produced using a nozzle coaxial to the needle. The emanated polymer/carrier streams flowed into a beaker containing approximately 1,000 mL of 0.5% PVA. To extract the solvent, incipient polymer droplets were stirred for 3-4 h. Subsequently, the hardened microspheres were filtered and rinsed with distilled water (~1 L) to remove residual PVA. Finally, microspheres were lyophilized (Freezone, Labconco benchtop model) for 2 days and stored at –20°C under desiccant. In a similar manner, fluorescent dye-loaded microspheres were prepared for concentration profile assessment (discussed later) by using PLG solution (~30% w/v in DCM) co-dissolved with rhodamine B or fluorescein.

Particle size distribution

The size distribution of microsphere preparations was determined using a Coulter Multisizer 3 (Beckman Coulter Inc., Fullerton, CA) equipped with a 560-μm aperture. Freeze-dried particles were suspended in Isoton electrolyte that was stirred

at low speeds to prevent particles from settling. A minimum of 5,000 microspheres was analyzed for each set of particles.

Scaffold fabrication

Two sets of freeze-dried microspheres were separately loaded into two syringes in the form of suspensions, prepared by suspending microspheres (~1% w/v) in distilled water/PVA solution (volume ratio PVA:distilled water 1:20 (PVA 0.5% w/v)). The syringes were then installed in the scaffold fabrication apparatus (Fig. 6.1). The suspensions were pumped through the attached tubing to a cylindrical glass mold (6 mm diameter) in a controlled manner using programmable syringe pumps (PHD 22/2000, Harvard Apparatus, Inc., Holliston, MA). Through the bottom of the mold, the distilled water/PVA solution was filtered, while the microparticles stacked in the mold. The suspensions in the syringes were constantly stirred magnetically to keep them homogeneous. To prevent microspheres from rapid settling or sticking to the walls of the mold, a constant level of distilled water was maintained in the mold, controlled by an additional infusion syringe pump (Harvard Apparatus, Inc.) and a vacuum pump. The stacked microspheres were washed with distilled water (~100 mL), were allowed to soak in ethanol (100%) for 50 min, then the ethanol was pulled out using a vacuum pump. Ethanol-soak resulted in physical attachment of adjacent microspheres, due to adhesion and/or reptation, resulting in the formation of a matrix. To compare the effects of the duration of ethanol-soak on scaffold morphology, porosity and mechanical characteristics, additional scaffolds with various ethanol

soak times (i.e., 30 min, 1 h, 2 h or 4 h) were prepared. The molds (containing the scaffolds) were freeze-dried (Freezone, Labconco benchtop model, Kansas City, MO) for a minimum of 2 days, and then the scaffolds were retrieved from the molds. In some cases, the scaffolds were prepared using suspension(s) of dye-loaded microspheres with predefined distinct flow profiles, which were later used in concentration profile assessment studies.

Scanning electron microscopy

Both microspheres and scaffolds were freeze-dried overnight and cryofractured with a razor blade, then sputter coated with gold. The imaging was performed using a Leo 1550 field emission scanning electron microscope at an accelerating voltage of 5 kV under a high vacuum.

Differential scanning calorimetry

Differential scanning calorimetry (DSC) (Q100, TA Instruments, Inc., New Castle, DE) was used to measure the change in glass transition temperature (T_g) of the PLG following the microparticle and scaffold preparations. Prior to the analysis, raw PLG and one set of microspheres were lyophilized for 1 day, and a scaffold (prepared by ethanol-soak of 50 min) was lyophilized for 2 days. The experiments were carried out in triplicate on the samples (~15-20 mg each) packed in sealed aluminum pans. For each sample, a nonisothermal scan was performed from –10°C to +80°C at a

heating rate of 10°C min^{-1} under nitrogen atmosphere, and the corresponding T_g was recorded.

Porosity estimation and measurement

Porosity measurements were performed by imaging the scaffolds (prepared by 50 min ethanol-soak) using microCT (μCT 40, Scanco Medical, Southeastern, PA). Using 3-D MicroCT reconstruction and a segmentation value of 75, porosities and degrees of anisotropy were directly determined from scaffold sections (height 0.44-0.47 mm) (n = 4). Using NIH ImageJ software, 2-D microCT images were also analyzed. In addition, theoretical porosities of the scaffolds were calculated using the density of the raw PLG and the apparent densities of the scaffolds prepared by 30 min, 50 min, 1 h, 2 h, and 4 h of ethanol exposure.[342] The diameter (d), thickness (h) and mass (m) of the cylindrical scaffolds were measured, and porosities were calculated as:

$$\text{Porosity} = \left(1 - \rho_{\text{app}} / \rho\right) \times 100\%,$$

where ρ_{app} is the apparent density of the scaffold, given by $\rho_{app} = 4m / \pi d^2 h$, and ρ is the density of the stock PLG.

Mechanical characterization

Unconfined compression tests were performed using a uniaxial testing apparatus (Instron Model 5848, Canton, MA) with a 50 N load cell. A custom-made

stainless steel bath and compression- plate assembly was mounted in the apparatus. Cylindrical scaffold samples prepared with an ethanol-soak duration of 30 min, 1 h, 2h and 4 h (2.7 to 6 mm height, diameter ~6 mm) were tested at a strain rate of 5 mm/min under simulated physiological conditions (i.e., under PBS (phosphate buffered saline – 0.138 M sodium chloride, 0.0027 M potassium chloride) at 37 ºC). A strain rate in this range, i.e., ~1 to 2 %/s, is considered to be a moderate value for compressive testing of cartilaginous tissues.[314-317] Moduli of elasticity were obtained from the initial linear regions of the stress-strain curves (rationale explained later).[343] The stress was defined as the ratio of the load to the initial cross-sectional area, and the strain was defined as the ratio of the change in the length to the original length.

Cell seeding on scaffolds and viability

Porcine chondrocytes were harvested from a hog ankle (Duroc breed, 6 months old, female) obtained from a local slaughterhouse in a manner described previously.[344] The cells were then plated for expansion in monolayer and incubated at 37°C in 5% CO_2, with media changed every 2–3 days. The cell culture medium consisted of Dulbecco's Modified Eagle medium, 10% fetal bovine serum (ES cell quantified), 1% penicillin–streptomycin–fungizone, 1% non-essential amino acids (all from Invitrogen Life Technologies, Carlsbad, CA) and 50 μg/mL L-ascorbic acid (tissue culture grade; Fisher Scientific, Pittsburgh, PA). The cells were expanded and passaged twice before being seeded onto the scaffolds.

Cylindrical scaffolds (~6 mm diameter, 1mm height) were prepared using a 50 min ethanol soak, as mentioned earlier. Cells were seeded onto these scaffolds at a density of 3×10^6 cells per scaffold using the orbital shaker method as described previously,[345] and cultured for 18 days with half of the media refreshed every other day. Following this incubation period, the scaffolds were stained with LIVE/DEAD reagent (dye concentration 2 mM calcein AM, 4 mM ethidium homodimer-1; Molecular Probes, Carlsbad, CA) and incubated for 45 min, before being subjected to fluorescence microscopy (Olympus/Intelligent Innovations Spinning Disk Confocal Microscope, University of Kansas).

Concentration profile assessment study – Spatial control over composition of the scaffold

Four specific scaffolds were prepared, as mentioned earlier, using two different microsphere types (rhodamine-loaded and fluorescein-loaded microspheres, or rhodamine-loaded and blank microspheres). The syringes were loaded individually with one microsphere type and attached to the scaffold fabrication apparatus. Microspheres were pumped in a predefined manner using specific flow profiles (Fig. 6.2), and then the scaffolds were prepared by physically attaching the microspheres together with an ethanol-soak of 50 min. The resulting scaffolds were imaged under UV light using a UV lamp (254/365 nm; UVGL-25, UVP, Inc., Upland, CA) and a high-resolution camera, and images were analyzed using NIH ImageJ software to assess spatial control over the composition of the scaffolds.

Statistical analyses

The effects of microparticle preparation and ethanol-soak on the T_g of PLG were statistically analyzed using a three-level single factor analysis of variance (ANOVA) and a Tukey's Honestly Significant Difference *post hoc* test when significance was detected (n = 3). Moduli of elasticity and theoretical porosities of scaffolds prepared using varying ethanol soak-times were analyzed in a similar manner using a four-level single factor ANOVA, followed by a Tukey's Honestly Significant Difference *post hoc* test when significance was detected (n = 5).

RESULTS

Preparation of microspheres

Microspheres having a uniform diameter were created using the previously reported Precision Particle Fabrication method[341] and were characterized for their size and morphology. Four sets of microparticles were produced; a) blank-220 μm, b) blank-160 μm, c) rhodamine B-loaded (10% w/w)-150 μm, and d) fluorescein-loaded (10% w/w)-150 μm. Uniform solid PLG microspheres of 220 μm diameter were used to form scaffolds for all sub-studies, except the scaffolds used in scanning electron microscopic imaging (160 μm diameter was also used) and the flow profile assessment study (dye-loaded microspheres were also used). The microspheres had relatively monodisperse size distribution and a solid interior morphology (Fig. 6.3). Specifically, microsphere sizes in the range of 100-300 μm were chosen, as it is our

hypothesis for future *in vitro* tissue engineering investigations that this range may provide optimal pore sizes to allow cellular infiltration and cell-to-cell interaction.

Fabrication and characterization of scaffolds

A novel scaffold fabrication apparatus was designed, as mentioned earlier, to construct microsphere-based scaffolds with spatial control over their structure. Microsphere matrices were constructed using blank microspheres of 160 μm or 220 μm diameter with 50 min ethanol soak-time (denoted by $S_{\text{microsphere-size-time in minutes;}}$ $S_{160\text{-}50}$ group and $S_{220\text{-}50}$, respectively). In addition, to observe the effect of ethanol soak times on scaffold morphology and mechanical properties, scaffolds were prepared using microspheres of 220 μm diameter with varying ethanol soak-times of 30 min, 1 h, 2 h and 4 h ($S_{220\text{-}30}$, $S_{220\text{-}60}$, $S_{220\text{-}120}$ and $S_{220\text{-}240}$, respectively). The ethanol soak-time was selected based on preliminary scaffold fabrication results, which indicated that a minimum of a 30 min ethanol-soak was required to attain some partial integration between the microspheres. It was also observed that exceeding a soaking time of 70 min resulted in reduced porosities. In general, the optimum range of ethanol soak-time was a function of the polymer properties (co-polymer ratio, molecular weight, etc.). Microspheres composed of PLG with lower molecular weights are expected to require shorter ethanol soak-times or dilution of ethanol for production of mechanically integrated porous matrices.

Cylindrical scaffolds, 6 mm in diameter and 2.7 to 6 mm in height, were prepared and their morphology was analyzed (Fig. 6.4). Scanning electron

micrographs of a representative scaffold from the $S_{160\text{-}50}$ group revealed that the scaffolds were porous, having interconnected pores. In addition, to investigate the effect of the duration of ethanol-soak on the microspheres, $S_{220\text{-}30}$, $S_{220\text{-}60}$, $S_{220\text{-}120}$ and $S_{220\text{-}240}$ scaffolds were analyzed using SEM (Fig. 6.5). Microsphere morphology and pore sizes in the scaffolds were found to be a function of the duration of ethanol soak, where soak-times longer than 1 h resulted in visible distortion from spherical morphology and pore closure at several places (Fig. 6.5A-D). Representative pore size range from one representative time group (1 h ethanol soak) measured from the SEM images was found to be ~20-120 μm. Higher magnification images (Fig. 6.5E-H) show the points of contact between the microspheres. Surface film layers formed as a result of plasticization of PLG with ethanol. Integration of these surface films led to the formation of a well-connected matrix.

The mechanical integrity of the scaffolds were analyzed by unconfined compression testing at simulated physiological conditions. A characteristic plot obtained from the testing of a scaffold sample demonstrated that the curve had a typical nature: an initial linear region (0 to ~25% strain), a middle non-linear region (~25 to 70% strain) and a final linear region of considerably higher linear slope (post 70% strain) (Fig. 6.6A). The hypothesized mechanism of compression is somewhat analogous to the compression of closed-foam cellular solids.[343] Accordingly, the initial linear region (0 to ~25% strain) was used to determine the stiffness of the scaffolds (142 – 308 kPa) (Fig. 6.6B). The middle non-linear region (~25 to 70% strain), the onset of which begins after achieving a yield stress, signifies the

phenomenon of pore collapse, causing a continuous increase in scaffold density and stiffness. The final linear region (post 70% strain) corresponds to the material densification regime due to the absence of pores or any further changes in pore volume. Unlike the observations in cellular solids,[343, 346] a collapse plateau region was absent from the stress-strain curve, probably owing to the differences in testing conditions (i.e., simulated physiological condition as opposed to testing in air at ambient temperature). Mechanical test results indicated that the average modulus of elasticity of $S_{220\text{-}60}$ was significantly higher than the moduli of the $S_{220\text{-}30}$ and $S_{220\text{-}240}$ scaffolds ($p<0.05$). While it may be expected that an increase in ethanol soak-time would result in an increased stiffness and reduced porosity of the scaffolds, no such trends were seen in the range of ethanol-soak times examined. Visual inspection of the scaffolds revealed that scaffolds prepared by a 30 min soak did not have well-integrated microspheres, and microspheres were falling off of the ends of the scaffolds. When the ethanol soak-time exceeded 1 h (i.e., for $S_{220\text{-}120}$ and $S_{220\text{-}240}$ groups), the reduction in mechanical integrity might be a result of increased morphological distortion of the microspheres from a spherical shape that may have resulted in a poor packing of the microspheres. Thus, an ethanol soak of 1 h was found to provide optimal mechanical properties.

The effect of microsphere preparation and scaffold fabrication on T_g of PLG was analyzed by DSC (Table 6.1). Microsphere preparation led to a small drop (~1.4 %) in the T_g of the raw polymer ($p<0.005$). However, the ethanol treatment during

the fabrication of scaffolds resulted in reduced T_g of the PLG, where the average T_g dropped by 14 % compared to raw PLG ($p<10^{-6}$).

Changing the ethanol soak time resulted in the slight variation in the overall morphology of the scaffold. The mean theoretical porosities of $S_{220\text{-}30}$, $S_{220\text{-}60}$, $S_{220\text{-}120}$ and $S_{220\text{-}240}$ scaffolds were 41.1, 38.8, 32.8 and 40.4%, respectively (n=5). Unexpectedly, the theoretical porosity for the $S_{220\text{-}240}$ group was found to be higher than that for the $S_{220\text{-}60}$ and $S_{220\text{-}120}$ groups; however, no statistically significant differences were noticed among the groups. For the measurement of porosities of the scaffolds experimentally, scaffolds prepared using a 50 min ethanol soak-time were imaged using microCT (Fig. 6.7), and average porosities determined directly from scaffold sections using 3-D reconstruction were found to be 41.1%. The values were found to be considerably similar to the corresponding porosity value obtained using 2-D imageJ analysis (41.5%) and similar to the average theoretical porosities (44.9%) (Table 6.2). MicroCT analysis also confirmed that the scaffolds were isotropic; the average degree of anisotropy was 1.06 ± 0.1. In addition, interconnectivity of the pore structure was confirmed by microCT.

Viability assessment

Porcine ankle chondrocytes, dynamically seeded and cultured on $S_{220\text{-}50}$ group scaffolds, were assessed for their viability. The majority of the cell population was identified as viable after a total of 18 days in culture (Fig. 6.8).

Concentration profile assessment study – Spatial control over the composition

Images of scaffolds that were prepared using specific flow profiles with dye-loaded or blank microsphere suspensions (described in Fig. 6.2) are shown in Fig. 6.9 (A–D). Images of the scaffolds captured under UV light were modified by pseudo-coloring them to create black and white images. Each image was divided in five equal parts, and particle distribution in the direction perpendicular to the interface was analyzed using ImageJ software to create relative intensity vs. relative distance plots. The plots demonstrated successful fabrication of bi-layered, multi-layered and gradient scaffolds (Fig. 6.9 E–H). Irrespective of the scaffolds, standard deviations were higher at the interface, probably due to imprecise settling of the microspheres in the mold and/or wetting effects on the walls of the mold. The characteristic nature of each plot, however, was similar to the corresponding flow profile applied during the scaffold fabrication. The plots demonstrated the ability of the scaffold fabrication set-up to create scaffolds of various predefined profiles with spatial control. In addition, the orientation of the interface may also be varied (compare Fig. 6.9B and 9C), which can be controlled by manipulating the vertical orientation of the cylindrical mold. Note that similar flow profiles were used to prepare these two scaffolds (Fig. 6.2B and 6.2C), the only difference being the pitch of the mold.

DISCUSSION

Spatial control over the release of the bioactive molecules is a critical aspect that, along with the temporal control, may provide the possibility of mimicking

complex signal patterns, such as those during embryonic development.[238] In the present study, we designed a novel scaffold fabrication apparatus and demonstrated our ability to produce microsphere-based scaffolds with spatial control over molecular composition. Proof-of-concept was provided using blank or dye-loaded microspheres, which were used as building blocks to fabricate bi-layered, multi-layered and gradient scaffolds.

In comparison to traditional microsphere preparation methods, our ability to synthesize monodisperse microspheres may lead to improved systems to explore the effects of microparticle size on microsphere-based scaffolds. Scaffolds made of uniform microspheres are ideal to study the influence of microparticle size on the degradation patterns and rates within scaffolds. In addition, as observed in the case of colloidal crystal-templated gel-based scaffolds,[347, 348] uniform microspheres can pack closely compared to randomly-sized microspheres, providing better control over the pore-sizes and porosity of the scaffold, and may considerably aid the mechanical integrity of the scaffolds. Moreover, local release of growth factor**s** from the microspheres in a bulk scaffold is related to individual microsphere size and polymer properties. Reproducibility and predictability associated with uniform microsphere-based scaffolds may make them suitable for a systematic study of physical and chemical effects in order to achieve control over local release of growth factor within such a scaffold.

Integrated microsphere matrices have been created in the past by employing a heat-sintering technique, which requires heating of microspheres above their T_g. Heat

sintering is suitable for the preparation of bioconductive microsphere-based scaffolds; however, inclusion of growth factors in the microspheres before exposing them to heat may severely affect protein activity. The sintering temperatures and durations of heat exposure used in some previous studies were 160ºC for 4 h (PLG; 85:15 lactic acid:glycolic acid),[331] 65ºC for 4 h (PLG/bioactive glass),[337] 70ºC for 4 h (poly(D,L-lactide)/poly(ethylene glycol)),[270] and 62ºC for varied times of 4, 24, 48 and 72 h (PLG; 58:42 lactic acid:glycolic acid).[349] Such elevated temperatures for extended durations may lead to reduction in the bioactivity or complete denaturation of encapsulated proteins.[270] In the present study, we introduced an ethanol treatment technique as an alternative for the production of microsphere-based matrices, which may alleviate such concerns. For example, the proprietary process used by Alkermes, Inc. (Cambridge, MA) utilizes low temperature casting of microspheres with ethanol as the anti-solvent.[350] Recently, another technique for creating microsphere-based scaffolds was reported that utilized dichloromethane vapor treatment, a benign process that was shown not to affect the activity of bioactive signals.[282, 338] Dichloromethane is an organic solvent commonly used in microsphere preparation methods for dissolving polymeric materials. Ethanol, on the other hand, is an organic solvent of higher polarity, which is arguably a more common chemical in tissue engineering protocols (applied as a sterilizing agent) and possesses an ability to physically attach aliphatic polyesters. As predicted by the Hildebrand theory involving the polymer/solvent solubility,[351] ethanol is a poor solvent for PLG in comparison to dichloromethane. When ethanol came in physical contact with PLG,

dissolution of a thin surface layer of PLG microspheres was previously observed,[352] typically resulting in the formation of a "skin layer" or a "thin film" around the microsphere, as can also be evidenced from the SEM images (Fig. 6.5). Due to ethanol treatment, a drop in T_g and subsequent plasticization of PLG scaffolds were reported.[353] Based on these reports and our observations, the mechanism of microsphere attachment appears to be that the treatment with ethanol leads to a drop in T_g, resulting in softening of the wetted microspheres near the surface. The surface films that form in the process adjoin, and then the subsequent freeze-drying step removes the ethanol from the integrated microsphere-based matrix. In the ethanol-free dry state, a recovery in mechanical properties of the scaffold is expected.[353] The duration of the ethanol soak was an important process parameter, as longer durations were expected to lead to increased thicknesses of the surface film layer by affecting the diffusion of ethanol into the microspheres. Figure 6.5 provides supporting evidence, where increased durations of ethanol exposure were observed to lead to increased deformation from a spherical morphology. In addition, the extent of interconnection between the microspheres was also increased with increasing ethanol soak. Plasticization of PLG with ethanol is also a function of polymer properties, such as molecular weight and crystallinity. For example, Perugini *et al.*[354] reported softening of lower molecular weight PLG (~12,000 Da) with an ethanol wash, while the same treatment did not affect the physical integrity of higher molecular weight PLG (~34,000 Da). When contrasted to solvent/anti-solvent sintering techniques,[339,

[340] the ethanol treatment process is an anti-solvent treatment method, which requires a longer time exposure comparatively, however, to a relatively mild organic solvent.

Because a highly porous substrate may provide more surface area for cellular attachment, high porosity and interconnectivity is a desired feature for tissue engineering scaffolds, which often comes at the expense of mechanical integrity. In this regard, an ethanol soak of 1 h was found to be the optimum that led to acceptable porosities and improved mechanical characteristics. The average porosity of the ethanol-treated scaffolds, as determined in the present study by 3-D microCT analysis, was found to be 41.1% for an ethanol soak of close to 1 h. These values were found to be similar to the corresponding theoretical porosity measurement and porosity values determined using 2-D image analysis (Table 6.2). The degradable nature of the substrate material suggests that the porosity of such a construct may eventually increase with time, thus porosities in this range (~38-43%) may be acceptable. Moreover, a previous *in vivo* study utilizing microparticle-based scaffolds provides supporting evidence regarding the suitability of such scaffolds for *in vivo* defect repair.[331] However, to enhance the porosity as well as interconnectivity of the pores in the scaffolds, one possible future approach would be to utilize hollow or porous microspheres in the preparation of the scaffolds.[355, 356] Our group has demonstrated the ability to create porous microspheres in the past,[357] and scaffolds made of such entities will be investigated in the future. In addition, future work will be directed to improve the cell seeding efficiency and cell distribution within such matrices.

Unidirectional compression testing was performed in a simulated physiological environment, since these scaffolds are designed for *in vitro*/*in vivo* tissue engineering. Mechanical properties are direction-independent due to the isotropic nature of the scaffolds. The moduli of elasticity of the scaffolds were found to be ~140-300 kPa, after which the scaffold material began to deform plastically. The primary reason for such a low range of elastic moduli was the testing conditions (hydrated conditions, 37 °C), known to affect the mechanical properties of similar polymeric materials.[353] Due to the degradable nature of the used polymer, one may expect a further decrease in the mechanical integrity of the scaffold with degradation. Although the degradation effects may be counteracted by tissue regeneration in the pores, which could enhance the mechanical properties, a few strategies can be investigated in the future in this regard. First, selection of an adequate PLG polymer (e.g., a higher lactic acid content, higher molecular weight, ester-end group chemistry and a higher T_g) can be utilized in microsphere preparation that may significantly decrease the reduction in mechanical properties with hydration and temperature, and may allow tailoring the degradation rate of the scaffold for specific needs. Second, a bimodal distribution of spheres can be utilized in scaffold preparation that will allow for a better mechanical integrity and closer packing of the microspheres (although it may lead to a reduced pore volume that can potentially reduce cellular infiltration). Finally, one may encapsulate nano-phase materials in the microspheres to create composite spheres that may improve the mechanical characteristics of the building units. For example, one may encapsulate nano-phase biocompatible calcium salts as

a filler material in the microspheres that may improve the mechanical characteristics, and also act as a buffering agent to reduce pH changes that occur with the degradation of PLG (due to the formation of acidic by-products).[224] This approach may also enhance the overall cellular viability over a long-term culture. Finally, effects of adding haptotactic cues, such as RGD (Arg-Gly-Asp) and YIGSR (Tyr-Ile-Gly-Ser-Arg), can be explored to improve the overall cell viability.[358]

The effect of ethanol treatment on the T_g of the raw PLG was found to be significant. It may indicate a possibility that residual levels of ethanol may be present in the scaffold. More importantly, the T_g dropped below 37ºC, which is not desired as it may considerably affect the mechanical properties of the scaffolds when placed *in vivo*. To keep the T_g of the scaffolds above the limit of 37ºC, some possible strategies could be to use PLG with higher molecular weights, or with a higher lactic acid to glycolic acid ratio.

From the perspective of osteochondral tissue engineering, there are only a few previous reports of scaffold designs having heterogeneous distribution of growth factors embedded within an integrated scaffold. Holland *et al.* created bi-layered oligo(polyethylene glycol) hydrogel based scaffolds, designed to release transforming growth factor-β1 (TGF-β1) and/or insulin like growth factor-I (IGF-I) in the cartilage-forming layer, while no growth factors were added to the bone forming layer.[359] In a similar previous study from the same group, single growth factor (TGF- β1) release from the cartilage-forming layer was investigated.[360] The concept of zonal release for multiple growth factor delivery was demonstrated by Suciati *et al.*[270] In their work,

poly(D,L-lactic acid) microsphere-based scaffolds were created using poly(ethylene glycol) as a plasticizer, and subsequently zonal release of horseradish peroxidase and bone morphogenic protein-2 (BMP-2) from tri-layered and bi-layered scaffolds, respectively, was demonstrated. As the release kinetics of growth factors from such carriers is a diffusion-controlled phenomenon, a step transitioning of the carriers of signaling molecules in bi-layered scaffolds, as applied in the aforementioned studies, may be sufficient to promote the interfacial tissue regeneration successfully. The approach described here offers the potential advantage of a seamless transition at the osteochondral interfaces using spatially controlled macroscopic gradients of bioactive signal molecules at the interface. Although a single cell *per se* will not be able to sense such a macroscopic gradient (unless it is a migrating cell), spatial variations in the signals will cause an individual cell *A* at point 1 to experience different signals than cell *B* at point 2, and individual cell responses combined with cell-to-cell signaling may lead to a commensurate cell response that may benefit interfacial tissue regeneration. In addition, microsphere-based gradient scaffolds made of subcellular-sized microspheres may provide an alternative to generate stable gradients of soluble bioactive signals over a long time periods by acting as sustained delivery vehicles, and thus may prove helpful in the study of chemotaxis.

CONCLUSIONS

We have demonstrated a novel approach to creating microparticle-based gradient scaffolds, which may be designed to release opposing gradients of bioactive

signals at the interface of a biphasic scaffold. The methodology may also be extended to create biphasic scaffolds with more than two growth factors or multiphasic scaffolds with more than one interface. In addition, utilizing microspheres made of two different materials, one may employ this technique to create transversely isotropic substrates that contain a macroscopic gradient in composition and stiffness. We reported use of ethanol treatment to create interconnected microsphere-based matrices, as an alternative to heat sintering and solvent treatment methods. For example, growth factor-loaded microspheres may be used to create similar heterogeneous three-dimensional scaffolds to deliver growth factors with pre-defined spatial and temporal release profiles. Future studies will be directed to quantify the release of active factors from the scaffolds, improve the mechanical properties, investigate the effect of microsphere size, and evaluate the performance of seamless gradient scaffolds, compared to bi-layered scaffolds, for osteochondral tissue regeneration.

CHAPTER 7: Three-Dimensional Stiffness Gradient Scaffolds for Functional Regeneration of Interfacial Tissues*

Continuous transitional gradients in cellular-extracellular architecture exist throughout the human body, within tissues and at tissue interfaces, to satisfy spatially diverse functional needs.[361, 362] Interfacial tissue engineering, an emerging field that focuses on regenerating interfaces between the tissues (e.g., bone-cartilage, muscle-tendon, etc.), is a strategic approach to create functional tissue interfaces that 1) may resolve the issues of graft failure at the interface, and 2) may be able to provide mutually inductive endogenous signals from the adjacent tissues that are involved during tissue formation *in vivo*.[269] In certain cases, interfacial tissue engineering may also provide an alternative to tissue adhesives,[363, 364] where bridging a tissue-engineered prosthetic/biomaterial to a native tissue could be achieved by successful integration of one (or both) end(s) of the tissue-engineered substrate directly with the native tissue to facilitate regeneration. Approaches to engineer tissue interfaces, to date, have largely focused on creating graded-structures (e.g., biphasic, triphasic) in cellular/biomaterial composition, which do not closely mimic the continuous transitioning of native tissue, and which may lead to stress concentrations at each interface and eventual failure of the implant.[361, 362]

Delivery of genes or growth factors in a continuous gradient manner across a tissue engineering scaffold via biomaterials is a relatively new avenue of research to

*Chapter to be submitted to Adv Mater as Singh, Dormer, Salash, Christian, Moore, Berkland and Detamore, "Three-Dimensional Stiffness Gradient Scaffolds for Functional Regeneration of Interfacial Tissues", Oct 2008

engineer heterogeneous tissue substrates, where gradation in material properties may be achieved via matrix deposition *in vitro* or *in vivo*.[361] An alternative approach could be to utilize a three-dimensional scaffold that contains a continuous gradient in mechanical properties from the beginning, as a functional culture substrate or a functional implant. Various approaches used to create continuous gradient scaffolds at macro- and micro-scales included diffusion-based or controlled photopolymerization processes, where gradients were generated by controlled photo-exposure (using a gradient photomask or by varying photo-exposure time) or by altering the cross-linker concentration via diffusion.[126, 129, 130, 138, 139] A major limitation is that these approaches are primarily restricted to the construction of 2-D gel-based substrates. Here, we demonstrate a novel approach to construct biocompatible, macroporous 3-D tissue engineering scaffolds containing a continuous gradient in stiffness. Using polymeric microspheres, made of poly(D,L-lactic-*co*-glycolic acid) (PLGA), and composite microspheres encapsulating a higher stiffness nano-phase material (PLGA encapsulating $CaCO_3$ or TiO_2 nanoparticles), microsphere-based homogeneous and gradient scaffolds were constructed. The controllable mechanical characteristics and biocompatible nature of these scaffolds makes them an attractive alternative for a variety of interfacial tissue engineering applications.

PLGA/composite microspheres were prepared via an emulsion/solvent extraction method using technology from our previous reports, resulting in a relatively monodisperse microsphere size distribution compared to traditional

microsphere fabrication techniques.[269, 341] Composite suspensions were prepared by dispersing nano-phase materials in a PLGA solution (dissolved in dichloromethane (DCM)) in different proportions (% by weight). Controlled regular jet instabilities created by an ultrasonic transducer resulted in cleaving the polymer/composite stream into uniform droplets that harden into microspheres following solvent extraction.[269] Microspheres were characterized for their size and morphology (Fig. 7.1). Coulter Multisizer size distribution plots demonstrated the high monodispersity of microspheres, with their average diameters each in the range of 130-175 μm following solvent extraction (Fig. 7.1a). Morphological assessment of intact and cryofractured microspheres with scanning electron microscopy (SEM) indicated that encapsulation of nano-phase materials led to changes in the typically smooth surface and interior morphology of PLGA microspheres (Fig. 7.1B, D). In general, encapsulation of nano-phase $CaCO_3$ resulted in the formation of granular interior and exterior containing submicron-sized pores throughout the microspheres, possibly indicating that a portion of the $CaCO_3$ leached out of the microspheres during solvent evaporation (Fig. 7.1B). In contrast, TiO_2-encapsulated microspheres displayed a smooth exterior and less porous interior (Fig. 7.1D). SEM/Energy dispersive spectroscopy (EDS) was performed to determine the distribution of nano-phase materials within the microspheres. The presence of Ca and Ti were each confirmed via EDS. The elemental distribution of Ca and Ti, as observed via SEM/EDS on the surface and interiors of the microspheres, confirmed the presence of $CaCO_3$ and TiO_2

in respective composite microspheres (Fig. 7.1C, E), where agglomeration of nano-phase materials at several locations was evident.

Microsphere-based scaffolds were prepared using an ethanol sintering method, where ethanol is used as a plasticizer to fuse the adjoining microspheres.[269] Homogeneous cylindrical scaffolds, prepared using a 2 h duration of ethanol soaking, were characterized for their morphology and cytotoxicity (Fig. 7.2). Scanning electron micrographs of a representative scaffold, prepared by sintering the composite microspheres (90:10 PLGA:$CaCO_3$), displayed the typical porous nature of the scaffold and microsphere fusion sites (Fig. 7.2A, B). The compatibility of scaffolds with human umbilical cord mesenchymal stromal cells (HUCMSCs) was also assessed. For this study, cells were seeded on the scaffolds (90:10 PLGA:$CaCO_3$) drop-wise, and statically cultured for 2 wks. HUCMSCs inside the scaffolds were imaged by fluorescence imaging of a fractured scaffold using a Live/Dead assay, which demonstrated high cell viability (green fluorescence) (Fig. 7.2 C, D).

Gradient scaffolds containing an anisotropic distribution of $CaCO_3/TiO_2$ were prepared to demonstrate a continuous gradient of mechanical strength within constructs. Using a gradient generation methodology described earlier,[269] gradient scaffolds were prepared via controlled infusion of two separately-loaded microsphere suspensions (in ddH_2O) into a cylindrical glass mold using two programmable syringe pumps followed by an ethanol sintering for 2 h. The pumps were co-programmed to provide a linearly increasing flow profile for one microsphere

suspension and a linearly decreasing profile for the other suspension, thus, maintaining a constant overall flow rate. To visualize the gradient, a scaffold was created using dye (Rhodamine B)-loaded PLGA microspheres and composite (90:10 PLGA:$CaCO_3$) microspheres, which were flowed into the mold then fused using a 2 h ethanol soak (Fig. 7.3A). Two-dimensional image analysis revealed that the fluorescence intensity of white pixels increased in a continuous gradient across the length of the scaffold, indicating an increase in the ratio of composite to dye-loaded microspheres along the axis of the scaffold.

To determine the effect of the inclusion of nano-phase materials on the overall properties of the scaffolds, homogeneous scaffolds constructed using different microsphere types were subjected to uniaxial unconfined compression testing. Compression of microsphere-based scaffolds under hydrated conditions results in a typical stress-strain curve, where an initial linear region, representing the matrix stiffness, is followed by a non-linear pore-collapse regime and a material densification regime, respectively.[269] Pore-collapse for the composite scaffolds usually began at ~40% strain compared to ~25% strain corresponding to the control PLGA scaffolds. The moduli of elasticity evaluated at a fixed strain value (25% strain) and preceding the onset of pore-collapse (40% for the composite microspheres and 25% for the control microspheres) are reported (Fig. 7.3B). Although the inclusion of nano-phase materials in the microspheres was expected to lead to an increase in stiffness of the microspheres, the overall stiffness of the composite scaffolds decreased compared to control PLGA scaffolds at a fixed strain value (25%

strain). This suggested a lower extent of sintering of composite microspheres for a 2 h ethanol-soak, and likely a higher porosity, compared to the control PLGA microspheres. The maximum matrix stiffness, corresponding to the onset of the pore-collapse regime, was found to be higher for the scaffolds prepared using composite microspheres having a higher $CaCO_3$ content (20% and 30% by wt) compared to the controls. Scaffolds prepared using 95:5 PLGA:$CaCO_3$ and 90:10 PLGA:$CaCO_3$ (% by wt) demonstrated a lower matrix stiffness, in general. It is possible that the surface modifications resulting from the incorporation of nano-phase materials led to a decrease in the extent of sintering of the composite microspheres, thus yielding a lower stiffness of the scaffolds. For composite microspheres, increasing the relative content of $CaCO_3$, however, led to an increase in the scaffold stiffness. In addition, scaffolds constructed using TiO_2-encapsulated microspheres displayed relatively higher stiffness compared to corresponding $CaCO_3$-encapsulated microspheres.

Using composite microspheres (containing nano-phase $CaCO_3/TiO_2$) and polymeric microspheres, a method to prepare scaffolds containing a gradient distribution in the nano-phase material was demonstrated. The extent of sintering, composition of the microspheres and the relative content of the two microsphere types can be selectively varied to alter the stiffness of the matrix to create regular and inverse-gradients in mechanical properties. The approach described here offered biocompatible and porous macroscopic 3-D scaffolds with controllable mechanical properties for tissue engineering, and gradient scaffolds that may be particularly useful for interfacial tissue regeneration. Integration of controlled release strategies

(e.g., growth factors) via microspheres would be straightforward and would allow fabrication of acellular implantable devices for translational tissue regeneration applications.

EXPERIMENTAL

Materials

PLGA (50:50) (inherent viscosity: 0.36 dL g^{-1}) was purchased from Lakeshore Biomaterials. $CaCO_3$ nanoparticles (SOCAL® 31, mean particle size 70 μm) were generously donated by Solvay Chemicals. TiO_2 nanoparticles (<100 nm (BET)) were purchased from Sigma. Poly(vinyl alcohol) (PVA; 88% hydrolyzed, 25,000 Da) was obtained from Polysciences, Inc. Rhodamine B was purchased from MP Biomedicals, Inc. All cell culture media was supplied by Invitrogen, unless otherwise stated. Dichloromethane (DCM; HPLC grade) was obtained from Fisher Scientific (Pittsburgh, PA). Ethanol (Absolute - 200 Proof) was obtained in house.

Preparation of microspheres

Uniform microspheres were prepared using technology from our previous reports.[269, 341] Briefly, PLGA dissolved in DCM (20% w/v) was sprayed through a small-gauge needle. Using acoustic excitation produced by an ultrasonic transducer, regular jet instabilities were created in the polymer stream that produced uniform polymer droplets. An annular carrier non-solvent stream (0.5% PVA w/v in ddH_2O) surrounding the droplets was produced using a nozzle coaxial to the needle. The emanated polymer/carrier streams flowed into a beaker containing the non-solvent.

Incipient polymer droplets were stirred for 3-4 h to allow solvent evaporation, which were then filtered and rinsed with ddH_2O to remove residual PVA. Finally, microspheres were lyophilized for ca. 2 days and stored at –20°C under desiccant. Composite microspheres were prepared likewise, where the polymer stream was replaced with a composite stream that also contained a nano-phase material ($CaCO_3/TiO_2$) suspended in the PLGA/DCM solution (sonicated at 50% amplitude for 1 min; in different proportions, % by weight).

Preparation of scaffolds

Gradient scaffolds were prepared in a manner described earlier.[269] Briefly, two sets of lyophilized microspheres were dispersed in ddH_2O 2.5 % w/v, and separately loaded into two syringes. The suspensions were pumped to a cylindrical glass mold (6 mm diameter) in a controlled manner using programmable syringe pumps (PHD 22/2000, Harvard Apparatus, Inc.). Using an additional infusion syringe pump and a vacuum pump, a constant level of distilled water was maintained in the mold. Using a filter (particle retention > 3μm) at the bottom of the mold, ddH_2O was filtered, while the microparticles stacked in the mold. The stacked microspheres were then sintered using an ethanol treatment (100%) for 2 h.[269] The molds (containing the scaffolds) were freeze-dried for a ca. 2 days, and then the scaffolds were retrieved from the molds.

Characterization of microspheres and scaffolds

The sizes of the different types of microspheres were determined using a Coulter Multisizer 3 (Beckman Coulter Inc., Fullerton, CA) equipped with a 560-μm aperture. SEM/EDS analysis was performed on intact and cryofractured microspheres using a LEO 1550 field emission scanning electron microscope equipped with an energy dispersive system (EDAX). Scaffolds prepared using dye-loaded microspheres were imaged under UV light using a UV lamp (254/365 nm; UVGL-25, UVP, Inc., Upland, CA) and a high-resolution camera, and images were analyzed using NIH ImageJ software to assess spatial distribution of the dye molecules.

Mechanical testing

Mechanical characterization of the scaffolds (~2 to 6 mm height, diameter ~6 mm) was performed under uniaxial, unconfined compression (Instron Model 5848, Canton, MA; 50 N load cell). Samples were tare-loaded (0.1 N, i.e., ~3.5 kPa), then compressed at a strain rate of 1% s^{-1} under phosphate buffered saline (0.138 M NaCl, 0.0027 M KCl) at 37 ºC. Moduli of elasticity were obtained from the initial linear regions of the stress-strain curves.[269, 343]

Cell Culture and seeding

HUCMSCs were harvested from one human umbilical cord obtained from the University of Kansas Medical Center (KU Medical Center IRB approval no. 10951, KU-Lawrence IRB approval no. 15402; informed signed consent was obtained prior

to the delivery) as described earlier.[365] The cell culture medium consisted of low glucose Dulbecco's Modified Eagle's Medium (DMEM-LG), 10%FBS (Gemini), and 1% penicillin streptomycin (PS). Cells (expanded to passage 4, suspended in 75 μL medium) were seeded onto scaffolds (90:10 PLGA:$CaCO_3$; sterilized using ethylene oxide) drop-wise at a density of 10×10^6 cells mL^{-1} in a 24 well untreated plate, then 1 mL of culture medium was added into wells.

Viability assessment

Cells were cultured for 2 weeks onto scaffolds, with half of the media changed every other day. Subsequently, cell viability was evaluated by staining the scaffolds using a LIVE/DEAD reagent (2 mM calcein AM, 4 mM ethidium homodimer-1; Molecular Probes) followed by a 45 min incubation at room temperature, before being subjected to fluorescence microscopy (Olympus/Intelligent Innovations Spinning Disk Confocal Microscope).

.

CHAPTER 8: Microsphere-Based Scaffolds for Cartilage Tissue Engineering: Using Sub-critical CO_2 as a Sintering Agent*

ABSTRACT

Shape-specific, macroporous tissue engineering scaffolds were fabricated and homogeneously seeded with cells in a single step. This method brings together CO_2 polymer processing and microparticle-based scaffolds in a manner that allows each to solve the key limitation of the other. Specifically, microparticle-based scaffolds have suffered from the limitation that conventional microsphere sintering methods (e.g., heat, solvents) are not cytocompatible, yet we have shown that cell viability was sustained with sub-critical (i.e., gaseous) CO_2 sintering of microspheres in the presence of cells at near-ambient temperatures. On the other hand, the fused microspheres provided the pore interconnectivity that has eluded supercritical CO_2 foaming approaches. Here, fused poly(lactide-co-glycolide) microsphere scaffolds were seeded with human umbilical cord mesenchymal stromal cells to demonstrate the feasibility of utilizing these matrices for cartilage regeneration. We also demonstrated that the approach may be modified to produce thin cell-loaded patches as a promising alternative for skin tissue engineering applications.

INTRODUCTION

*Chapter submitted to Nat Mater as Singh, Sandhu, Scurto, Berkland and Detamore, "Microsphere-Based Scaffolds for Cartilage Tissue Engineering: Using Sub-critical CO_2 as a Sintering Agent", Oct 2008.

Microsphere-based tissue engineering scaffold designs have attracted significant attention in recent years[269, 329-334] because the microspheres as building blocks offer several benefits, including ease of fabrication, control over morphology and physicochemical characteristics, and versatility of controlling the release kinetics of encapsulated factors.[328] The properties of a scaffold, in turn, can be tailored by altering the microsphere design and fabrication method, for example to create gradient-based scaffolds.[269, 355, 356] Similarly, macromechanical properties and degradability can be altered with the selection of the raw material. The polymer also offers flexibility in the degradation kinetics, modulated by altering one or more of the factors, such as the molecular weight, co-polymer ratio, tacticity, crystallinity, etc.[335, 336] To date, the methods used to produce microsphere-based scaffolds have utilized heat-sintering,[331, 337] a solvent vapor treatment (dichloromethane),[282, 338] a solvent/non-solvent sintering method (acetone and ethanol treatment),[339, 340] or a non-solvent sintering technique (ethanol treatment),[269] all of which involve exposure to elevated temperatures or organic solvents that may be a potential limitation for their pharmaceutical or medical applications.[366]

In lieu of conventional temperature-regulated or organic solvent-assisted scaffold fabrication, supercritical fluid (SCF)-technology has offered an alternative method of melt processing of the polymers.[367] Specifically, supercritical carbon dioxide (CO_2) has been widely used as it is inexpensive, non-toxic, non-flammable, recoverable and reusable[366]. Exploiting the ability of supercritical CO_2 (T_c = 304.1 K, P_c = 73.8 bar) to dissolve/plasticize many polymeric materials, some polymeric

scaffold fabrication techniques have been developed including gas foaming and emulsion templating (see reviews by Davies *et al.*[367] and Barry *et al.*[368]), which allow incorporation of bioactive factors and/or cells during the scaffold fabrication.[369, 370] Near-critical or liquid CO_2 exposure (pressure ~ 55-60 bar) has been used to produce regular or intricate-shaped scaffolds using gas foaming or particulate consolidation.[371-373] However, one inherent limitation of gas foaming-based techniques is the closed-cell structure and lack of pore interconnectedness, and alternative modified techniques such as gas foaming/particulate are usually time-consuming and present challenges in incorporating bioactive factors.[367, 374]

For microsphere-based scaffolds, microsphere size is one of the major determinants of polymer degradation rate, governing the release kinetics of loaded molecules and providing the control over pore-sizes and macro-porosity.[269] Utilizing our ability to create highly monodisperse microspheres[341] and capitalizing on the plasticizing ability of CO_2, a novel microsphere-based scaffold fabrication technique is presented here using poly(D,L-lactide-co-glycolide) (PLG) microspheres, which also allows the production of shape-specific scaffolds. Using chondrocytes and human umbilical cord mesenchymal stromal cells (HUCMSC),[344, 365, 375, 376] preliminary evaluations of the scaffolds for cartilage tissue engineering applications were performed. Perhaps most importantly, the CO_2 sintering technique is amenable to produce cell-containing, shape-specific matrices (patches and scaffolds) under relatively mild conditions via a single-step sintering of microspheres in the presence of cells, with high cell viability.

RESULTS AND DISCUSSION

Relatively monodisperse microspheres having uniform nominal diameters were created using a previously reported method.[341] These microspheres demonstrate a solid interior morphology.[269] The nominal particle sizes were: 120 μm, 140 μm (both with an intrinsic viscosity (i.v.) of 0.37 dL/g), and 5 μm, 100 μm, 175 μm, 240 μm and 500 μm (i.v. = 0.33 dL/g) (Fig. 8.1A). The sub-critical CO_2 sintering method to manufacture microsphere-based scaffolds is a modification of the gas foaming technique. In the past, plasticization of PLG in pressurized CO_2 has been applied to create foamed scaffolds, where saturation of the polymer with CO_2 was performed at sub-critical pressures (~55 bar) with equilibration periods of greater than 24 h, and a rapid depressurization led to the nucleation of the gas (forming pores in the material) and restoration of the glass transition temperature.[371, 374, 377] To prepare microsphere-based matrices in the current study, the equilibration of CO_2 in the polymer was restricted by decreasing the pressure and the duration of CO_2 exposure, leading to a comparatively reduced plasticized state of the PLG. While this allowed the microspheres to primarily retain their shape, the plasticization of the microsphere surfaces led to the sintering of the adjoining microspheres, yielding a porous matrix (Fig. 8.2). The conditions of CO_2 exposure are likely a prime factor responsible for promoting the mutual-penetration and increasing the chain mobility at the interfaces of adjoining microspheres.[378] Based on preliminary investigations, the pressure (15 bar) and duration of CO_2 exposure (1 h) were selected to allow sintering of all the

microspheres (with different sizes and i.v. of PLG). Usually, microspheres with smaller sizes may require milder conditions (less pressure or shorter exposure) to achieve optimal sintering. As shown earlier, a similar consolidation technique applied to attach PLG fiber aggregates (700-1400 μm) required only a 15 s duration, however with liquid CO_2 at 55 bar pressure.[373] In addition, the rate of depressurization was an important factor that governed the basic morphology of the scaffolds in the current study. A moderate rate of depressurization (0.14–0.21 bar/s) was found to be optimal for the production of sintered matrices. For typical CO_2 sintering conditions, instantaneous depressurization (i.e., in less than 5 s; for 64 μm diameter microspheres, i.v. = 0.33 dL/g) or depressurization at very slow rates (i.e., < 0.07 bar/s; for 240 μm diameter microspheres, i.v. = 0.33 dL/g) led to foaming of the prepared scaffolds, depending on the microsphere size and i.v. of the polymer.

Microsphere-based cylindrical scaffolds were constructed in cylindrical plastic molds using monodisperse microspheres (~20-80 mg) of all of the sizes except for the 5 μm group. In addition, to prepare scaffolds with a bimodal population of microspheres, a mixture of two different particle types (sizes: 5 μm and 140 μm) were used. By utilizing custom rubber molds of different shapes and microspheres of size 140 μm, a variety of shape-specific scaffolds were also constructed in a similar manner (Fig. 8.1B). Morphological assessment of the scaffolds using scanning electron microscopy revealed that the microsphere matrices were porous, where the microspheres largely retained their shape. Under the typical CO_2 sintering conditions, the extent of sintering of the microspheres was found, in general, to be a

factor of the microsphere size (compare Fig. 8.2 (A and B) with (C and D), respectively). Also, the PLG microspheres of lower i.v. (i.e., 0.33 dL/g) displayed a distortion from the spherical morphology and a higher degree of sintering (compare Fig. 8.2 (A and C) with (B and D), respectively). Both the size of the microsphere and the intrinsic viscosity of the polymer were found to affect the pore sizes. As can be observed in Fig. 8.2, the pore sizes for the scaffolds prepared with PLG microspheres of lower i.v. had anisotropic pores with closed pores at several places. Roughly, the average pore-sizes were around 70 μm (Fig. 8.2A and 8.2B), 50 μm (Fig. 8.2C) and 40 μm (Fig. 8.2D). Micrographs of a single microsphere (140 μm) revealed the modifications in the surface of the microspheres following the CO_2 sintering, including the microsphere connection sites (Fig. 8.2E). The microsphere morphology, closely resembling the appearance of a microsphere reported earlier in an ethanol melding method,[269] showed the presence of a surface film of PLG containing ripples, indicating the surface swelling of PLG. To improve the inter-microsphere connection that could improve the mechanical characteristics of the scaffolds, scaffolds were prepared using two different groups of microspheres (140 μm and 5 μm) (mixed together in a ratio of 1:8 by weight, respectively). Additional connecting bridges between the large microspheres were formed, however, at the loss of overall scaffold porosity, with reduced pore-sizes (Fig. 8.2F).

Mechanical characterization of the scaffolds was performed by unconfined compression under simulated physiological conditions. The hypothesized mechanism of compression for microsphere-based matrices is somewhat analogous to the

compression of closed-foam cellular solids.[343] Following an initial linear region, a non-linear pore collapse region follows.[269] The moduli of elasticity were determined from the stress-strain plots using the end of the initial linear regions before the onset of non-linear region (extending to ~ 40% strain, in general), which indicate the scaffold elasticity[269]. The average moduli of the scaffolds ranged from 71 to 196 kPa (Fig. 8.3), matching the moduli of native cartilaginous tissues.[379] The stiffnesses of the scaffolds revealed a somewhat inverse relationship between average microsphere size and average mechanical modulus. Also, a higher intrinsic viscosity of the polymer also seemed to improve the mechanical characteristics, probably because of a spherical morphology and more ordered packing of the microspheres (as mentioned before, see Fig. 8.2). In addition, inclusion of smaller interstitial spheres in the pores led to an increase in the average mechanical modulus (compare i.v. = 0.37 vs. bimodal for the 140 μm diameter microspheres) of the scaffolds. The differences between the average moduli of all the groups, however, were not statistically significant, probably owing to imperfect packing of the microspheres (inter-specimen variability leading to large standard deviations).

Cell culture studies were performed to determine the suitability of these scaffolds for tissue engineering. Porcine chondrocytes, dynamically seeded and cultured on the scaffolds, were assessed for their viability. The majority of the cell population was identified as viable after 3 week in culture (Fig. 8.4-I). Immunohistochemistry revealed positive staining for collagen types I and II following the 3 week culture (Fig. 8.4-II). In addition, Safranin-O staining revealed signs of

glycosaminoglycan (GAG) formation for both the groups (Fig. 8.4-II). Biochemical analysis also revealed positive indications of cartilage-like matrix formation, where the presence of GAGs and collagen were detected (Table 8.1). However, biochemical analysis revealed that the cell number per construct considerably dropped, and the majority of the cells could not attach to the scaffolds. A possible reason could be the cell seeding method, where cell infiltration into the scaffolds was probably affected by seeding them dynamically.[269] To address this issue and to allow for homogeneous seeding of the constructs, cell loaded matrices were fabricated via a one-step CO_2 sintering of microspheres with the HUCMSCs. The conditions of sintering were altered to minimize the time of exposure (4 min or less, excluding the depressurization time), while keeping the CO_2 pressure to a relatively low value (30 bar). Interestingly, when performed in the presence of the culture medium, the sintering process resulted in a thin patch formation, where only a few microsphere layers at the top of the mold were sintered together (Fig. 8.5). In contrast, in the absence of the medium, a mixture of cells with the microspheres yielded completely sintered matrices. The difference between the thin patch formation (with culture medium) and full 3D scaffold formation (absence of medium) can be attributed to the thermodynamic limitation of CO_2 solubility in the liquid phase (Henry's Law). Viability assessment of the cell-loaded thin patch and the scaffolds revealed that virtually the entire cell population survived the sintering process (Fig. 8.5B and C). The pioneering work by Ginty *et al.*,[369] where cell survival in a brief exposure to supercritical CO_2 was demonstrated, and less than 5 min of overall CO_2 exposure was

shown to be primarily non-malignant for a variety of cells, formed the basis of selecting the exposure time range. Although CO_2 at high pressures for long durations may not be cytocompatible due to known sterilization efficacy of supercritical CO_2 achieved by lowering the cytoplasmic pH from the formation of carbonic acid and the shear forces of intercellular bubble formation upon depressurization, we have demonstrated that the milder conditions with milder gaseous CO_2 conditions are highly conducive to cell viability. Based on the size of the microspheres, the type of PLG, and the type of cells under consideration, various sub-critical CO_2 sintering conditions may exist (i.e., a number of combinations of sub-critical pressures and exposure times), which may allow the formation of cell-loaded matrices without affecting the cell viability. Future *in vitro* and *in vivo* investigations will shed more light on the long-term performance of cell-loaded constructs prepared in this manner for the purposes of tissue regeneration.

Gaseous CO_2 sintering was found to be a straightforward method to fabricate cell-seeded, microsphere-based, shape-specific constructs in a single step. These constructs of course retain the numerous advantages of microsphere-based scaffolds such as spatiotemporal control for creating 3D signal and stiffness gradients for interfacial tissue engineering within a single scaffold. Compared to the other methods of microsphere-based scaffold fabrication, which utilize heat, solvent and/or anti-solvent–induced plasticization,[269, 282, 331, 337-340] the CO_2 sintering method may be a more benign process. The resulting scaffolds were porous, exhibited moduli similar to the native cartilaginous tissues, and displayed support for chondrogenesis and

cartilage-like tissue growth. The process of sub-critical CO_2 sintering is also amenable to produce cell-containing matrices under relatively mild conditions. The ability to create cell-loaded scaffolds and patches may have important implications for cartilage and skin tissue engineering, respectively, where growth factor-encapsulated microspheres can be used to design cell-loaded controlled release vehicles in a single-step as a regenerative medicine.

MATERIALS AND METHODS

Uniform PLG (50:50 lactic acid:glycolic acid; acid end group, Mw ~40,000-45,000 Da of intrinsic viscosity (i.v.) 0.33 dL/g (Lactel, Pelham, AL) and of i.v. 0.37 dL/g (Lakeshore Biomaterials, Birmingham, AL)) microspheres were fabricated using technology from our previous reports.[269, 341] The size distribution of microspheres was determined using a Coulter Multisizer 3 (Beckman Coulter Inc., Fullerton, CA). Particles of different average diameters were separately loaded into cylindrical molds, and exposed to CO_2 at sub-critical levels, commonly ~ 15 bars (220 psig) at 25°C for 1 h followed by depressurization at ~0.14-0.21 bar/s, unless otherwise specified. CO_2 exposure was accomplished with a high-pressure vessel, consisting of a stainless steel body with view windows rated to 400 bar of pressure. Scaffolds containing a bimodal distribution of particles were prepared using a mixture of particles of two different sizes. Preparation of shape-specific scaffolds was carried out in a similar manner in rubber molds cut into specific designs.

For morphological assessment, freeze-dried scaffolds were sputter coated with gold and observed using a Leo 1550 field emission scanning electron microscope at an accelerating voltage of 5 kV. Mechanical characterization of the scaffolds (1 to 4 mm height, diameter ~6 mm) was performed under uniaxial, unconfined compression (Instron Model 5848, Canton, MA; 50 N load cell). Samples were tare-loaded (~10 kPa), then compressed at a strain rate of 0.5 mm/min under phosphate buffered saline (0.138 M sodium chloride, 0.0027 M potassium chloride) at 37 ºC.[269] Moduli of elasticity were obtained from the initial linear regions of the stress-strain curves.[269, 343]

Chondrocytes were harvested from hog ankles and mandibular condyles (Duroc breed, 6 months old, female) as described previously.[344] Frozen HUCMSCs (P1) for 3 week cell culture studies were generously donated by Dr. Mark Weiss's group at Kansas State University (The Kansas State University IRB approval no. 3966).[365] All cells were plated for expansion in monolayer and incubated at 37°C in 5% CO_2, with media changed every 2–3 days. The culture medium for HUCMSCs was composed of Dulbecco's Modified Eagle medium (DMEM; low glucose), 1% penicillin–streptomycin (both from Invitrogen Life Technologies, Carlsbad, CA) and 10% fetal bovine serum (FBS; Gemini, West Sacramento, CA). The culture medium for chondrocytes consisted of DMEM (high glucose), 1% penicillin–streptomycin–fungizone, 1% non-essential amino acids (NEAA) (all from Invitrogen Life Technologies), 10% FBS and 25 μg/mL L-ascorbic acid (Sigma, St. Louis, MO). Chondrocytes from the porcine mandibular condyle (P3) and ankle (P2) were mixed

before being seeded onto one set of scaffolds, whereas HUCMSCs (P4) were seeded onto another set of scaffolds.

Cylindrical scaffolds (6 mm diameter, ~2 mm height) were produced using microspheres of 175 μm diameter at CO_2 sintering conditions of ~13 bar (190 psig) pressure and 1 hour exposure followed by depressurization at ~0.14-0.21 bar/s. Cells were then seeded on scaffolds (sterilized using ethylene oxide) at a density of approximately 20×10^6 cells per mL of scaffold using the orbital shaker method as described previously,[345] and cultured for 3 week with half of the media refreshed every other day. During the cell culture, the culture medium for HUCMSC-seeded scaffolds was replaced with a chondrogenic medium.[365] At week 3, scaffolds were analyzed for matrix production using histology (Safranin-O staining for GAG production), immunohistochemistry (for collagen types I and II), and biochemical assays (picogreen, hydroxyproline, and dimethylmethylene blue (DMMB) assays for determining the cell number, collagen content and GAG content, respectively), as described previously.[365] Cell viability was evaluated with a LIVE/DEAD assay (2 mM calcein AM, 4 mM ethidium homodimer-1; Molecular Probes Carlsbad, CA) with fluorescence microscopy (Olympus/Intelligent Innovations Spinning Disk Confocal Microscope).[269]

To assess cell survival during sub-critical CO_2 sintering, HUCMSCs were harvested from one human umbilical cord obtained from the University of Kansas Medical Center (KU Medical Center IRB approval no. 10951, KU-Lawrence IRB approval no. 15402) as described earlier.[365] To prepare cell-loaded constructs, cell

pellets of HUCMSCs (P4; 1×10^6 cells) were mechanically mixed with ethylene oxide-sterilized microspheres (diameter: 120 μm, ~200 mg) using a sterile spatula. The cell-particle mixture was loaded into cylindrical molds and exposed to CO_2 at subcritical conditions (30 bar, 4 min, 25°C, depressurization rate ~3psi/s). A modified processing was performed for another set of particles (size: 120 μm, ~100 mg), where the particles were suspended in 100 μL of medium containing HUCMSCs (P4; 2×10^6 cells), then exposed to CO_2 at subcritical conditions (30 bar, 2 min, 25°C, depressurization rate ~3psi/s). The prepared constructs were assessed for HUCMSC viability using the LIVE/DEAD staining as described above.

The effects of microsphere size on the mechanical properties of the scaffolds were statistically analyzed using a seven-level single factor analysis of variance (ANOVA) followed by Tukey's Honestly Significant Difference *post hoc* test (n = 5, except for scaffolds prepared with 240 μm and bimodal spheres (n =4), and 140 μm (n = 6)).

CHAPTER 9: Osteochondral Tissue Engineering Using Bioactive Signal Gradients*

ABSTRACT

Continuous transitional gradients in cellular-extracellular architecture exist at osteochondral interfaces, which may be engineered by applying spatially patterned gradients of biological cues. In the present study, a protein-loaded microsphere-based scaffold fabrication strategy was applied to achieve spatially and temporally controlled delivery of bioactive signals in three-dimensional (3-D) tissue engineering scaffolds. Bone morphogenic protein-2 and transforming growth factor-β_1 -loaded poly(lactic-co-glycolic acid) microspheres were utilized with a gradient scaffold fabrication technology to produced microsphere-based scaffolds, containing opposing gradients of these signals. Using bone marrow stromal cells, single cell source-based osteochondral tissue regeneration was assessed in the gradient scaffolds, and compared to the blank controls. Following a 6 wk cell culture, the gradient scaffolds were shown to outperform the blank control scaffolds in cell number and GAG production. Gradient scaffolds also demonstrated a sign of increase osteoblastic activity during the 6 wk culture.

INTRODUCTION

*Chapter *in preparation* to be submitted to Biomaterials as Singh, Wang, Zhao, Berkland, and Detamore, "Osteochondral Tissue Engineering Using Bioactive Signal Gradients", 2008.

Spatial patterning of biological cues is vital to some of the most fundamental aspects of life, from embryogenesis to wound healing to nerve cell signaling, all involving concentration gradients of signaling molecules. Gradient-based signal delivery strategies have so far gained the most attention in the fields of neural tissue engineering[243, 245, 247] and in the study of chemotaxis.[254, 256] Continuous gradient-based bioactive signal delivery systems have been seldom applied in the area of interfacial tissue regeneration. For example, a recent study reported a gradient-gene delivery strategy, where a zonal organization of osteoblastic and fibroblastic cellular phenotypes was engineered in a single construct for the purposes of interfacial tissue engineering.[361] Interfacial tissue engineering using gradients of bioactive signals provides a promising alternative for the regeneration of multiple tissues in a single construct with functional interfaces. Moreover, such interfacial tissue engineering strategies also address a biomimetic approach towards tissue regeneration, where regeneration of a tissue may be enhanced by the presence of endogenous signals provided by the neighboring tissue.[280] Furthermore, using gradients of multiple bioactive factors, multiple tissue regeneration could be addressed via a single cell source, where, for example, stem cells can be differentiated along different lineages within the same constructs.

From the perspective of osteochondral tissue engineering, an *in vitro* culture study reported that only co-culture with chondrocytes (as opposed to fibroblasts or osteoblasts) was successful at promoting osteogenic differentiation of mesenchymal stem cells in a selective manner,[280] indicating the importance of simultaneous

triggering of osteo- and chondro-induction for osteochondral tissue regeneration. An integrated scaffold with embedded gradients of growth factors at the interface may trigger simultaneous tissue formation, and may have a synergistic effect on tissue regeneration. For osteochondral tissue engineering, there are only a few previous reports of scaffold designs having a heterogeneous distribution of growth factors embedded within an integrated scaffold.[359, 360] Continuous gradient-based signal delivery, to date, has never before been applied in the area of osteochondral tissue engineering.

While various strategies have been developed to create gradients of bioactive signals (see review[362]), a major limitation with many of these techniques is that they allow the delivery of only haptotactic cues via gel-based substrates. Integration of controlled release technology with graded-signal delivery from macroporous polymeric scaffolds may be a valuable tool to the tissue engineering community.

Microsphere-based tissue engineering scaffold designs have gained increasing interest over the past few years. Microspheres as the building block of a scaffold offer several benefits, which include the ease of fabrication, control over morphology and physicochemical characteristics, and versatility of controlling the release kinetics of encapsulated factors.[328] The properties of a scaffold, in turn, can be tailored by altering the microsphere design. For example, the pore size and porosity of a scaffold at micro-levels can be made application-specific by altering the size or changing the interior morphology of the microspheres.[355, 356] Similarly, macromechanical properties and degradability can be altered with the selection of the raw material. To

design biodegradable matrices, poly(D,L-lactide-co-glycolide) (PLG), an aliphatic α-hydroxy polyester, is one of the most widely used FDA-approved polymers. The polymer also offers the flexibility in the degradation kinetics, modulated by altering one or more of the factors, such as molecular weight, co-polymer ratio, tacticity, crystallinity, etc.[335, 336]

The present study aimed towards the integration of controlled release technology with a gradient scaffold fabrication strategy, where microsphere-based scaffolds containing opposing gradients of chondrogenic and osteogenic factors were fabricated using monodisperse protein-loaded microspheres and an ethanol sintering method. The constructs were utilized for osteochondral tissue engineering using bone marrow stromal cells.

MATERIALS AND METHODS

Materials

Poly(D,L-lactide-co-glycolic acid) copolymer (PLGA; 50:50 lactic acid:glycolic acid; acid end group, Mw ~40,000-45,000 Da) of intrinsic viscosity (i.v.) 0.37 dL/g was purchased from Lakeshore Biomaterials (Birmingham, AL). Poly(vinyl alcohol) (PVA; 88% hydrolyzed, 25,000 Da) was obtained from Polysciences, Inc. (Warrington, PA). Transforming growth factor (TGF)-β_1 and bone morphogenic protein (BMP)-2 were purchased from Peprotech, Inc. (Rocky Hill, NJ). BMSCs (P1, i.e., plated once) were purchased from STEMCELL Technologies (Vancouver, Canada). Dichloromethane (DCM; HPLC grade) was obtained from

Fisher Scientific (Pittsburgh, PA). Ethanol (Absolute - 200 Proof) was obtained in house.

Preparation of protein-loaded microspheres

BMP-2 (100 μg) was reconstituted in 0.5 ml of 10 mg/mL bovine serum albumin (BSA; Sigma, St. Louis) in PBS to get 0.2 mg/mL BMP-2 stock solution. TGF-β_1 (50 μg) was reconstituted according to the manufacturer's instructions to 25 μg/mL with a final BSA concentration of 1 mg/mL. The reconstituted protein solutions were individually mixed with PLGA dissolved in DCM (wt 6.5 g; 20% w/v), and sonicated over ice (50% amplitude, 20 s). Using PLGA-protein emulsions, uniform protein-loaded PLGA microspheres were prepared using technology from our previous reports.[269, 341] Briefly, using acoustic excitation produced by an ultrasonic transducer, regular jet instabilities were created in the polymer stream that produced uniform polymer droplets. An annular carrier non-solvent stream (0.5% PVA w/v in ddH_2O) surrounding the droplets was produced using a nozzle coaxial to the needle. The emanated polymer/carrier streams flowed into a beaker containing the non-solvent. Incipient polymer droplets were stirred for 3-4 h to allow solvent evaporation, which were then filtered and rinsed with ddH_2O to remove residual PVA, and stored at -20°C. Control microspheres were prepared in a similar manner, where the protein solution was replaced with an equivalent volume of BSA solution (1 mg/mL). The size distribution of microsphere preparations was determined using a

Coulter Multisizer 3 (Beckman Coulter Inc., Fullerton, CA) equipped with a 560-μm aperture.

Scaffold fabrication

Gradient scaffolds were prepared using a technology reported previously.[269] Briefly, lyophilized protein-loaded microspheres were dispersed in ddH_2O 2.5 % w/v, and separately loaded into two syringes. The suspensions were pumped into a cylindrical glass mold (6 mm diameter) in a controlled manner using programmable syringe pumps (PHD 22/2000, Harvard Apparatus, Inc.). Using a filter (particle retention > 3μm) at the bottom of the mold, ddH_2O was filtered, while the microparticles stacked in the mold. Using an additional infusion syringe pump and a vacuum pump, a constant level of distilled water was maintained in the mold. The stacked microspheres were then sintered using an ethanol treatment (100%) for 1 h.[269] The molds (containing the scaffolds) were freeze-dried for 2 days, then the gradient scaffolds were retrieved and stored at -20°C. Blank scaffolds were prepared in a similar manner using control microspheres.

Cell seeding, culture and construct analyses

Frozen BMSCs were thawed, plated at a density of 4000 cells/cm^2 and cultured. The culture medium consisted of Dulbecco's Modified Eagle medium (DMEM; low glucose), 1% penicillin–streptomycin (PS) (both from Invitrogen Life Technologies, Carlsbad, CA) and 10% fetal bovine serum (FBS-MSC quantified).

When 80-90% confluent, the cells were trypsinized and re-plated at the same plating density. Cells (~ 60×10^6; P4) were then seeded on the dry scaffolds using a drop-wise seeding protocol. Scaffolds (diameter 5.3 mm, height 2.5 mm) were sterilized using ethylene oxide, and placed in a 48 well plate. Cells were then seeded on the scaffolds at a density of 10×10^6 cells/mL. Approximately 28 μL (50% of the scaffold volume, approximately corresponding to pore volume[269]) of cell solution was placed directly above a scaffold, which was soaked into the scaffold via a capillary mechanism. Cells were allowed to attach to the scaffolds for 2 h, then 1 mL of a defined medium was added, and the scaffolds were cultured statically. Up to day 3, the defined medium consisted of DMEM (low glucose), 1% PS, 1X Insulin-Transferrin-Selenium (ITS)-premix (BD Biosciences, San Jose, CA), 40 μg/mL L-proline (Sigma, St. Louis); 100μM sodium pyruvate (Fisher Scientific) and 50 μg/mL L-ascorbic acid (Sigma, St. Louis), which was refreshed twice a day. Following day 3, the defined culture medium was supplemented with 4 mM β-glycerophosphate (Disodium Salt, Pentahydrate; Calbiochem) and 100 nM dexamethasone, which was refreshed every 24 h. Constructs were analyzed for matrix production using biochemical assays (picogreen and a dimethylmethylene blue (DMMB) assays for determining the cell number and GAG content), in a manner described before.[365] Alkaline phosphatase (ALP) activity was determined, as a measure of p-nitrophenol concentration/min using an ALP assay, as described elsewhere.[380] Mechanical characterization of the constructs was performed using a uniaxial testing apparatus (Instron Model 5848, Canton, MA; 50 N load cell) under unconfined compression.

Tare-loaded (0.05 N) constructs were compressed to 15 % strain at a rate of 1 %/s under simulated physiological conditions (i.e., under PBS (phosphate buffered saline – 0.138 M sodium chloride, 0.0027 M potassium chloride) at 37 ºC), followed by stress relaxation for a duration of 30 min. Moduli of elasticity were obtained from the linear regions of the stress-strain curves. Relaxed moduli were calculated as the ratio of the final stress value (at the end of 30 min duration) to the step strain. The stress was defined as the ratio of the load to the initial cross-sectional area, and the strain was defined as the ratio of the change in the length to the original length.

Statistical analyses

To compare the cell numbers and GAG production, a three-level single factor analysis of variance (ANOVA) was performed, followed by a Tukey's Honestly Significant Difference *post hoc* test when significance was detected (n = 4).

RESULTS AND DISCUSSION

Protein-loaded microspheres having uniform diameter were created using the previously reported Precision Particle Fabrication method.[341] The microspheres displayed high monodispersity, with a ~220 μm nominal diameter for all of the three types of microspheres prepared (BMP-2 loaded "osteogenic" microspheres, TGF-β_1 loaded "chondrogenic" microspheres, and control "blank" microspheres). Specifically, microsphere sizes in the range of 100-300 μm were chosen, as it was our

hypothesis that this range may provide optimal pore sizes to allow cellular infiltration and cell-to-cell interaction.

Cylindrical gradient scaffolds containing opposing gradients of chondrogenic and osteogenic factors along the axis of the molds were produced.[269] The scaffolds were seeded with BMSCs and cultured for a 6 wk duration. The overall cell number per construct increased by ~ 100% during the 6 wk cell culture, and the differences were found to be statistically significant ($p < 10^{-5}$) (Fig. 9.1). Gradient scaffolds displayed a higher mean cell number per construct compared to the blank scaffolds, although the difference was not statistically significant. GAG content per scaffold increased approximately 6-7 fold during the 6 wk culture, and the results were found to be statistically significant ($p < 10^{-5}$) (Fig. 9.2). At wk 6, the GAG content per construct was found to be ~ 20% higher for the gradient scaffolds compared to the blank scaffolds, and the results were found to be statistically significant ($p < 0.05$). The mechanical integrity of the scaffolds at wk 6 was very similar, reflected by their similar moduli of elasticity and relaxed moduli (Fig. 9.3). In comparison to the blank scaffolds at wk 0 (elastic modulus = 126.6 kPa relaxed modulus = 2.1 kPa), the elastic modulus of the scaffolds dropped drastically, although the relaxed modulus was not significantly changed. The ALP activity of the scaffolds showed a consistently decreasing trend from wk 0 to wk 3 for the blank scaffolds (Fig. 9.4). The ALP activity for the gradient scaffolds decreased up to wk 2; however, there was an increasing trend in the ALP activity afterwards (up to wk 6).

Based on these results, it could be speculated that the effects of chondrogenesis were prominent during the 6 wk cell culture, demonstrated by a significantly higher GAG content for the gradient scaffolds compared to the blank scaffolds at wk 6. The increasing trend in ALP activity for the gradient scaffold started at wk 3, which might be indicative of the osteoblastic activity that began after an initial culture period. The drastic drop in the mechanical integrity of the constructs was most likely a consequence of microsphere degradation that led to the disappearance of the sintering sites with time, transitioning to the mechanical integrity of the neo-synthesized tissue. To improve the mechanical characteristics of the constructs, one method could be to utilize microspheres with a bimodal distribution in the design of the scaffolds, which would provide additional "connecting bridges" between the microspheres and a closer packing, however at the expense of porosity. Moreover, with the proof-of-concept established here, it may stand to reason that the gradient-based scaffolds will be better suited for *in vivo* application, where faster healing rates, more conducive to the scaffold degradation rate, would of course be expected.

CONCLUSIONS

A new gradient-based approach was introduced for osteochondral tissue regeneration *in vitro*. BMSC cell culture for 6 wks demonstrated signs for cartilage-like tissue regeneration, while an increasing trend in ALP activity was indicative of osteoblastic activity. Matrix analysis at wk 6 demonstrated that the gradient scaffolds outperformed blank scaffolds in cell number, GAG production and ALP activity,

while mechanical properties were similar for the two groups. Future work will include the incorporation of stiffness gradients and expanded *in vivo* studies to evaluate the efficacy of gradient-based materials in osteochondral defect repair.

CHAPTER 10: Conclusion

Addressing mandibular condylar tissue regeneration, the first obstacle was the unknown mechanical design parameters for the cartilage part of the tissue, known to have cellular and extracellular characteristics intermediate to the hyaline cartilages and fibrocartilages. To obtain important mechanical properties relevant to the tissue engineering community and to develop a structure-function correlation, regional tensile and compressive characterization of the tissue was performed, together comprising the most comprehensive biomechanical characterization effort for the condylar cartilage to date. It also led to the first incidence of characterizing the stress relaxation behavior of the tissue under tension or compression. A direct correlation between directional tensile properties and the collagen fiber orientation was demonstrated, which was the first incidence of establishing the directional structure-property correlation with respect to condylar cartilage under tension (Chapter 4). The compression study provided clear validation of cartilage heterogeneity and indicated a correlation between the regional thickness and stiffness of the tissue (Chapter 5). Both the studies together set the gold standard reference for future condylar cartilage and mandibular condyle tissue engineering studies in our group and for the TMJ tissue engineering community.

Next, to address osteochondral/interfacial tissue regeneration using a controlled release approach, a microsphere-based gradient scaffold fabrication technology was developed, which allowed spatial control over the positioning of the microspheres along the axis of cylindrical molds (Chapter 6). Using dye-loaded

microspheres, a proof-of-concept was provided for the generation of bi-layered, multi-layered and gradient scaffolds. Novel routes to fabricate microsphere-based scaffolds were developed. An ethanol-treatment method was developed to create monodisperse microsphere-based sintered matrices, which were comprehensively characterized for their morphology, glass transition temperature, porosity, mechanical properties and cytotoxicity (Chapter 6). The method allowed the fabrication of porous and non-cytotoxic microsphere-based scaffolds. Moreover, to address functional regeneration of interfacial tissues, nanoparticle-encapsulated composite microspheres were used to fabricate ethanol-sintered stiffness gradient scaffolds (Chapter 7). While the stiffness of the individual microspheres was expected to increase by the encapsulation of nanoparticles, it was observed that the scaffolds prepared with composite microspheres exhibited a lower stiffness compared to corresponding blank microspheres with a 2 h ethanol-soaking duration. Changes that occurred on the surfaces of the microspheres following nanoparticle encapsulation was a likely cause of the decrease in the extent of sintering. Although the individual building blocks were stiffer, the structure as a whole demonstrated a lower stiffness due to lower than optimal sintering. Nevertheless, the composite microspheres demonstrated an increasing trend in stiffness with the increase in the nanoparticle content. The method can thus be extended to prepare scaffolds with a gradient or inverse-gradient in stiffness. Furthermore, an alternative route to prepare fused microsphere-based scaffolds using sub-critical CO_2 sintering was explored (Chapter 8). The scaffolds demonstrated a porous morphology, and stiffnesses comparable to

native cartilage stiffness. In addition, using porcine chondrocytes and human umbilical cord mesenchymal stromal cells, the feasibility of utilizing these scaffolds for cartilage tissue engineering was assessed using biochemical assays and immunohistochemistry. Perhaps even more importantly, it was demonstrated that gaseous CO_2 processing allows fabrication of cell-loaded three-dimensional matrices and patches in a cytocompatible way without adversely affecting the cell viability (Chapter 8). Finally, signal gradient scaffolds, with opposing gradients of chondrogenic and osteogenic factors, were utilized for osteochondral tissue engineering (Chapter 9). A single cell source-based approach was taken, where bone marrow stromal cells were selectively differentiated into cartilage-like and bone-like cells. Following a 6 wk cell culture, the gradient scaffolds were shown to outperform the blank control scaffolds in cell number and GAG production. Gradient scaffolds also demonstrated a sign of increased osteoblastic activity during the 6 wk culture.

Cumulatively, the characterization studies of this dissertation fill voids in the current TMJ biomechanics literature (Chapters 4 – 5), and a combination of novel gradient-based tissue regeneration approaches were taken toward osteochondral tissue engineering (Chapters 6 – 9). This dissertation lays down the foundation for a combined growth factor-stiffness gradient approach that could lead to a translational-level regenerative solution to osteochondral tissue regeneration with extended applications in other areas, including tissue engineering of heterogeneous/interfacial tissues.

REFERENCES

1. Piette, E. Anatomy of the human temporomandibular joint. An updated comprehensive review. Acta Stomatol Belg **90**, 103, 1993.

2. Carlsson, G.E., and LeResche, L. Epidemiology of Temporomandibular Disorders. In: Sessle, B.J., Bryant, P.S., and Dionne, R., eds. Temporomandibular Disorders and Related Pain Conditions. Seattle: IASP Press, 1995, pp. 211-226.

3. Buescher, J.J. Temporomandibular joint disorders. Am Fam Physician **76**, 1477, 2007.

4. Detamore, M.S., and Athanasiou, K.A. Structure and function of the temporomandibular joint disc: implications for tissue engineering. J Oral Maxillofac Surg **61**, 494, 2003.

5. Detamore, M.S., and Athanasiou, K.A. Motivation, characterization, and strategy for tissue engineering the temporomandibular joint disc. Tissue Eng **9**, 1065, 2003.

6. Milam, S.B. Pathophysiology and epidemiology of TMJ. J Musculoskelet Neuronal Interact **3**, 382, 2003.

7. Fung, Y.C. Biomechanics: Mechanical Properties of Living Tissues. Springer-Verlag New York, 1993.

8. Kuboki, T., Shinoda, M., Orsini, M.G., and Yamashita, A. Viscoelastic properties of the pig temporomandibular joint articular soft tissues of the condyle and disc. J Dent Res **76**, 1760, 1997.

9. Singh, M., and Detamore, M.S. Tensile properties of the mandibular condylar cartilage. J Biomech Eng **130**, 011009, 2008.

10. Teramoto, M., Kaneko, S., Shibata, S., Yanagishita, M., and Soma, K. Effect of compressive forces on extracellular matrix in rat mandibular condylar cartilage. J Bone Miner Metab **21**, 276, 2003.

11. Hinton, R.J., and Carlson, D.S. Regulation of mandibular condylar cartilage growth. Semin Orthod **11**, 209, 2005.

12. Luder, H.U. Frequency and distribution of articular tissue features in adult human mandibular condyles: a semiquantitative light microscopic study. Anat Rec **248**, 18, 1997.

13. Detamore, M.S., and Athanasiou, K.A. Tensile properties of the porcine temporomandibular joint disc. J Biomech Eng **125**, 558, 2003.

14. Mow, V.C., Kuei, S.C., Lai, W.M., and Armstrong, C.G. Biphasic creep and stress relaxation of articular cartilage in compression: Theory and experiments. J Biomech Eng **102**, 73, 1980.

15. Huang, C.Y., Mow, V.C., and Ateshian, G.A. The role of flow-independent viscoelasticity in the biphasic tensile and compressive responses of articular cartilage. J Biomech Eng **123**, 410, 2001.

16. Pietila, K., Kantomaa, T., Pirttiniemi, P., and Poikela, A. Comparison of amounts and properties of collagen and proteoglycans in condylar, costal and nasal cartilages. Cells Tissues Organs **164**, 30, 1999.

17. Kang, H., Bao, G., Dong, Y., Yi, X., Chao, Y., and Chen, M. [Tensile mechanics of mandibular condylar cartilage]. Hua Xi Kou Qiang Yi Xue Za Zhi **18**, 85, 2000.

18. Tanaka, E., Iwabuchi, Y., Rego, E.B., Koolstra, J.H., Yamano, E., Hasegawa, T., Kawazoe, A., Kawai, N., and Tanne, K. Dynamic shear behavior of mandibular condylar cartilage is dependent on testing direction. J Biomech **41**, 1119, 2008.

19. Tanaka, E., Rego, E.B., Iwabuchi, Y., Inubushi, T., Koolstra, J.H., van Eijden, T.M., Kawai, N., Kudo, Y., Takata, T., and Tanne, K. Biomechanical response of condylar cartilage-on-bone to dynamic shear. J Biomed Mater Res A **85**, 127, 2008.

20. Shibata, S., Baba, O., Ohsako, M., Suzuki, S., Yamashita, Y., and Ichijo, T. Ultrastructural observation on matrix fibers in the condylar cartilage of the adult rat mandible. Bull Tokyo Med Dent Univ **38**, 53, 1991.

21. de Bont, L.G., Boering, G., Havinga, P., and Liem, R.S. Spatial arrangement of collagen fibrils in the articular cartilage of the mandibular condyle: a light microscopic and scanning electron microscopic study. J Oral Maxillofac Surg **42**, 306, 1984.

22. Klinge, R.F. The structure of the mandibular condyle in the monkey (Macaca mulatta). Micron **27**, 381, 1996.

23. Luder, H.U., and Schroeder, H.E. Light and electron microscopic morphology of the temporomandibular joint in growing and mature crab-eating monkeys (Macaca fascicularis): the condylar articular layer. Anat Embryol (Berl) **181**, 499, 1990.

24. Mizuno, I., Saburi, N., Taguchi, N., Kaneda, T., and Hoshino, T. The fine structure of the fibrous zone of articular cartilage in the rat mandibular condyle. Shika Kiso Igakkai Zasshi **32**, 69, 1990.

25. Berkovitz, B.K. Collagen crimping in the intra-articular disc and articular surfaces of the human temporomandibular joint. Arch Oral Biol **45**, 749, 2000.

26. Appleton, J. The ultrastructure of the articular tissue of the mandibular condyle in the rat. Arch Oral Biol **20**, 823, 1975.

27. Detamore, M.S., Hegde, J.N., Wagle, R.R., Almarza, A.J., Montufar-Solis, D., Duke, P.J., and Athanasiou, K.A. Cell type and distribution in the porcine temporomandibular joint disc. J Oral Maxillofac Surg **64**, 243, 2006.

28. Mizoguchi, I., Takahashi, I., Nakamura, M., Sasano, Y., Sato, S., Kagayama, M., and Mitani, H. An immunohistochemical study of regional differences in the distribution of type I and type II collagens in rat mandibular condylar cartilage. Arch Oral Biol **41**, 863, 1996.

29. Delatte, M., Von den Hoff, J.W., van Rheden, R.E., and Kuijpers-Jagtman, A.M. Primary and secondary cartilages of the neonatal rat: the femoral head and the mandibular condyle. Eur J Oral Sci **112**, 156, 2004.

30. Milam, S.B., Klebe, R.J., Triplett, R.G., and Herbert, D. Characterization of the extracellular matrix of the primate temporomandibular joint. J Oral Maxillofac Surg **49**, 381, 1991.

31. Visnapuu, V., Peltomaki, T., Isotupa, K., Kantomaa, T., and Helenius, H. Distribution and characterization of proliferative cells in the rat mandibular condyle during growth. Eur J Orthod **22**, 631, 2000.

32. Beek, M., Aarnts, M.P., Koolstra, J.H., Feilzer, A.J., and van Eijden, T.M. Dynamic properties of the human temporomandibular joint disc. J Dent Res **80**, 876, 2001.

33. Kim, K.W., Wong, M.E., Helfrick, J.F., Thomas, J.B., and Athanasiou, K.A. Biomechanical tissue characterization of the superior joint space of the porcine temporomandibular joint. Ann Biomed Eng **31**, 924, 2003.

34. Nickel, J.C., and McLachlan, K.R. In vitro measurement of the stress-distribution properties of the pig temporomandibular joint disc. Arch Oral Biol **39**, 439, 1994.

35. Tanaka, E., Tanaka, M., Hattori, Y., Aoyama, J., Watanabe, M., Sasaki, A., Sugiyama, M., and Tanne, K. Biomechanical behaviour of bovine temporomandibular articular discs with age. Arch Oral Biol **46**, 997, 2001.

36. Teng, S., Xu, Y., Cheng, M., and Li, Y. Biomechanical properties and collagen fiber orientation of temporomandibular joint discs in dogs: 2. Tensile mechanical properties of the discs. J Craniomandib Disord **5**, 107, 1991.

37. Del Santo, M., Jr., Marches, F., Ng, M., and Hinton, R.J. Age-associated changes in decorin in rat mandibular condylar cartilage. Arch Oral Biol **45**, 485, 2000.

38. Mao, J.J., Rahemtulla, F., and Scott, P.G. Proteoglycan expression in the rat temporomandibular joint in response to unilateral bite raise. J Dent Res **77**, 1520, 1998.

39. Herring, S.W., and Liu, Z.J. Loading of the temporomandibular joint: anatomical and in vivo evidence from the bones. Cells Tissues Organs **169**, 193, 2001.

40. Marks, L., Teng, S., Artun, J., and Herring, S. Reaction strains on the condylar neck during mastication and maximum muscle stimulation in different condylar positions: an experimental study in the miniature pig. J Dent Res **76**, 1412, 1997.

41. Nomura, T., Gold, E., Powers, M.P., Shingaki, S., and Katz, J.L. Micromechanics/structure relationships in the human mandible. Dent Mater **19**, 167, 2003.

42. Teng, S., and Herring, S.W. A stereological study of trabecular architecture in the mandibular condyle of the pig. Arch Oral Biol **40**, 299, 1995.

43. Hu, K., Radhakrishnan, P., Patel, R.V., and Mao, J.J. Regional structural and viscoelastic properties of fibrocartilage upon dynamic nanoindentation of the articular condyle. J Struct Biol **136**, 46, 2001.

44. Patel, R.V., and Mao, J.J. Microstructural and elastic properties of the extracellular matrices of the superficial zone of neonatal articular cartilage by atomic force microscopy. Front Biosci **8**, a18, 2003.

45. Tanaka, E., Yamano, E., Dalla-Bona, D.A., Watanabe, M., Inubushi, T., Shirakura, M., Sano, R., Takahashi, K., van Eijden, T., and Tanne, K. Dynamic compressive properties of the mandibular condylar cartilage. J Dent Res **85**, 571, 2006.

46. Allen, K.D., and Athanasiou, K.A. Viscoelastic characterization of the porcine temporomandibular joint disc under unconfined compression. J Biomech **39**, 312, 2006.

47. Roth, S., Muller, K., Fischer, D.C., and Dannhauer, K.H. Specific properties of the extracellular chondroitin sulphate proteoglycans in the mandibular condylar growth centre in pigs. Arch Oral Biol **42**, 63, 1997.

48. Kantomaa, T., Pirttiniemi, P., Tuominen, M., and Poikela, A. Glycosaminoglycan synthesis in the mandibular condyle during growth adaptation. Acta Anat (Basel) **151**, 88, 1994.

49. Kantomaa, T., and Pirttiniemi, P. Changes in proteoglycan and collagen content in the mandibular condylar cartilage of the rabbit caused by an altered relationship between the condyle and glenoid fossa. Eur J Orthod **20**, 435, 1998.

50. Bermejo, A., Gonzalez, O., and Gonzalez, J.M. The pig as an animal model for experimentation on the temporomandibular articular complex. Oral Surg Oral Med Oral Pathol **75**, 18, 1993.

51. Bibb, C.A., Pullinger, A.G., and Baldioceda, F. Serial variation in histological character of articular soft tissue in young human adult temporomandibular joint condyles. Arch Oral Biol **38**, 343, 1993.

52. Hansson, T., Oberg, T., Carlsson, G.E., and Kopp, S. Thickness of the soft tissue layers and the articular disk in the temporomandibular joint. Acta Odontol Scand **35**, 77, 1977.

53. Pullinger, A.G., Baldioceda, F., and Bibb, C.A. Relationship of TMJ articular soft tissue to underlying bone in young adult condyles. J Dent Res **69**, 1512, 1990.

54. Verteramo, A., and Seedhom, B.B. Zonal and directional variations in tensile properties of bovine articular cartilage with special reference to strain rate variation. Biorheology **41**, 203, 2004.

55. Soltz, M.A., and Ateshian, G.A. Experimental verification and theoretical prediction of cartilage interstitial fluid pressurization at an impermeable contact interface in confined compression. J Biomech **31**, 927, 1998.

56. Beek, M., Koolstra, J.H., van Ruijven, L.J., and van Eijden, T.M. Three-dimensional finite element analysis of the human temporomandibular joint disc. J Biomech **33**, 307, 2000.

57. Koolstra, J.H. Number crunching with the human masticatory system. J Dent Res **82**, 672, 2003.

58. Peck, C.C., and Hannam, A.G. Human jaw and muscle modelling. Arch Oral Biol **52**, 300, 2007.

59. Hirose, M., Tanaka, E., Tanaka, M., Fujita, R., Kuroda, Y., Yamano, E., van Eijden, T.M., and Tanne, K. Three-dimensional finite-element model of the human temporomandibular joint disc during prolonged clenching. Eur J Oral Sci **114**, 441, 2006.

60. Tanaka, E., Tanne, K., and Sakuda, M. A three-dimensional finite element model of the mandible including the TMJ and its application to stress analysis in the TMJ during clenching. Med Eng Phys **16**, 316, 1994.

61. Tanaka, E., Rodrigo, D.P., Miyawaki, Y., Lee, K., Yamaguchi, K., and Tanne, K. Stress distribution in the temporomandibular joint affected by anterior disc displacement: a three-dimensional analytic approach with the finite-element method. J Oral Rehabil **27**, 754, 2000.

62. Tanaka, E., del Pozo, R., Tanaka, M., Asai, D., Hirose, M., Iwabe, T., and Tanne, K. Three-dimensional finite element analysis of human temporomandibular joint with and without disc displacement during jaw opening. Med Eng Phys **26**, 503, 2004.

63. Tanaka, E., Rodrigo, D.P., Tanaka, M., Kawaguchi, A., Shibazaki, T., and Tanne, K. Stress analysis in the TMJ during jaw opening by use of a three-dimensional finite element model based on magnetic resonance images. Int J Oral Maxillofac Surg **30**, 421, 2001.

64. Beek, M. Three-dimensional finite element analysis of the cartilaginous structures in the human temporomandibular joint. J Dent Res **80**, 1913, 2001.

65. Koolstra, J.H., and van Eijden, T.M. The jaw open-close movements predicted by biomechanical modelling. J Biomech **30**, 943, 1997.

66. Koolstra, J.H., and van Eijden, T.M. Dynamics of the human masticatory muscles during a jaw open-close movement. J Biomech **30**, 883, 1997.

67. Koolstra, J.H., and van Eijden, T.M. Functional significance of the coupling between head and jaw movements. J Biomech **37**, 1387, 2004.

68. Koolstra, J.H., and van Eijden, T.M. Combined finite-element and rigid-body analysis of human jaw joint dynamics. J Biomech **38**, 2431, 2005.

69. del Palomar, A.P., and Doblare, M. 3D finite element simulation of the opening movement of the mandible in healthy and pathologic situations. J Biomech Eng **128**, 242, 2006.

70. Perez Del Palomar, A., and Doblare, M. Finite element analysis of the temporomandibular joint during lateral excursions of the mandible. J Biomech **39**, 2153, 2006.

71. Perez del Palomar, A., and Doblare, M. Influence of unilateral disc displacement on the stress response of the temporomandibular joint discs during opening and mastication. J Anat **211**, 453, 2007.

72. Perez del Palomar, A., and Doblare, M. An accurate simulation model of anteriorly displaced TMJ discs with and without reduction. Med Eng Phys **29**, 216, 2007.

73. Perez del Palomar, A., and Doblare, M. Dynamic 3D FE modelling of the human temporomandibular joint during whiplash. Med Eng Phys **30**, 700, 2008.

74. Gallo, L.M. Modeling of temporomandibular joint function using MRI and jaw-tracking technologies--mechanics. Cells Tissues Organs **180**, 54, 2005.

75. Gallo, L.M., Chiaravalloti, G., Iwasaki, L.R., Nickel, J.C., and Palla, S. Mechanical work during stress-field translation in the human TMJ. J Dent Res **85**, 1006, 2006.

76. Palla, S., Gallo, L.M., and Gossi, D. Dynamic stereometry of the temporomandibular joint. Orthod Craniofac Res **6 Suppl 1**, 37, 2003.

77. del Pozo, R., Tanaka, E., Tanaka, M., Kato, M., Iwabe, T., Hirose, M., and Tanne, K. Influence of friction at articular surfaces of the temporomandibular joint on stresses in the articular disk: a theoretical approach with the finite element method. Angle Orthod **73**, 319, 2003.

78. Chen, J., Akyuz, U., Xu, L., and Pidaparti, R.M. Stress analysis of the human temporomandibular joint. Med Eng Phys **20**, 565, 1998.

79. Hu, K., Qiguo, R., Fang, J., and Mao, J.J. Effects of condylar fibrocartilage on the biomechanical loading of the human temporomandibular joint in a three-dimensional, nonlinear finite element model. Med Eng Phys **25**, 107, 2003.

80. Moses, J.J., and Topper, D.C. A functional approach to the treatment of temporomandibular joint internal derangement. J Craniomandib Disord **5**, 19, 1991.

81. Shen, G., and Darendeliler, M.A. The adaptive remodeling of condylar cartilage-- a transition from chondrogenesis to osteogenesis. J Dent Res **84**, 691, 2005.

82. Detamore, M.S., Athanasiou, K.A., and Mao, J. A call to action for bioengineers and dental professionals: directives for the future of TMJ bioengineering. Ann Biomed Eng **35**, 1301, 2007.

83. Strom, D., Holm, S., Clemensson, E., Haraldson, T., and Carlsson, G.E. Gross anatomy of the mandibular joint and masticatory muscles in the domestic pig (Sus scrofa). Arch Oral Biol **31**, 763, 1986.

84. Sun, Z., Liu, Z.J., and Herring, S.W. Movement of temporomandibular joint tissues during mastication and passive manipulation in miniature pigs. Arch Oral Biol **47**, 293, 2002.

85. Copray, J.C., Jansen, H.W., and Duterloo, H.S. Effects of compressive forces on proliferation and matrix synthesis in mandibular condylar cartilage of the rat in vitro. Arch Oral Biol **30**, 299, 1985.

86. Poikela, A., Kantomaa, T., Pirttiniemi, P., Tuukkanen, J., and Pietila, K. Unilateral masticatory function changes the proteoglycan content of mandibular condylar cartilage in rabbit. Cells Tissues Organs **167**, 49, 2000.

87. Shen, G., Rabie, A.B., Zhao, Z.H., and Kaluarachchi, K. Forward deviation of the mandibular condyle enhances endochondral ossification of condylar cartilage indicated by increased expression of type X collagen. Arch Oral Biol **51**, 315, 2006.

88. Xiong, H., Rabie, A.B., and Hagg, U. Neovascularization and mandibular condylar bone remodeling in adult rats under mechanical strain. Front Biosci **10**, 74, 2005.

89. Kang, H., Yi, X., Chen, M., and Bao, G. [A biomechanical study on the retrodiscal tissue of human temporomandibular joint]. Sheng Wu Yi Xue Gong Cheng Xue Za Zhi **17**, 143, 2000.

90. Tanaka, E., Del Pozo, R., Sugiyama, M., and Tanne, K. Biomechanical response of retrodiscal tissue in the temporomandibular joint under compression. J Oral Maxillofac Surg **60**, 546, 2002.

91. Tanaka, E., Hanaoka, K., Tanaka, M., Van Eijden, T., Iwabe, T., Ishino, Y., Sasaki, A., and Tanne, K. Viscoelastic properties of bovine retrodiscal tissue under tensile stress-relaxation. Eur J Oral Sci **111**, 518, 2003.

92. Beatty, M.W., Hohl, R.H., Nickel, J.C., Iwasaki, L.R., and Pidaparti, R.M. Mode I and Mode III fractures in intermediate zone of full-thickness porcine temporomandibular joint discs. Ann Biomed Eng **36**, 801, 2008.

93. Koolstra, J.H., Tanaka, E., and Van Eijden, T.M. Viscoelastic material model for the temporomandibular joint disc derived from dynamic shear tests or strain-relaxation tests. J Biomech **40**, 2330, 2007.

94. Koolstra, J.H., and van Eijden, T.M. Consequences of viscoelastic behavior in the human temporomandibular joint disc. J Dent Res **86**, 1198, 2007.

95. Koombua, K., Pidaparti, R.M., and Beatty, M.W. Fracture toughness estimation for the TMJ disc. J Biomed Mater Res A **79**, 566, 2006.

96. Perez del Palomar, A., and Doblare, M. The effect of collagen reinforcement in the behaviour of the temporomandibular joint disc. J Biomech **39**, 1075, 2006.

97. Snider, G.R., Lomakin, J., Singh, M., Gehrke, S.H., and Detamore, M.S. Regional Dynamic Tensile Properties of the TMJ Disc. Journal of dental research **Accepted**, 2008.

98. Kang, H., Bao, G.J., and Qi, S.N. Biomechanical responses of human temporomandibular joint disc under tension and compression. Int J Oral Maxillofac Surg **35**, 817, 2006.

99. Suresh, S. Graded Materials for Resistance to Contact Deformation and Damage. Science **292**, 2447, 2001.

100. Messersmith, P.B. Materials science. Multitasking in tissues and materials. Science **319**, 1767, 2008.

101. Lo, C.M., Wang, H.B., Dembo, M., and Wang, Y. Cell movement is guided by the rigidity of the substrate. Biophys J **79**, 144, 2000.

102. Haga, H., Irahara, C., Kobayashi, R., Nakagaki, T., and Kawabata, K. Collective movement of epithelial cells on a collagen gel substrate. Biophys J **88**, 2250, 2005.

103. Righetti, P.G. Electrophoresis: the march of pennies, the march of dimes. J Chromatogr A **1079**, 24, 2005.

104. Lapizco-Encinas, B.H., and Rito-Palomares, M. Dielectrophoresis for the manipulation of nanobioparticles. Electrophoresis **28**, 4521, 2007.

105. Niino, M., and Maeda, S. Recent Development Status of Functionally Gradient Materials. ISIJ International **30**, 699, 1990.

106. Jandeleit, B., Schaefer, D.J., Powers, T.S., Turner, H.W., and Weinberg, W.H. Combinatorial materials science and catalysis. Angew Chem Int Ed Engl **38**, 2495, 1999.

107. Oh, S.H., Park, I.K., Kim, J.M., and Lee, J.H. In vitro and in vivo characteristics of PCL scaffolds with pore size gradient fabricated by a centrifugation method. Biomaterials **28**, 1664, 2007.

108. Yang, S., Leong, K.F., Du, Z., and Chua, C.K. The design of scaffolds for use in tissue engineering. Part I. Traditional factors. Tissue Eng **7**, 679, 2001.

109. Karageorgiou, V., and Kaplan, D. Porosity of 3D biomaterial scaffolds and osteogenesis. Biomaterials **26**, 5474, 2005.

110. Malda, J., Woodfield, T.B.F., van der Vloodt, F., Kooy, F.K., Martens, D.E., Tramper, J., Blitterswijk, C.A., and Riesle, J. The effect of PEGT/PBT scaffold architecture on oxygen gradients in tissue engineered cartilaginous constructs. Biomaterials **25**, 5773, 2004.

111. Ma, P.X., and Zhang, R. Microtubular architecture of biodegradable polymer scaffolds. J Biomed Mater Res **56**, 469, 2001.

112. Zmora, S., Glicklis, R., and Cohen, S. Tailoring the pore architecture in 3-D alginate scaffolds by controlling the freezing regime during fabrication. Biomaterials **23**, 4087, 2002.

113. Zeltinger, J., Sherwood, J.K., Graham, D.A., Mueller, R., and Griffith, L.G. Effect of pore size and void fraction on cellular adhesion, proliferation, and matrix deposition. Tissue Eng **7**, 557, 2001.

114. Woodfield, T.B., Van Blitterswijk, C.A., De Wijn, J., Sims, T.J., Hollander, A.P., and Riesle, J. Polymer scaffolds fabricated with pore-size gradients as a model for studying the zonal organization within tissue-engineered cartilage constructs. Tissue Eng **11**, 1297, 2005.

115. Sherwood, J.K., Riley, S.L., Palazzolo, R., Brown, S.C., Monkhouse, D.C., Coates, M., Griffith, L.G., Landeen, L.K., and Ratcliffe, A. A three-dimensional osteochondral composite scaffold for articular cartilage repair. Biomaterials **23**, 4739, 2002.

116. Schwarz, K., and Epple, M. Hierarchically structured polyglycolide– a biomaterial mimicking natural bone. Macromol Rapid Commun **19**, 613, 1998.

117. Harley, B.A., Hastings, A.Z., Yannas, I.V., and Sannino, A. Fabricating tubular scaffolds with a radial pore size gradient by a spinning technique. Biomaterials **27**, 866, 2006.

118. Roy, T.D., Simon, J.L., Ricci, J.L., Rekow, E.D., Thompson, V.P., and Parsons, J.R. Performance of degradable composite bone repair products made via three-dimensional fabrication techniques. J Biomed Mater Res A **66**, 283, 2003.

119. Rodbard, D., Kapadia, G., and Chrambach, A. Pore gradient electrophoresis. Anal Biochem **40**, 135, 1971.

120. Vlierberghe, S.V., Cnudde, V., Dubruel, P., Masschaele, B., Cosijns, A., Paepe, I.D., Jacobs, P.J., Hoorebeke, L.V., Remon, J.P., and Schacht, E. Porous gelatin hydrogels: 1. Cryogenic formation and structure analysis. Biomacromolecules **8**, 331, 2007.

121. Dubruel, P., Unger, R., Van Vlierberghe, S., Cnudde, V., Jacobs, P.J.S., Schacht, E., and Kirkpatrick, C.J. Porous Gelatin Hydrogels: 2. In Vitro Cell Interaction Study. Biomacromolecules **8**, 338, 2007.

122. Discher, D.E., Janmey, P., and Wang, Y. Tissue cells feel and respond to the stiffness of their substrate. Science **310**, 1139, 2005.

123. Schwarz, U. Soft matters in cell adhesion: rigidity sensing on soft elastic substrates. Soft Matter **3**, 263, 2007.

124. Li, S., Guan, J.L., and Chien, S. Biochemistry and biomechanics of cell motility. Annu Rev Biomed Eng **7**, 105, 2005.

125. Pelham Jr, R.J., and Wang, Y. Cell locomotion and focal adhesions are regulated by substrate flexibility. Proc Natl Acad Sci U S A **94**, 13661, 1997.

126. Engler, A., Bacakova, L., Newman, C., Hategan, A., Griffin, M., and Discher, D. Substrate compliance versus ligand density in cell on gel responses. Biophys J **86**, 617, 2004.

127. Gray, D.S., Tien, J., and Chen, C.S. Repositioning of cells by mechanotaxis on surfaces with micropatterned Young's modulus. J Biomed Mater Res **66**, 605, 2003.

128. Kidoaki, S., and Matsuda, T. Microelastic gradient gelatinous gels to induce cellular mechanotaxis. J Biotechnol **133**, 225, 2008.

129. Wong, J.Y., Velasco, A., Rajagopalan, P., and Pham, Q. Directed movement of vascular smooth muscle cells on gradient-compliant hydrogels. Langmuir **19**, 1908, 2003.

130. Zaari, N., Rajagopalan, P., Kim, S.K., Engler, A.J., and Wong, J.Y. Photopolymerization in Microfluidic Gradient Generators: Microscale Control of Substrate Compliance to Manipulate Cell Response. Adv Mater **16**, 2133, 2004.

131. Georges, P.C., and Janmey, P.A. Cell type-specific response to growth on soft materials. Am Physiological Soc **98**, 1547, 2005.

132. Yeung, T., Georges, P.C., Flanagan, L.A., Marg, B., Ortiz, M., Funaki, M., Zahir, N., Ming, W., Weaver, V., and Janmey, P.A. Effects of substrate stiffness on cell morphology, cytoskeletal structure, and adhesion. Cell Motil Cytoskeleton **60**, 24, 2005.

133. Guo, W., Frey, M.T., Burnham, N.A., and Wang, Y. Substrate rigidity regulates the formation and maintenance of tissues. Biophys J **90**, 2213, 2006.

134. Flanagan, L.A., Ju, Y.E., Marg, B., Osterfield, M., and Janmey, P.A. Neurite branching on deformable substrates. Neuroreport **13**, 2411, 2002.

135. Engler, A.J., Richert, L., Wong, J.Y., Picart, C., and Discher, D.E. Surface probe measurements of the elasticity of sectioned tissue, thin gels and polyelectrolyte multilayer films: Correlations between substrate stiffness and cell adhesion. Surf Sci **570**, 142, 2004.

136. Engler, A.J., Griffin, M.A., Sen, S., Bonnemann, C.G., Sweeney, H.L., and Discher, D.E. Myotubes differentiate optimally on substrates with tissue-like stiffness: Pathological implications for soft or stiff microenvironments. J Cell Biol **166**, 877, 2004.

137. Peyton, S.R., and Putnam, A.J. Extracellular matrix rigidity governs smooth muscle cell motility in a biphasic fashion. J Cell Physiol **204**, 198, 2005.

138. Jacot, J.G., Dianis, S., Schnall, J., and Wong, J.Y. A simple microindentation technique for mapping the microscale compliance of soft hydrated materials and tissues. J Biomed Mater Res A **79**, 485, 2006.

139. Lin-Gibson, S., Landis, F.A., and Drzal, P.L. Combinatorial investigation of the structure-properties characterization of photopolymerized dimethacrylate networks. Biomaterials **27**, 1711, 2006.

140. Burdick, J.A., Khademhosseini, A., and Langer, R. Fabrication of gradient hydrogels using a microfluidics/photopolymerization process. Langmuir **20**, 5153, 2004.

141. Ruardy, T.G., Schakenraad, J.M., Van Der Mei, H.C., and Busscher, H.J. Preparation and characterization of chemical gradient surfaces and their application for the study of cellular interaction phenomena. Surf Sci Rep **29**, 1, 1997.

142. Ueda-Yukoshi, T., and Matsuda, T. Cellular responses on a wettability gradient surface with continuous variations in surface compositions of carbonate and hydroxyl groups. Langmuir **11**, 4135, 1995.

143. Plummer, S.T., and Bohn, P.W. Spatial dispersion in electrochemically generated surface composition gradients visualized with covalently bound fluorescent nanospheres. Langmuir **18**, 4142, 2002.

144. Li, B., Ma, Y., Wang, S., and Moran, P.M. A technique for preparing protein gradients on polymeric surfaces: effects on PC12 pheochromocytoma cells. Biomaterials **26**, 1487, 2005.

145. Kim, M.S., Khang, G., and Lee, H.B. Gradient polymer surfaces for biomedical applications. Prog Polym Sci **33**, 138, 2008.

146. Genzer, J., and Bhat, R.R. Surface-Bound Soft Matter Gradients. Langmuir **24**, 2294 2008.

147. Julthongpiput, D., Fasolka, M.J., Zhang, W., Nguyen, T., and Amis, E.J. Gradient chemical micropatterns: a reference substrate for surface nanometrology. Nano Lett **5**, 1535, 2005.

148. Kennedy, S.B., Washburn, N.R., Simon, C.G., and Amis, E.J. Combinatorial screen of the effect of surface energy on fibronectin-mediated osteoblast adhesion, spreading and proliferation. Biomaterials **27**, 3817, 2006.

149. Roberson, S., Sehgal, A., Fahey, A., and Karim, A. Time-of-flight secondary ion mass spectrometry (TOF-SIMS) for high-throughput characterization of biosurfaces. Appl Surf Sci **203**, 855, 2003.

150. Golander, C.G., and Pitt, W.G. Characterization of hydrophobicity gradients prepared by means of radio frequency plasma discharge. Biomaterials **11**, 32, 1990.

151. Pitt, W.G. Fabrication of a continuous wettability gradient by radio frequency plasma discharge. J Colloid Interface Sci **133**, 223, 1989.

152. Spijker, H.T., Bos, R., Busscher, H.J., Graaff, R., and Van Oeveren, W. Adhesion of blood platelets under flow to wettability gradient polyethylene surfaces made in a shielded gas plasma. J Adhes Sci Technol **16**, 1703, 2002.

153. Spijker, H.T., Bos, R., Busscher, H.J., van Kooten, T.G., and van Oeveren, W. Platelet adhesion and activation on a shielded plasma gradient prepared on polyethylene. Biomaterials **23**, 757, 2002.

154. Choee, J.H., Lee, S.J., Lee, Y.M., Rhee, J.M., Lee, H.B., and Khang, G. Proliferation rate of fibroblast cells on polyethylene surfaces with wettability gradient. J Appl Polym Sci **92**, 599, 2004.

155. Khang, G. Interaction of fibroblast cells on poly (lactide-co-glycolide) surface with wettability chemogradient. Biomed Mater Eng **9**, 179, 1999.

156. Lee, J., Kim, H.G.I., Khang, G., Lee, H., and Jhon, M.U.S. Characterization of wettability gradient surfaces prepared by corona discharge treatment. J Colloid Interface Sci **151**, 563, 1992.

157. Lee, J.H., and Lee, H.B. A wettability gradient as a tool to study protein adsorption and cell adhesion on polymer surfaces. J Biomater Sci Polym Ed **4**, 467, 1993.

158. Lee, J.H., Khang, G., Lee, J.W., and Lee, H.B. Interaction of different types of cells on polymer surfaces with wettability gradient. J Colloid Interface Sci **205**, 323, 1998.

159. Lee, J.H., and Lee, H.B. Platelet adhesion onto wettability gradient surfaces in the absence and presence of plasma proteins. J Biomed Mater Res **41**, 304, 1998.

160. Lee, J.H., Lee, S.J., Khang, G., and Lee, H.B. Interaction of fibroblasts on polycarbonate membrane surfaces with different micropore sizes and hydrophilicity. J Biomater Sci Polym Ed **10**, 283, 1999.

161. Lee, S.J., Khang, G., Lee, Y.M., and Lee, H.B. The effect of surface wettability on induction and growth of neurites from the PC-12 cell on a polymer surface. J Colloid Interface Sci **259**, 228, 2003.

162. Li, B., Ma, Y., Wang, S., and Moran, P.M. Influence of carboxyl group density on neuron cell attachment and differentiation behavior: Gradient-guided neurite outgrowth. Biomaterials **26**, 4956, 2005.

163. Harris, B.P., Kutty, J.K., Fritz, E.W., Webb, C.K., Burg, K.J.L., and Metters, A.T. Photopatterned polymer brushes promoting cell adhesion gradients. Langmuir **22**, 4467, 2006.

164. Herbert, C.B., McLernon, T.L., Hypolite, C.L., Adams, D.N., Pikus, L., Huang, C.C., Fields, G.B., Letourneau, P.C., Distefano, M.D., and Hu, W.S. Micropatterning gradients and controlling surface densities of photoactivatable

biomolecules on self-assembled monolayers of oligo (ethylene glycol) alkanethiolates. Chem Biol **4**, 731, 1997.

165. Hypolite, C.L., McLernon, T.L., Adams, D.N., Chapman, K.E., Herbert, C.B., Huang, C.C., Distefano, M.D., and Hu, W.S. Formation of microscale gradients of protein using heterobifunctional photolinkers. Bioconjug Chem **8**, 658, 1997.

166. Iwasaki, Y., Ishihara, K., Nakabayashi, N., Khang, G., Jeon, J.H., Lee, J.W., and Lee, H.B. Platelet adhesion on the gradient surfaces grafted with phospholipid polymer. J Biomater Sci Polym Ed **9**, 801, 1998.

167. Iwasaki, Y., Sawada, S., Nakabayashi, N., Khang, G., Bang Lee, H., and Ishihara, K. The effect of the chemical structure of the phospholipid polymer on fibronectin adsorption and fibroblast adhesion on the gradient phospholipid surface. Biomaterials **20**, 2185, 1999.

168. Jeong, B.J., Lee, J.H., and Lee, H.B. Preparation and characterization of comb-like PEO gradient surfaces. J Colloid Interface Sci **178**, 757, 1996.

169. Lee, J.H., Jeong, B.J., and Lee, H.B. Plasma protein adsorption and platelet adhesion onto comb-like PEO gradient surfaces. J Biomed Mater Res **34**, 105, 1997.

170. Lee, J.H., Khang, G., Lee, J.W., and Lee, H.B. Platelet adhesion onto chargeable functional group gradient surfaces. J Biomed Mater Res **40**, 180, 1998.

171. Lee, J.H., Lee, J.W., Khang, G., and Lee, H.B. Interaction of cells on chargeable functional group gradient surfaces. Biomaterials **18**, 351, 1997.

172. Alexander, M.R., Whittle, J.D., Barton, D., and Short, R.D. Plasma polymer chemical gradients for evaluation of surface reactivity: epoxide reaction with carboxylic acid surface groups. J Mater Chem **14**, 408, 2004.

173. Parry, K.L., Shard, A.G., Short, R.D., White, R.G., Whittle, J.D., and Wright, A. ARXPS characterisation of plasma polymerised surface chemical gradients. Surf Interface Anal **38**, 1497, 2006.

174. Zelzer, M., Majani, R., Bradley, J.W., Rose, F.R., Davies, M.C., and Alexander, M.R. Investigation of cell-surface interactions using chemical gradients formed from plasma polymers. Biomaterials **29**, 172, 2008.

175. Whittle, J.D., Barton, D., Alexander, M.R., and Short, R.D. A method for the deposition of controllable chemical gradients. Chem Commun **2003**, 1766, 2003.

176. Mei, Y., Elliott, J.T., Smith, J.R., Langenbach, K.J., Wu, T., Xu, C., Beers, K.L., Amis, E.J., and Henderson, L. Gradient substrate assembly for quantifying cellular response to biomaterials. J Biomed Mater Res A **79**, 974, 2006.

177. Chaudhury, M.K., and Whitesides, G.M. How to make water run uphill. Science **256**, 1539, 1992.

178. Elwing, H., Askendal, A., and Lundstrom, I. Competition between adsorbed fibrinogen and high-molecular-weight kininogen on solid surfaces incubated in human plasma(the Vroman effect): influence of solid surface wettability. J Biomed Mater Res **21**, 1023, 1987.

179. Elwing, H., Askendal, A., and Lundström, I. Protein exchange reactions on solid surfaces studied with a wettability gradient method. Colloid Polym Sci **74**, 103, 1987.

180. Elwing, H., Welin, S., Askendal, A., Nilsson, U., and Lundstrom, I. A wettability gradient method for studies of macromolecular interactions at the liquid/solid interface. J Colloid Interface Sci **119**, 203, 1987.

181. Hlady, V. Spatially Resolved Adsorption Kinetics of Immunoglobulin G onto the Wettability Gradient Surface. Appl Spectrosc **45**, 246, 1991.

182. Golander, C.G., Caldwell, K., and Lin, Y.S. A new technique to prepare gradient surfaces using density gradient solutions. Colloids Surf **42**, 165, 1989.

183. Wijesundara, M.B.J., Fuoco, E., and Hanley, L. Preparation of chemical gadient surfaces by hyperthermal polyatomic ion deposition: A new method for combinatorial materials science. J Colloid Interface Sci **119**, 203, 1987.

184. Wu, T., Tomlinson, M., Efimenko, K., and Genzer, J. A combinatorial approach to surface anchored polymers. J Mater Sci **38**, 4471, 2003.

185. Zhao, B. A combinatorial approach to study solvent-induced self-assembly of mixed poly (methyl methacrylate)/polystyrene brushes on planar silica substrates: Effect of relative grafting density. Langmuir **20**, 11748, 2004.

186. Bhat, R.R., Tomlinson, M.R., and Genzer, J. Orthogonal surface-grafted polymer gradients: A versatile combinatorial platform. J Polym Sci B Polym Phys **43**, 3384, 2005.

187. Iqbal, P., Critchley, K., Bowen, J., Attwood, D., Tunnicliffe, D., Evans, S.D., and Preece, J.A. Fabrication of a nanoparticle gradient substrate by thermochemical manipulation of an ester functionalized SAM. J Mater Chem **17**, 5097, 2007.

188. Morgenthaler, S., Lee, S., Zurcher, S., and Spencer, N.D. A simple, reproducible approach to the preparation of surface-chemical gradients. Langmuir **19**, 10459, 2003.

189. Morgenthaler, S., Zink, C., Städler, B., Vörös, J., Lee, S., Spencer, N.D., and Tosatti, S.G.P. Poly (L-lysine)-grafted-poly (ethylene glycol)-based surface-chemical gradients. Preparation, characterization, and first applications. Biointerphases **1**, 156, 2006.

190. Kunzler, T.P., Huwiler, C., Drobek, T., Vörös, J., and Spencer, N.D. Systematic study of osteoblast response to nanotopography by means of nanoparticle-density gradients. Biomaterials **28**, 5000, 2007.

191. Krämer, S., Xie, H., Gaff, J., Williamson, J.R., Tkachenko, A.G., Nouri, N., Feldheim, D.A., and Feldheim, D.L. Preparation of protein gradients through the controlled deposition of protein-nanoparticle conjugates onto functionalized surfaces. J Am Chem Soc **126**, 5388, 2004.

192. Meier, M.A.R., Hoogenboom, R., and Schubert, U.S. Combinatorial methods, automated synthesis and high-throughput screening in polymer research: The evolution continues. Macromol Rapid Commun **25**, 21, 2004.

193. Meier, M.A.R., and Schubert, U.S. Combinatorial polymer research and high-throughput experimentation: powerful tools for the discovery and evaluation of new materials. J Mater Chem **14**, 3289, 2004.

194. Smith, A.P., Douglas, J.F., Meredith, J.C., Amis, E.J., and Karim, A. Combinatorial study of surface pattern formation in thin block copolymer films. Phys Rev Lett **87**, 15503, 2001.

195. Smith, A.P., Douglas, J.F., Meredith, J.C., Amis, E.J., and Karim, A. High-throughput characterization of pattern formation in symmetric diblock copolymer films. J Polym Sci B Polym Phys **39**, 2141, 2001.

196. Washburn, N.R., Yamada, K.M., Simon, C.G., Kennedy, S.B., and Amis, E.J. High-throughput investigation of osteoblast response to polymer crystallinity: influence of nanometer-scale roughness on proliferation. Biomaterials **25**, 1215, 2004.

197. Eidelman, N., and Simon Jr, C.G. Characterization of combinatorial polymer blend composition gradients by FTIR microspectroscopy. J Res Natl Inst Stand Technol **109**, 219, 2004.

198. Meredith, J.C., Karim, A., and Amis, E.J. High-throughput measurement of polymer blend phase behavior. Macromolecules **33**, 5760, 2000.

199. Meredith, J.C., Sormana, J.L., Keselowsky, B.G., Garcia, A.J., Tona, A., Karim, A., and Amis, E.J. Combinatorial characterization of cell interactions with polymer surfaces. J Biomed Mater Res **66**, 483, 2003.

200. Simon Jr, C.G., Eidelman, N., Kennedy, S.B., Sehgal, A., Khatri, C.A., and Washburn, N.R. Combinatorial screening of cell proliferation on poly (L-lactic acid)/poly (D, L-lactic acid) blends. Biomaterials **26**, 6906, 2005.

201. Sung, H.J., Su, J., Berglund, J.D., Russ, B.V., Meredith, J.C., and Galis, Z.S. The use of temperature–composition combinatorial libraries to study the effects of biodegradable polymer blend surfaces on vascular cells. Biomaterials **26**, 4557, 2005.

202. Smith, A.P., Sehgal, A., Douglas, J.F., Karim, A., and Amis, E.J. Combinatorial mapping of surface energy effects on diblock copolymer thin film ordering. Macromol Rapid Commun **24**, 131, 2003.

203. Bhat, R.R., Tomlinson, M.R., and Genzer, J. Assembly of nanoparticles using surface-grafted orthogonal polymer gradients. Macromol Rapid Commun **25**, 270, 2004.

204. Meredith, J.C., Smith, A.P., Karim, A., and Amis, E.J. Combinatorial materials science for polymer thin-film dewetting. Macromolecules **33**, 9747, 2000.

205. Cukierman, E., Pankov, R., Stevens, D.R., and Yamada, K.M. Taking cell-matrix adhesions to the third dimension. Science **294**, 1708, 2001.

206. Gelain, F., Bottai, D., Vescovi, A., and Zhang, S. Designer self-assembling peptide nanofiber scaffolds for adult mouse neural stem cell 3-dimensional cultures. PLoS ONE **1**, e119, 2006.

207. Chen, C.C., Huang, T.H., Kao, C.T., and Ding, S.J. Characterization of functionally graded hydroxyapatite/titanium composite coatings plasma-sprayed on Ti alloys. J Biomed Mater Res B Appl Biomater **78**, 146, 2006.

208. Hedia, H.S., and Mahmoud, N.A. Design optimization of functionally graded dental implant. Biomed Mater Eng **14**, 133, 2004.

209. Hsu, Y.H., Turner, I.G., and Miles, A.W. Fabrication of porous bioceramics with porosity gradients similar to the bimodal structure of cortical and cancellous bone. J Mater Sci Mater Med **18**, 2251, 2007.

210. Xu, H.H., Burguera, E.F., and Carey, L.E. Strong, macroporous, and in situ-setting calcium phosphate cement-layered structures. Biomaterials **28**, 3786, 2007.

211. Gruner, H. Coating of implants. Chem Abstr **106**, 55966g, 1987.

212. Wang, M., Yang, X.Y., Khor, K.A., and Wang, Y. Preparation and characterization of bioactive monolayer and functionally graded coatings. J Mater Sci Mater Med **10**, 269, 1999.

213. Lagoa, A.L., Wedemeyer, C., von Knoch, M., Loer, F., and Epple, M. A strut graft substitute consisting of a metal core and a polymer surface. J Mater Sci Mater Med **19**, 417, 2008.

214. Kim, H.M., Takadama, H., Miyaji, F., Kokubo, T., Nishiguchi, S., and Nakamura, T. Formation of bioactive functionally graded structure on Ti-6Al-4V alloy by chemical surface treatment. J Mater Sci Mater Med **11**, 555, 2000.

215. Kim, H.W., Kim, H.E., and Knowles, J.C. Hard-tissue-engineered zirconia porous scaffolds with hydroxyapatite sol-gel and slurry coatings. J Biomed Mater Res **70**, 270, 2004.

216. Zhu, L., Ye, X., Tang, G., Zhao, N., Gong, Y., Zhao, Y., Zhao, J., and Zhang, X. Corrosion test, cell behavior test, and in vivo study of gradient TiO2 layers produced by compound electrochemical oxidation. J Biomed Mater Res A **78**, 515, 2006.

217. Muratoglu, O.K., O'Connor, D.O., Bragdon, C.R., Delaney, J., Jasty, M., Harris, W.H., Merrill, E., and Venugopalan, P. Gradient crosslinking of UHMWPE using irradiation in molten state for total joint arthroplasty. Biomaterials **23**, 717, 2002.

218. Shen, F.W., and McKellop, H. Surface-gradient cross-linked polyethylene acetabular cups: oxidation resistance and wear against smooth and rough femoral balls. Clin Orthop Relat Res **430**, 80, 2005.

219. Beauregard, G.P., and James, S.P. Synthesis and characterization of a novel UHMWPE interpenetrating polymer network. Biomed Sci Instrum **35**, 415, 1999.

220. Thieme, M., Wieters, K.P., Bergner, F., Scharnweber, D., Worch, H., Ndop, J., Kim, T.J., and Grill, W. Titanium powder sintering for preparation of a porous functionally graded material destined for orthopaedic implants. J Mater Sci Mater Med **12**, 225, 2001.

221. Tampieri, A., Celotti, G., Sprio, S., Delcogliano, A., and Franzese, S. Porosity-graded hydroxyapatite ceramics to replace natural bone. Biomaterials **22**, 1365, 2001.

222. Vaz, L., Lopes, A.B., and Almeida, M. Porosity control of hydroxyapatite implants. J Mater Sci Mater Med **10**, 239, 1999.

223. Werner, J., Linner-Krcmar, B., Friess, W., and Greil, P. Mechanical properties and in vitro cell compatibility of hydroxyapatite ceramics with graded pore structure. Biomaterials **23**, 4285, 2002.

224. Eufinger, H., Rasche, C., Lehmbrock, J., Wehmoller, M., Weihe, S., Schmitz, I., Schiller, C., and Epple, M. Performance of functionally graded implants of polylactides and calcium phosphate/calcium carbonate in an ovine model for computer assisted craniectomy and cranioplasty. Biomaterials **28**, 475, 2007.

225. Boughton, P., Ferris, D., and Ruys, A.J. Ceramic-polymer functionally gradient material: A novel disc prosthesis. Ceram Eng Sci Proc **22**, 593, 2001.

226. Bogdanski, D., Köller, M., Müller, D., Muhr, G., Bram, M., Buchkremer, H.P., Stöver, D., Choi, J., and Epple, M. Easy assessment of the biocompatibility of Ni–Ti alloys by in vitro cell culture experiments on a functionally graded Ni–NiTi–Ti material. Biomaterials **23**, 4549, 2002.

227. Watari, F., Yokoyama, A., Omori, M., Hirai, T., Kondo, H., Uo, M., and Kawasaki, T. Biocompatibility of materials and development to functionally graded implant for bio-medical application. Compos Sci Technol **64**, 893, 2004.

228. Yang, J., and Xiang, H.J. A three-dimensional finite element study on the biomechanical behavior of an FGBM dental implant in surrounding bone. J Biomech **40**, 2377, 2007.

229. Moritz, T., Riedel, H., Werner, G., and Tomandl, G. Simulation and investigation of pore size graded titania layers during sintering. J Mater Sci **35**, 2235, 2000.

230. Mortensen, A., and Suresh, S. Functionally graded metals and metal-ceramic composites. Part 1. Processing. Int Mater Rev **40**, 239, 1995.

231. Kieback, B., Neubrand, A., and Riedel, H. Processing techniques for functionally graded materials. Mater Sci Eng A Struct Mater **362**, 81, 2003.

232. Gurdon, J.B., and Bourillot, P.Y. Morphogen gradient interpretation. Nature **413**, 797, 2001.

233. Eichmann, A., Le Noble, F., Autiero, M., and Carmeliet, P. Guidance of vascular and neural network formation. Curr Opin Neurobiol **15**, 108, 2005.

234. Tessier-Lavigne, M. The Molecular Biology of Axon Guidance. Science **274**, 1123, 1996.

235. Parent, C.A., and Devreotes, P.N. A Cell's Sense of Direction. Science **284**, 765, 1999.

236. Vunjak-Novakovic, G., and Kaplan, D.L. Tissue engineering: The next generation. Tissue Eng **12**, 3261, 2006.

237. Ingber, D.E., Mow, V.C., Butler, D., Niklason, L., Huard, J., Mao, J., Yannas, I., Kaplan, D., and Vunjak-Novakovic, G. Tissue engineering and developmental biology: going biomimetic. Tissue Eng **12**, 3265, 2006.

238. Chen, R.R., and Mooney, D.J. Polymeric growth factor delivery strategies for tissue engineering. Pharm Res **20**, 1103, 2003.

239. Alberts, B., Johnson, A., Lewis, J., Raff, M., Roberts, K., and Walter, P. Molecular Biology of the Cell. Garland Science, New York, 2002.

240. Yamada, K.M. Adhesive recognition sequences. J Biol Chem **266**, 12809, 1991.

241. Hersel, U., Dahmen, C., and Kessler, H. RGD modified polymers: biomaterials for stimulated cell adhesion and beyond. Biomaterials **24**, 4385, 2003.

242. Cao, X., and Shoichet, M.S. Defining the concentration gradient of nerve growth factor for guided neurite outgrowth. Neuroscience **103**, 831, 2001.

243. Cao, X., and Shoichet, M.S. Investigating the synergistic effect of combined neurotrophic factor concentration gradients to guide axonal growth. Neuroscience **122**, 381, 2003.

244. Dertinger, S.K.W., Jiang, X., Li, Z., Murthy, V.N., and Whitesides, G.M. Gradients of substrate-bound laminin orient axonal specification of neurons. Proc Natl Acad Sci U S A **99**, 12542, 2002.

245. Dodla, M.C., and Bellamkonda, R.V. Anisotropic scaffolds facilitate enhanced neurite extension in vitro. J Biomed Mater Res A **78**, 213, 2006.

246. Halfter, W. The behavior of optic axons on substrate gradients of retinal basal lamina proteins and merosin. J Neurosci **16**, 4389, 1996.

247. Kapur, T.A., and Shoichet, M.S. Immobilized concentration gradients of nerve growth factor guide neurite outgrowth. J Biomed Mater Res **68**, 235, 2004.

248. Moore, K., MacSween, M., and Shoichet, M. Immobilized concentration gradients of neurotrophic factors guide neurite outgrowth of primary neurons in macroporous scaffolds. Tissue Eng **12**, 267, 2006.

249. Rosoff, W.J., Urbach, J.S., Esrick, M.A., McAllister, R.G., Richards, L.J., and Goodhill, G.J. A new chemotaxis assay shows the extreme sensitivity of axons to molecular gradients. Nat Neurosci **7**, 678, 2004.

250. Dodla, M.C., and Bellamkonda, R.V. Differences between the effect of anisotropic and isotropic laminin and nerve growth factor presenting scaffolds on nerve regeneration across long peripheral nerve gaps. Biomaterials **29**, 33, 2008.

251. Kang, C.E., Gemeinhart, E.J., and Gemeinhart, R.A. Cellular alignment by grafted adhesion peptide surface density gradients. J Biomed Mater Res A **71**, 403, 2004.

252. DeLong, S.A., Moon, J.J., and West, J.L. Covalently immobilized gradients of bFGF on hydrogel scaffolds for directed cell migration. Biomaterials **26**, 3227, 2005.

253. DeLong, S.A., Gobin, A.S., and West, J.L. Covalent immobilization of RGDS on hydrogel surfaces to direct cell alignment and migration. J Control Release **109**, 139, 2005.

254. Knapp, D.M., Helou, E.F., and Tranquillo, R.T. A Fibrin or Collagen Gel Assay for Tissue Cell Chemotaxis: Assessment of Fibroblast Chemotaxis to GRGDSP. Exp Cell Res **247**, 543, 1999.

255. Chen, G., and Ito, Y. Gradient micropattern immobilization of EGF to investigate the effect of artificial juxtacrine stimulation. Biomaterials **22**, 2453, 2001.

256. Boyden, S. The chemotactic effect of mixtures of antibody and antigen on polymorphonuclear leucocytes. J Exp Med **115**, 453, 1962.

257. Nelson, R.D. Chemotaxis under agarose: a new and simple method for measuring chemotaxis and spontaneous migration of human polymorphonuclear leukocytes and monocytes. J Immunol **115**, 1650, 1975.

258. Zigmond, S.H., and Hirsch, J.G. Leukocyte locomotion and chemotaxis: New methods for evaluation, and demonstration of a cell-derived chemotactic factor J Exp Med **137**, 387, 1973.

259. Fisher, P.R. Quantitative analysis of cell motility and chemotaxis in Dictyostelium discoideum by using an image processing system and a novel chemotaxis chamber providing stationary chemical gradients. J Cell Biol **108**, 973, 1989.

260. Zicha, D., Dunn, G.A., and Brown, A.F. A new direct-viewing chemotaxis chamber. J Cell Sci **99**, 769, 1991.

261. Adams, D.N., Kao, E.Y.C., Hypolite, C.L., Distefano, M.D., Hu, W.S., and Letourneau, P.C. Growth cones turn and migrate up an immobilized gradient of the laminin IKVAV peptide. J Neurobiol **62**, 134, 2005.

262. Clark, R.A.F. Wound repair: Overview and general considerations. Plenum Press, New York, 1996.

263. Rosoff, W.J., McAllister, R., Esrick, M.A., Goodhill, G.J., and Urbach, J.S. Generating controlled molecular gradients in 3D gels. Biotechnol Bioeng **91**, 754, 2005.

264. Moghe, P.V., Nelson, R.D., and Tranquillo, R.T. Cytokine-stimulated chemotaxis of human neutrophils in a 3-D conjoined fibrin gel assay. J Immunol Methods **180**, 193, 1995.

265. Dertinger, S.K.W., Chiu, D.T., Jeon, N.L., and Whitesides, G.M. Generation of gradients having complex shapes using microfluidic networks. Anal Chem **73**, 1240, 2001.

266. Gunawan, R.C., Silvestre, J., Gaskins, H.R., Kenis, P.J.A., and Leckband, D.E. Cell migration and polarity on microfabricated gradients of extracellular matrix proteins. Langmuir **22**, 4250, 2006.

267. Jeon, N.L., Dertinger, S.K.W., Chiu, D.T., Choi, I.S., Stroock, A.D., and Whitesides, G.M. Generation of solution and surface gradients using microfluidic systems. Langmuir **16**, 8311, 2000.

268. Walker, G.M., Sai, J., Richmond, A., Stremler, M., Chung, C.Y., and Wikswo, J.P. Effects of flow and diffusion on chemotaxis studies in a microfabricated gradient generator. Lab Chip **5**, 611, 2005.

269. Singh, M., Morris, C.P., Ellis, R.J., Detamore, M.S., and Berkland, C. Microsphere-Based Seamless Scaffolds Containing Macroscopic Gradients of Encapsulated Factors for Tissue Engineering. Tissue Eng Part C Methods, 2008.

270. Suciati, T., Howard, D., Barry, J., Everitt, N.M., Shakesheff, K.M., and Rose, F.R. Zonal release of proteins within tissue engineering scaffolds. J Mater Sci Mater Med **17**, 1049, 2006.

271. Vepari, C.P., and Kaplan, D.L. Covalently immobilized enzyme gradients within three-dimensional porous scaffolds. Biotechnol Bioeng **93**, 1130, 2006.

272. Caelen, I., Bernard, A., Juncker, D., Michel, B., Heinzelmann, H., and Delamarche, E. Formation of gradients of proteins on surfaces with microfluidic networks. Langmuir **16**, 9125, 2000.

273. Ilkhanizadeh, S., Teixeira, A.I., and Hermanson, O. Inkjet printing of macromolecules on hydrogels to steer neural stem cell differentiation. Biomaterials **28**, 3936, 2007.

274. Harris, B.P., and Metters, A.T. Generation and characterization of photopolymerized polymer brush gradients. Macromolecules **39**, 2764, 2006.

275. Tomkoria, S., Patel, R.V., and Mao, J.J. Heterogeneous nanomechanical properties of superficial and zonal regions of articular cartilage of the rabbit proximal radius condyle by atomic force microscopy. Med Eng Phys **26**, 815, 2004.

276. Weeber, H.A., Eckert, G., Pechhold, W., and van der Heijde, R.G. Stiffness gradient in the crystalline lens. Graefes Arch Clin Exp Ophthalmol **245**, 1357, 2007.

277. Marshall, G.W., Jr., Balooch, M., Gallagher, R.R., Gansky, S.A., and Marshall, S.J. Mechanical properties of the dentinoenamel junction: AFM studies of nanohardness, elastic modulus, and fracture. J Biomed Mater Res **54**, 87, 2001.

278. Horb, M.E. Patterning the endoderm: the importance of neighbours. Bioessays **22**, 599, 2000.

279. Murry, C.E., and Keller, G. Differentiation of embryonic stem cells to clinically relevant populations: Lessons from embryonic development. Cell **132**, 661, 2008.

280. Gerstenfeld, L.C., Cruceta, J., Shea, C.M., Sampath, K., Barnes, G.L., and Einhorn, T.A. Chondrocytes provide morphogenic signals that selectively induce osteogenic differentiation of mesenchymal stem cells. J Bone Miner Res **17**, 221, 2002.

281. Focus, W., and Contact, N.P.G. Changing neighbours, changing behaviour: cell adhesion molecule-mediated signalling during tumour progression. The EMBO Journal **22**, 2318, 2003.

282. Jaklenec, A., Hinckfuss, A., Bilgen, B., Ciombor, D.M., Aaron, R., and Mathiowitz, E. Sequential release of bioactive IGF-I and TGF-beta(1) from PLGA microsphere-based scaffolds. Biomaterials **29**, 1518, 2008.

283. Richardson, T.P., Peters, M.C., Ennett, A.B., and Mooney, D.J. Polymeric system for dual growth factor delivery. Nat Biotechnol **19**, 1029, 2001.

284. Jagger, R.G., Bates, J.F., and Kopp, S. Temporomandibular Joint Dysfunction: The Essentials. Wright (Butterworth Heinemann), Oxford1994.

285. Farrar, W.B., and McCarty, W.L., Jr. The TMJ dilemma. J Ala Dent Assoc **63**, 19, 1979.

286. Stegenga, B. Osteoarthritis of the temporomandibular joint organ and its relationship to disc displacement. J Orofac Pain **15**, 193, 2001.

287. Tanaka, E., Detamore, M.S., and Mercuri, L.G. Degenerative disorders of the temporomandibular joint: etiology, diagnosis, and treatment. J Dent Res **87**, 296, 2008.

288. Tanaka, E., Sasaki, A., Tahmina, K., Yamaguchi, K., Mori, Y., and Tanne, K. Mechanical properties of human articular disk and its influence on TMJ loading studied with the finite element method. J Oral Rehabil **28**, 273, 2001.

289. Tanne, K., Tanaka, E., and Sakuda, M. The elastic modulus of the temporomandibular joint disc from adult dogs. J Dent Res **70**, 1545, 1991.

290. Akizuki, S., Mow, V.C., Muller, F., Pita, J.C., Howell, D.S., and Manicourt, D.H. Tensile properties of human knee joint cartilage: I. Influence of ionic conditions, weight bearing, and fibrillation on the tensile modulus. J Orthop Res **4**, 379, 1986.

291. Charlebois, M., McKee, M.D., and Buschmann, M.D. Nonlinear tensile properties of bovine articular cartilage and their variation with age and depth. J Biomech Eng **126**, 129, 2004.

292. Elliott, D.M., Guilak, F., Vail, T.P., Wang, J.Y., and Setton, L.A. Tensile properties of articular cartilage are altered by meniscectomy in a canine model of osteoarthritis. J Orthop Res **17**, 503, 1999.

293. Setton, L.A., Mow, V.C., Muller, F.J., Pita, J.C., and Howell, D.S. Mechanical behavior and biochemical composition of canine knee cartilage following periods of joint disuse and disuse with remobilization. Osteoarthritis Cartilage **5**, 1, 1997.

294. Swann, A.C., and Seedhom, B.B. Improved techniques for measuring the indentation and thickness of articular cartilage. Proc Inst Mech Eng [H] **203**, 143, 1989.

295. Elliott, D.M., and Setton, L.A. Anisotropic and inhomogeneous tensile behavior of the human anulus fibrosus: experimental measurement and material model predictions. J Biomech Eng **123**, 256, 2001.

296. Ferguson, S.J., Bryant, J.T., and Ito, K. The material properties of the bovine acetabular labrum. J Orthop Res **19**, 887, 2001.

297. Park, S., and Ateshian, G.A. Dynamic response of immature bovine articular cartilage in tension and compression, and nonlinear viscoelastic modeling of the tensile response. J Biomech Eng **128**, 623, 2006.

298. Woo, S.L., Lubock, P., Gomez, M.A., Jemmott, G.F., Kuei, S.C., and Akeson, W.H. Large deformation nonhomogeneous and directional properties of articular cartilage in uniaxial tension. J Biomech **12**, 437, 1979.

299. Grodzinsky, A.J., Roth, V., Myers, E., Grossman, W.D., and Mow, V.C. The significance of electromechanical and osmotic forces in the nonequilibrium swelling behavior of articular cartilage in tension. J Biomech Eng **103**, 221, 1981.

300. Parsons, J.R., and Black, J. Mechanical behavior of articular cartilage: quantitative changes with alteration of ionic environment. J Biomech **12**, 765, 1979.

301. Allen, K.D., and Athanasiou, K.A. A surface-regional and freeze-thaw characterization of the porcine temporomandibular joint disc. Ann Biomed Eng **33**, 951, 2005.

302. Scapino, R.P., Obrez, A., and Greising, D. Organization and function of the collagen fiber system in the human temporomandibular joint disk and its attachments. Cells Tissues Organs **182**, 201, 2006.

303. Forgacs, G., Foty, R.A., Shafrir, Y., and Steinberg, M.S. Viscoelastic properties of living embryonic tissues: a quantitative study. Biophys J **74**, 2227, 1998.

304. Murdock, D.R., Ermilov, S.A., Spector, A.A., Popel, A.S., Brownell, W.E., and Anvari, B. Effects of chlorpromazine on mechanical properties of the outer hair cell plasma membrane. Biophys J **89**, 4090, 2005.

305. Palevski, A., Glaich, I., Portnoy, S., Linder-Ganz, E., and Gefen, A. Stress relaxation of porcine gluteus muscle subjected to sudden transverse deformation as related to pressure sore modeling. J Biomech Eng **128**, 782, 2006.

306. Sverdlik, A., and Lanir, Y. Time-dependent mechanical behavior of sheep digital tendons, including the effects of preconditioning. J Biomech Eng **124**, 78, 2002.

307. Kirk, W.S., Jr. Morphologic differences between superior and inferior disc surfaces in chronic internal derangement of the temporomandibular joint. J Oral Maxillofac Surg **48**, 455, 1990.

308. Kondoh, T., Westesson, P.L., Takahashi, T., and Seto, K. Prevalence of morphological changes in the surfaces of the temporomandibular joint disc associated with internal derangement. J Oral Maxillofac Surg **56**, 339, 1998.

309. Athanasiou, K.A., Rosenwasser, M.P., Buckwalter, J.A., Malinin, T.I., and Mow, V.C. Interspecies comparisons of in situ intrinsic mechanical properties of distal femoral cartilage. J Orthop Res **9**, 330, 1991.

310. Cohen, B., Chorney, G.S., Phillips, D.P., Dick, H.M., and Mow, V.C. Compressive stress-relaxation behavior of bovine growth plate may be described by the nonlinear biphasic theory. J Orthop Res **12**, 804, 1994.

311. Mow, V.C., Gibbs, M.C., Lai, W.M., Zhu, W.B., and Athanasiou, K.A. Biphasic indentation of articular cartilage--II. A numerical algorithm and an experimental study. J Biomech **22**, 853, 1989.

312. Covell, D.A., Jr., and Herring, S.W. Periosteal migration in the growing mandible: an animal model. Am J Orthod Dentofacial Orthop **108**, 22, 1995.

313. Herring, S.W. TMJ anatomy and animal models. J Musculoskelet Neuronal Interact **3**, 391, 2003.

314. Li, L.P., Buschmann, M.D., and Shirazi-Adl, A. Strain-rate dependent stiffness of articular cartilage in unconfined compression. J Biomech Eng **125**, 161, 2003.

315. Li, L.P., and Herzog, W. Strain-rate dependence of cartilage stiffness in unconfined compression: the role of fibril reinforcement versus tissue volume change in fluid pressurization. J Biomech **37**, 375, 2004.

316. Slivka, M.A., Leatherbury, N.C., Kieswetter, K., and Niederauer, G.G. Porous, resorbable, fiber-reinforced scaffolds tailored for articular cartilage repair. Tissue Eng **7**, 767, 2001.

317. DiSilvestro, M.R., Zhu, Q., and Suh, J.K. Biphasic poroviscoelastic simulation of the unconfined compression of articular cartilage: II--Effect of variable strain rates. J Biomech Eng **123**, 198, 2001.

318. Liu, Z.J., and Herring, S.W. Bone surface strains and internal bony pressures at the jaw joint of the miniature pig during masticatory muscle contraction. Arch Oral Biol **45**, 95, 2000.

319. Hohl, T.H., and Tucek, W.H. Measurement of condylar loading forces by instrumented prosthesis in the baboon. J Maxillofac Surg **10**, 1, 1982.

320. Elliott, D.M., Robinson, P.S., Gimbel, J.A., Sarver, J.J., Abboud, J.A., Iozzo, R.V., and Soslowsky, L.J. Effect of Altered Matrix Proteins on Quasilinear Viscoelastic Properties in Transgenic Mouse Tail Tendons. Ann Biomed Eng **31**, 599, 2003.

321. Woo, S.L., Gomez, M.A., and Akeson, W.H. The time and history-dependent viscoelastic properties of the canine medical collateral ligament. J Biomech Eng **103**, 293, 1981.

322. Provenzano, P.P., Lakes, R.S., Corr, D.T., and Vanderby, R. Application of nonlinear viscoelastic models to describe ligament behavior. Biomech Model Mechanobiol **1**, 45, 2002.

323. Provenzano, P., Lakes, R., Keenan, T., and vanderby, R. Nonlinear Ligament Viscoelasticity. Ann Biomed Eng **29**, 908, 2001.

324. Fiford, R.J., and Bilston, L.E. The mechanical properties of rat spinal cord in vitro. J Biomech **38**, 1509, 2005.

325. García, J.J., and Cortés, D.H. A biphasic viscohyperelastic fibril-reinforced model for articular cartilage: Formulation and comparison with experimental data. J Biomech **40**, 1737, 2007.

326. Langer, R., and Vacanti, J.P. Tissue engineering. Science **260**, 920, 1993.

327. Park, T.H., and Shuler, M.L. Integration of cell culture and microfabrication technology. Biotechnol Prog **19**, 243, 2003.

328. Berkland, C., Kim, K., and Pack, D.W. PLG microsphere size controls drug release rate through several competing factors. Pharm Res **20**, 1055, 2003.

329. Chun, K.W., Yoo, H.S., Yoon, J.J., and Park, T.G. Biodegradable PLGA microcarriers for injectable delivery of chondrocytes: effect of surface modification on cell attachment and function. Biotechnol Prog **20**, 1797, 2004.

330. Holland, T.A., Tabata, Y., and Mikos, A.G. Dual growth factor delivery from degradable oligo(poly(ethylene glycol) fumarate) hydrogel scaffolds for cartilage tissue engineering. J Control Release **101**, 111, 2005.

331. Borden, M., Attawia, M., Khan, Y., El-Amin, S.F., and Laurencin, C.T. Tissue-engineered bone formation in vivo using a novel sintered polymeric microsphere matrix. J Bone Joint Surg Br **86**, 1200, 2004.

332. Ruhe, P.Q., Hedberg-Dirk, E.L., Padron, N.T., Spauwen, P.H., Jansen, J.A., and Mikos, A.G. Porous poly(DL-lactic-co-glycolic acid)/calcium phosphate cement composite for reconstruction of bone defects. Tissue Eng **12**, 789, 2006.

333. Goraltchouk, A., Scanga, V., Morshead, C.M., and Shoichet, M.S. Incorporation of protein-eluting microspheres into biodegradable nerve guidance channels for controlled release. J Control Release **110**, 400, 2006.

334. Rosner, B.I., Siegel, R.A., Grosberg, A., and Tranquillo, R.T. Rational design of contact guiding, neurotrophic matrices for peripheral nerve regeneration. Ann Biomed Eng **31**, 1383, 2003.

335. Wu, L., and Ding, J. In vitro degradation of three-dimensional porous poly(D,L-lactide-co-glycolide) scaffolds for tissue engineering. Biomaterials **25**, 5821, 2004.

336. Tracy, M.A., Ward, K.L., Firouzabadian, L., Wang, Y., Dong, N., Qian, R., and Zhang, Y. Factors affecting the degradation rate of poly(lactide-co-glycolide) microspheres in vivo and in vitro. Biomaterials **20**, 1057, 1999.

337. Yao, J., Radin, S., Leboy, P.S., and Ducheyne, P. The effect of bioactive glass content on synthesis and bioactivity of composite poly (lactic-co-glycolic acid)/bioactive glass substrate for tissue engineering. Biomaterials **26**, 1935, 2005.

338. Jaklenec, A., Wan, E., Murray, M.E., and Mathiowitz, E. Novel scaffolds fabricated from protein-loaded microspheres for tissue engineering. Biomaterials **29**, 185, 2008.

339. Brown, J.L., Nair, L.S., and Laurencin, C.T. Solvent/non-solvent sintering: a novel route to create porous microsphere scaffolds for tissue regeneration. J Biomed Mater Res B Appl Biomater **86B**, 396, 2008.

340. Nukavarapu, S.P., Kumbar, S.G., Brown, J.L., Krogman, N.R., Weikel, A.L., Hindenlang, M.D., Nair, L.S., Allcock, H.R., and Laurencin, C.T. Polyphosphazene/Nano-Hydroxyapatite Composite Microsphere Scaffolds for Bone Tissue Engineering. Biomacromolecules **9**, 1818, 2008.

341. Berkland, C., Kim, K., and Pack, D.W. Fabrication of PLG microspheres with precisely controlled and monodisperse size distributions. J Control Release **73**, 59, 2001.

342. Thomson, R.C., Yaszemski, M.J., Powers, J.M., and Mikos, A.G. Fabrication of biodegradable polymer scaffolds to engineer trabecular bone. J Biomater Sci Polym Ed **7**, 23, 1995.

343. Gibson, L.J., and Ashby, M.F. Cellular Solids: Structure and Properties. University Press, Cambridge, UK, 1997.

344. Bailey, M.M., Wang, L., Bode, C.J., Mitchell, K.E., and Detamore, M.S. A comparison of human umbilical cord matrix stem cells and temporomandibular joint condylar chondrocytes for tissue engineering temporomandibular joint condylar cartilage. Tissue Eng **13**, 2003, 2007.

345. Almarza, A.J., and Athanasiou, K.A. Seeding techniques and scaffolding choice for tissue engineering of the temporomandibular joint disk. Tissue Eng **10**, 1787, 2004.

346. Zein, I., Hutmacher, D.W., Tan, K.C., and Teoh, S.H. Fused deposition modeling of novel scaffold architectures for tissue engineering applications. Biomaterials **23**, 1169, 2002.

347. Liu, Y., Wang, S., Krouse, J., Kotov, N.A., Eghtedari, M., Vargas, G., and Motamedi, M. Rapid aqueous photo-polymerization route to polymer and polymer-composite hydrogel 3D inverted colloidal crystal scaffolds. J Biomed Mater Res A, 2007.

348. Stachowiak, A.N., Bershteyn, A., Tzatzalos, E., and Irvine, D.J. Bioactive Hydrogels with an Ordered Cellular Structure Combine Interconnected Macroporosity and Robust Mechanical Properties. Adv Mater **17**, 399 2005.

349. Borden, M., Attawia, M., Khan, Y., and Laurencin, C.T. Tissue engineered microsphere-based matrices for bone repair: design and evaluation. Biomaterials **23**, 551, 2002.

350. Tracy, M.A. Development and scale-up of a microsphere protein delivery system. Biotechnol Prog **14**, 108, 1998.

351. Eser, H., and Tihminlioglu, F. Determination of thermodynamic and transport properties of solvents and non solvents in poly (L-lactide-co-glycolide). J Appl Polym Sci **102**, 2426, 2006.

352. Chung, T.W., Tsai, Y.L., Hsieh, J.H., and Tsai, W.J. Different ratios of lactide and glycolide in PLGA affect the surface property and protein delivery characteristics of the PLGA microspheres with hydrophobic additives. J Microencapsul **23**, 15, 2006.

353. Wu, L., Zhang, J., Jing, D., and Ding, J. "Wet-state" mechanical properties of three-dimensional polyester porous scaffolds. J Biomed Mater Res A **76**, 264, 2006.

354. Perugini, P., Genta, I., Conti, B., Modena, T., Cocchi, D., Zaffe, D., and Pavanetto, F. PLGA microspheres for oral osteopenia treatment: preliminary “in vitro”/“in vivo” evaluation. Int J Pharm **256**, 153, 2003.

355. Botchwey, E.A., Pollack, S.R., El-Amin, S., Levine, E.M., Tuan, R.S., and Laurencin, C.T. Human osteoblast-like cells in three-dimensional culture with fluid flow. Biorheology **40**, 299, 2003.

356. Botchwey, E.A., Pollack, S.R., Levine, E.M., and Laurencin, C.T. Bone tissue engineering in a rotating bioreactor using a microcarrier matrix system. J Biomed Mater Res **55**, 242, 2001.

357. Arnold, M.M., Gorman, E.M., Schieber, L.J., Munson, E.J., and Berkland, C. NanoCipro encapsulation in monodisperse large porous PLGA microparticles. J Control Release **121**, 100, 2007.

358. Nuttelman, C.R., Tripodi, M.C., and Anseth, K.S. Synthetic hydrogel niches that promote hMSC viability. Matrix Biol **24**, 208, 2005.

359. Holland, T.A., Bodde, E.W., Cuijpers, V.M., Baggett, L.S., Tabata, Y., Mikos, A.G., and Jansen, J.A. Degradable hydrogel scaffolds for in vivo delivery of single and dual growth factors in cartilage repair. Osteoarthritis Cartilage **15**, 187, 2007.

360. Holland, T.A., Bodde, E.W., Baggett, L.S., Tabata, Y., Mikos, A.G., and Jansen, J.A. Osteochondral repair in the rabbit model utilizing bilayered, degradable oligo(poly(ethylene glycol) fumarate) hydrogel scaffolds. J Biomed Mater Res A **75**, 156, 2005.

361. Phillips, J.E., Burns, K.L., Le Doux, J.M., Guldberg, R.E., and Garcia, A.J. Engineering graded tissue interfaces. Proc Natl Acad Sci U S A **105**, 12170, 2008.

362. Singh, M., Berkland, C., and Detamore, M.S. Strategies and Applications for Incorporating Physical and Chemical Signal Gradients in Tissue Engineering. Tissue Eng Part B Rev, 2008.

363. Mahdavi, A., Ferreira, L., Sundback, C., Nichol, J.W., Chan, E.P., Carter, D.J., Bettinger, C.J., Patanavanich, S., Chignozha, L., Ben-Joseph, E., Galakatos, A., Pryor, H., Pomerantseva, I., Masiakos, P.T., Faquin, W., Zumbuehl, A., Hong, S., Borenstein, J., Vacanti, J., Langer, R., and Karp, J.M. A biodegradable and biocompatible gecko-inspired tissue adhesive. Proc Natl Acad Sci U S A **105**, 2307, 2008.

364. Wang, D.A., Varghese, S., Sharma, B., Strehin, I., Fermanian, S., Gorham, J., Fairbrother, D.H., Cascio, B., and Elisseeff, J.H. Multifunctional chondroitin sulphate for cartilage tissue-biomaterial integration. Nat Mater **6**, 385, 2007.

365. Wang, L., Sheshareddy, K., Weiss, M.L., and Detamore, M.S. Effect of Initial Seeding Density on Human Umbilical Cord Mesenchymal Stromal Cells for Fibrocartilage Tissue Engineering. Tissue Eng Part A, 2008.

366. Duarte, A.R., Roy, C., Vega-Gonzalez, A., Duarte, C.M., and Subra-Paternault, P. Preparation of acetazolamide composite microparticles by supercritical anti-solvent techniques. Int J Pharm **332**, 132, 2007.

367. Davies, O.R., Lewis, A.L., Whitaker, M.J., Tai, H., Shakesheff, K.M., and Howdle, S.M. Applications of supercritical CO2 in the fabrication of polymer systems for drug delivery and tissue engineering. Adv Drug Deliv Rev **60**, 373, 2008.

368. Barry, J.J., Silva, M.M., Popov, V.K., Shakesheff, K.M., and Howdle, S.M. Supercritical carbon dioxide: putting the fizz into biomaterials. Philos Transact A Math Phys Eng Sci **364**, 249, 2006.

369. Ginty, P.J., Howard, D., Rose, F.R., Whitaker, M.J., Barry, J.J., Tighe, P., Mutch, S.R., Serhatkulu, G., Oreffo, R.O., Howdle, S.M., and Shakesheff, K.M. Mammalian cell survival and processing in supercritical CO(2). Proc Natl Acad Sci U S A **103**, 7426, 2006.

370. Howdle, S.M., Watson, M.S., Whitaker, M.J., Davies, M.C., Shakesheff, K.M., Popov, V.K., Mandel, F.S., and Wang, J.D. Supercritical fluid mixing: preparation of thermally sensitive polymer composites containing bioactive materials. Chem Commun **2001**, 109, 2001.

371. Mooney, D.J., Baldwin, D.F., Suh, N.P., Vacanti, J.P., and Langer, R. Novel approach to fabricate porous sponges of poly(D,L-lactic-co-glycolic acid) without the use of organic solvents. Biomaterials **17**, 1417, 1996.

372. Nawaby, A.V., Farah, A.A., Liao, X., Pietro, W.J., and Day, M. Biodegradable open cell foams of telechelic poly(epsilon-caprolactone) macroligand with ruthenium (II) chromophoric subunits via sub-critical CO2 processing. Biomacromolecules **6**, 2458, 2005.

373. Maspero, F.A., Ruffieux, K., Muller, B., and Wintermantel, E. Resorbable defect analog PLGA scaffolds using CO2 as solvent: structural characterization. J Biomed Mater Res **62**, 89, 2002.

374. Harris, L.D., Kim, B.S., and Mooney, D.J. Open pore biodegradable matrices formed with gas foaming. J Biomed Mater Res **42**, 396, 1998.

375. Can, A., and Karahuseyinoglu, S. Concise review: human umbilical cord stroma with regard to the source of fetus-derived stem cells. Stem Cells **25**, 2886, 2007.

376. Troyer, D.L., and Weiss, M.L. Wharton's jelly-derived cells are a primitive stromal cell population. Stem Cells **26**, 591, 2008.

377. Nof, M., and Shea, L.D. Drug-releasing scaffolds fabricated from drug-loaded microspheres. J Biomed Mater Res **59**, 349, 2002.

378. Wang, X., and Sanchez, I.C. Welding immiscible polymers with a supercritical fluid. Langmuir **23**, 12192, 2007.

379. Almarza, A.J., and Athanasiou, K.A. Design characteristics for the tissue engineering of cartilaginous tissues. Ann Biomed Eng **32**, 2, 2004.

380. Boyan, B.D., Schwartz, Z., Bonewald, L.F., and Swain, L.D. Localization of 1,25-(OH)2D3-responsive alkaline phosphatase in osteoblast-like cells (ROS 17/2.8, MG 63, and MC 3T3) and growth cartilage cells in culture. J Biol Chem **264**, 11879, 1989.

APPENDIX A: FIGURES

- CHAPTER 1: n/a
- CHAPTER 2: Fig. 2.1
- CHAPTER 3: n/a
- CHAPTER 4: Figs. 4.1 – 4.7
- CHAPTER 5: Figs. 5.1 – 5.5
- CHAPTER 6: Figs. 6.1 – 6.9
- CHAPTER 7: Figs. 7.1 – 7.3
- CHAPTER 8: Figs. 8.1 – 8.5
- CHAPTER 9: Figs. 9.1 – 9.4
- CHAPTER 10: n/a

Figure 2.1: (A) Schematic of a sagittal section of the human TMJ, showing the position of the condyle with respect to the TMJ disc and eminence-fossa. The cartilaginous surfaces are dark gray. (B) A schematic of the zonal architecture of the condylar cartilage, enlarged from the boxed region of (A), showing four explicit zones: fibrous, proliferative, mature and hypertrophic. This figure highlights fiber organization and cellular composition of these zones.

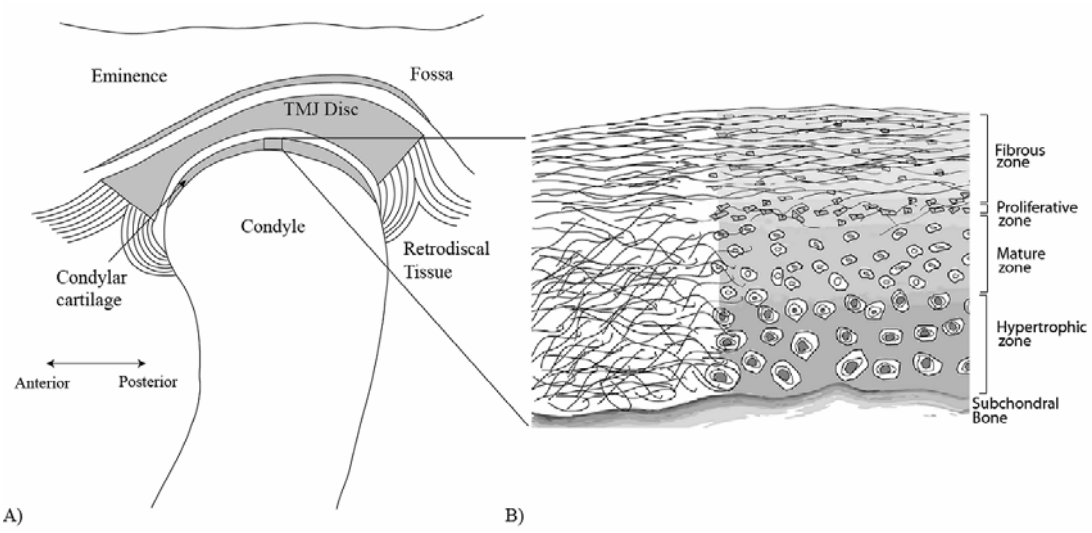

Figure 4.1: A) Posterior view of a left porcine condyle with the articular condylar cartilage intact. B) An enlarged superior view of condylar cartilage isolated from a right porcine condyle, displaying the different regions of the cartilage: anterior, posterior, superior, medial and lateral.

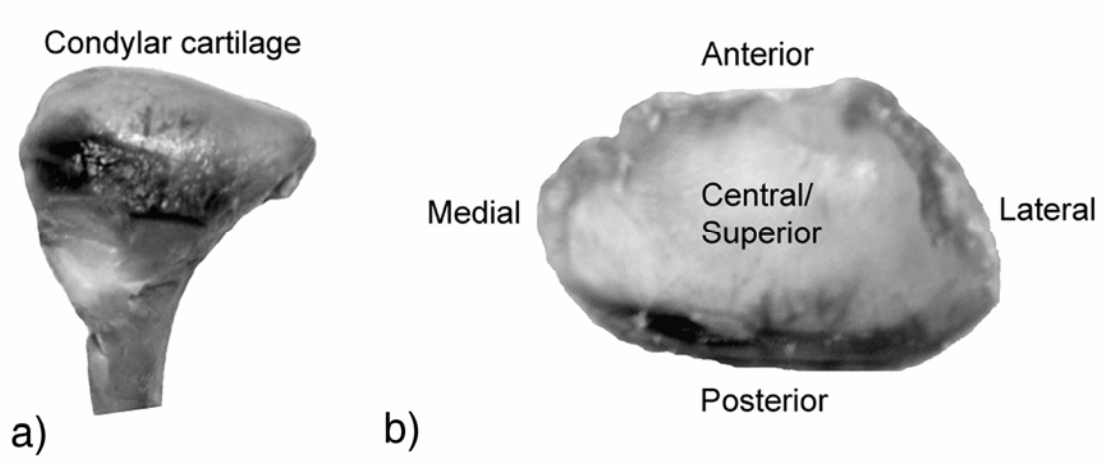

Figure 4.2: A superior view of condylar cartilage superimposed with the specimen preparation scheme. Three specimens from each condylar cartilage were tested, either in the mediolateral direction or in the anteroposterior direction. In the mediolateral direction, specimens were prepared from the anterior, superior and posterior regions. In the anteroposterior direction, specimens were prepared from the medial, central and lateral regions.

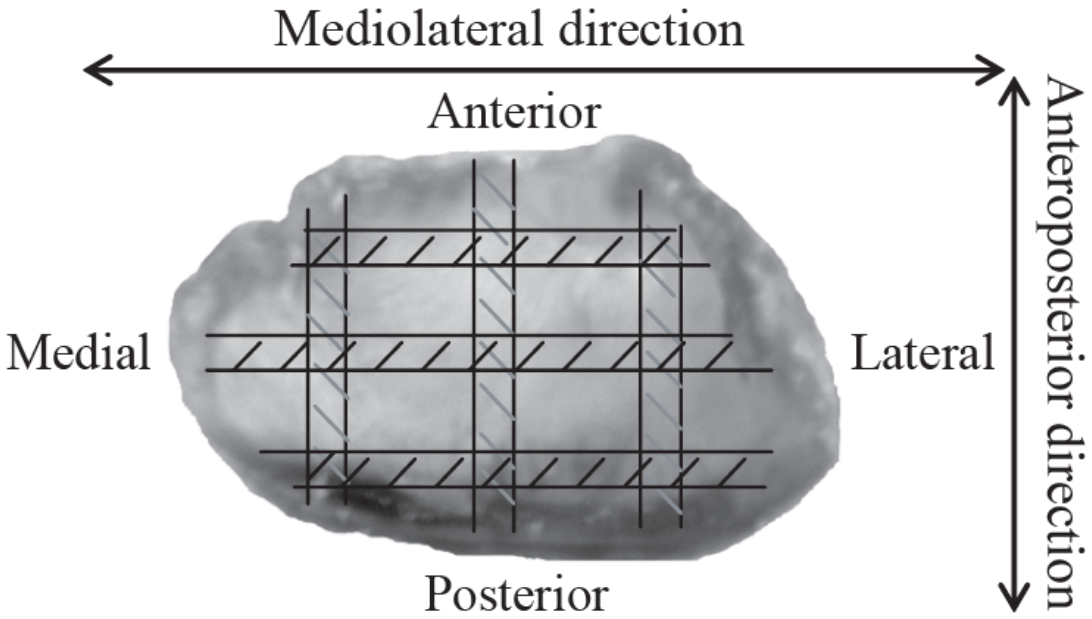

Figure 4.3: Photograph of the custom-built tensile bath and grip assembly. Shown here is the bath (1) to which the lower grip (2) was clamped. The upper grip (3) was attached to the movable crosshead that carried a load cell (4) of 50 N capacity. The temperature was controlled using an immersion heater (5) and a temperature probe (6), both connected to a temperature controller.

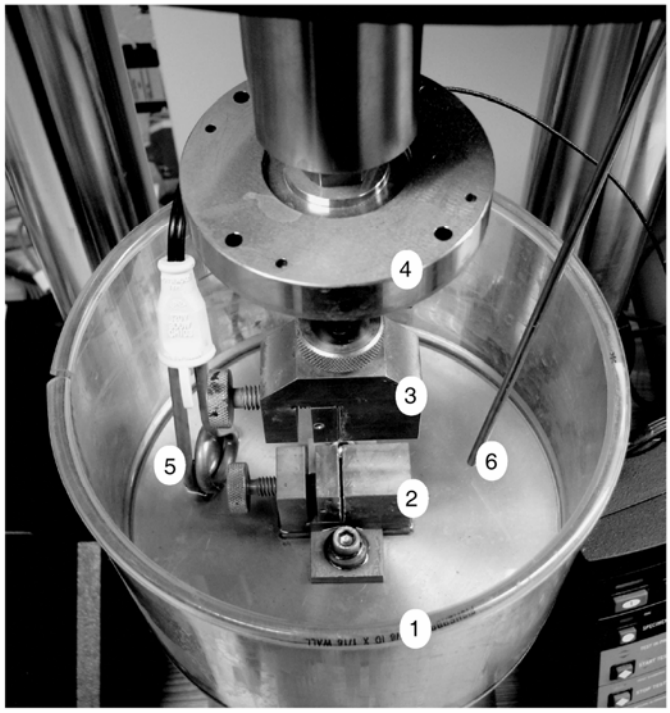

Figure 4.4: Typical stress-strain response of a condylar cartilage specimen, when stretched to 20% strain. The example curve provided here belonged to a specimen from the superior region, tested in the mediolateral direction. The curve demonstrates a non-linear region extending to approximately 6% strain, followed by a linear region.

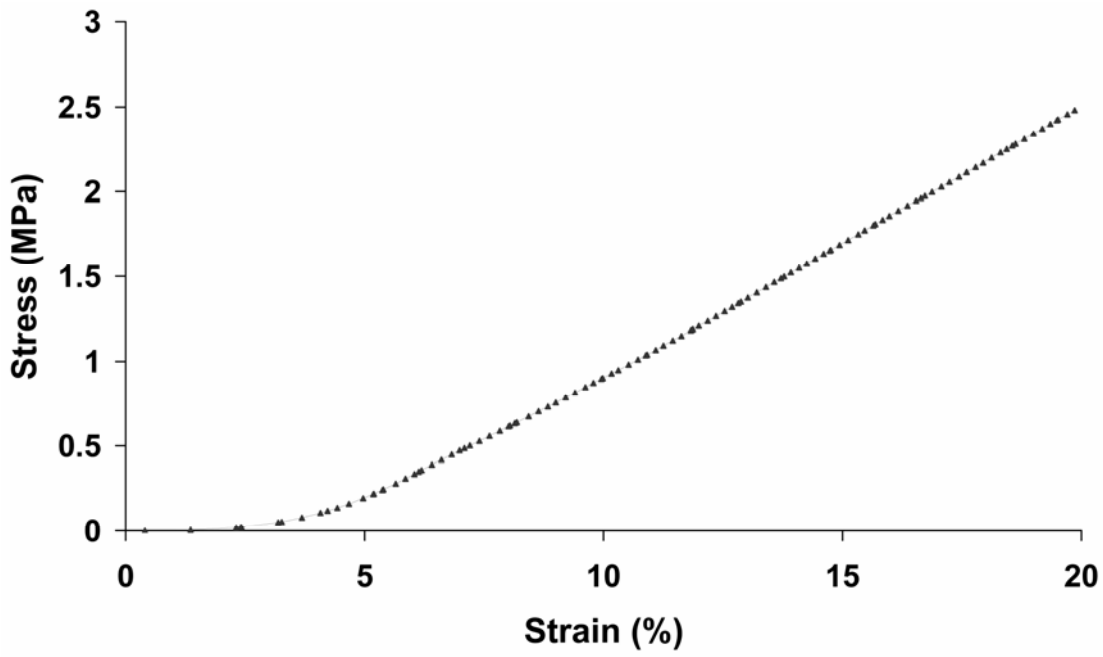

Figure 4.5: Example of a typical stress relaxation response curve-fitted to the linear viscoelastic models. The specimen provided here was from the superior region, tested in the mediolateral direction. The solid line represents the experimental data, showing the bi-exponential stress relaxation behavior of the specimen. The Kelvin model could not provide a close fit for the entire data. Therefore, the Kelvin model was fitted to only the slow relaxation phase and was used to obtain the equilibrium modulus. Using this equilibrium modulus, the second order generalized Kelvin model provided a close fit to the experimental data.

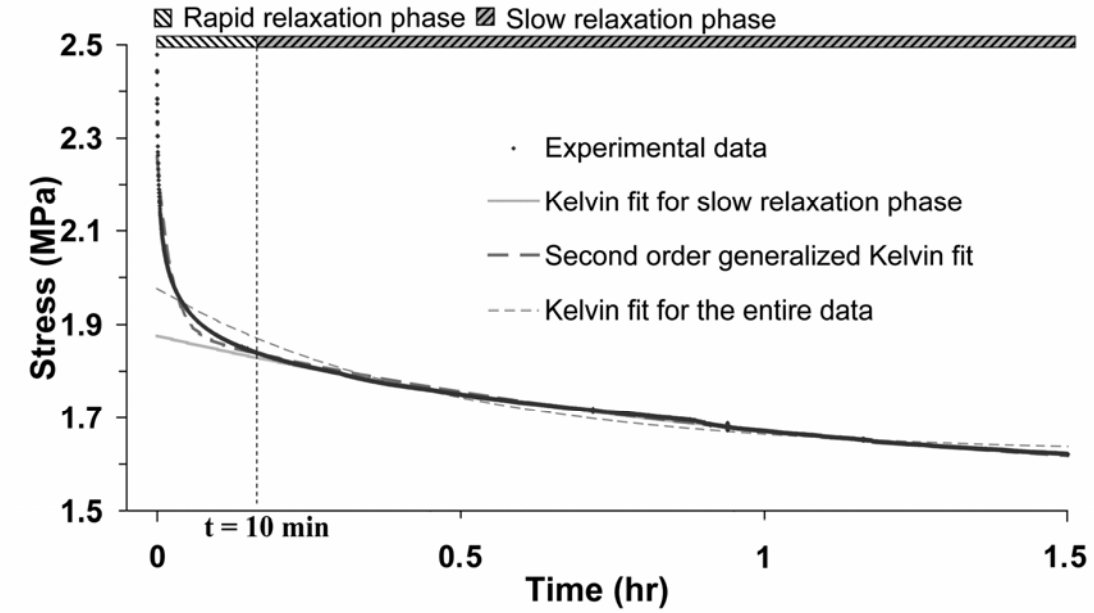

Figure 4.6: Polarized light micrographs displaying the collagen fibers from the fibrous zone of condylar cartilage from a right condyle at 100X magnification (scale bar = 100 μm). The locations from where the micrographs were captured are shown in the schematic of condylar cartilage in R1:C1 (denoted by white dots). The three columns (C2-4) correspond to tensile specimens tested in the anteroposterior direction and correspond to the specimens from the medial, central and lateral regions, respectively. The three rows (R1-3) correspond to tensile specimens tested in the mediolateral direction, where the middle row (R2) corresponds to the specimens from the superior region of the cartilage, and other two rows (R1 and R3) belong to regions close to the anterior and posterior edges of the cartilage. Micrographs from the peripheral regions (R1, R3, C1, C5) show that fibers ran in a ring-like fashion around the periphery. Micrographs from the interior regions (R2:C2-4) show that fiber orientation was predominantly anteroposterior inside the periphery. A: Anterior, P: Posterior, M: Medial, L: Lateral.

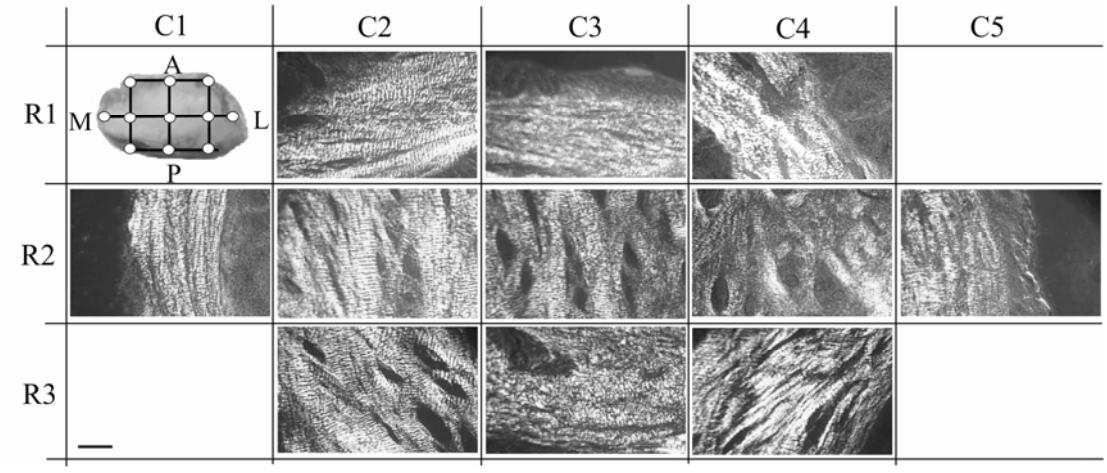

Figure 4.7: Superior view of a left porcine condyle superimposed with a simplified schematic of macroscopic fiber orientation of the fibrous zone, where only the predominant fiber orientation is shown. The schematic is based on the polarized light micrographs and visual inspection of the articular surface of the cartilage.

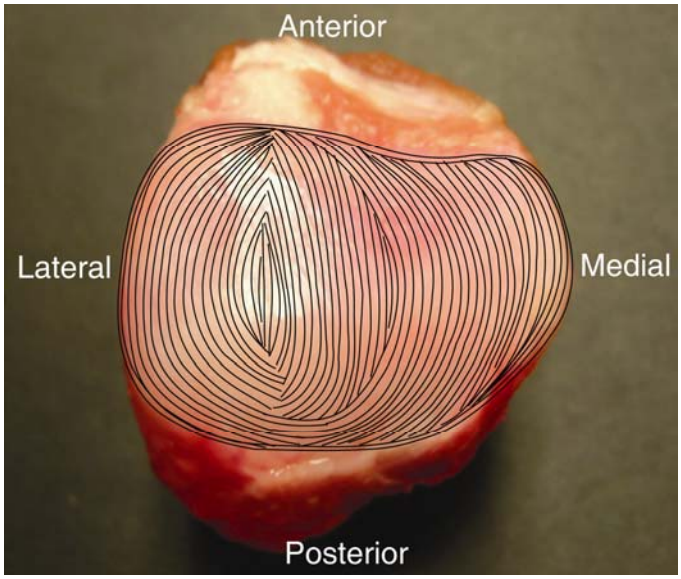

Figure 5.1: Superior view of a left porcine condyle, displaying the different regions of the condylar cartilage (A: Anterior, M: Medial, C: Central, L: Lateral, P: Posterior). The circles represent the locations from where cylindrical specimens of 5 mm diameter were prepared (shown to scale).

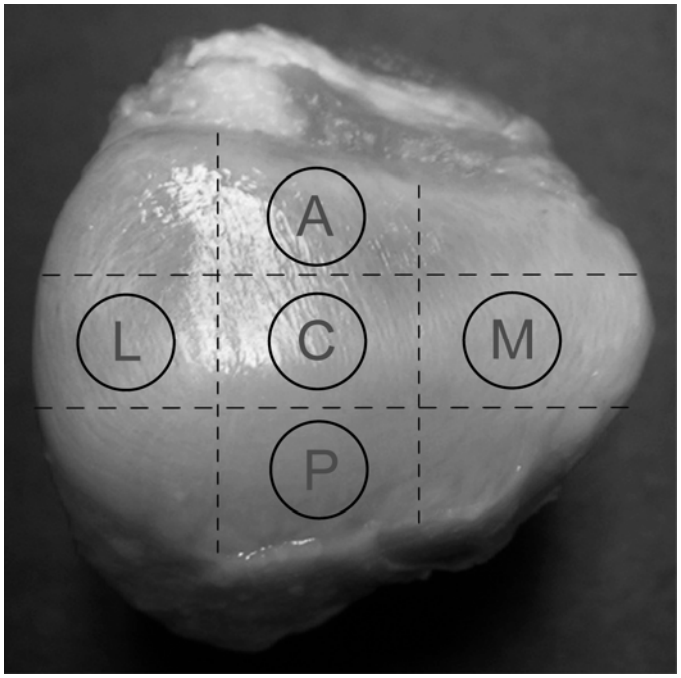

Figure 5.2: Photograph of the custom-built bath and compression platen assembly. Shown here is the bath (1) to which the lower compression platen (2) was affixed. The upper compression platen (3) was attached to the movable crosshead that carried a load cell (4) of 10 N capacity. The temperature was controlled using an immersion heater (5) and a temperature probe (6), both connected to a temperature controller.

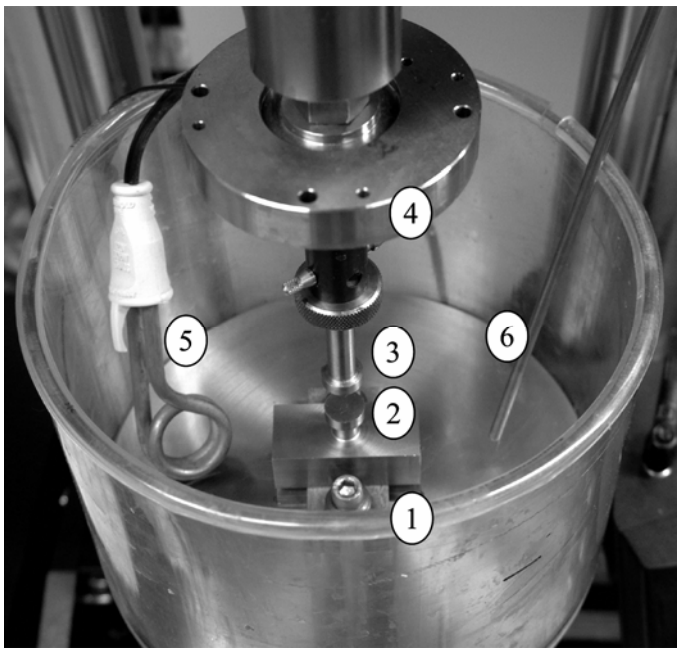

Figure 5.3: Typical stress-strain response of a condylar cartilage specimen, when compressed to 50% strain. The example curve provided here belongs to a specimen from the posterior region. The curve demonstrates a non-linear region extending to approximately 30% strain, followed by a linear region. The inset displays an enlarged view of stress-strain response for the initial strain values.

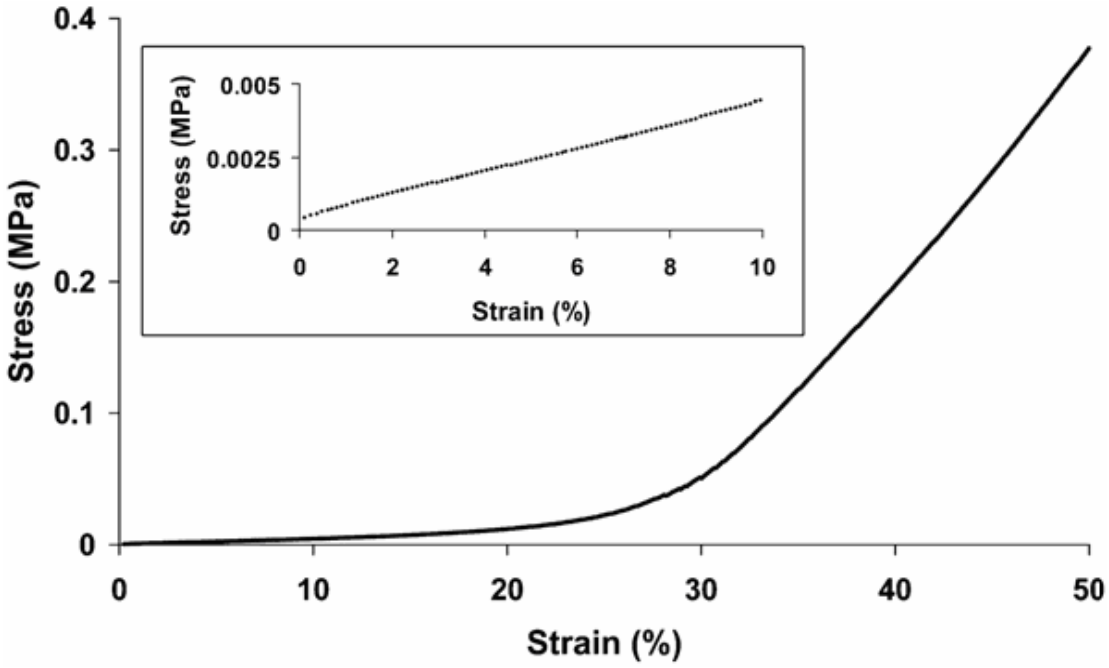

Figure 5.4: Example of a typical stress relaxation response curve-fitted to the linear viscoelastic models. The specimen provided here was from the posterior region. The Kelvin model could not provide a close fit for the entire data. Therefore, the Kelvin model was fitted to only the slow relaxation phase and was used to obtain the equilibrium modulus. Using this equilibrium modulus, the second order generalized Kelvin model provided a close fit to the experimental data.

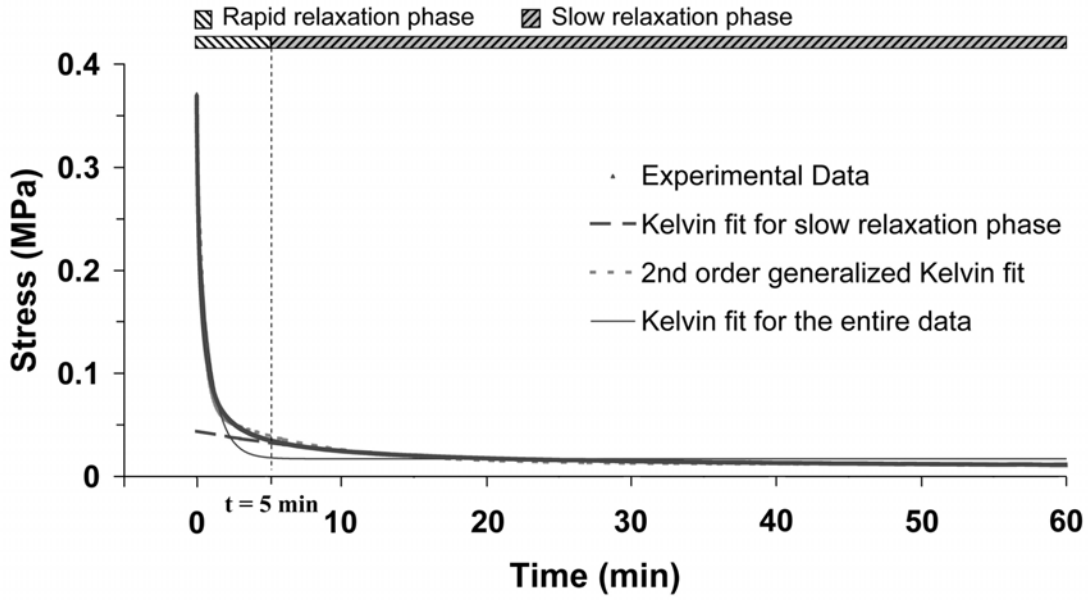

Figure 5.5: Additional compression tests conducted for the validation of the model. The data presented here corresponds to three specimens tested from the lateral region. Stress relaxation behavior was contrasted against the corresponding second order generalized Kelvin model, which displays the consistency of the model in predicting the relaxation behavior. The values were found to primarily lie within the upper and lower bounds set by the predicted model. It should be noted that there were breed and weight differences between the porcine tissues used in the original tests and validation tests.

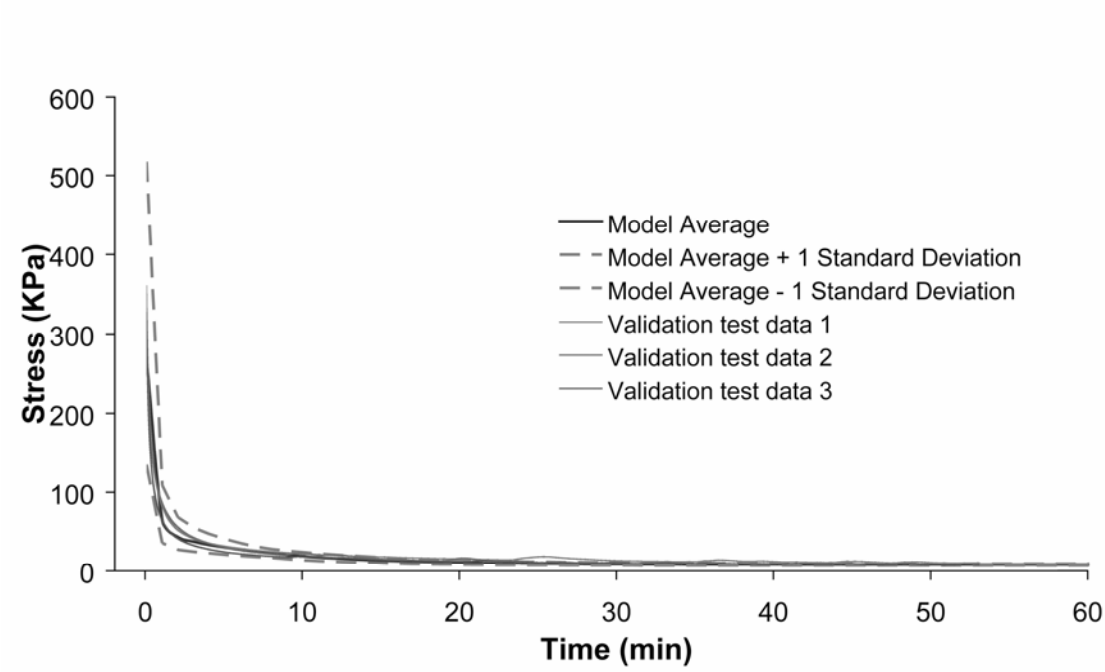

Figure 6.1: An over-simplified schematic of the design of the scaffold fabrication apparatus. The syringes (1), containing dye-loaded or blank microsphere suspensions in distilled water/PVA solution, were attached to two programmable syringe pumps. The suspensions were pumped in a predefined controlled manner through the attached tubings to a cylindrical glass mold (2). Through the bottom of the mold, the distilled water/PVA solution was constantly filtered, while the microparticles settled in the mold. At the end of the process, distilled water was completely pulled out using the vacuum pump, leaving microparticles stacked in the mold.

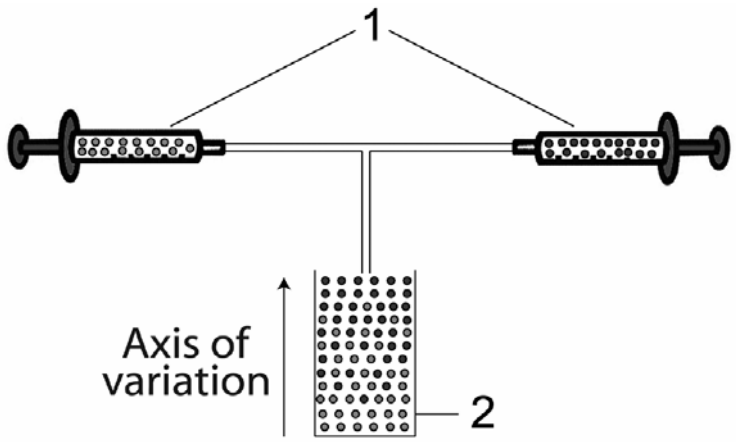

Figure 6.2: Specific flow profiles programmed into the two syringe pumps. The black line represents flow profile of Rhodamine B-loaded microspheres (A–D), and the gray line represents the flow profile of fluorescein-loaded (A–C) or blank (D) microspheres.

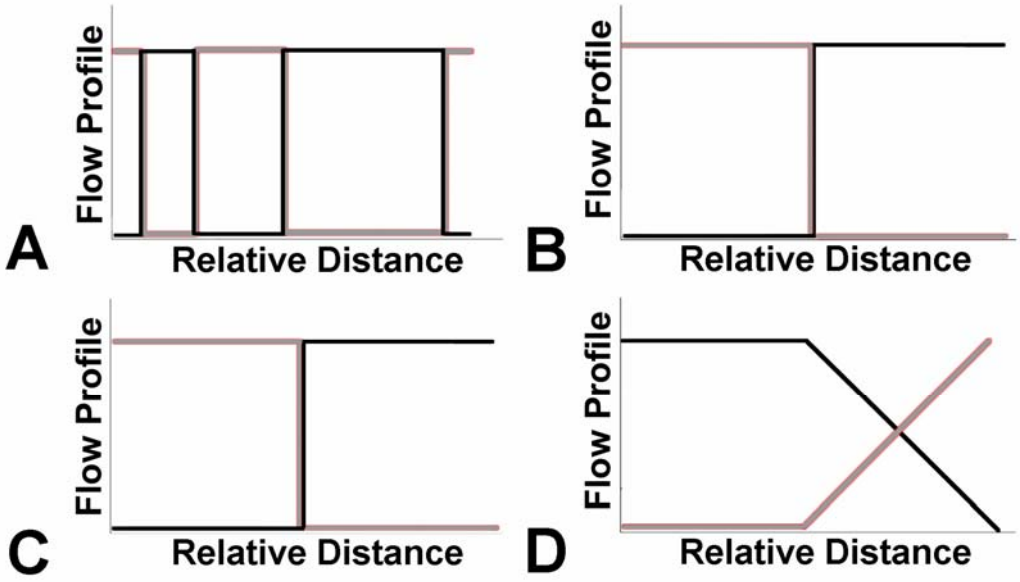

Figure 6.3: A) Coulter multisizer size distribution plot of PLG microspheres, displaying the monodispersity of the microspheres with a discrete peak at 220 μm. B) Scanning electron micrographs of the interior and exterior morphology of cryofractured microspheres.

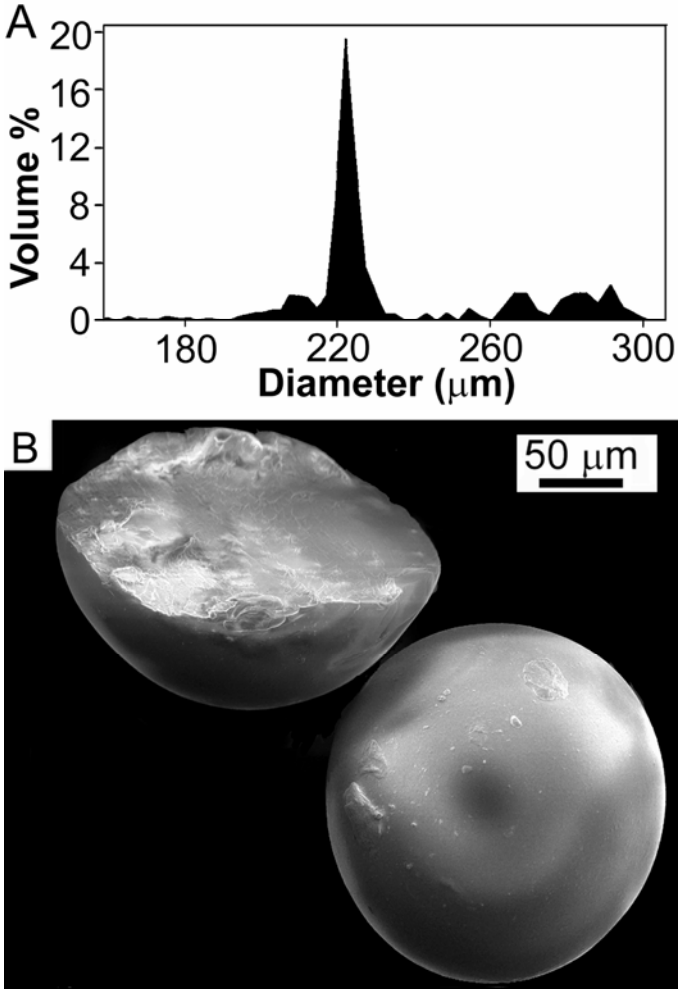

Figure 6.4: The near-perfect cylindrical geometry of bulk scaffolds (A) fabricated using blank microspheres of 220 μm diameter with 50 min ethanol soak time. Scanning electron micrographs of a scaffold fabricated using blank microspheres of 160 μm diameter (B–D), displaying the outside appearance of a bulk scaffold (B), the physical attachment of microspheres by ethanol (C) and interconnectivity of the pores (D).

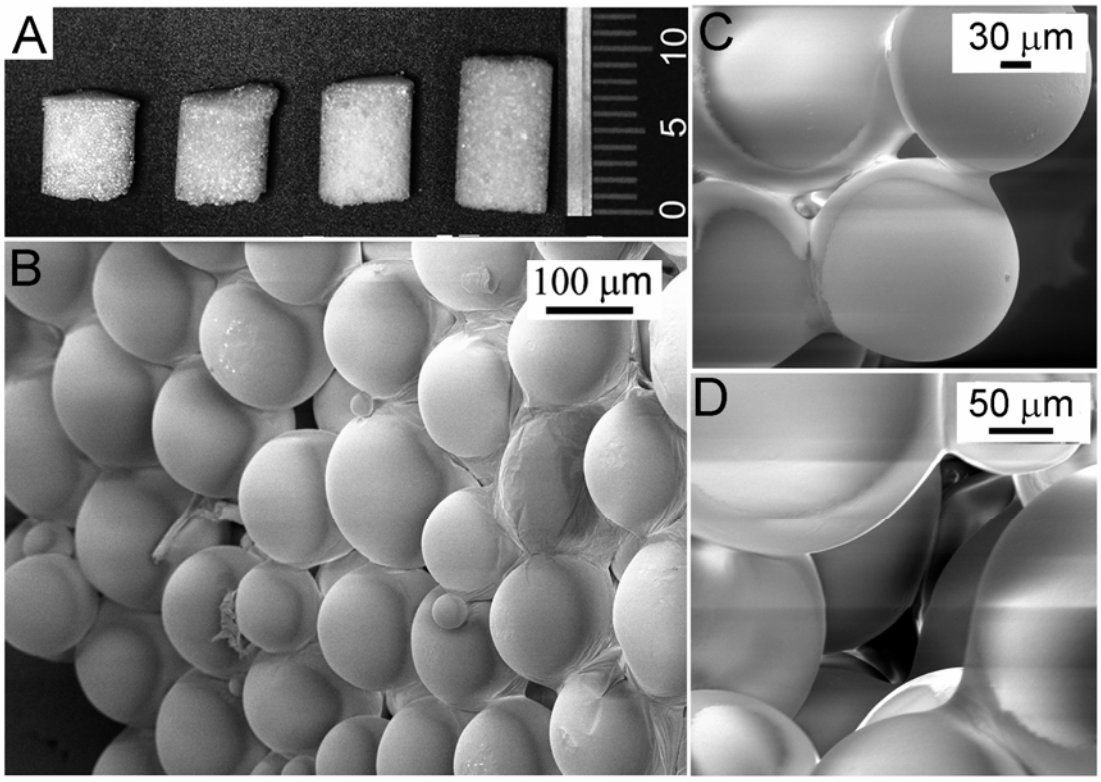

Figure 6.5: Scanning electron micrographs of scaffolds fabricated using blank PLG microspheres of 220 μm diameter with varying ethanol soak-times: 30 min (A, E), 1 h (B, F), 2 h (C, G) and 4 h (D, H). (Scale bar: 100 μm for A-D and 20 μm for E-H).

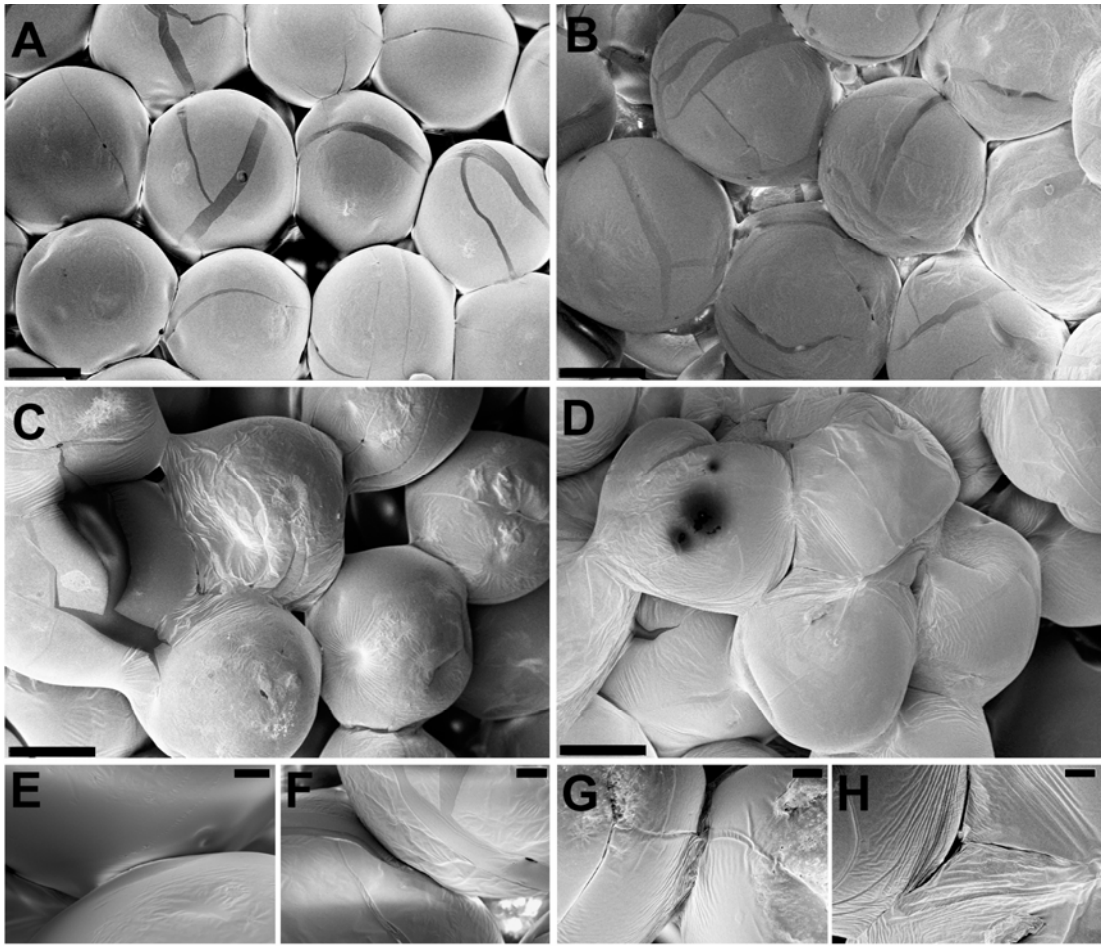

Figure 6.6: A) Characteristic stress-strain plot obtained from the compression of a scaffold prepared using a 1 h ethanol soak-time (see *Results – Fabrication and characterization of scaffolds*). B) Modulus of elasticity of the scaffolds prepared using varying ethanol soak-times (30 min, 1 h, 2 h and 4 h) (* indicates that the results were found to be statistically significant.) ($p < 0.05$).

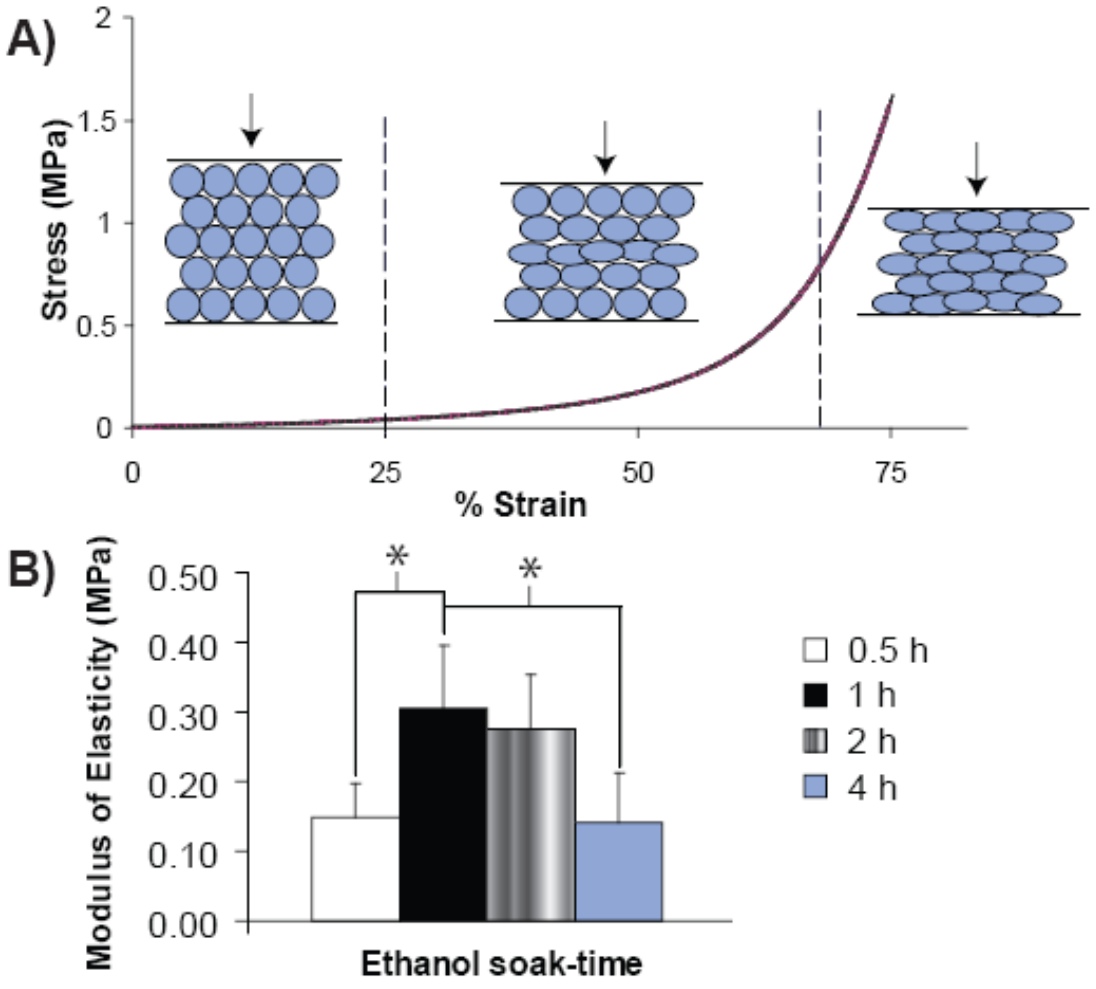

Figure 6.7: A) A representative three-dimensional microCT image of a scaffold (prepared using a 50 min soak-time). B) Top-view of the scaffold displaying a cross-sectional layer of microspheres.

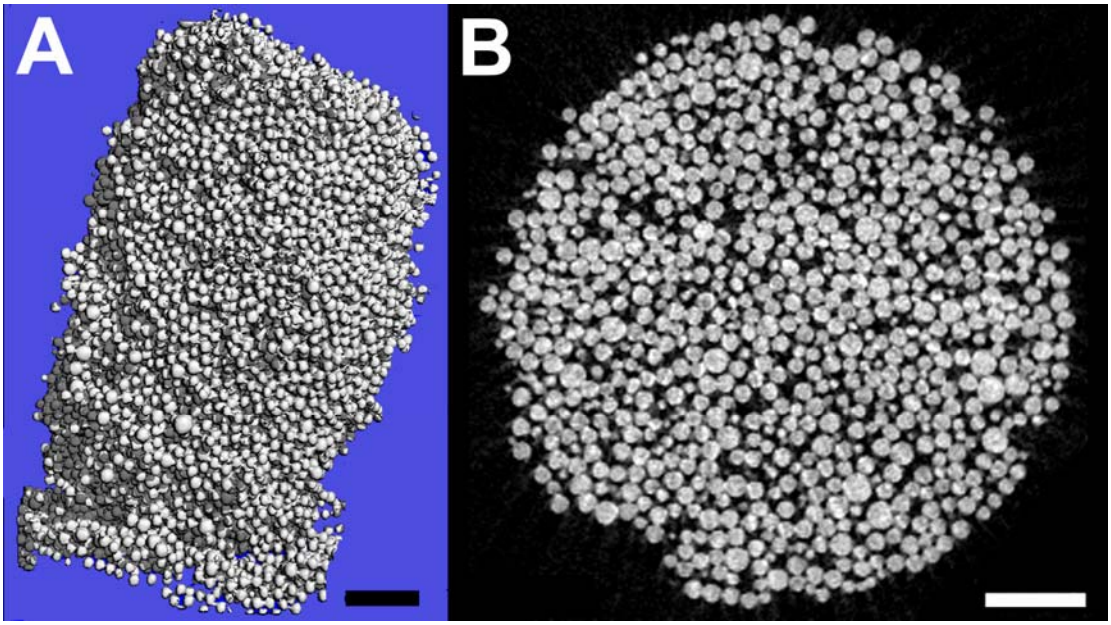

Figure 6.8: Fluorescence micrographs of "Live/Dead" dye-stained porcine chondrocytes seeded on scaffolds (50 min soak-time) following 18 day cell culture period – A) live cells, B) dead cells, and C) live and dead cells.

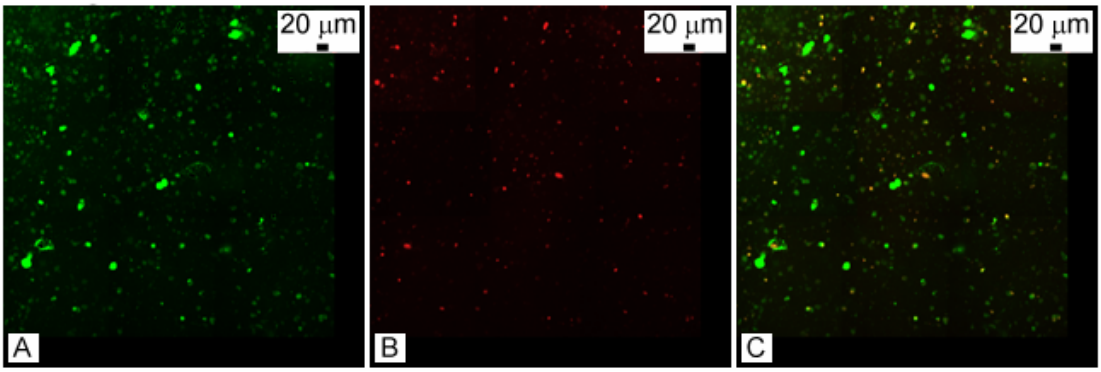

Figure 6.9: Concentration profiles of bi-layered, multi-layered and gradient scaffolds created using rhodamine B-loaded, fluorescein-loaded and blank microspheres (A–D). *Top row:* Rhodamine B-loaded microspheres (red) were transitioned into fluorescein-loaded (orange; A–C) or blank microspheres (white; D) using flow profiles described in Fig. 2. *Middle rows:* The scaffolds were imaged under UV light (365/254 nm). There was a characteristic change in appearance of fluorescein-loaded microspheres to blue color. *Bottom row:* Red pixels from the previous images were pseudocolored as white (A–C) or black (D) against a black background. The pseudocolored images were analyzed using ImageJ software to create relative intensity vs. relative distance plots (E–H corresponding to A–D, respectively).

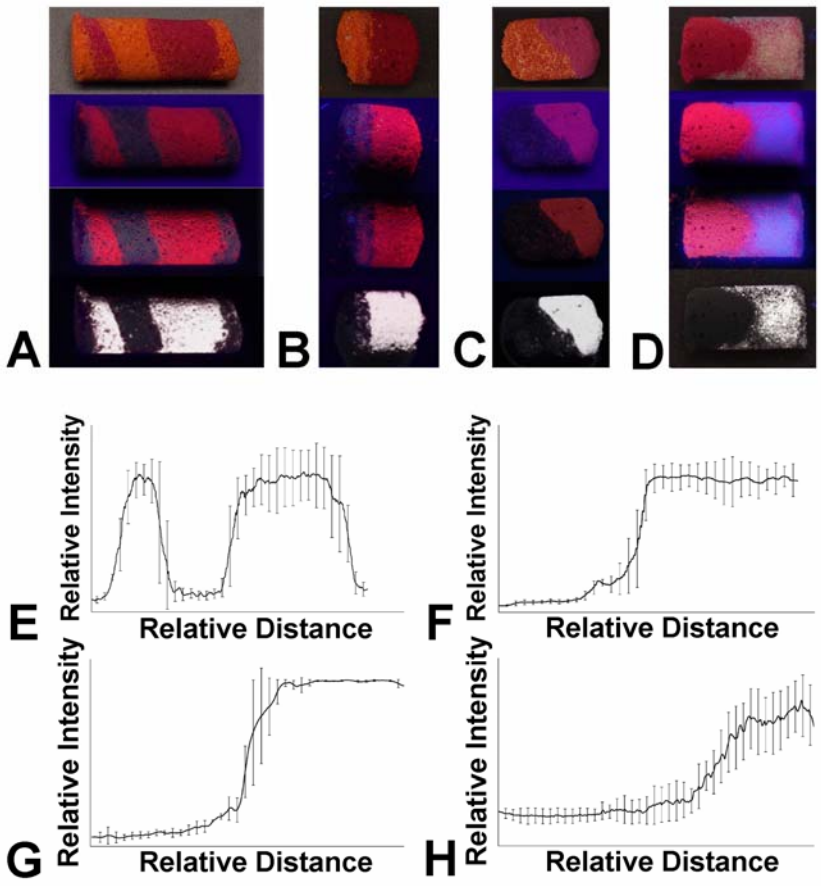

Figure 7.1: (A) Coulter multisizer size distribution plot of microspheres of different types (PLGA-$CaCO_3$/TiO_2) prior to lyophilizing, displaying their relative monodispersity and nominal sizes (average diameters: 130-175 µm) (peaks with % volume less than 0.5 have been omitted for the sake of clarity). (B-E) Morphological analysis of microspheres using scanning electron microscopy/energy dispersive spectroscopy (SEM/EDS). Panels B and D display representative SEM images of intact (left) and cryofractured (right) microspheres, corresponding to 90:10 PLGA:$CaCO_3$ and 90:10 PLGA:TiO_2, respectively. Panels C and E show the elemental distribution of the microspheres obtained using EDS, displaying an overlay of C, O, and Ca/Ti (left) and corresponding Ca/Ti distribution (right) (Panel C – cryofractured 90:10 PLGA:$CaCO_3$, color scheme C/O/Ca blue/red/green; Panel E – intact 90:10 PLGA:TiO_2, color scheme C/O/Ti blue/green/red). Scale bar: 20 µm (B-D) and 50 µm (E).

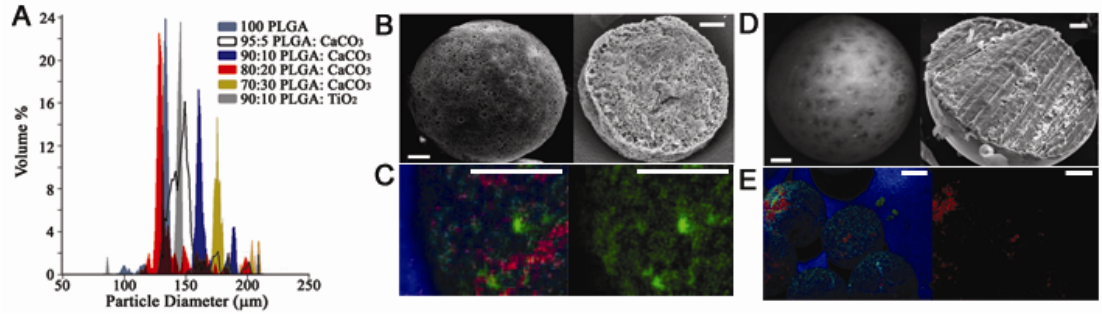

Figure 7.2: (A, B) Characteristic SEM micrographs of a scaffold, prepared by sintering the microspheres (90:10 PLGA:$CaCO_3$) using ethanol sintering, displaying the porous nature of the scaffold (A) and typical microsphere connection sites (B). Scale bar: 100 and 50 μm for A and B, respectively. (C, D) Live-dead images of human umbilical cord mesenchymal stromal cells cultured on these scaffolds for a period of 2 weeks, demonstrating high viability. The representative images of cells in a single plain (C) and a 100 μm thick section (D) were taken from an interior section of a scaffold. Scale bar: 100 μm (C).

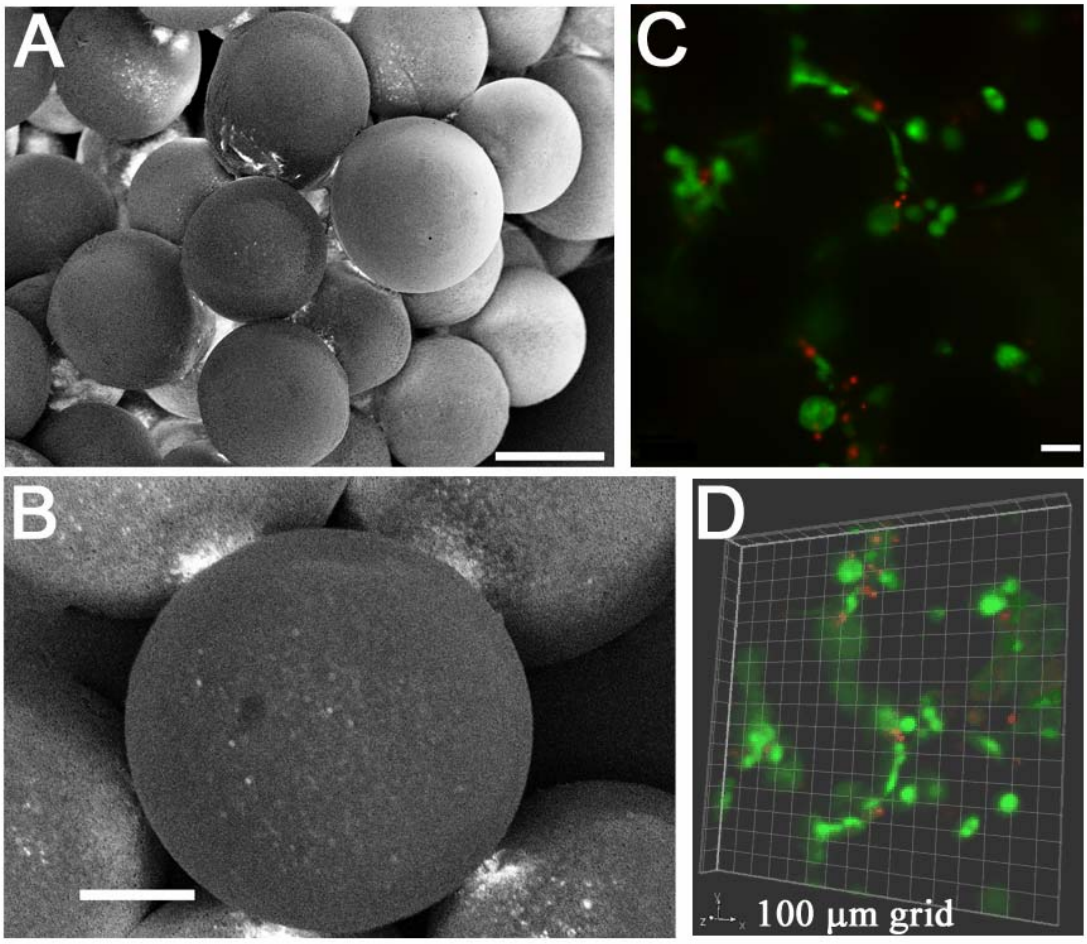

Figure 7.3: (A) A proof-of-concept gradient scaffold prepared using dye (Rhodamine B)-loaded PLGA microspheres and 90:10 PLGA:$CaCO_3$ microspheres using a 2 h ethanol soak. The image was taken under UV light using a UV lamp (254/365 nm; UVGL-25, UVP, Inc.) and a high-resolution camera, and analyzed using NIH ImageJ software to plot relative intensity as a function of pixel distance. (n = 5) (B) Moduli of elasticity of the homogeneous scaffolds prepared using different types of microspheres. The moduli were obtained from the initial linear regions of the stress-train curve: 1) at 25% strain (preceding the onset of pore-collapse for PLGA scaffolds), and 2) preceding the onset of pore-collapse, in general (at 40% strain for composite scaffolds). Surface modifications (see Fig. 1) that result due to the incorporation of nano-phase materials led to a decrease in the extent of sintering of the composite microspheres compared to the control PLGA microspheres for a 2 h ethanol-soak.

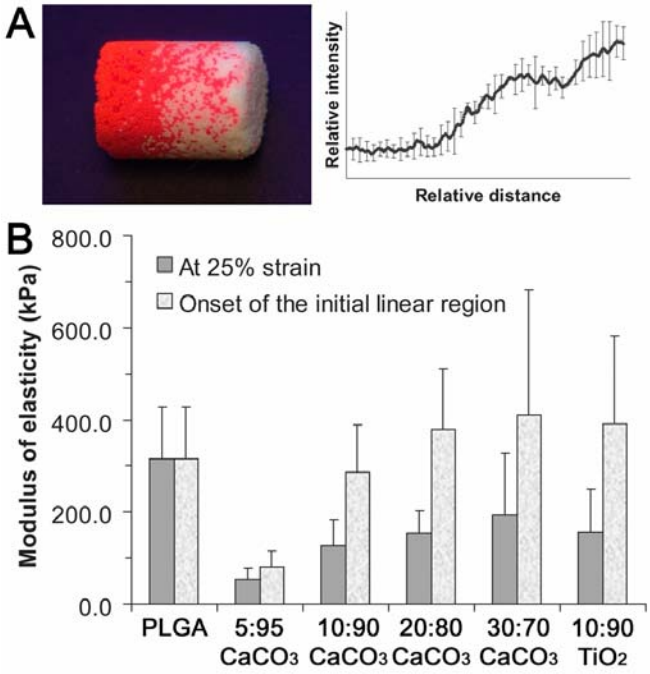

Figure 8.1: (A) Coulter multisizer size distribution plot of PLG microspheres of different nominal sizes used in these studies, displaying the monodispersity of the microspheres with discrete peaks (peaks with % volume less than 0.5 have been omitted for the sake of clarity). (B) An image of various shape-specific scaffolds that were produced with PLG microspheres (140 μm) using CO_2 at sub-critical conditions (15 bar for 1 h at 25°C followed by depressurization at ~0.14–0.21 bar/s) utilizing rubber molds of different shapes. From left to right: cylinder, bilayered cylinder, tube, plus-sign, and star.

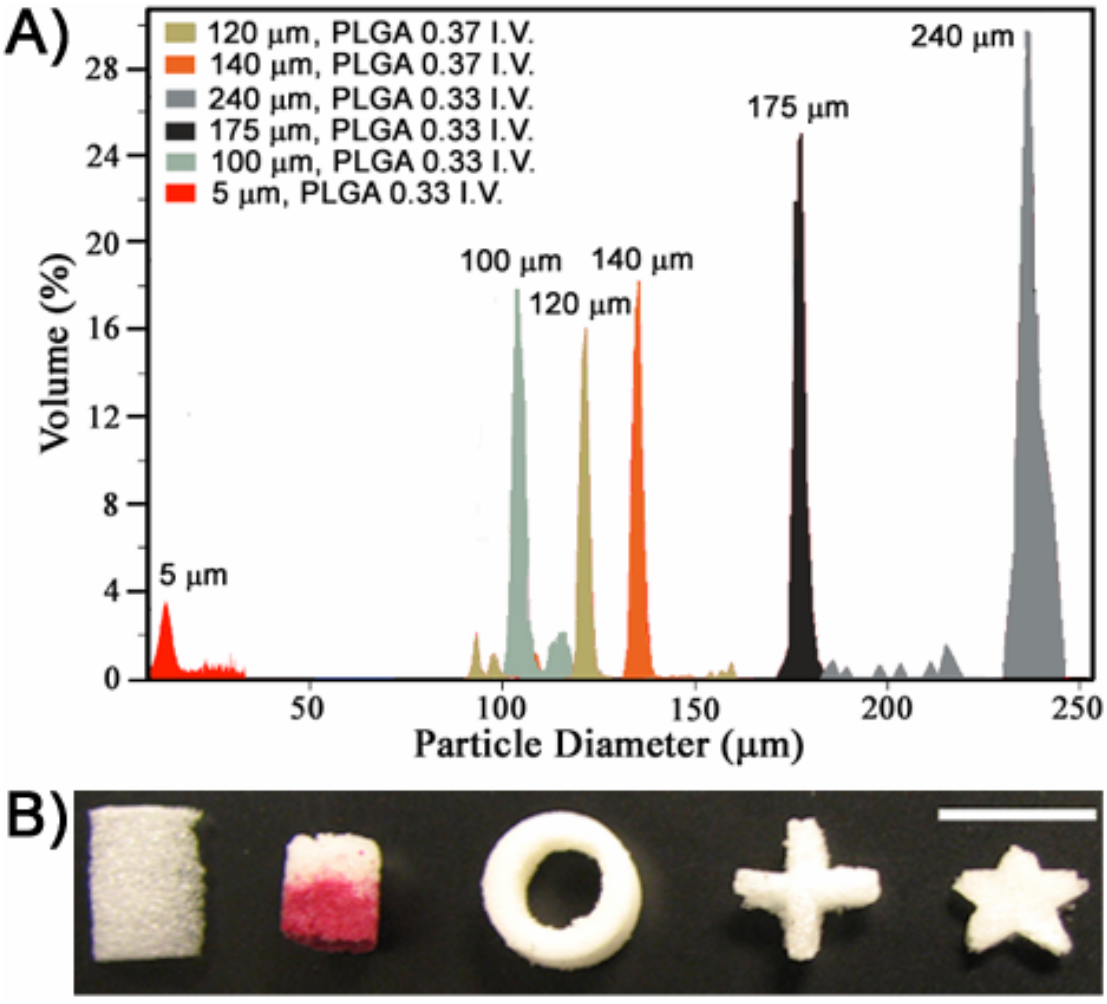

Figure 8.2: Characteristic scanning electron micrographs of scaffolds fabricated using different types of PLG microspheres at the typical processing conditions for sintering (CO_2 exposure at 15 bar for 1 h at 25°C followed by depressurization at ~0.14–0.21 bar/s). Sizes of the microspheres used were 240 μm (A, B), 175 μm (C), 140 μm (D, E), and (140 μm together with 5 μm) (F). The morphology of a microsphere following the CO_2 sintering (E) is also displayed, where enlarged images of the microsphere connection site (top panel) and sub-micron level surface modifications (bottom panel) are shown. The microspheres were made using PLG (with acid-end group chemistry) of either 0.33 or 0.37 dL/g intrinsic viscosity (i.v.) (see Fig. 1 and text). Scale bar: 100 μm unless labeled otherwise.

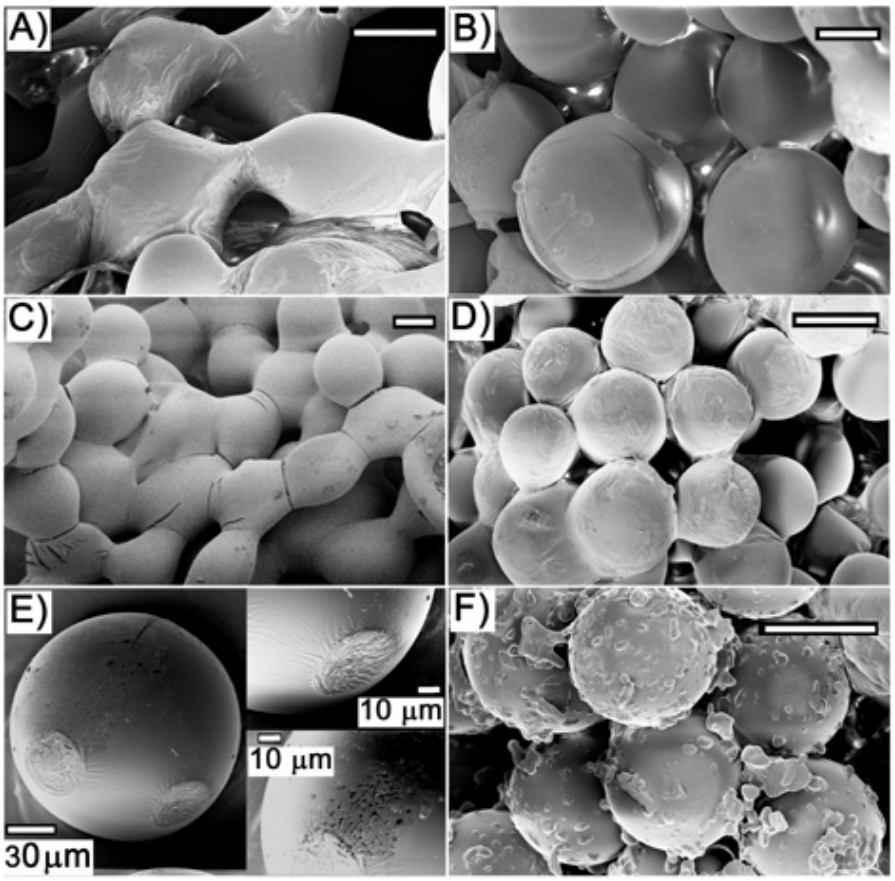

Figure 8.3: Modulus of elasticity of the scaffolds prepared using different microspheres sizes (corresponding to Fig. 1). The differences in the moduli were not statistically significant ($p > 0.05$).

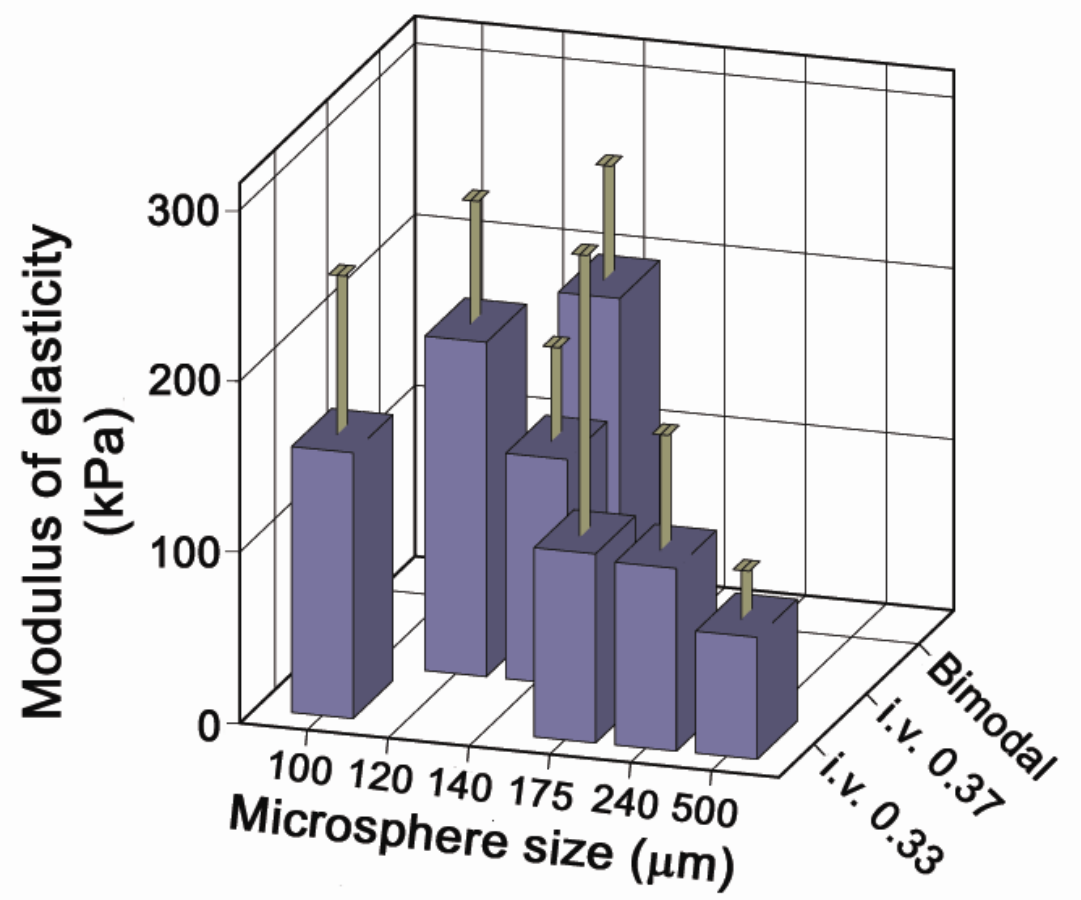

Figure 8.4: I. Fluorescence micrographs of Live/Dead dye-stained porcine chondrocytes seeded on scaffolds (175 μm) following a 3 wk cell culture period – A) live (green) and dead (red) cells, B) live cells only, and C) dead cells only. Scale bar: 100 μm. II. Immunohistochemistry for collagen types I and II (purple indicates positive stain) and Safranin-O staining for GAGs (orange indicates positive stain) at week 3 (n = 2). HUCMSCs = human umbilical cord mesenchymal stromal cells, CI = collagen type I, CII = collagen type II, and GAG = glycosaminoglycan. Scale bar: 100 μm.

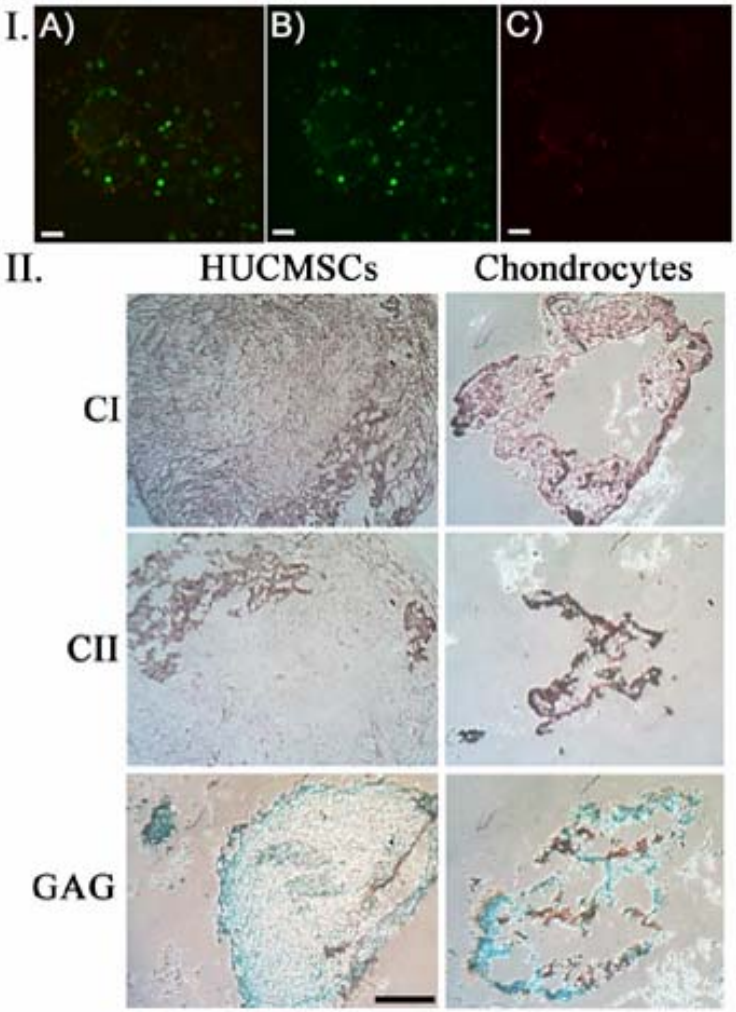

Figure 8.5: (A) A schematic of producing a microsphere-based cell-loaded scaffold or thin patch is shown. The process of combining the cells and microparticles in a liquid medium results in a melded thin patch (top), whereas mechanically mixing a loose cell pellet in a minimal liquid volume with the microparticles results in a homogeneously seeded scaffold. Scale bar: 6 mm. (B, C) Fluorescence micrographs of Live/Dead dye-stained HUCMSCs display cell survival during CO_2 sintering of microspheres (120 μm) at sub-critical conditions. Processing conditions (pressure, duration of exposure, depressurization rate, presence/absence of culture medium) for the production of the thin patch (B) and the macroscopic scaffold (C) were (30 bar, 2 min, ~0.21 bar/s, medium present) and (30 bar, 4 min, ~0.21 bar/s, medium absent), respectively. Green indicates live cells and red indicates dead cells. Note the dark circular areas, corresponding to the locations of the microspheres. Scale bar: 100 μm.

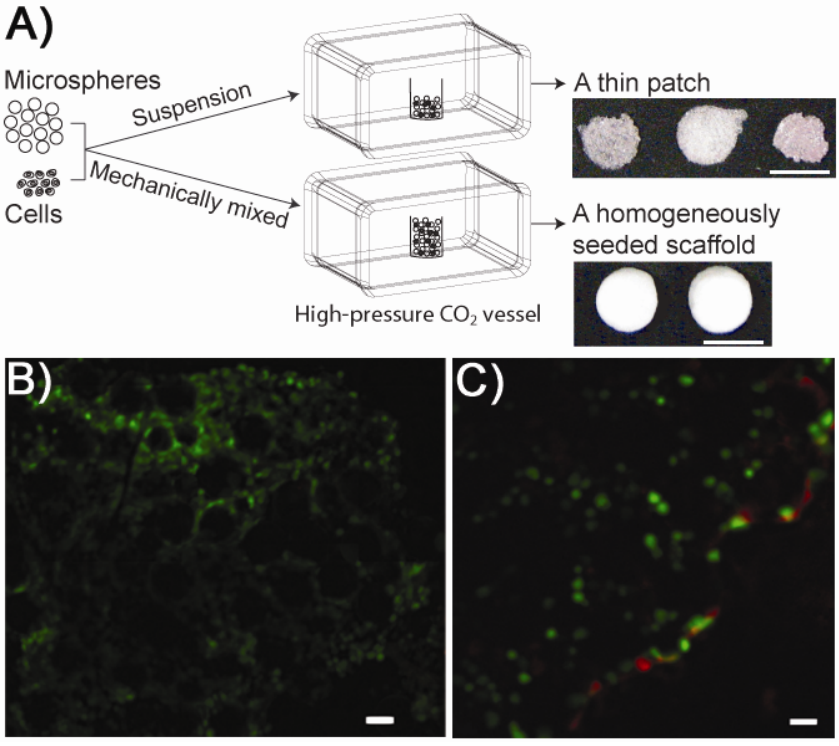

Figure 9.1: Cell number per construct at wk 0 and wk 6. Note that the cell number nearly doubled over the duration of the study. *Statistically significant difference ($p < 10^{-5}$). Error bars represent standard deviations.

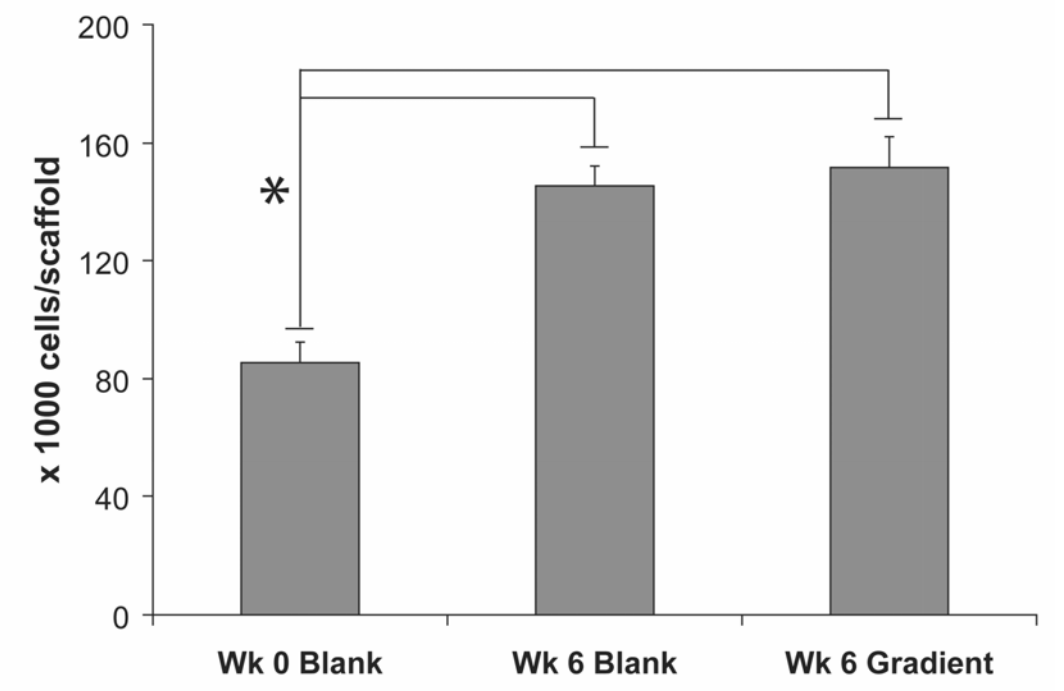

Figure 9.2: Glycosaminoglycan (GAG) content per construct at wk 0 and wk 6. The GAG content increased by ~6-7 fold over time, with a significantly higher content in the gradient scaffolds. *Statistically significant differences between wk 0 and wk 6. #Statistically significant differences between gradient and blank scaffolds at wk 6. Error bars represent standard deviations.

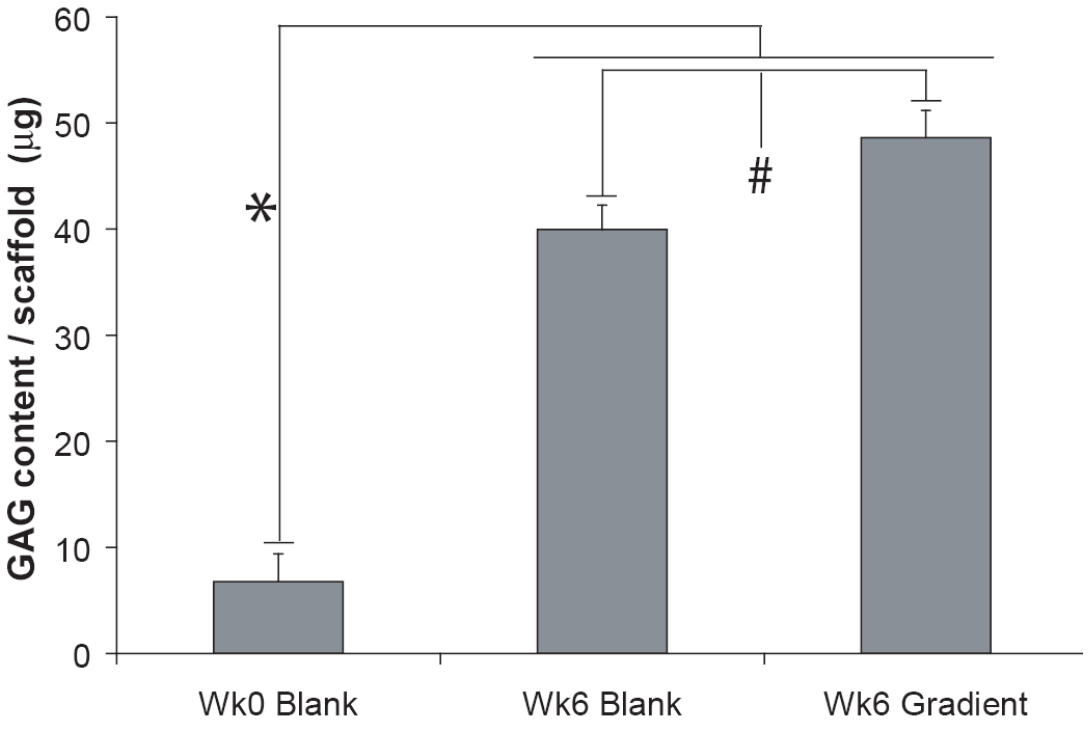

Figure 9.3: Moduli of elasticity and relaxed modulus of constructs at wk 6. The differences in the moduli were not statistically significant.

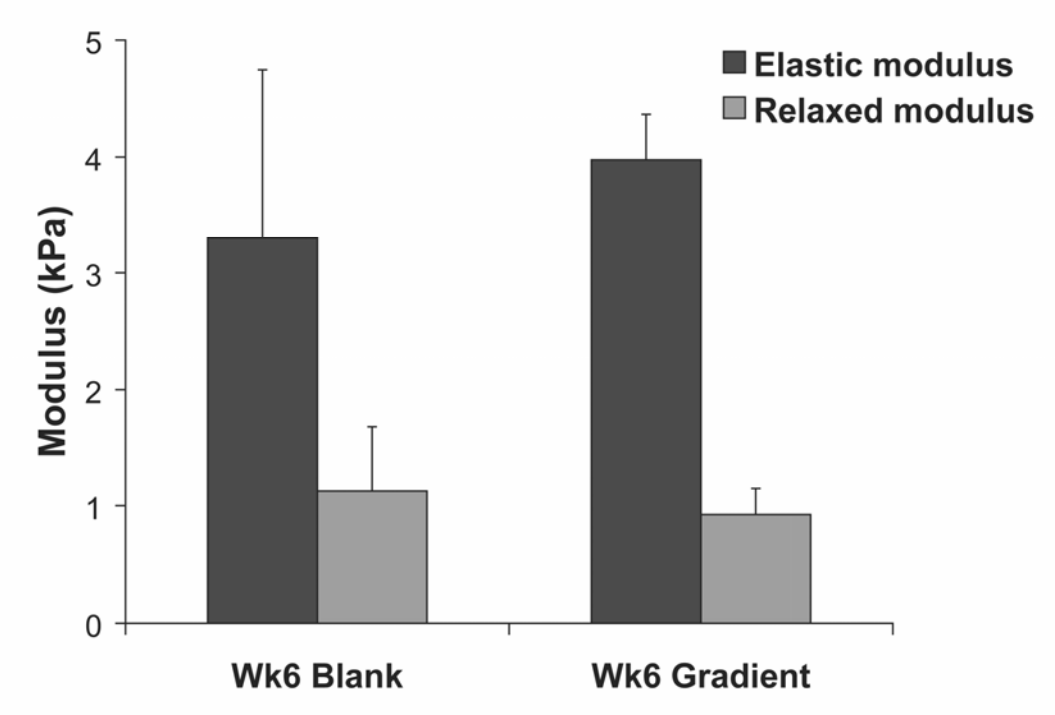

Figure 9.4: p-nitrophenol concentrations (nM)/min as a measure of ALP activity.

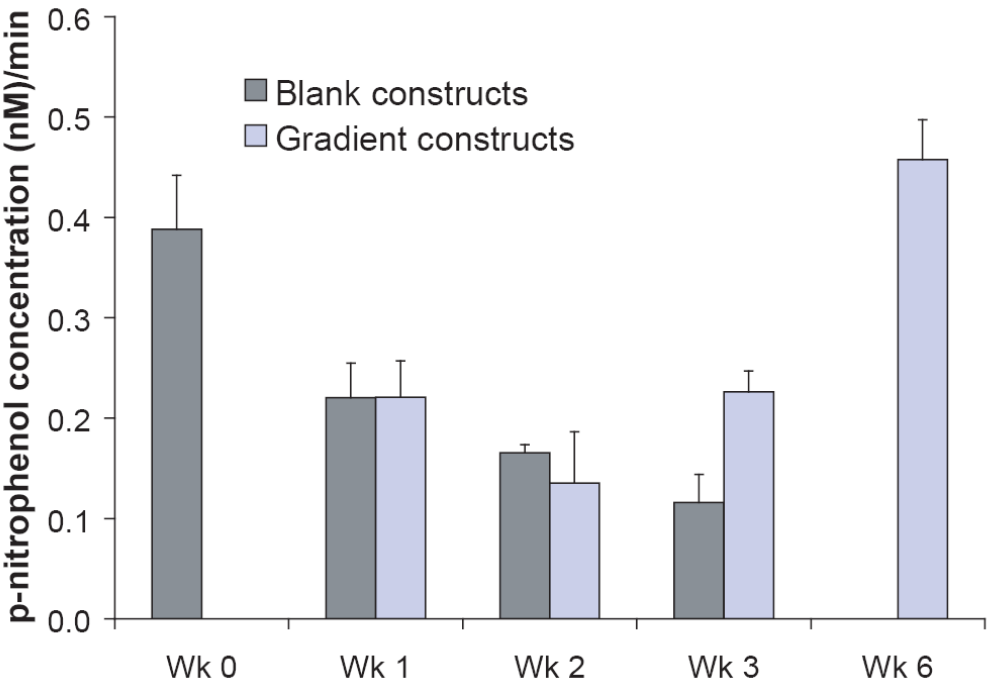

APPENDIX B: TABLES

- CHAPTER 1: n/a
- CHAPTER 2: Tables 2.1 – 2.5
- CHAPTER 3: Tables 3.1 – 3.6
- CHAPTER 4: Tables 4.1 – 4.2
- CHAPTER 5: Tables 5.1 – 5.3
- CHAPTER 6: Tables 6.1
- CHAPTER 7: Tables 7.1
- CHAPTER 8: n/a
- CHAPTER 9: n/a
- CHAPTER 10: n/a

Table 2.1. Mechanical properties of condylar cartilage under different testing modalities

Group	Sample	Method	Region[a]	Direction[b]	Loading profile	Specimens tested	Testing parameters		Mechanical properties[c]			Regional differences[d]	Species (Age)
Compression													
							Ramp stress (MPa)	Strain rate (mm/min)[i] frequency (Hz)	*Modulus of elasticity (Mpa)*	*Creep time constant (s)*	*Equilibrium modulus (MPa)*		
Kuboki *et al.*, 1997[e]	Cartilage-bone, entire cartilage intact	Indentation (creep)	A	Normal	Sustained	10	0.51 1.02 1.53	1.04/-	-	125.5 ± 23.3 112.5 ± 33.0 104.0 ± 28.8	2.684 3.591 4.751	-	Porcine (7 months)
					Intermittent	10	0.51 1.02 1.53	1.04/0.33[f]		146.5 ± 35.2 134.4 ± 15.0 139.8 ± 25.0	3.355 5 6.623		
							Ramp stress (MPa)	Frequency (Hz)	*Modulus of elasticity (MPa)*	*Poisson's ratio*	*Equilibrium modulus (MPa)*		
Hu *et al.*, 2001	Cartilage-bone, rectangular plugs	Atomic force microscopy	AM AL PM PL	Normal	Dynamic	18	-	14	2.34 ± 0.26 1.51 1.11 ± 0.07 0.95 ± 0.06	0.46 ± 0.05 0.41 0.38 0.31 ± 0.05	-	AM vs. others AL vs. others PM vs. others PL vs. others	Rabbit (6 weeks)
Patel & Mao, 2003	Cartilage-bone, rectangular plugs	Atomic force microscopy	AM PL	Normal	Dynamic	18	-	14	0.95 ± 0.15 1.02 ± 0.22	- -	-	-	Rabbit (7 days)
							Applied % strain range	Frequency (Hz)	*Dynamic complex modulus[g] (MPa)*	*Storage and loss moduli[g] (MPa)*	*Equilibrium modulus (MPa)*		
Tanaka *et al.*, 2006	Cartilage-bone, rectangular plugs	Indentation (dynamic)	AM AL PM PL	Normal	Dynamic	10	1 ± 0.2	0.01 - 10[h]	1.40 ± 0.39 1.15 ± 0.33 0.81 ± 0.21 0.73 ± 0.26	1.36 ± 0.38, 0.34 ± 0.07 1.12 ± 0.32, 0.24 ± 0.07 0.79 ± 0.21, 0.16 ± 0.04 0.72 ± 0.25, 0.16 ± 0.05	-	AM vs. PM AM vs. PL AL vs. PM AL vs. PL	Porcine (6-9 months)
Shear													
							% strain Amplitude	Frequency (Hz)	*Complex shear modulus[i] (MPa)*	*Storage and loss moduli[i] (MPa)*	*Equilibrium modulus (MPa)*		
Tanaka *et al.*, 2007	Cartilage-bone, rectangular plugs	Shear (dynamic), compressive strain (10%)	C	AP	Dynamic	10	1 2 3	0.01 - 10[h]	1.56 ± 0.27 1.82 ± 0.26 2.10 ± 0.33	1.50 ± 0.27, 0.41 ± 0.06 1.77 ± 0.26, 0.45 ± 0.06 2.03 ± 0.33, 0.51 ± 0.10	-	-	Porcine (6-9 months)
Tanaka et al., 2008	Cartilage-bone, rectangular plugs	Shear (dynamic), compressive strain (10%)	C	AP	Dynamic	7	1 2 3	0.01 - 10[h]	1.56 ± 0.27 1.82 ± 0.26 2.10 ± 0.33	1.50 ± 0.27, 0.41 ± 0.06 1.77 ± 0.26, 0.45 ± 0.06 2.03 ± 0.33, 0.51 ± 0.10	-	AP vs. ML	Porcine (6-9 months)
				ML		10	1 2 3		0.34 ± 0.08 0.43 ± 0.12 0.57 ± 0.10	0.33 ± 0.08, 0.09 ± 0.02 0.42 ± 0.11, 0.11 ± 0.03 0.55 ± 0.10, 0.15 ± 0.04			
Tension													
							Ramp strain (%)	Strain rate (mm/s)	*Young's modulus (MPa)*	*Ultimate tensile strength (MPa)*	*Equilibrium modulus (MPa)*		
Kang et al., 2000a	Cartilage-bone, rectangular plugs	Unidirectional tension	-	AP	Sustained	26	To failure	0.05	9.04 ± 1.73	2.92 ± 0.84	-	AP vs. ML	Porcine (10-14 months)
				ML					6.55 ± 1.24	2.15 ± 0.64			
							Ramp Strain (%)	Strain rate (mm/s)	*Young's modulus (MPa)*	*Stress relaxation time constant (min)*	*Equilibrium modulus (MPa)*		
Singh & Detamore, 2008	Cartilage, rectangular sections	Unidirectional tension (stress relaxation)	M C L A S P	AP ML	Sustained	7	20	0.1	21.7 ± 4.4 29 ± 13 22 ± 11 11.3 ± 7.9 8.7 ± 3.7 10.2 ± 4.5	38.5 ± 5.8 32.4 ± 8.2 42.5 ± 9.6 38 ± 12 40 ± 13 39 ± 19	6.2 ± 4.4 8.8 ± 4.1 7.3 ± 4.6 3.9 ± 3.5 3.6 ± 2.0 3.9 ± 1.9	AP vs. ML	Porcine (6 months)

[a] A: Ant, AL: Anterolateral, AM: Anteromedial, C: Central, L: Lateral, M: Medial, P: Posterior, PL: Posterolateral, PM: Posteromedial, S: Superior

[b] AP: Anteroposterior, ML: Mediolateral

[c] Mean ± standard deviation

[d] Regional and/or directional comparisons of stiffness values (complex, Young's or elastic modulus) that were found to be statistically significant, if any.

[e] The results tabulated here are obtained by comparing the function curve-fitted by Kuboki *et al.*, *i.e.*, A(1-exp(-t/ζ)), to the Kelvin model having the assumption that μ1 << μ0. The equilibrium modulus of elasticity reported has been calculated using the mean values of A.

[f] Intermittent compression of 1 second duration at 2 seconds interval

[g] Numerical values provided via personal communication, representing a frequency of 1 Hz

[h] Frequency sweep

[i] Corresponding to an excitation frequency of 2 Hz

Table 2.2. Fibril/fiber dimensions and major collagen types in condylar cartilage

Group	Specimen		Property	Results	Location [a]	Species (Age)	Method [b]
	Orientation	Region					
Appleton, 1975	Longitudinal, oblique and transverse	-	Elastic fiber diameter Elastic fibril diameter	350nm 8nm	All zones	Rats (20 & 80 days)	TEM
Klinge, 1996	-	-	Collagen fibril diameter Width of fiber layers	40-100nm 1-4µm	F	Monkeys	TEM
Mizuno *et al.,* 1990	Longitudinal (ML)	-	Collagen fibril diameter	30-100nm	F	Rats (3 weeks)	TEM
Shibata *et al.,* 1991	Longitudinal (ML)	-	Collagen fibril diameter	65nm 45nm 70-180nm	F P, M L	Rats (15 weeks)	TEM
			Collagen type	collagen I	F, L		IHC
Teramoto *et al.*, 2003	Longitudinal (AP)	Anterior and posterior	Collagen type	collagen II collagen X	M, H, PCM M, H, PCM	Rats (8 weeks)	IHC
Delatte *et al.,* 2004	Longitudinal (AP)	-	Collagen type	collagen I collagen II collagen III	F, P, M M,H F	Rats (neonatal)	IHC
Mizoguchi *et al.*, 1996	Longitudinal (AP)	Anterior, Superior & Posterior	Collagen type	collagen I collagen II	F, P, M, H M, H	Rats (4 weeks)	IHC
Milam *et al.,* 1991	Longitudinal (AP)	-	Collagen type	collagen I collagen II	F, P, M, H M, H	Baboons (9.5 years)	IHC
Berkovitz, 2000	Longitudinal (AP)	-	Mean crimp periodicity	19.4 µm	A	Human (4.5 to 58 years)	PLM & DIC

[a] A- Articular layer, F- Fibrous zone, P- Proliferative zone, M- Mature zone, H- Hypertrophic zone, L- Lacunar, UF- Upper fibrous zone, PCM- Pericellular matrix
[b] TEM- Transmission electron microscopy, IHC- Immunohistochemistry, PLM- Polarized light microscopy, DIC- Differential interference contrast microscopy

Table 2.3. Quantified values of extracellular matrix components in condylar cartilage

Group	Region	Condition	Properties	Values	Method	Dry/Wet weight?	Species (Age)
Pietila *et al.* , 1999	Anterior half	Normal	Total dry weight	2.6 mg	Density-gradient ultracentrifugation	Dry	Rabbits (25 days)
			Sulfated GAG content	~0.192 mg	Dimethylmethylene blue assay		
			Collagen content	165.7 nmol/mg [a]	Hydroxyproline assay		
Poikela *et al.* , 2000	Anterior half	Induced unilateral mastication [b]	Total dry weight	2.1 mg	Density-gradient ultracentrifugation	Dry	Rabbits (25 days)
			Sulfated GAG content	~0.154 mg	Dimethylmethylene blue assay		
		Normal [c]	Total dry weight	2.6 mg	Density-gradient ultracentrifugation		
			Sulfated GAG content	~0.181 mg	Dimethylmethylene blue assay		
Delatte *et al.* , 2004	-	Normal	Sulfated GAG content	6.4 ± 0.6 µg/mg	Dimethylmethylene blue assay	Wet	Rats (4 days)
			Collagen content	2.2 ± 0.3 µg/mg	Hydroxyproline assay		

[a] nmol hydroxyproline per mg of dry-weight guanidium chloride extractant

[b] 15 days unilateral mastication subjected to right condyles

[c] Controls from the same experiment

Table 2.4. Thickness data for healthy mandibular condylar cartilage

Group	Region	Location	Number of condyles examined	Thickness (mm) [a, b]	Specimen preparation	Method	Species (Age-range)
Hansson *et al.*, 1977	Mediocentral	Anterior	46	0.41 ± 0.14	Hematoxylin-eosin van Geison Toluidine Blue	Light microscopy	Human (1 day to 93 years)
		Superior	47	0.48 ± 0.18			
		Posterior	46	0.25 ± 0.17			
	Lateral	Anterior	36	0.37 ± 0.11			
		Superior	35	0.37 ± 0.15			
		Posterior	35	0.15 ± 0.11			
Bibb *et al.*, 1993	Central	Anterior	50	0.438 ± 0.191	Hematoxylin - triosin	Light microscopy	Human (16 to 38 years)
		Superior	50	0.507 ± 0.186			
		Posterior	45	0.322 ± 0.173			
Pullinger *et al.*, 1990	Medial	Anterior	49	0.39 ± 0.11	Hematoxylin - triosin	Light microscopy	Human (16 to 38 years)
		Superior	49	0.41 ± 0.14			
		Posterior	47	0.28 ± 0.17			
	Central	Anterior	53	0.40 ± 0.11			
		Superior	53	0.41 ± 0.14			
		Posterior	48	0.26 ± 0.16			
	Lateral	Anterior	45	0.38 ± 0.10			
		Superior	45	0.38 ± 0.14			
		Posterior	43	0.21 ± 0.11			
Bosshardt-Luehrs and Luder, 1991	Mediocentral & Lateral-central	Anterior	4	0.094 ± 0.007 F 0.053 ± 0.004 P 0.066 ± 0.007 M 0.066 ± 0.004 H 0.279 ± 0.022 O	Unstained	Radiography followed by morphometric image analysis	Monkey (14 months to 46 months)[c]
		Superior	4	0.131 ± 0.016 F 0.092 ± 0.012 P 0.096 ± 0.009 M 0.120 ± 0.011 H 0.439 ± 0.048 O			

[a] Mean ± Standard Deviation

[b] F: Fibrous zone, P: Proliferative zone, M: Mature zone, H: Hypertrophic zone (Endochondral ossification front excluded), O: Overall Thickness

[c] Corresponds to prepubertal age

Table 2.5. Macromechanical properties of the condylar part of retrodiscal tissue

Group	Test type (Load profile)	Specimens tested	Strain rate	Modulus of elasticity[a] (MPa)	Additional property[a]	Equilibrium modulus?	Species (Age)	Method	Model used
					Tensile stress (MPa) and % strain at fracture				
Kang *et al.*, 2000b	Tension (up to failure)	13	0.05 mm/s	4.35 ± 3.27	1.76 ± 1.01 & 95.25 ± 33.19	No	Human (8 15 years)	Uniaxial tensile test	Quasi-linear viscoelastic
					Time constant (s)				
Tanaka *et al.*, 2003	Tension (Step strain)	10	10% s^{-1}	2.08 and 4.30 [b]	30.5 and 39.1 (Stress relaxation)[b] 49.1 and 63.8 (Creep)[b]	No	Bovine (3 years)	Uniaxial tensile test	Standard linear solid
Tanaka *et al.*, 2002	Compression (Step strain)	10	50% s^{-1}	1.54 (Instantaneous) 0.21 (Equilibrium)	11.6 (Stress relaxation) 84.9 (Creep)	Yes	Bovine (10 years)	Unconfined compression	Standard linear solid

[a] Mean ± standard deviation

[b] The two values correspond to the two segments of the bilinear model.

Table 3.1. A summary of various forms of physical and chemical stimuli, gradients of which are known to provide a control over cell movement or "taxis" (adapted from Lo *et al.* [3] and Haga *et al* .[4])

Stimulus		Form of "-taxis"
Type	Form	
Chemical	Dissolved form	Chemotaxis
	Immobilized form	Haptotaxis
Physical	Substrate rigidity	Durotaxis/mechanotaxis
	Electrostatic potential	Galvanotaxis
	Light intensity	Phototaxis
	Gravitational potential	Geotaxis
	Extracellular tension	Tensotaxis

Table 3.2. Fabrication techniques used to prepare continuous macroscopic gradients in porosity and/or pore size in three-dimensional scaffolds

Gradient type	Fabrication method	Geometry/ Gradient direction	Materials used[a]	Primary gradient shape-controlling process parameter(s)[b]	Application	Ref.
Pore-size and porosity gradient	Centrifugation - heat sintering	Cylindrical/axial	PCL-pluronic F127	f(centrifugal speed) E.g., pore sizes ~88 to ~405 μm and porosities ~80 to 94% at 3000 rpm	To investigate the cell/tissue interaction with the scaffold in order to optimize the pore-size	107
	Centrifugation - freeze drying	Tubular/radial	Collagen-GAG	f(centrifugal speed, time) E.g., pore sizes <5 μm (at the wall) to ~20 μm (near the lumen) at 30,000 rpm for 15 min spinning time	"Mold-less" creation of tubular scaffolds; to study myofibroblast migration during peripheral nerve regeneration	117
	Phase separation (by temperature gradient-driven cryogenic treatment) - freeze drying	Cuboid-shaped/normal (in the direction of heat transfer)	Gelatin hydrogel (Chemically cross-linked)	f(cooling rate, temperature gradient) E.g., pore sizes 20-30 to 330 μm and porosities 61 to 82% for 30 °C temperature gradient at 0.15 °C/min cooling rate with 10% (w/v) gelatin	Gelatin scaffolds for tissue engineering with controllable pore-size, pore geometry and porosity	120
	Solid state polymerization - melt pressing - porogen leaching	Cylindrical/radial or axial	PGA	f(porogen content and porogen size) E.g., macroscopic pore size ~300 μm and microscopic pore size 0.3 μm	Scaffold that mimics natural bone	116
Porosity and material composition gradient	3-D printing (TheriForm™) - porogen leaching	A disc on a cloverleaf/axial	PLGA-PLA-TCP	Programmable porosity gradient: f(axial porogen content) (55 to 90%), pore-size: f(porogen particle diameter) 106-150 μm	Scaffold for osteochondral defect repair	115
Porosity gradient	3-D printing (TheriForm™) - porogen leaching	Disc/axial	PLGA with 20% β-TCP	Programmable porosity gradient: f(axial porogen content), pore-size: f(porogen particle diameter) 125-150 μm	A composite material for bone defect repair	118
Pore-size gradient	3-D fiber deposition technique	Disc/axial	PEGT-PBT	Programmable pore-size gradient: f(fiber deposition pattern) (200-1650 μm)	Scaffolds with anisotropic pore architecture to engineer cartilage with native zonal organization	114

[a]GAG: Glycosaminoglycan, PBT: Poly(butylene terephthalate), PCL: Poly(caprolactone), PEGT: Poly(ethylene glycol)-terephthalate, PGA: Poly(glycolic acid), PLA: Poly(lactic acid), PLGA: Poly(lactic-co-glycolic acid), TCP: Tricalcium phosphate

[b]Primary "gradient-controlling" parameter is the parameter investigated and found to have a profound effect over the gradient profile; the influencing parameters are reported as: f(process-dependent parameter(s)).

Table 3.3. Methods to create surface chemistry gradients on two-dimensional substrates including functional group gradients and oligomers/polymer-grafted surfaces

Method	Possible gradient controlling parameter(s)	Materials[a]			Gradient type(s) characterized	Bioactive or model factors used (if any)	Cell type(s) investigated (if any)[b]	Refs
		Grafted species	Substrate	Final graded functionality/surface characteristics				
Diffusive deposition (vapor or liquid phase adsorbent)	Diffusion controlling factors	dichlorodimethylsilane or other organosilanes (hydrophobic)	Hydrophilic substrates (Silicon dioxide, silica, quartz)	Hydrophobic (methyl groups) gradient on hydrophilic substrate	Functional group density, wettability	Fibroinogen, γ-globulin, lysozyme, kininogen, IgG	-	177-181
Grafting from initiator gradients generated via diffusion (ATRP and/or NMRP)[c]	Time, monomer concentration, temperature[α]	PAA/(PMM & PS) grafted from organisilane-based initiators	Silicon wafer	(-COOH) functionality	Polymer graft density, thickness, wettability	-	-	184,185
Continuous depletion of monomer solution (ATRP)	Monomer solution removal rate, MCl_2 concentration (governing reaction rate and polydispersity)[δ]	PMM, (PHEMA and PMM)	Silicon wafer with chemisorbed initiator	(-COOH) functionality	Molecular weight (orthogonal)**, thickness	-	-	184,186
Initiator gradient via diffusior - continuous depletion of monomer solution (ATRP)	(As mentioned above)[ε,&]	PDMAEMA, PHEMA	Silicon wafer	(-COOH) functionality	Polymer graft density & molecular weight (orthogonal)** (others, e.g., thickness, wettability)	Lysozye, fibronectin	Osteoblast-like cells	186,203
Thermochemical manipulation of aliphatic tert butyl ester functionalized SAM	Temperature(s), pH, nanoparticle colloidal solution properties	(-NR2) and(-COOH) functionalized polystyrene nanospheres	Au substrate with functionalized SAM	Nanosphere gradient (built on SAM containing -COOH gradient)	Functional group density, nanoparticle density	-	-	187
Density gradient method	Reactant concentration, reaction time (i.e., flow rates)	dichlorodimethylsilane or other organosilanes (hydrophobic)	Hydrophilic substrates (Silicon dioxide, silica, quartz)	Hydrophobic (methyl groups) gradient on hydrophilic substrate	Functional group density, wettability	Fibroinogen, IgG, lysozyme	-	182
Hyperthermal polyatomic ion deposition	Flurocarbon ($C_3F_5^+$) ion fluence ($ions/cm^2$)	Flurocarbon	PMM, PS	Fluorocarbon	Functional group density, wettability	-	-	183
Spatially varying electrochemical desorption/adsorption of alkane thiols	Applied potentials, time	Carboxylic acid-modified PS nanospheres	Au electrode with assembled amine-terminated alkane thiol layer	($-NH_2$) functionality translated into PS surface	Functional group density, nanopsphere surface density	-	-	143
Continuous immersion in NaOH solution	Immersion speed (time), temperature, $[OH^-]$	(hydrolysis of the surface groups)	PVC films	Carbonate (hydrophobic) and hydroxyl (hydrophilic) groups	Functional group density, wettability	-	Endothelial cells	142
Continuous immersion of gold substrate in alkanethiol solution	Immersion speed (time)	Methyl and hydroxyl terminated alkanethiol	Au coated Si wafers	($-CH_3$) or (-OH) groups	Functional group density, wettability	-	-	188
Continuous immersion in initiator solution (ATRP)	Immersion speed (time)	PHEMA	Si wafer	(-COOH) functionality	Functional group density	Fibronectin	Fibroblasts	176
Ultraviolet (UV) (or photo)-irradiation	UV properties, exposure time using a motorized stage, exposure intensity using a mask or filter[α]	Etching (ozonolysis)	Silane monolayer (on glass), Polymeric substrates (PCL)	Hydrophilic functionailities OH, -COOH)	Surface energy, wettability	Fibronectin	Osteoblast-like cells	148,149
		Etching (ozonolysis)	Silane monolayer on Si substrate masked with a elastomeric stamp	Hydrophilic (-COOH groups) gradient on hydrophobic SAM (methyl groups)	Surface energy, wettability	-	-	147
		BP-TEG-PE polymerization (using a heterobifunctional photolinker)/BP-RGD	Glass, alkanethiolate monolayer on gold-coated Si wafer	Model factor	Graft density, model factor	R-Phycoerythrin	-	164,165
		Graded pre-irradiation to induce -COOH functionality followed by PAAcid grafting	Polyethylene terephthalate	Model factor and -COOH functionality	Graft density, model factor	Laminin (covalently attached)	PC12 cells	144
		EBPDMA, TEGDMA	Glass	Functionality of casted polymers	Methacrylate conversion, mechanical properties	-	-	139
		MMA	SBDC monolayer on Si wafer	(-COOH) functionality	Graft density, thickness, model factor	RGD	Fibroblasts	163
Radio-frequency gas plasma discharge	Plasma composition, electrode-substrate gap width, power, time, exposure area using a graded or partially covering mask/exposure time using a moving mask, diffusion[β]	Peroxide initiators (surface oxidation or etching)	Polyethylene (inert), PDMS, PS, PTFE	Oxygen-based functionailities (such as, hydroxyl, ester, acid, ether, ketone, aldehyde groups)	Functional group density, surface energy, wettability	Constituents in blood, Albumin, IgG, fibrinogen	Platelets	150-153
		ppAAm and ppHEX (graft co-polymerization)	Glass	Hydrophobic alkane groups to hydrophilic allylamine groups	Thickness, functional group density, wettability	-	Fibroblasts	174
		ppAAm/octa-1,7-diene and ppAA (graft co-polymerization)	Glass	Amine/hydrocarbon and carboxyl functionalities	Thickness, functional group density, wettability	IgG	-	172,173,175
UV irradiation-plasma discharge	(As mentioned above)[α,β]	AA	Polymeric substrate	Hydrophilic (-COOH)	Functional group density, wettability	Serum proteins	Neurons	162
Power-graded corona discharge treatment	Substrate translation velocity, electrode-substrate gap width, power, time	Peroxide initiators (surface oxidation)	Polyethylene (inert)	Oxygen-based functionailities (such as, hydroxyl, ester, acid, ether, ketone, aldehyde groups)	Functional group density, wettability	Fetal bovine serum, Calf serum and NGF, Human albumin, Plasma proteins	CHO cells, fibroblasts, endothelial cells, PC-12 cells, platelets	154,156-159,161
		"	PLGA/ Polycarbonate	"	"	Fetal bovine serum	Fibroblasts	155,160
		PEO-MA	Polyethylene (inert)	PEO	Functional group density, wettability	Plasma proteins	Platelets	168,169
		AA/NaSS/DMAPAA (graft co-polymerization)	Polyethylene (inert)	Charged functionalities (AA/NaSS: -ve, DMAPAA: +ve)	Functional group density, charge density, wettability	Plasma proteins	CHO cells, platelets	170,171
		MAPC (graft co-polymerization)	Polyethylene (inert)	Groups with high phospholipid affinity	Functional group density, wettability	Plasma proteins, fibronectin	Platelets, fibroblasts	166,167

Table 3.3 (contd). Methods to create surface chemistry gradients on two-dimensional substrates including functional group gradients and oligomers/polymer-grafted surfaces

Method	Possible gradient controlling parameter(s)	Materials[a]			Gradient type(s) characterized	Bioactive or model factors used (if any)	Cell type(s) investigated (if any)[b]	Refs
		Grafted species	Substrate	Final graded functionality/surface characteristics				
Thin film casting (using knife-edge flow coating) followed by annealing	Polymer solution composition, annealing temperature(s) and time, knife-substrate gap width, coating velocity and acceleration	PS-b-PMM	Silicon wafer	PS (function of film thickness)	Thickness, nanostructure	-	-	194,195
Thin film casting followed by annealing (utilizing a temperaure gradient)	Annealing temperature(s) and time[δ]	PLLA	Silanized Si wafer	Functionality of casted polymers	Crystallinity, nanoscale-roughness	Fetal bovine serum	Osteoblast-like cells	196
	(As mentioned above)[δ]	PS	Silicon wafer	PS	Thickness and temperature (orthogonal)** (others, e.g., roughness)	-	-	204
Gradient mixing (with a 3-syringe pump system) - Thin film casting - Melt annealing	Sample collection rate, annealing temperature(s) and time, knife-substrate gap width, coating velocity[η]	PDLLA & PLLA	Glass	Functionality of casted polymers	Material composition, crystallinity, stiffness, roughness	-	Osteoblast-like cells	197,200
Gradient mixing - Melt annealing (utilizing a temperaure gradient)	(As mentioned above)[δ,η]	(PDLLA & PCL)/ (PS & PVME)/ (PLGA & PCL)	Glass, silicon wafer	"	Material composition and temperature (orthogonal)** (others, e.g., Chemistry, microstructure, crystallinity, roughness, hydrophillicity, stiffness, degradation rate)	-	Osteoblast-like cells, VSMCs	198,199, 201
UV (ozonolysis) treatment - Thin film casting -annealing	(As mentioned above)[α,δ]	PS-b-PMM with an underlying oxidized chlorosilane monolayer	Silicon wafer	(PS or PMM) (function of surface energy)	Surface energy and thickness (orthogonal)** (others, e.g., microstructure)	-	-	202
Electrostatic interaction (Continuous immersion of a charged substrate into a suspension of nanoparticles carrying the opposite charge)	Immersion rate/colloidal solution filling rate	anionic nanospheres (silica, gold, silver)	Poly(ethylene imine) coated Si wafer, Glass slide modified with cationic moeties	PLL-g-PEG-RGD coated nanospheres/protein conjugated nanospheres	Nanoparticle density gradient, nanostructure, nanoscale-roughness, protein gradient	Bovine serum almbumin, ephrin-A5, ephrin B1	Osteoblasts, hippocampal cells	190,191
Electrostatic interaction (Continuous immersion of a metal oxide substrate into a solution of polycationic polymer)	Immersion rate	PLL-g-PEG	TiO_2/Nb_2O_5	Functionality of grafted polymer, surface adsorbed protein	Polymer graft density, thicknesss, adsorbed or conjugated protein surface density	Human serum albumin, fibrinogen, IgG, blood serum and blood plasma	-	189

[a]AA: Acrylic acid, BP: Benzophenone, DMAPAA: N,N-Dimethyl aminopropyl acrylamide, EBPDMA: Ethoxylated bis-dimethacrylate, MMA: Methacrylic acid, MAPC: ω-methacryloyloxyalkyl phosphorylcholine, NaSS: Sodium p-styrene sulfonate, PAA: poly(acrylamide), PAAcid: Poly(acrylic acid), PCL: Poly(ε-caprolactone), PDLLA: Poly(D,L-lactic acid), PDMAEMA: Poly(dimethyl aminoethyl methacrylate), PDMS: Polydimethylsiloxane, PE: Polyethylene, PEO: Polyethylene oxide; PEO-MA: Polyethylene oxide-monomethacrylate, PHEMA: Poly(2-hydroxy ethyl methacrylate), PLGA: Poly(lactic-*co*-glycolic acid), PLL-g-PEG: Poly(L-lysine)-graft-poly(ethylene glycol), PLLA: Poly(L-lactic acid), PMM: Poly(methyl methacrylate), ppAA: Plasma polymerized acrylic acid, ppAAm: Plasma polymerized allylamine, ppHex: Plasma polymerized hexane, PS: polystyrene, PS-b-PMM: Polystyrene-b-poly(methyl methacrylate), PTFE: Poly(tetrafluoro ethylene), PVC: Poly(vinyl carbonate), PVME: Poly(vinyl methyl ether), RGD: (arginine-glycine-aspartic acid), SAM: Self assembled monolayer, SBDC: N,N-(diethyl-aminodithicarbamoylbenzyl(tri-methoxy)silane), TEG: Tetraethylene glycol, TEGDMA: Triethylene glycol dimethacrylate

[b]CHO: Chinese hamster ovary, PC-12: Pheochromocytoma, VSMCs: Vascular smooth muscle cells

[c]ATRP: Atom transfer radical polymerization, NMRP: Nitroxide mediated radical polymerization

Table 3.4. Gradient-based approaches highlighting current trends of application in implant desi

Application	Gradient type (transition type)	Fabrication method	Geometry - Gradient direction	Implant/coating thickness scale	Thickness scale of the gradient region or number of step transitions[a]	Materials used[b]	Ref
Bioceramic materials with bimodal pore structure for bone replacement	Porosity and pore size (step gradients)	Differential impregnation - heat sintering	Cylindrical - axial	≥ mm	1 transition	HA and a cellulosic sponge	221
		Dip casting - vacuum impregnation - stiching/press fitting	Cylindrical - radial	≥ mm	1 transition	HA/TCP and polymeric foams	209
		Multiple slip-casting - heat sintering	Cylindrical - radial	≥ mm	1 transition	HA, PVC and Li_3PO_4	222
		Multiple tape-casting - sintering - heat induce removal of porogens	Bar or disc - Axial	≥ mm	4 transitions	HA, PBMA	223
Graded orthopaedic replacement to reduce stress-shielding	Porosity and stiffness (step gradients)	Liquid phase sintering	Bar - longitudinal	≥ mm	2 transitions	Ti, Si powder	220
UHMWPE wear resistance (for total joint arthroplasty, etc.)	Cross-linking density (continuous gradients)	Irradiation (low energy electron beam)	Finished acetabular liner - radial	≥ mm	mm	UHMWPE	218
		Melt-irradiation (low energy electron beam)	Hemispherical - radial	≥ mm	mm	UHMWPE	217
	Material composition [diffusion-based IPN[c]] (continuous gradient)	Swelling at elevated temperature with ultrasonics	-	> monolayer	-	UHMWPE, PLL	219
Bioceramic coatings on metallic implants	Material composition (step gradients)	Plasma spray	-	660 μm (coating thickness)	3 Transitions	HA, Ti-6Al-4V, TCP/TiO_2	212
		Plasma spray	-	-	3 Transitions	HA, Ti	211
	Material composition (continuous gradients)	Plasma spray	-	100 μm	40 μm	HA, Ti	207
Bioceramic-polymer based skull implant (e.g., calvarial defect repair)	Material composition and porosity (Step gradients)	Hot pressing - gas foaming	Custom (CAD/CAM assisted)	~ cm	4 transitions	PLA, $CaCO_3$, $Ca_3(PO_4)_2$	224
Bioceramic-polymer intervertebral disc prosthesis	Material composition (continuous gradient)	Centrifugation	Cylindrical - radial	≥ mm	across the sample (100%)	HA, polycarbonate-urethane	225
Polymeric coatings on metallic implants	Material composition (step gradients)	Dip coating	-	1 mm (coating thickness)	2 transitions	Ti, PLA, HA, $CaCO_3$	213
Gradient surface treatment of metallic implant to improve biocompatibility/osteoconductivity	Material composition (Sodium titanate and apatite) (Continuous gradient)	Sodium hydroxide treatment - heat treatment	-	≥ mm	Nano scale	Ti-6Al-4V, Sodium titanate	214
	Material composition (apatite) (step gradient)	Sol-gel and slurry dip coating - drying and sintering	-	< 100 μm	3 transitions	ZrO_2, HA, Fluorapatite	215
	Degree of oxidation (porous outer layer- dense inner layer) (Continuous gradient)	Electrochemical oxidation (Pre-anodic oxidation - Micro-arc oxidation)	-	16 μm (coating thickness)	< 1 μm (nano scale)	Ti, TiO_2	216
As a fast-screening tool for biocompatibility assessment of the metallic implants	Material composition (step and continuous gradient)	Sedimentation/Powder packing - sintering (furnace/high frequency induction heating/spark plasma sintering)	Cylindrical - axial	≥ mm	(see the articles for details)	Ti, HA (and others)	227,228
	Material composition (step gradients)	Powder packing - hot isotactic pressing	Bar	≥ cm	9 transitions	Ti, Ni	226

[a] For continuous gradient approaches, % thickness of the gradient region compared to the overall thickness of the structure is indicated. To elilminate/reduce interfacial stresses that may cause delamination, a higher % value of the thickness of the gradient region compared to the overall thickness of the implant/coating can be selected. However, one must also take the envisioned application into consideration. Some of the studies utilized step gradients, where dual/multiple layers were present having sharp (discontinuous) interfaces in between. The diffusive effects may have led to a blurred region at the interface; however, we do not treat it as a continuous gradient unless measured. Studies, where multi-layered structures were created and the overall gradient region comprised of several step transitions that spanned the entire implant/coating, are marked by the number of such transitions.

[b] HA: Hydroxyapatite, PBMA: Poly(butylmethacrylate), PLA: poly(lactic acid), PVC: Polyvinyl polyacrylate, TCP: Tricalcium phosphate, UHMWPE: Ultra high molecular weight polyethylene

[c] IPN: Inter-penetrating network

Table 3.5. Example studies involving concentration/surface density gradients of peptides, proteins or other model factors for tissue engineering

		Gradient type						
Factors[a]	2-D/3-D	Profile	Soluble/ Immobilized	Materials used to incorporate the factor[b]	Notes	Application	Cell type investigated[c]	Ref
CAMs/Peptides								
RGD-containing peptides	2-D[d]	Linear	Immobilized (covalently bound)	Poly(acrylic acid), Poly(methacrylic acid) (photoiniferter SAM), Poly(ethylene glycol)	Acryloyl derivatization to induce photopolymerization	Controlled cell adhesion, alignment, and motility (temporally and spatially)	Fibroblasts, endothelial cells	140,163, 251,253
	3-D	Non-linear	Soluble	Collagen or fibrin gel	-	Styding chemotaxis	Fibroblasts	254
IKVAV	2-D	Linear	Immobilized (covalently bound)	Polystyrene substrate	Benzophenone derivatization to induce photopolymerization	Probing axon guidance	DRG neurons	261
Laminin	2-D	Linear	Immobilized (Adsorbed or covalently bound)	Glass/Poly-L-Lysine coated-substrate, Carboxy-terminated alkathiol monolayer on gold	-	Probing neurnal development and axon guidance, Cell migration	Hippocampal neurons, Intestinal IEC-6 cells	244,246, 266
	2-D	Sigmoidal	Immobilized	Polyethylene terephthalate	Carbodiimide chemistry	Probing axon guidance	PC12 cells	144
	3-D	Quadratic	Immobilized (covalently bound)	Agarose	SANPAH (hetero bifunctional crosslinker) Photoreactive perfluoro arylazide group	Improved neurite ougrowth and nerve regeneration in 3-D environment	DRG neurons, sciatic nerve regeneration (in vivo)	245,250
Fibronectin	2-D	(Function of alkyl chain length)/ Sigmoidal	Immobilized (adsorbed)	ω-methacryloyloxyalkyl phosphorylcholine grafted PE/ Poly(2-hydroxyethyl methacrylate)	-	Manipulating cell adhesion and spreading	Fibroblasts	167,176
Growth factors								
EGF	2-D	Custom	Immobilized (covalently bound)	Azidophenyl-derivatized poly(allylamine)-coated polystyrene	Azidophenyl derivatization	Concentration dependent effects of immobilized biosignals on cellular mobility and localization, artificial juxtracrine simulation	Chinese hamster ovary cells	255
bFGF	2-D*	Linear	Immobilized (covalently bound)	Poly(ethylene glycol)	Acryloyl derivatization to induce photopolymerization	Directed cellular migration and alignment	VSMCs	252
NGF	3-D	Custom/Linear	Soluble	Collagen gel/Agarose gel	-	Axonal guidance, studying chemotaxis and morphogenesis	DRG neurons/PC12 cells	242,249
		Linear	Immobilized (entrapped)	Poly(2-hydroxyethyl methacrylate)	-	Axonal guidance	PC12 cells	247
NGF and NT3	3-D	Linear	Soluble	Agarose	-	Axonal guidance	DRG neurons	243
	3-D	Linear	Immobilized (entrapped)	Poly(2-hydroxyethyl methacrylate)	-	Axonal guidance	DRG neurons	248
Model proteins and others								
Human serum albumin/FMLP/ AGG	2-D	Non-linear/Linear /Linear	Soluble	Culture medium	-	Studying chemotaxis	Polymorphouclear leukocytes/Neutrophils	256,258, 260
cAMP	3-D	Linear	Soluble	Agarose gel	-	Studying chemotaxis	*Dictyostelium discoideum* Amoebae	259
ZAS	3-D	Linear	Soluble	Agarose gel	-	Studying chemotaxis	Leukocytes	257
Casein-b	3-D	Custom	Soluble	Collagen gel	-	Axonal guidance, studying chemotaxis and morphogenesis	-	263
HRP	3-D	Linear	Immobilized	Silk fibroin	Carbodiimide chemistry	Chemotaxis, tissue engineering, biosensors	-	271
R-phycoerythrin	2-D	Linear	Immobilized	Polystyrene substrate	Carbodiimide chemistry, benzophenone derivatization	Probing biological responses	-	165
Fluorescent dye, antigens and/or antibodies	2-D	Custom	Soluble/surface adsorbed	PDMS	-	Chemotaxis, haptotaxis, etching, nucleation and growth, Marangoni effects, antibody-antigen binding		267,272

[a] bFGF: Basic fibroblast growth factor, cAMP: 3'-5'-cyclic adenosine monophosphate, CAMs: Cell adhesion molecules, EGF: Epidermal growth factor, HRP: Horseradish peroxidase, NGF: Nerve growth factor, NT-3: Neurotrophin-3, RGD: Arginine-glycine-aspartic acid, SANPAH: Sulfosuccinimidyl-6-[4'-azido-2'-nitrophenylamino] hexanoate, ZAS: Zymosan activated serum

[b] PDMS: Polydimethylsiloxane, PE: Polyethylene, SAM: Self-assembled monolayer

[c] DRG: Dorsal root ganglion, PC12: Pheochromocytoma, VSMCs: Vascular smooth muscle cells,

[d] Some of these studies (e.g., Delong *et al.* (156)) employed the techniques that were capable of generating gradients of immobilized factors in 3-D. However, cellular interactions were monitored on the surfaces of the gels (i.e., in 2-D).

Table 3.6. Methods to create surface density/concentration gradients of peptides and proteins for tissue engineering applications

Fabrication Technique	Process driving phenomenon (-a)	Additional processing	Primary gradient-shape controlling parameter(s)	Gradient-scale	2-D/3-D	Gradient-shape control?	Refs
Soluble factor gradients							
Boyden/Zigmond/Dunn Chambers	Diffusion (in solution)	-	Time	Macroscale	2-D[a]	Limited	256, 258, 260
Single source/chamber (of bioactive factor) approaches	Diffusion (in macroporous gels)	-	Time	Macroscale	3-D	Limited	254, 264
Dual/multi - source/chamber approaches	Diffusion (in macroporous gel)	-	Time	Macroscale	3-D	Limited	242, 243, 257, 259
	Monomer flow, diffusion (in solution)	Microfluidics[b]	Channel design, monomer flow	Micro to macro-scale	2-D	Yes	265, 267, 268
Microprinting	Concevtion and diffusion (in macroporous gels)	Contact-less controlled microdispensing	Droplet ejection rate, stage translation rate	Macroscale	2-D or 3-D	Yes	249, 263
Soluble factor gradients (controlled release approach)[b]							
Phosphatidyl choline-based lipid microtubules (LMTs) in gels	LMT loading in gels	Gelation by cooling	LMT loading profile (the step size)	Macro-scale	3-D	Limited	250
Microsphere-based scaffolds	Matrix preparation using microspheres loaded with the active factors	Melding the microspheres (using heat-sintering, ethanol-melding or dichloromethane treatment)	Microsphere size, polymer properties (degradation, molecular weight, etc)	Macro-scale	3-D	Limited	269, 270
Immobilized factor gradients							
Single source/chamber approaches	Diffusion (in macroporous scaffolds) (covalently bound)	EDC-NHS chemistry	-	Macroscale	3-D	Limited	271
	Diffusion (adsorbtion on surface)	Capillary method	-	Macroscale	2-D	Limited	246
Dual source/chamber approaches	Diffusion (in gels)	Hetero-bifunctional crosslinker	-	Micro to macro-scale	3-D	Limited	245, 250
Pump-/gravity-driven flow of factor solution	Convection (in macroporous scaffolds)	EDC-NHS chemistry	Suction rate	Macroscale	3-D	Yes	271
	Convection (monomer flow)	Photopolymerization (factor entrapped)	Monomer flow rate	Micro to macro-scale	2-D or 3-D	Yes	247, 248
		Photopolymerization (factor covalently attached)	Monomer flow rate	Micro to macro-scale	2-D or 3-D	Yes	251-253
	Monomer flow, diffusion	Microfluidics, photopolymerization (factor covalently attached)/factor adsorbed	Channel design, monomer flow	Micro to macro-scale	2-D	Yes	140, 244, 266
Capillary force-driven flow of factor solution	Monomer flow, diffusion (adsorption on surface)	Microfluidics (factor adsorbed)	Capillary forces, channel geometry, substrate affinity for the factor	Micro to macro-scale	2-D	Limited	272
Grafting/Micropatterning	Differential photo-exposure (photomask)	Protein conjuagtion to a photoreactive species	Mask pattern	Micro to macro-scale	2-D	Yes	255
	Controlled-time exposure	Gradients of protein conjuagted to a photoreactive species	Photo exposure time controlled using a motorized stage	Micro to macro-scale	2-D	Yes	165, 261
		polymer graft density/thickness gradient (using motorized stage/photomask or differential dipping in an initiator solution (ATRP))	Photo exposure time, mask pattern and/or initiator exposure time (filling/removal rate)	Micro to macro-scale	2-D	Yes	144, 176, 163, 274
	Computerized printing (inkjet printing)	-	Pattern design, substrate and solution properties	Macroscale	2-D	Yes	273

[a] Solution-based gradients can be generated in 3-D. However, cells cannot be kept suspened and eventually attach to the substratur
[b] Some approaches of gradient generation have potential to provide spatial as well as temporal control; such as, microfluidic-based and controlled release approache
ATRP: Atom transfer radical polymerization, EDC: ethyl(dimethylaminopropyl) carbodiimide, NHS: N-hydroxysuccinimide

Table 4.1. Regional and directional tensile stiffness of the porcine condylar cartilage[a]

Modulus (MPa)	Anteroposterior (AP) Direction				Mediolateral (ML) Direction				AP vs ML *p* value[d]
	Medial	Central	Lateral	Overall AP	Anterior	Superior	Posterior	Overall ML	
Young's[b]	21.7 ± 4.4	29 ± 13	22 ± 11	24 ± 12	11.3 ± 7.9	8.7 ± 3.7	10.2 ± 4.5	10.1 ± 5.5	<0.0001
Instantaneous[c]	10.4 ± 6.4	14.3 ± 5.4	11.7 ± 6.5	12.2 ± 6.0	6.5 ± 5.2	6.1 ± 2.6	6.9 ± 3.0	6.5 ± 3.6	0.003
Relaxed	6.2 ± 4.4	8.8 ± 4.1	7.3 ± 4.6	7.4 ± 4.3	3.9 ± 3.5	3.6 ± 2.0	3.9 ± 1.9	3.8 ± 2.5	0.0009

[a] Errors are standard deviations, n=7.

[b] Slope of the stress-strain curve generated from continuous pull (6 mm/min).

[c] Obtained from the second order generalized Kelvin model.

[d] Significance of the results between the two directions tested. Note that no significant differences were observed between regions in a given direction.

Table 4.2. Regional and directional time constants for the porcine condylar cartilage[a]

Time constants (min)		Anteroposterior (AP) Direction				Mediolateral (ML) Direction			
		Medial	Central	Lateral	Overall AP	Anterior	Superior	Posterior	Overall ML
Kelvin model	τ_ε	43.3 ± 8.4	37.3 ± 8.4	47 ± 11	42.6 ± 9.7	44 ± 12	43 ± 13	42 ± 19	43 ± 14
	τ_σ	51.8 ± 8.4	43 ± 10	57 ± 13	50 ± 12	53 ± 12	53 ± 16	53 ± 23	53 ± 17
2nd order	$\tau_{\varepsilon 1}$	38.5 ± 5.8	32.4 ± 8.2	42.5 ± 9.6	37.8 ± 8.7	38 ± 12	40 ± 13	39 ± 19	39 ± 14
generalized Kelvin	$\tau_{\sigma 1}$	49.3 ± 5.7	40 ± 11	54 ± 13	48 ± 11	49 ± 12	52 ± 17	53 ± 22	52 ± 17
	$\tau_{\varepsilon 2}$	0.84 ± 0.31	0.72 ± 0.16	1.12 ± 0.43	0.89 ± 0.35	0.80 ± 0.45	0.90 ± 0.31	0.86 ± 0.39	0.85 ± 0.37
	$\tau_{\sigma 2}$	1.25 ± 0.45	1.04 ± 0.21	1.61 ± 0.62	1.30 ± 0.50	1.18 ± 0.49	1.29 ± 0.29	1.38 ± 0.91	1.28 ± 0.59

[a] τ_ε and τ_σ are stress relaxation and creep time constants, respectively. Errors are standard deviations, n=7.
Italicized time constants correspond to the slow relaxation phase.

Table 5.1. Previous studies of the condylar cartilage under compression

Group	Region	Load profile	Testing parameters		Modulus of elasticity[b] (MPa)	Additional property[b]	Equilibrium modulus?	Species (Age)	Method
			Step stress (MPa)	Frequency (Hz)					
						Creep time constant (s)			
Kuboki *et al.* , 1997 [a] [8]	Anterior	Sustained	0.51	-	2.684	125.5 ± 23.3	Yes	Porcine	Indentation
			1.02		3.591	112.5 ± 33.0		(7 months)	
			1.53		4.751	104.0 ± 28.8			
		Intermittent	0.51	0.33 [c]	3.355	146.5 ± 35.2			
			1.02		5	134.4 ± 15.0			
			1.53		6.623	139.8 ± 25.0			
						Poisson's ratio			
Hu *et al.* , 2001 [43]	Anteromedial	Dynamic	-	14	2.34 ± 0.26	0.46 ± 0.05	No	Rabbit	Atomic Force
	Anterolateral				1.51	0.41		(6 weeks)	Microscopy
	Posteromedial				1.11 ± 0.07	0.38			
	Posterolateral				0.95 ± 0.06	0.31 ± 0.05			
Patel and Mao, 2003 [44]	Anteromedial	Dynamic	-	14	0.95 ± 0.15	-	No	Rabbit	Atomic Force
	Posterolateral				1.02 ± 0.22	-		(7 days)	Microscopy
					Complex modulus[e]	Storage & loss moduli[e]			
Tanaka *et al.* , 2006 [45]	Anteromedial	Dynamic	-	0.01 - 10 [d]	1.40 ± 0.39	1.36 ± 0.38, 0.34 ± 0.07	No	Porcine	Indentation
	Anterolateral				1.15 ± 0.33	1.12 ± 0.32, 0.24 ± 0.07		(6-9 months)	
	Posteromedial				0.81 ± 0.21	0.79 ± 0.21, 0.16 ± 0.04			
	Posterolateral				0.73 ± 0.26	0.72 ± 0.25, 0.16 ± 0.05			

[a] The results tabulated here are obtained by comparining the function curve-fitted by Kuboki *et al.* , i.e. A(1-exp(-t/ζ)), to the Kelvin model having the assumption that $\mu_1 << \mu_0$. The equilibrium modulus of elasticity reported has been calculated using the mean values of A.

[b] Mean ± standard deviation

[c] Intermittent compression of 1 second duration at 2 second intervals

[d] Frequency sweep

[e] Numerical values provided via personal communication, representing a frequency of 1 Hz

Table 5.2. Viscoelastic compressive properties of the porcine condylar cartilage [a]

	Modulus (kPa)			Time constants (min) [b]					
	Elastic [c]	Instantaneous [d]	Relaxed	Kelvin		2nd order generalized Kelvin			
				τ_{ε}	τ_{σ}	$\tau_{\varepsilon 1}$	$\tau_{\sigma 1}$	$\tau_{\varepsilon 2}$	$\tau_{\sigma 2}$
Anterior	826 ± 323	238 ± 132	9.4 ± 3.5	11.8 ± 1.1	37.0 ± 6.5	8.4 ± 1.4	49.1 ± 9.7	0.4 ± 0.1	6.6 ± 1.5
Medial	1297 ± 384	487 ± 162	16.1 ± 8.5	11.5 ± 1.0	39.4 ± 5.6	7.4 ± 1.1	54.8 ± 9.3	0.4 ± 0.2	10.0 ± 2.0
Central	1316 ± 229	526 ± 122	16.4 ± 5.7	10.2 ± 2.2	34.2 ± 7.8	6.8 ± 1.7	50.7 ± 8.2	0.4 ± 0.1	10.9 ± 2.6
Lateral	1411 ± 238	555 ± 150	16.0 ± 2.3	11.1 ± 1.8	33.6 ± 4.8	7.0 ± 1.5	46.2 ± 6.3	0.4 ± 0.1	11.2 ± 3.2
Posterior	1526 ± 400	519 ± 186	22.5 ± 7.5	12.5 ± 1.3	35.9 ± 4.6	8.8 ± 1.4	46.1 ± 5.5	0.4 ± 0.1	7.4 ± 1.9

[a] Mean ± S.D., n = 9, except for medial and lateral regions with n = 8.

[b] τ_{ε} and τ_{σ} are stress relaxation and creep time constants, respectively, and subscripts 1 and 2 refer to slow and rapid relaxation, respectively.

[c] Slope of the linear region of the stress-strain curve generated from continuous pull.

[d] Obtained from the second order generalized Kelvin model.

Italicized time constants correspond to the slow relaxation phase.

Table 5.3. Statistical evaluation of the differences in regional compressive properties of the porcine condylar cartilage (p values) [a]

Comparison	Modulus			Time constants[b]					
	Elastic	Instantaneous	Relaxed	Kelvin		2nd order generalized Kelvin			
				τ_{ε}	τ_{σ} [c]	$\tau_{\varepsilon 1}$	$\tau_{\sigma 1}$ [c]	$\tau_{\varepsilon 2}$ [c]	$\tau_{\sigma 2}$
Anterior vs. Medial	**0.04**	**0.01**	0.2	1.0	-	0.6	-	-	**0.04**
Anterior vs. Central	**0.02**	**0.002**	0.1	0.2	-	0.1	-	-	**0.003**
Anterior vs. Lateral	**0.005**	**0.001**	0.2	0.9	-	0.3	-	-	**0.002**
Anterior vs. Posterior	**<0.0005**	**0.003**	**<0.0005**	0.9	-	1.0	-	-	1.0
Medial vs. Central	1.0	1.0	1.0	0.4	-	0.9	-	-	0.9
Medial vs. Lateral	1.0	0.9	1.0	1.0	-	1.0	-	-	0.8
Central vs. Lateral	1.0	1.0	1.0	0.7	-	1.0	-	-	1.0
Medial vs. Posterior	0.6	1.0	0.2	0.7	-	0.3	-	-	0.2
Central vs. Posterior	0.6	1.0	0.2	**0.03**	-	**0.05**	-	-	**0.02**
Lateral vs. Posterior	0.9	1.0	0.2	0.4	-	0.1	-	-	**0.01**

[a] Bold indicates statistically significance differences. n = 9, except for medial and lateral regions with n = 8.

[b] τ_{ε} and τ_{σ} are stress relaxation and creep time constants, respectively.

[c] Significance level of $p<0.05$ was not detected by ANOVA.

Table 6.1: Comparison of Glass Transition Temperatures (T_g) using Differential Scanning Calorimetry [a]

	T_g (°C)
Pure PLGA 50:50	41.62 ± 0.37
Microspheres	41.04 ± 0.17
Scaffold [b]	33.98 ± 0.09

[a] Errors are standard deviations, n = 3.
[b] Prepared by using 50 min ethanol soak.

Table 6.2: Comparison of different evaluation methods employed to evaluate the porosity of the scaffolds [a]

Evaluation Method	% Porosity [b]
MicroCT 3-D reconstruction	41.1 ± 2.1
MicroCT image analysis using ImageJ	41.5 ± 4.9
Theoretical porosity	44.9 ± 1.9

[a] Scaffolds prepared using 50 min ethanol soak-time.
[b] Errors are standard deviations, n = 4.

Table 8.1. Biochemical assay results following 3 wk cell culture [a]

Scaffold Group	Number of cells	GAG content (μg)	Hydroxyproline content (μg)
Chondrocytes	$5.8 \pm 1.0 \times 10^4$	12.8 ± 7.1	1.8 ± 0.8
HUCMSCs	$5.9 \pm 1.0 \times 10^4$	2.8 ± 1.0	1.8 ± 0.4

Mean ± S.D.; n = 4, except for cell number for the chondrocyte-seeded group with n = 3.